INVESTIGATION OF SENSING BEHAVIOR OF MoS_2 BASED NANO-COMPOSITES

Thesis Submitted for the Award of the Degree of

DOCTOR OF PHILOSOPHY

in

Physics

By
Seema Sharma

Registration Number: 12009839

Supervised By
Dr. Kawaljeet Singh (16468)
Department of Physics (Professor)
Lovely Professional University

LOVELY PROFESSIONAL UNIVERSITY, PUNJAB
2024

DECLARATION

I, hereby declare that the presented work in the thesis entitled "**Investigation of sensing behavior of MoS_2 based nanocomposites"** in fulfillment of degree of **Doctor of Philosophy (Ph. D.)** is an outcome of research work carried out by me under the supervision of Dr. Kawaljeet Singh Samra, working as Professor of Physics, in the School of Chemical Engineering and Physical Sciences, of Lovely Professional University, Punjab, India. In keeping with the general practice of reporting scientific observations, due acknowledgments have been made whenever the work described here has been based on the findings of other investigators. This work has not been submitted in part or full to any other University or Institute for the award of any degree.

Seema Sharma

(Signature of Scholar)

Name of the scholar: Seema Sharma
Registration No.: 12009839
Department/School: Department of Physics
Lovely Professional University,
Punjab, India

CERTIFICATE

This is to certify that the work reported in the Ph. D. thesis entitled "**Investigation of sensing behavior of MoS_2 based nanocomposites**" submitted in fulfillment of the requirement for the award of degree of **Doctor of Philosophy (Ph.D.)** in the School of Chemical Engineering and Physical Sciences, is a research work carried out by Seema Sharma, 12009839, is bonafide record of his/her original work carried out under my supervision and that no part of thesis has been submitted for any other degree, diploma or equivalent course.

(Signature of Supervisor)

Name of supervisor: Dr. Kawaljeet Singh Samra
Designation: Professor
Department/School: Department of Physics
University: Lovely Professional University

ACKNOWLEDGMENT

I am deeply grateful to God for granting me the health and financial means to complete my Ph. D. research. A heartfelt gratitude goes to my Ph.D. supervisor, Dr. Kawaljeet Singh Samra, Professor of Physics, at Lovely Professional University. Dr. Samra accepted me as his student and provided invaluable scientific guidance and support throughout my doctoral journey. His mentorship has shaped not only my research but also my academic and personal growth. I would like to express my appreciation to Prashant Kumar, Assistant Professor of Physics, at Lovely Professional University, whose discussions and camaraderie enriched my academic experience and provided a supportive environment. My mother, Smt. Lata Devi has been an integral part of my life since my very beginning. She has gone beyond the role of a mother, making sacrifices to ensure I could pursue academic excellence. Words are insufficient to express my gratitude, and I pray for more time together to bring endless smiles to her face. I would like to express my deepest gratitude to my husband, Rohit Sharma, for his unwavering support and encouragement throughout the course of this thesis. His patience, understanding, and belief in my abilities have been a constant source of motivation. Without his support, this achievement would not have been possible. Thank you for being my rock and for always standing by my side as I pursued my goals. I am grateful for the companionship and support of my colleagues, Shakra Jabeen, Sandeep Kumar, and Anjori Sharma. Finally, I want to express my profound appreciation to everyone who contributed to my thesis, whether directly or indirectly, including friends, mentors, and study participants. The contributions you made were not overlooked and are much appreciated. The present research is committed to the quest for knowledge and the progress of science, with the goal of making a significant addition to our understanding of electrochemical biosensing.

List of Figures

List of Tables

ABSTRACT

Chapter 1 is a minireview based on molybdenum disulfide and its sensing applications. Diagnosing health-related issues, environment monitoring, meteorology, and detecting toxic reagents are serious issues to be taken care of with the assistance of a suitable sensor. This review explores the competence of molybdenum disulfide within the sensing province. The physical and chemical properties of molybdenum disulfide have been discussed thoroughly in order to justify its suitability as an electrochemical sensing material. A detailed outline of various synthesis techniques used to prepare molybdenum disulfide has been explored. In this work, an overview of the materials which have been detected by employing molybdenum disulfide-based nanocomposites is given. The main highlight of this review is to explore electrochemical sensing applications of molybdenum disulfide-based nanocomposites in multiple sectors. Further issues are discussed, giving future scope to emerging researchers to work in this field.

Chapter 2 will cover the synthesis procedure of various MoS_2-based nanocomposites, chemicals used, characterization techniques, and the technical details of the instruments used for characterization. Methods used for structural studies; X-ray diffraction, Raman spectroscopy; morphological studies field emission scanning electron microscopy, energy dispersive X-ray analysis, high-resolution transmission electron microscopy, Brunauer-Emmett-Teller Method; compositional studies; Fourier transform infrared spectroscopy, ultraviolet-visible spectrometry, X-ray photoelectron spectroscopy, and electrochemical characterizations like cyclic voltammetry, differential pulse voltammetry, and impedance spectroscopy are discussed in detail. The fundamental principles and workings of these techniques are explained comprehensively.

In Chapter 3, we investigated the influence of reduced graphene oxide (RGO) in the MoS_2-RGO nanocomposite for the sensing of ascorbic acid. The MoS_2-RGO nanocomposite was synthesized using an in-situ microwave-assisted technique, and confirmation of the nanocomposite formation was conducted through field emission scanning electron microscopy, X-ray diffraction, and Raman Spectroscopy. Electrochemical measurements were performed using cyclic voltammetry, differential pulse voltammetry (DPV), and impedance spectroscopy (EIS). The developed sensing material exhibited a noticeable linear increase in current concerning the analyte's concentration. It demonstrated a precise limit of detection of approximately 0.43 μM/0.16 μM and a remarkable sensitivity of about 2.9 $\mu A \mu M^{-1}$ cm^{-2}/1508

Ω μM^{-1} cm^{-2} with DPV/EIS. The Nyquist plots revealed an inductive behavior attributed to the intercalation process on the electrode surface and analyte dissociation in the buffer solution, which contributed to the MoS_2-RGO@GCE's remarkable sensing capability towards ascorbic acid. For MoS_2-RGO, it was observed that introducing uric acid (UA) into the buffer solution alongside ascorbic acid (AA) led to the emergence of two separate peaks. However, as the concentration of uric acid gradually increased, there was a concurrent increase in the peak current of ascorbic acid, affecting the sensor's selectivity.

Chapter 4 presents the synthesis of cobalt-doped MoS_2/reduced graphene oxide (Co-MoS_2/RGO) nanocomposites employing a microwave-assisted synthesis method. These nanocomposites were meticulously characterized, revealing intricate details of their nanostructure and surface morphology. Electrochemical analyses demonstrated distinct sensing mechanisms for the electrochemical oxidation of ascorbic acid and uric acid at the Co-MoS_2/RGO interface. The sensor exhibited a diffusion-controlled behavior, achieving remarkable limit of detections of 0.07 μM for AA, 0.22 μM for UA, 0.27 μM for AA in the solution having UA, and 0.47 μM for UA in the solution having AA. Additionally, the Co-MoS_2/RGO composite demonstrated impressive individual and selective sensitivities for AA, measuring 8.42 and 2.786 μA μM^{-1} cm^{-2}, respectively, and for UA, measuring 10.628 and 7.25 μA μM^{-1} cm^{-2}, respectively. These results highlight the exceptional capability of the Co-MoS_2/RGO nanocomposite to distinguish and accurately quantify concentrations of AA and UA, both individually and simultaneously. Furthermore, the Co-MoS_2/RGO sensor demonstrated outstanding repeatability and reproducibility, consistently delivering high performance even after 15 days. These findings underscore the potential of the Co-MoS_2/RGO-based electrochemical sensor as an ultra-sensitive, highly selective, and dependable tool for real-time sample analysis in practical applications.

In Chapter 5, we introduce an electrochemical biosensor based on manganese-doped molybdenum disulfide/reduced graphene oxide (Mn-MRG) for the selective sensing of uric acid in the solution having interfering species, particularly ascorbic acid. The Mn-MRG composites have been synthesized utilizing a fast and efficient microwave-assisted synthesis technique, harnessing the synergistic effects of Mn-MoS_2 and RGO for enhanced electrochemical properties. The designed biosensor demonstrates exceptional performance exhibiting a low detection limit of 80 nM for UA. The biosensor also demonstrates a broad linear response range from 30μM to 1.1mM, showcasing its versatility for various

concentration levels. Interestingly, the biosensor exhibited a concurrent increase in the identification peak of AA alongside UA when using MRG, highlighting the challenge of selectivity. However, after doping with 9% manganese, the biosensor demonstrated exclusive and selective detection of uric acid, effectively eliminating interference from ascorbic acid. This remarkable selectivity can be attributed to the specific interactions and improved electron transfer kinetics enabled by Mn doping. MoS_2 and RGO contribute to the oxidation of both UA and AA. However, Manganese behaves differently. It acts as an oxidizing agent for UA and a reducing agent for AA. Furthermore, as the doping level increases, Mn accelerates its role as a redox agent, simultaneously contributing to the oxidation of UA and the reduction of AA. The Mn-MRG biosensor's exceptional performance, coupled with its selectivity even in the solution having interfering substances, suggests its promising potential for practical applications in biomedical and clinical settings for precise UA detection.

In Chapter 6, we have reported the successful synthesis of MoS_2, MoS_2/reduced graphene oxide (RGO), and cobalt-doped MoS_2/RGO (Co-MoS_2/RGO) nanocomposites using a microwave-assisted technique. We comprehensively characterize the nanocomposites through XRD, FESEM, HRTEM, and Raman spectroscopy, providing detailed insights into their nanostructure and surface morphology. Electrochemical investigations utilizing CV and DPV reveal that the electrochemical oxidation of Resorcinol (RS) at the Co-MoS_2/RGO interface follows a stepwise electro-oxidation process. With a linear detection range for RS of 1 to 10.0 μM and an astoundingly low detection limit of 20 nM, the sensor displays diffusion-controlled behavior. Selectivity studies demonstrate that potential interferents, such as AA and UA, do not affect sensor performance. Moreover, the Co-MoS_2/RGO sensor shows excellent repeatability and reproducibility, maintaining high performance even after two weeks. These findings highlight the potential of the Co-MoS_2/RGO-based electrochemical sensor as a highly sensitive, selective, and reliable tool for practical applications in real-time sample analysis.

Table of contents

Chapter 1

Molybdenum Disulfide as a Propitious Electrochemical Sensing Material: A Mini Review

The advancement of sensor technology has greatly enhanced our quality of life and allowed us to accomplish previously impossible tasks. For instance, sensors are utilized in the healthcare sector to track vital signs, monitor patients remotely, and identify potential health issues. Sensors are also widely used in daily life applications such as home automation, smart appliances, security systems, and transportation [1]. Different types of sensors are required, depending on the specific application. Several sensors, such as electrochemical, pressure, thermal, magnetic, etc., are listed in Table 1.1, along with the purpose for which they are designed. According to World Health Organization (WHO) data from 2019, the global average healthy life expectancy at birth was estimated to be around 63.7 years. The concept of healthy life expectancy refers to the number of years a person is expected to live in good health without significant disability or illness. It provides a measure of quality of life and is an important indicator of population health. Due to socioeconomic conditions, lifestyle choices, and healthcare access all over the world, healthy life expectancy is hampered [27]. This increases the demand for modern techniques and tools to find and diagnose various diseases. Electrochemical sensors are the most suitable for diagnosing health-related issues among all the sensors listed in Table 1.1. These types of sensors use chemical reactions to produce an electrical response that can be measured and investigated. They are highly sensitive and selective, allowing them to detect even small concentrations of target molecules [28]. Advances in sensor design and integration techniques have facilitated the development of electrochemical sensors capable of detecting multiple analytes simultaneously. These sensors are essential for applications that require monitoring complex chemical environments. The use of electrochemical sensors in biomedical chemistry, the food processing industry, and ecological research show their versatility and applicability [4]. The current research trend focuses on emerging chemical approaches and challenges related to performance, attributes such as high specificity, high sensitivity, quick response, and versatile applicability. Applications of electrochemical biosensors based on DNA interactions are particularly promising, given the ability to discriminate and withstand challenges in nucleic acid chemistry. These electrochemical sensors might improve forensic science, drug screening, environmental monitoring, differential genetic expression assessment, infectious agent detection, and genetic illness diagnosis [29].

Table 1.1 Various types of sensors and their respective applications

Types of sensors	**Working Principle**	**Scope**
Electrochemical Sensor: Incorporating a chemically selective layer within an electrochemical transducer to extract information about the composition of the system [2].	Chemical reactions in a system lead to changes in electrical potential [3].	Clinical diagnosis, food analysis, chemicals, Pharmaceuticals, etc.[4],
Radiation Sensor: Employing light-matter interaction to detect an element of interest [5].	The interaction of target molecules causes a shift in the characteristic optical signal.	Digital imaging, Scanning, law enforcement, etc., [6]
Thermal Sensor: Used to measure the amount of heat exchanged in a system and it's surroundings [7].	A change in temperature leads to a change in the system's resistance.	Forest monitoring [8], microwave ovens, refrigerators, air conditioners, etc., [9]
Pressure Sensor: Measure strain imposed on a system.	A change in pressure causes a change in resistance or voltage.	Flexible electronic skin, games, cars, etc., [10]
Acoustic Sensor: detect mechanical vibrations produced due to the inflection in the surface acoustic waves [11]	Moving diaphragm which transduces its deflection into an electrical signal	Microphones [12], headphones, and hydrophones [13]
Magnetic Sensor: Determine the magnitude of magnetism caused by current or any magnetic material [14].	A change in the magnetic moment is produced while exposing a magnetic substance under the influence of a magnetic field	Navigation [15], Labeling with immunoassays [16], position tracking [15], and switches [17].
Biosensor: A transducer that provides the selective information of the analyte by using a biologically approved element [18].	The interaction of the bioreceptor with the analyte produces a change in the output signal	Food adulteration [19], Diagnosing various health issues such as thyroid [20], uric acid [21], and diabetes [22].
Gas Sensor: A device that identifies and measures the change in the concentration of gasses or vapors [23].	The amount of gas adsorbed on the active surface of the substance produces a noticeable response [24]	Detection of toxic gasses [25], and gas leakage detection [26].

Moreover, the integration of chemical and biological methodologies with technical advancements in micromachining and microfabrication processes is gaining momentum. As a result, disposable single-use devices, sensor arrays, or more advanced gadgets that can fully integrate numerous analytical procedures have been developed [30]. Electrochemical sensors have advanced the Point-of-Care Diagnostic (POCD) field by enabling rapid and on-site analysis of analytes. It's fascinating to see the rapid progress in the realm of electrochemical sensing technologies. Overall, electrochemical sensing has enormous potential for extensive applications. The alertness of the scientific community has redirected the evolution of nanotechnology from conventional sensing techniques and constructed highly selective sensors with the nano-molar level sensing of bio-analytes [31]. For designing a good electrochemical sensor, it must have high selectivity, stability, and operating life; linearity of response; quick reaction time and recovery time; sensitivity; and reproducibility of the signal response [32]. Contrary to bulk materials, two-dimensional (2D) materials have great potential in applications like sensing, supercapacitors, gas storage, and electronics. 2D materials allow free charges to move in two dimensions [33]. Therefore, these materials show extraordinary catalytic activities as they offer a specific surface area to adsorb various aromatic compounds on their basal plane due to van der Waals interactions [34, 35]. In semiconducting 2D materials, graphene research has gained much interest. Graphene is obtained by the chemical delamination of graphite [36]. Even though graphene is among the ultra-thin and durable compounds, a lightweight material, and a good conductor of electricity and heat at ambient temperature, it has several limitations when it comes to sensing. Graphene has no bandgap, which results in lower sensitivity. This limitation prompted researchers to look at other materials, such as Transition metal dichalcogenides (TMDs), which exhibit indirect energy gaps typically ranging from 1.0 to 2.0 eV, making them suitable for electronic devices [37]. Transition Metal Dichalcogenides (TMDs), due to their unique electrocatalysts, electronics, and optical properties, have attracted new interests that can be utilized in the development of novel sensing platforms [38].

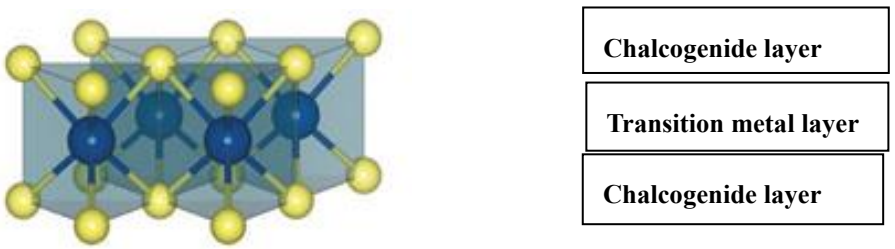

Fig. 1.1 Sandwich diagram demonstrating TMDs. Copyright Royal Society Chemistry 2023.

TMDs consist of a transition metal layer wedged between two chalcogenide layers, forming an MX_2 structure as shown in Fig.1.1 [39]. Molybdenum disulfide (MoS_2) is the highly promising 2-D material among the many blends of TMDCs due to the fact that its primary components are abundant and innocuous. The production of the material is the crucial experimental stage before deploying it in various sectors. Different synthesis techniques, like physical vapor deposition [40] and chemical vapor deposition [41], determine the material's qualities for various uses. When compared to the equivalent selenides and tellurides, the fabrication of MoS_2 in a single or few layers in TMDCs is readily achievable [42]. Fig. 1.2 displays the basic chemical structure of MoS_2, and it gives a glimpse of the fundamental nature of Mo and S atoms individually. Sulfur atoms can create vacancy defects in the MoS_2 structure, which can lead to changes in the properties of the material [47]. These vacancy defects can introduce additional active sites for electrochemical reactions, which can revamp the sensitivity and selectivity of MoS_2-based sensors. In addition, sulfur vacancies can also alter the optoelectronic properties of MoS_2, such as changing its bandgap and enhancing its photoluminescence. This can make MoS_2 more suitable for certain sensing applications, such as fluorescence-based detection of biomolecules [49].

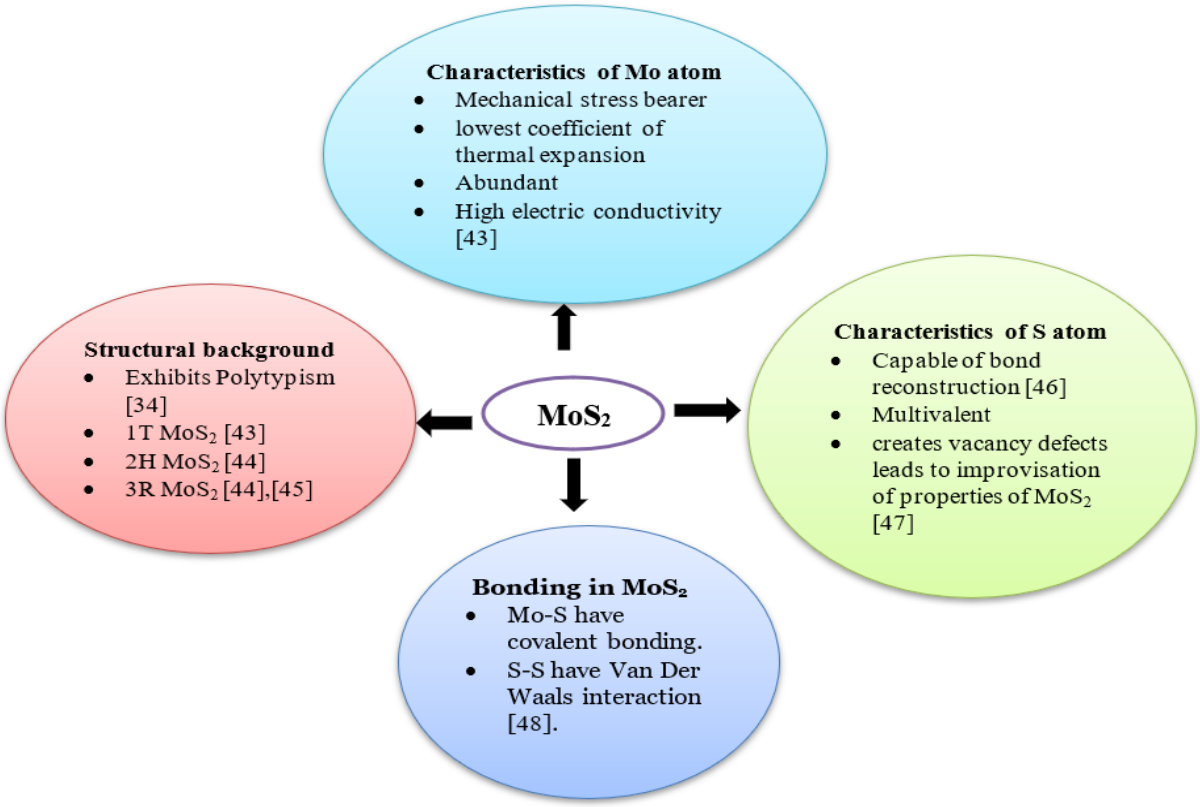

Fig. 1.2 The chemical structure of MoS_2.

However, it's noteworthy that the existence of sulfur vacancies can also lead to increased chemical reactivity and instability of MoS_2, which can affect the lasting stability and reliability of MoS_2-based sensors. Therefore, controlling and optimizing vacancy defects in MoS_2 synthesis is crucial for developing high-performance sensors. For highly responsive electrochemical sensing of intriguing redox species linked to biological molecules, medicines, environmental pollutants, and gaseous particles, numerous types of MoS_2-based nanocomposite electrodes have been developed recently [4]. These electrochemical studies indicate that MoS_2 nanostructures have outstanding electrocatalytic efficiency and a broad range of analytical applications. Overall, this review offers a holistic sketch of the composition, properties, synthesis methods, and real-world utilization of MoS_2-based electrochemical sensors in the realm of sensing.

1.2 Properties of MoS_2

1.2.1 Structural properties

Same like Graphene MoS_2 has a multilayered structure that can be chemically exfoliated into a monolayer and this thing motivated researchers to recruit this material for novel sensing [50]. MoS_2 exhibits three different crystal phases, 1T MoS_2 (Single layer tetragonal molybdenum disulfide) [43] having octahedral symmetry, 2H MoS_2 (Double layered hexagonal molybdenum disulfide) having trigonal prismatic symmetry [44], 3R MoS_2 (Triple-layered Rhombohedral molybdenum disulfide) possessing trigonal prismatic symmetry shown in Fig 1.3. [44],[45]. The crystal phases of MoS_2 can significantly affect its electrochemical sensing properties. The 1T form of MoS_2 is a metastable phase that can be attained through multiple methods such as doping or strain engineering. The 1T phase MoS_2 has a smaller band gap or even becomes metallic, resulting in enhanced electrical conductivity and improved electrocatalytic activity [51].

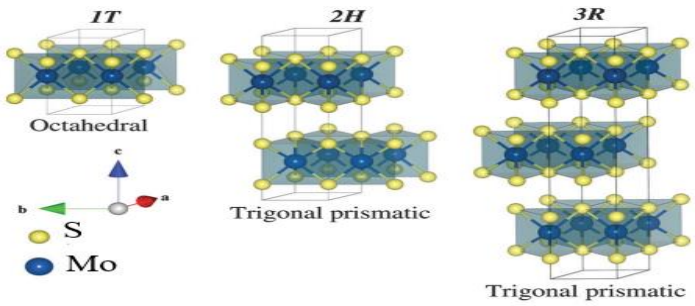

Fig. 1.3 Crystal phase Structure of 1T, 2H and 3R MoS_2 polymorphs side by side with their metal atom coordination. The numbers suggest the no. of layers in the unit cell and the letters represent trigonal, hexagonal and rhombohedral, respectively. Copyright Royal Society Chemistry 2023.

It can facilitate electron transfer during electrochemical reactions, leading to enhanced sensitivity and improved detection limits in sensing applications. These characteristics render it more appropriate for electrochemical sensing applications. Out of three different crystal phases the most stable one is 2H MoS_2. It comprises of the stacked lamina of MoS_2 bonded together by weak van der waals forces. MoS_2, in its 2H phase, is an indirect energy gap semiconductor with a comparatively high bandgap. (around 1.2-1.8 eV) [52]. This phase exhibits lower electrocatalytic activity due to its wider bandgap, limiting its potential for electrochemical sensing applications. At lower temperatures, it reflects semiconducting behavior, but at temperatures greater than 800º C, it shows metallic behavior when high pressure is applied. If 2H-MoS_2 is doped with Rubidium at low temperature it can show superconducting behavior [53]. The 3R phase of MoS_2 has thermodynamic stability which makes it more promising in the field of photonics, optoelectronics, and catalysis. The different crystal phases of MoS_2 can also affect the selectivity of the electrochemical sensor. The surface chemistry and exposed active sites may vary with the crystal phase, influencing the interactions with target analytes. This can lead to differences in the sensor's selectivity towards specific analytes or the existence of interfering species. Overall, the crystal phase of MoS_2 performs a pivotal role in influencing its electrochemical sensing performance, including catalytic activity, conductivity, and selectivity. Controlling and tailoring the crystal phase can be important for optimizing the sensor's performance for specific applications. One of the amazing properties of MoS_2 is that it is protean with respect to morphological structure. The morphological structure of MoS_2 can affect its surface area, which in turn can influence its sensing behavior. F. Chen et al. have experimentally demonstrated that MoS_2 can easily acquire different morphologies under different growth conditions, and these morphologies can have different surface areas as shown in Fig. 1.4 [54].

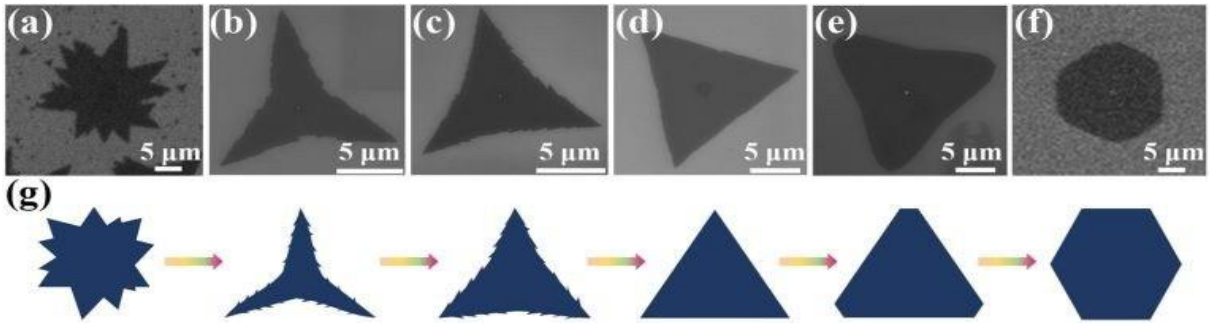

Fig. 1.4 (a)-(f) SEM images of synthesized MoS_2 flakes with different shapes; (g) schematic of morphological evolution of MoS_2 flakes at changing growth conditions. Copyright Royal Society Chemistry 2023.

MoS_2 with a larger surface area can provide more reactive sites for electrochemical reactions, which can lead to better detection of analytes [55]. Therefore, the morphology of MoS_2 can be tailored to optimize its sensing properties for specific applications.

1.2.2 Chemical properties

MoS_2 is part of a family of transition metal dichalcogenides. It is an inorganic compound that is found in nature in the mineral molybdenite. MoS_2 is generally sublime at low temperatures which is extremely useful for purification [56]. In the non-oxidizing environment, no other compound can replace MoS_2 as a lubricant due to its low friction coefficient [57]. MoS_2 is insoluble in water and dissolves properly in NMP [58], DMF [59], aqueous ammonia [60], and ethylene glycol [58]. MoS_2 quantum dots are synthesized by exfoliation techniques using NMP and DMF [61]. Weak Van Der Waals interactions illustrated in Fig. 1.5 are helpful to exfoliate MoS_2 from bulk to a few layers by simply Li intercalation [62]. The weak bonding between the layers also makes it possible to introduce defects into the structure of MoS_2 using suitable dopants. The defects created in MoS_2 can be utilized to enhance its electrochemical sensing characteristics. For example, the defects can enhance the surface area of MoS_2, leading to more reactive sites for electrochemical reactions and improved sensing performance. Considering that chemical doping of heteroatoms into the S planes of MoS_2 can change the material's electrical and optical characteristics and enhance its sensing capabilities, the topic has attracted a lot of study interest. The insertion of selenium (Se) into MoS_2 sheets for generating $MoS_{2(1-x)}Se2_x$ is one example of this doping [63].

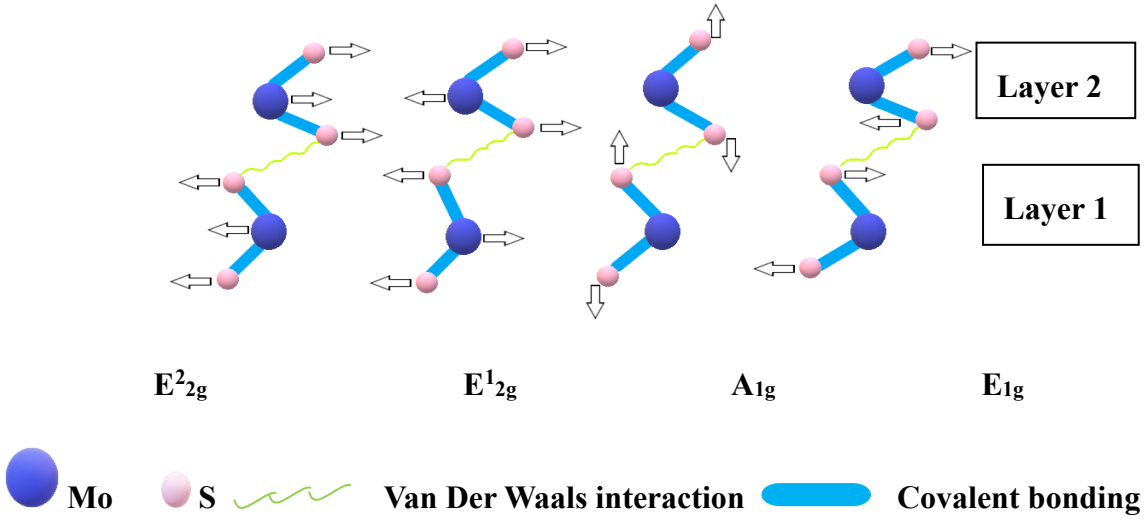

Fig.1. 5 Showing strong covalent bonding within the layer and weak Van der Waals interaction between two layers of MoS_2 sheets. Here arrows are showing various types of molecular vibrations in MoS_2.

The chemical and physical vapor deposition processes can be employed to fabricate these doped sheets, which have tunable chemical compositions, tunable band gaps, and enhanced optical properties [40],[41]. The characteristics of $MoS_{2(1-x)}Se_{2x}$ can be customized to fit certain sensing applications by adjusting the doping concentration. For instance, the $MoS_{2(1-x)}Se_{2x}$'s tunable band gap can be exploited to increase its sensitivity to particular analytes, while the increased optical characteristics can raise its detection limits [63]. In brief, the chemical doping of heteroatoms into MoS_2 sheets is a promising research area that could significantly enhance the sensing capabilities of MoS_2-based sensors.

1.2.3 Optical properties

We all are familiar with the well-known relationship $E=hc/\lambda$, where E is band gap energy, h is Planck's constant, c is the speed of light and λ is the wavelength of the photon. For optical phenomena like absorption to take place this condition has to be fulfilled. In the case of MoS_2 recent work displays the absorption coefficient of monolayer MoS_2 and multilayer MoS_2 lies in between the visible region [64]. One of the best qualities of MoS_2 is that it has a tunable bandgap as shown in Fig. 1.6. Unlike graphene, it has proven an ultimate contender in optical sensing platforms [65], [66]. MoS_2 can also be mechanically exfoliated from bulk to monolayer and hence bandgap tuning can be done [67]. Single layer MoS_2 has electrons typically, fermions with parabolic energy dispersion curve. It has a direct bandgap of 1.8 eV and shows semiconducting behavior. Under the influence of biaxial compression semiconductor-to-metal transition is predicted in single-layer MoS_2 using first principle calculations.

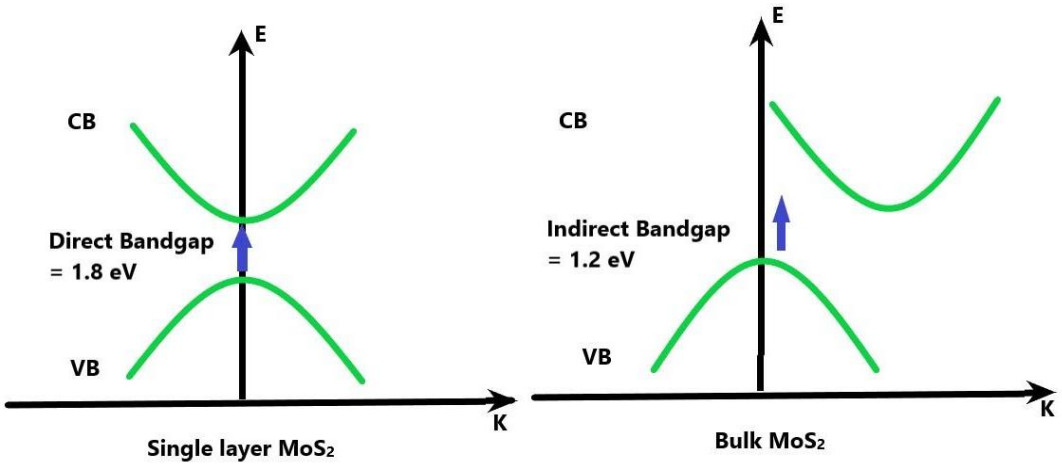

Fig. 1.6 Tunable band gap in MoS_2.

In a study, it was discovered that monolayer MoS_2 had a photoresponsivity of up to 880 $A.W^{-1}$ for incident light with a 561 nm wavelength [68]. Based on the graphene/MoS_2 heterostructure, the photodetector can achieve a photosensitivity value of over 10^7 A/W and a photogain of about 10^8 at room temperature ranging from 400 to 680 nm [69]. The enhanced photosensitivity can be explained due to the interaction between Dirac and parabolic bands of graphene and MoS_2 respectively.

1.2.4 Mechanical properties

Having sound knowledge of the mechanical properties of MoS_2 is important for realizing the strains in MoS_2 sheets due to the mismatching of lattice constants to enhance its carrier mobility [70]. It is vital when developing parts or structures for practical uses. For altering the structural and functional properties of nanomaterials mechanical properties play an important role [48]. Good mechanical stability is crucial as nanoscale devices have a high surface-to-volume ratio and are thus vulnerable to external perturbations. Young's modulus, yield stress, bending modulus, and buckling phenomenon are a few of the fundamental mechanical properties that are covered in this thesis. The formula for Young's modulus is $Y = E^{2D}/h$, where h is the film thickness and E^{2D} is the effective Young's modulus that is thickness independent. Through experimentation, the effective Young's modulus of monolayer MoS_2 was calculated as 120±30 $N \cdot m^{-1}$ indicating good elasticity in the material. The theoretical value for effective monolayer MoS_2 is given as 139.5 $N.m^{-1}$ mentioned in Table 1.2 [71]. The theoretical value of yield stress under a biaxial strain in monolayer MoS_2 was estimated by first-principles calculations to be 17.5 Nm^{-1}. The yield stress in monolayer MoS_2 was determined to be 15±3 $N \cdot m^{-1}$ using nanoindentation tests [72].

While there haven't been many investigations on the yield stress in monolayer MoS_2, the new structural transition has drawn a lot of interest. If a high yield stress is applied to MoS_2 it can tune its electronic properties and change it into metallic from a semiconductor. Bending occurs when perpendicular strain is applied to the molecule. The bending motion of MoS_2 is studied using the bending modulus. The bending modulus for MoS_2 is determined by:

$$D = \partial^2 W/\partial k^2 \quad \text{(I)}$$

where W is the bending energy density and k is the bending curvature. The bending modulus of monolayer MoS_2 was calculated as 9.61 eV [75].

Table 1.2 Mechanical properties of MoS_2

Mechanical Properties	Theoretical Value	Experimental Value
1. Young's modulus	139.5 $N \cdot m^{-1}$	120±30 $N \cdot m^{-1}$ [71]
2. Yield Stress	17.5 $N \cdot m^{-1}$	15±3 $N \cdot m^{-1}$ [72]
3. Buckling Strain	$\varepsilon_c = -43.52/L^2$	$\varepsilon_c = -0.0169$ [73]
4. Bending Modulus	6.62 to 13.24 eV	9.61 eV [74]

There will be more cross-plane interactions due to the trilayered sandwich atomic structure of monolayer MoS_2, which will offset the bending motion in it. An abrupt lateral deflection of one of the structural components is a defining characteristic of buckling, which is defined as instability leading to structural failure. According to recent studies, a number of conditions can cause nano-buckling. Among the causes, a temperature mismatch is the most significant. When exposed to temperature changes, substances' ability to maintain their structural integrity may be compromised since they frequently change their volume, shape, and area in reaction to temperature. According to the Euler buckling theorem, the buckling critical strain can be calculated using the following formula using the effective Young's modulus and the bending modulus:

$$\varepsilon_c = -4\pi^2 D/E^{2D}L^2 \quad (II)$$

where L is the length of the system in Å, D is the bending modulus and E^{2D} is the effective Young's modulus. For monolayer MoS_2, the values of E^{2D} = 139.5 $N \cdot m^{-1}$ and D = 9.61 eV, using it in equation (II)

$$\varepsilon_c = -43.52/L^2 \quad (III)$$

MoS_2 has a buckling critical strain that is twenty times greater than that of graphene for samples of the same length, meaning it is more difficult to buckle under external compression [74]. Molecular dynamics (MD) simulations and phonon analysis have both been used to study this phenomenon. There is one major issue associated with pristine MoS_2 which is restacking of interatomic layers. Restacking reduces the effective surface area and hence contributes to low electrochemical sensing. A deep understanding of mechanical properties mentioned in Table 1.2 is required to obtain untwisted MoS_2 nanosheets which will provide ordered nanosheets and thus help in overcoming this limitation. Theoretical values of buckling strain and bending modulus of monolayer MoS_2 predict it has superior mechanical properties as that of monolayer graphene. But there is limited experimental research related to its mechanical properties such as the mass sensitivity of MoS_2. These properties help to introduce defects at the atomic level

which is very helpful in enhancing electrochemical sensing. Thus, more intensive studies related to the mechanical properties of MoS_2 are needed to examine the electrochemical sensing behavior of MoS_2.

1.3 Synthesis methods of MoS_2

Recent methods to synthesize molybdenum disulfide include hydrothermal [75], chemical exfoliation [76], microwave-assisted synthesis [77], co-precipitation, chemical vapor deposition [35], atomic layer deposition [78], and mechanical exfoliation [79]. On comparing, we found that microwave-assisted synthesis, chemical exfoliation method, and hydrothermal method have drawn much attention in organic reactions as well as in the synthesis of sulfide materials. As mentioned above, the synthesis of MoS_2-based biosensor electrodes will be done by using mainly the co-precipitation hydrothermal method, chemical exfoliation, and microwave annealing methods mentioned in Table 1.3. As the different methods give different morphology, it is an important task to see which synthesis method gives the best morphological structure which further enhances the sensing properties of the nanocomposite. Here, we have discussed the synthesis methods which are suitable for electrochemical sensing.

1.3.1 Microwave annealing:

Microwave-assisted synthesis method requires less time with a high yield; it is the most common synthesis method to prepare MoS_2. Microwave radiations are non-ionizing electromagnetic radiations with a high penetration depth, which can significantly enhance the compound's nucleation rate and thus reduce the synthesis time [80]. Moreover, the microwave method is also featured with low reaction temperature [81], simple experimental setup, and environmental friendliness. It involves uniform heating, easy to prepare, energy-saving, small particle size distribution, and has very less impurities [82]. MoS_2/RGO nanocomposite synthesized via in-situ microwave-assisted synthesis is most promising for electrochemical sensing due to hierarchical granular morphology [83]. In a review paper, hydrothermal & solvothermal synthesis, thermal & chemical reduction, microwave & electrochemical synthesis, and chemical vapor deposition methods have been discussed thoroughly. For different applications suitable method is adopted as per the desired properties such as the number of reactive sites, morphology, thickness, etc., It summarized that microwave-assisted synthesis is the best suitable method for designing biosensors as they can be directly designed by electrochemists without using any chemical reductant and toxic compound at low cost consuming less energy [84].

Table 1.3 Synthesis of MoS_2-based nanocomposites with different methods and their application in sensing.

Method	Nanocomposite	Analyte	Detection Limit	References
Two-step hydrothermal synthesis	MoS_2-OCu	H_2O_2	0.077 µM	[86]
One-Pot hydrothermal process	MoS_2-PANI/RGO	Ascorbic acid Dopamine Uric Acid	22.2 µM 0.70 µM 0.36 µM	[89]
Solvent exfoliated method	MoS_2/GCE	Hg^{2+}	10^{-15}M	[90]
Exfoliation method	MoS_2-DNPs	Valproic acid	0.27 µm	[88]
Liquid Exfoliation Method	2DMoS_2/GCE	Free radical and hypochlorous acid	10 pM & 1 nM Respectively	[91]
Sol-gel Process	aptamer-MoS_2	Cardiac troponin I	0.95 pM	[92]
Electrodeposition	AuNPs@MoS_2/GCE	Ascorbic acid	100 µM	[93]
Single-step hydrothermal method	MoS_2/Aluminum	Uric acid	1.169 µM	[94]
L-cysteine assisted solution-phase method	MoS_2-Gr\GCE	acetaminophen	$2*10^{-8}$M	[95]
Hydrothermal method	rGO/MoS_2	Humidity Sensing	10 ppm NO_2, 1000 ppm NH_3, 50 ppm H_2 and 50 ppm C_2H_5OH	[96]

1.3.2 Hydrothermal/Solvothermal autoclave synthesis:

As the water is used as a solvent at high temperatures, it is termed as "Hydro+ Thermal= Hydrothermal method". This method is an artificial technique by which depending on the solubility of solutes in hot water at high temperature and high pressure, we can synthesize single-crystal nanoparticles having a particular size and morphology [85]. Basically, hydrothermal reactions are nothing but heterogeneous reactions that occur in the solution having an aqueous solution at high temperature and pressure. One of the main advantages of the hydrothermal method is that it can be employed with other synthesis techniques to obtain desirable morphology and it can be carried out in controlled conditions. No doubt it requires expensive autoclaves and is time-consuming. A two-step hydrothermal synthesis method is used for the preparation of MoS_2 nanosheets with organic copper nanowires to fabricate the

novel MoS_2-OCu nanohybrids. MoS_2-OCu nanohybrids being an active material have shown a remarkable performance in the electrochemical detection of H_2O_2 and Ascorbic Acid. The MoS_2 nanosheets possessing a large surface area offer reactive active sites for electrochemical processes making them an effective active material as the electrochemical substrate. OCu nanowire plays the role of spacers to isolate MoS_2 nanohybrid and increases the surface area and active sites of MoS_2 nanocomposite [86].

1.3.3 Chemical exfoliation method:

Exfoliation, in general, is the process by which materials expand along the spatial axis by factors as high as hundreds, producing puffed-up materials that are resistant to high temperatures and have low density [87]. We can obtain monolayered MoS_2 sheets from bulk MoS_2 using this method as mentioned in Table 1.3. An electrochemical sensor interlaced with DNPs (Diamond nanoparticles) and MoS_2 Nanocomposite was prepared by exfoliation method, and after that, the DNPs were straight away disseminated in H_2O and successively dropcasted on a glassy carbon electrode (GCE). The Differential Pulse Voltammetry (DPV) feedback of the working electrode was confronted with that of sensors including either of the nanomaterials (Diamond Nanoparticles (DNPs) or MoS_2). MoS_2-DNP nanosheets have boosted the performance of electrodes in sensing valproic acid. The electrode incorporating nanomaterials exhibited excellent sensitivity (740 $\mu A \cdot mM^{-1} \cdot cm^{-2}$), a 0.27 μM LOD, and an 8% RSD [88].

1.4 MoS_2 in the field of electrochemical sensing

Electrochemical sensing is a field of analytical chemistry that focuses on the sensing and quantification of biochemical species using electrochemical principles. It involves the implication of electrochemical techniques to measure the electrical properties of a system or a chemical reaction occurring at an electrode-electrolyte interface. Electrochemical sensors exhibit high selectivity towards various chemical processes, enabling efficient detection of different molecular species, even at the particle level [97].

1.4.1 Electrochemical techniques

Electrochemical sensing surpasses other sensing techniques as it is highly selective, more sensitive, provides more reliable information regarding complex chemical reactions, and is easy to design [98]. The versatility of electrochemical techniques allows for the sensing and quantification of diverse analytes including ions, small molecules, biomolecules, and gasses. Electrochemical measurements offer the advantage of real-time monitoring, enabling continuous or near-instantaneous measurements of analyte concentrations or reaction kinetics.

Electrochemical sensing has been extensively studied using materials such as graphene, MoS_2, carbon nanotubes (CNTs), metal nanoparticles, conducting polymers etc. [99]. Due to its amazing qualities, MoS_2 has become very well-known among them. MoS_2 can be employed as an electrode material, either as a standalone electrode or in hybrid structures with other materials. These hybrid architectures harness the synergistic effects of different materials, combining the special attributes of MoS_2 with the advantages of other components to further enhance electrochemical sensing. The detection and quantification of analytes in electrochemical sensing rely on measuring electrical signals generated during the electrochemical reaction. There are several key electrochemical techniques used in sensing various target analytes using MoS_2-based nanocomposites for electrochemical sensing enlisted below:

1.4.1.(a) Conductometry: It measures the conductance of the analyte in an electrolytic solution under the effect of applied potential. It consists of two electrode systems. They are simulated by an equivalent circuit [100],[101]. A (reduced graphene oxide) rGO/MoS_2-based hybrid electrochemical sensor is used for sensing the humidity content at room temperature using the conductometry technique as shown in Table 1.3. MoS_2 is known for its large surface area, which provides ample sites for moisture adsorption. This property makes it an excellent candidate for detecting humidity levels. On the other hand, rGO possesses functional groups on its upper layer, including oxygen-containing groups. These functional groups can interact with water molecules, making rGO sensitive to changes in humidity. The combination of MoS_2 and rGO in the nanohybrid structure provides synergistic effects, enhancing the humidity-sensing capabilities of the material. The nanohybrid material is synthesized using the hydrothermal method. Different composition of MoS_2-rGO was dropped on the SiO_2 substrate and the response was observed. They observed at room temperature electrochemical sensors respond to 10 ppm NO_2, 1000 ppm NH_3, and 50 ppm H_2 at 4%, 2.8%, 0.2%, and 0.8% respectively [96]. It suggests that conductometric MoS_2-rGO sensors show great potential as humidity sensors for environmental monitoring applications, offering benefits regarding sensitivity, response time, and humidity detection range. Continued research and advancement in this field can pave the way for the practical implementation of MoS_2-rGO humidity sensors in various industries and settings.

1.4.1.(b) Potentiometry: It determines the conglomeration of charge potential near the surface of the working electrode relative to the reference electrode. It consists of a three-electrode system. Nernstian curves are plotted for studying the sensing behavior of the analyte. MoS_2

nanoflakes have been used for the potentiometric detection of Pb^{2+} ions. Potentiometric detection of Pb^{2+} using MoS_2 nanoflakes offers a promising avenue for sensitive and selective Pb^{2+} sensing. By incorporating functionalized MoS_2 nanoflakes into the ion-selective membrane of an electrode, the potential change resulting from Pb^{2+} binding can be quantified and related to the concentration of Pb^{2+} ions in the solution. The advantages of using MoS_2 nanoflakes for potentiometric Pb^{2+} detection include their elevated surface area, which provides multiple active sites for ion binding, and their excellent electrical conductivity, allowing for efficient electron transfer. The findings show that the suggested electrode has a quick reaction time of less than 5 s and a Nernstian response slope of 27 mV/decade over a broad concentration range of $1.0*10^{-3}$ to $5.1*10^{-8}$ mol/L. Real samples were taken from a factory and were compared with standard sensors. This suggests its potential application for analyzing Pb^{2+} concentrations in various applications such as environmental, industrial, or biological samples as mentioned below in section 1.4.2 [102].

1.4.1.(c) Voltammetry: In this technique, a varying potential is exerted on an electrochemical system and a change in current is quantified. It consists of a three-electrode system. Depending upon the mode of potential given, Cyclic Voltammetric (CV) [103] Differential Pulse Voltammetric (DPV) [104], Linear Sweep Voltammetric (LSV) [105], Square Wave [106], and Stripping curves [107] are used to extract the quantitative and qualitative performance of the designed sensor. The most important voltammetry methods are discussed further in brief:

(i) Cyclic Voltammetry: CV is a famous and powerful modus operandi generally employed to inspect redox processes of various chemical compounds. Traces in CV are called voltammograms. It is a gem to study electron transfer phenomena in various chemical reactions. In CV we have a plot between applied potential and current. Visually data reported will appear to be rotated by 180º. The potential to be scanned is controlled by the scan rate. For higher current peaks the scan rate should be high. We require large supporting electrolyte concentrations to increase the conductivity. In CV we have 3 electrodes ensemble i.e., the working electrode, counter electrode, and reference electrode. The main task is that electrochemical responses are produced by an electrode under investigation while the reference electrode serves as a testimonial point as it has a well-established stable equilibrium potential. The role of a counter electrode is just to complete the circuit [103]. CV is an amazing tool to check the working of the electrochemical sensor prepared. A molybdenum disulfide-graphene aerogel and PEDOT:PSS membrane coated on a hemoglobin-based sensing framework (PEDOT:PSS/Hb/MoS_2-GA/GCE) is used for the detection of bromate [108]. The

electrochemical behavior of the designed sensor was examined using CV as mentioned in Table 1.4. The designed electrode displays an outspread linear range from 1.0 µmol/L to 10.0 mmol/L, with a low LOD of 0.35 µmol/L. The efficacy of the PEDOT:PSS/Hb/MoS_2-GA/GCE improved electrode for electrochemical sensing of bromate was significantly better as compared to palladium multiwalled carbon nanotubes modified glassy carbon electrode (Pd/MWNT/GCE) which exhibits a detection range from $0.1*10^4$ mmol/L to $0.4*10^4$ mmol/L and 10.0 µmol/L limit of detection. This can be due to the use of graphene aerogel as a supporter for MoS_2 in electrochemical biosensors addresses the poor conductivity issue of MoS_2 and takes advantage of the unique properties of both materials. This nanocomposite provides a large surface area, abundant mesopores, and rich channels, which collectively inflate the electrochemical activity and sensitivity of the biosensor. Further, by utilizing voltammetry for bromate detection, water quality monitoring agencies, environmental laboratories, and researchers can effectively assess the existence and concentration of bromate in water samples in order to prevent serious health issues arising due to water contamination.

(ii) Differential Pulse voltammetry: DPV is employed for both quantifiable chemical analysis and to study the mechanism, dynamics, and thermodynamics of chemical reactions. It is generally used with dropping mercury electrodes. It is an effective method that is used to see electrochemical activities, with a plot between current measured before each potential change. Current is examined two times in every pulse period (initially before the pulse, and at the end of the pulse). The measured difference between two current values is noted and displayed on the screen. This method describes the movement of electrons to and from the electrodes in the electrochemical system. It provides better selectivity for observing various redox reactions. This technique is used in biosensors to see the working of electrodes [104]. MoS_2-PANI/RGO (molybdenum disulfide polyaniline reduced graphene oxide) is used for the concurrent detection of ascorbic acid (AA), dopamine (DA), and uric acid (UA) employing the DPV technique. In DPV, distinct anodic peaks corresponding to AA, DA, and UA can be observed at different potentials, indicating their individual electrochemical oxidation processes. These peaks are well-resolved, enabling the simultaneous measurement and quantification of all three analytes. The study likely revealed that protons (H^+) play a significant role in the electrochemical oxidation of AA, DA, and UA [89]. By leveraging the advantages of MoS_2-PANI/RGO, the detection of UA, DA, and AA in the body fluid can be achieved with improved sensitivity, selectivity, and stability. This has significant implications for clinical diagnostics,

disease monitoring, and personalized healthcare, where the accurate quantification of uric acid can aid in the early detection and effective management of various medical conditions.

(iii) Stripping Voltammetry: It is a two-step voltammetry technique in which the initial deposition of the analyte is done on an electrode surface at a fixed potential and this process is known as the pre-concentration step. This step can be done during either oxidation or reduction which will decide whether the stripping is anodic or cathodic. rGO/MoS_2/CS (chitosan) nanocomposite is employed for the detection of Pb (II) in tobacco leaves employing square wave anodic stripping voltammetry technique as mentioned in Table 1.4. This work provides a novel and promising approach for the detection of Pb (II) in real tobacco leaf samples. The use of rGO/MoS_2/CS nanocomposites as electrode modifiers offers enhanced electrocatalytic efficiency and sensitivity for detecting Pb (II). The developed sensor based on this nanocomposite exhibits excellent consistency, durability, and anti-interference capabilities, making it a reliable tool for useful implementation in the analysis of Pb (II) contamination in tobacco leaves. The LOD for Pb (II) using the rGO/MoS_2/CS/GCE sensor was determined to be 0.0016 μM (0.33 ppb). This indicates that the sensor is very sensitive and capable of detecting low levels of Pb (II) in solution [109]. *1.4.1. (d) Amperometry:* It is employed to detect the amount of steady-state current produced due to the concentration of ions in the electrolyte at a fixed oxidation or reduction potential. It consists of a three-electrode system. Single potential amperometric and pulsed amperometric curves are plotted to analyze the data [110]. From Table 4 we can see that MoS_2-Au-Ag has been used for the electrochemical detection of hydrogen peroxide released by cancer cells using amperometric technique. The designed sensor exhibits micromolar detection of H_2O_2 with a sensitivity of 405.24 ($\mu A\ mM^{-1}\ cm^{-2}$) [111]. The high sensitivity of the sensor allows for precise quantification of H_2O_2 concentrations, which can provide valuable insights into cellular oxidative stress and the progression of cancer. The amperometric technique enables real-time monitoring, making the sensor suitable for dynamic and continuous measurements. MoS_2-Au-Ag shows high sensitivity and micromolar detection range making it a valuable tool for cancer research, diagnostics, and monitoring of H_2O_2-related processes in biomedical applications. Today's rapid urbanization and industrialization have created a significant ecological imbalance as well as a number of anomalies in the body's biochemical processes that require monitoring for safety and point-of-care testing uses.

Table 1.4 MoS_2-based electrochemical sensors in different industries.

Nanocomposite	Analyte	Electrochemical technique	LOD	Application	References
1. 1. MoS_2-Au-Ag	H_2O_2	Amperometry	7.19(µM)	Gas Sensing	[111]
2. 2. rGO/MoS_2/CS	Pb (II)	SWASV	0.0016(µM)	Food Safety	[109]
3.2D-MoS_2-MoO_3CC	Riboflavin	LSV	1.5(µM)	Medicines, Food Safety	[145]
4. MoS_2-Ag-CNF	VB2	DPV	0.02(µM)	Medicines, Food safety	[146]
5. PEDOT:PSS/Hb/MoS_2-GA/GCE	Bromate	CV	0.35(µM)	Water Contaminant	[108]
6. Au-MoS_2/Ch	Monosodium Glutamate	CV, DPV & EIS	0.03(µM)	Food Safety	[112]
7. MoS_2-Gr	Acetaminophen	DPV	0.02(µM)	Medicines	[147]
8. MoS_2-AuNPs	Ascorbic acid	DPV	2.1(µM)	Medicines, Food Safety, Clinical Diagnosis	[148]
9. MoS_2-Au NPs/GCE	cancer antigen 72-4 (CA72-4)	DPV, CV, EIS	20 (µM)	Clinical Diagnosis	[140]
10. HPMo/MoS_2	RAC and CLB	DPV	0.029 µM for RAC 0.153 µM for CLB	Food Safety	[116]
11. MoS_2/N-rGO	Epinephrine	CV	3.9 µM	Medicines	[129]
12. CuO/MoS_2	Sulfamethoxazole	SWV	0.34 pg/L		[131]
13. MIP-washed/Pt NPs/MoS_2/SPE	Glycated Albumin	EIS & SWV	0.34 nM	Clinical Diagnosis	[150]
14. MoS_2/MW-CNT	Epinephrine	CV	3 µM	Medicines	[150]
15. MoS_2 modified SPE	Copper	CV	0.3125 µM	Water Contaminant	[126]
16. Ag-MoS_2	Thiabendazole	Colorimetric	0.24µM	Food Safety	[113]
17. MoS_2 microflowers	Sunset Yellow FCF	LSV & DPV	0.04 µM	Food Safety	[114]
18. MoS_2@$CuCo_2O_4$	Glucose	DPV	0.5 mol/L	Food Safety, Clinical Diagnosis	[115]

19. ZnO-MoS_2	2,4,6-trinitrotoluene	CV, DPV	5.2×10^{-5} ppm	Explosion Hazards	[117]
20. 2H-MoS_2/Co_3O_4	2,4,6-trinitrotoluene	CV	1 nM	Explosion Hazards	[118]
21. Pd-MoS_2	NO	PEC	70% at a concentration of 2 ppm	Gas Sensing	[120]
22. Ni-MoS_2	H_2S	PEC	80% at a concentration of 0.3 ppm	Gas Sensing	[120]
23. MoS_2/MoO_3	NH_3	PEC	RH 95%	Gas Sensing	[121]
24. ssDNA-MoS_2	Hg (II)	DPV	0.1 nM	Water Contaminants	[125]
25. MoS_2/GCE	Hg (II)	DPV	10^{-5}M	Water and Soil Contaminants	[91]
26. MoS_2/SPCE	Cu^{2+}	EIS	5.43 µM	Water and Soil Contaminants	[126]
27. Fe_3O_4/MoS_2	As (III)	SWASV	4.16 µA•ppb^{-1}	Water and Soil Contaminants	[127]
28. MoS_2/GCE	Metronidazole	DPV	0.36 µM	Medicines	[128]
29. CZTS/MoS_2/CNT	Paracetamol	CV	16 µM	Medicines	[129]
30. CuO/MoS_2	Sulfamethoxazole	DPV	0.34 pg/L	Medicines	[130]
31. MoS_2-NFO	Clenbuterol	DPV	0.471 µM	Medicines	[132]
32. MoS_2/GCE	Hydroxyurea	CV	22 nM	Medicines	[133]
33. Ni/MoS_2	Nitrates	DPV		Pesticides	[135]
34. CdTe-PANI@MoS_2	Carbendazim	PEC	1.74×10^{-10} M	Pesticides	[136]
35. CNT/MoS_2/NiNPs	Glucose	DPV	0.197 µM	Clinical Diagnosis	[138]
36. MoS_2-Graphene	Parathyroid Hormone	CV	5 ng Ml^{-1}	Clinical Diagnosis	[139]
37. MoS_2	Glutathione	DPV	704 pA/µM	Clinical Diagnosis	[142]
38. MoS_2/Au	Dopamine	CV, EIS, DPV	76 nM	Clinical Diagnosis	[143]
39. MoS_2 modified glassy carbon electrode	Resorcinol	DPV	1.13 µM	Clinical Diagnosis	[141]
40. MoS_2-AuNPs with E-DNA	Polynucleotide Kinase	SWV	2.18×10^{-4}U/ml	Clinical Diagnosis	[144]

1.4.2 Applications

MoS_2-based electrochemical sensors have found utilization in diverse areas, encompassing ecological monitoring, health care diagnostics, food safety, and energy storage. They can be employed for the sensing of multiple target molecules, such as heavy metals, biomarkers, pollutants, and neurotransmitters. Sinha et al. have discussed multidisciplinary targets of MoS_2-based electrochemicals for the last four years in 2018 [4]. Using their study as a foundation, this review examines the recent progress in applications of MoS_2-based nanomaterials in the realm of electrochemical sensing. MoS_2-based nanomaterials have capabilities to produce synergistic effects towards electrochemical sensing and thus provide wide applications in various industries as reflected in Fig. 1.7. These subsections demonstrate an extensive literature survey regarding the current progress of MoS_2-based nanocomposites in the realm of electrochemical sensing related to food safety, health-related issues, environmental toxins, and incendiary devices.

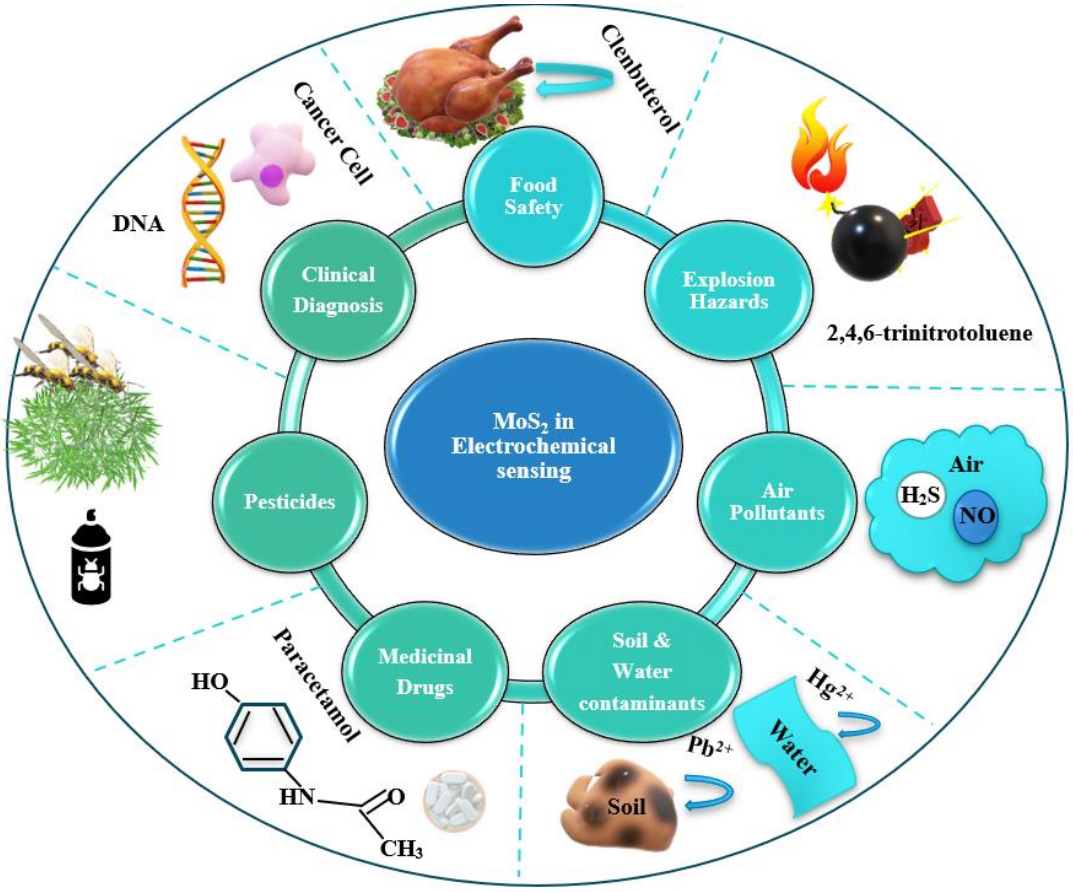

Fig. 1.7 Electrochemical sensing applications of MoS_2-based nanocomposites.

1.4.2. (a) Food Safety

Food is a fundamental necessity of survival for all living beings. Maintaining food safety is the utmost priority to prevent various health problems. Determining the trace level concentration of additives and flavor-enhancing supplements is very important for ensuring food safety. MoS_2 has proven a potential candidate for sensing various food-related target molecules. Monosodium Glutamate is added to various food items for enhancing their flavor. MoS_2 nanosheets furnished with chitosan and Au nanoparticles were employed for the detection of $C_5H_8NO_4Na$ i.e., monosodium glutamate. A nanohybrid consisting of Au-MoS_2/Ch was prepared to fasten the rate of electron transfer to amend the working of the electrode. Fabricated sensors exhibited an ultrahigh sensitivity towards mono sodium glutamate concentration on a large scale ranging from 0.05 μM to 200 μM [112]. Thiabendazole is used in fruits to fungicide them after harvesting. It can cause health-related issues like indigestion, nausea, dizziness etc., So, its detection in food samples is really important. Ag-MoS_2 Nanozyme is used for colorimetric detection of thiabendazole in fruit matrices. The sensor exhibits remarkable sensing with a detection limit of 0.24μM [113]. Color additives are now often found in a broad range of edibles, encompassing milk products, juices, oats, snacks, and frozen foods, to render them extra appealing and mouth-watering. Food colorants, along with other varieties of food additives, play a crucial role in foods because of their visual appeal and customer perceptions. Sunset yellow (SY), also widely recognized as evening yellow, E110, or edible yellow 3, is a popular azo dye. It is orange in color and is found in various fruit products such as sugary drinks, beverages, candy bars, and ice cream. MoS_2 microflowers decorated on screen-printed electrodes are used in the detection of Sunset Yellow for coloring food (FCF) in food samples. The designed sensor exhibits a LOD of 0.04 μM in the linear detection range of 0.1–150.0 μM [114]. Surplus sugar in food can be dangerous to its essential value and human health, necessitating the development of an extremely sensitive sensor for instantaneous glucose sensing in various food items. An electrochemical $C_6H_{12}O_6$ sensor based on a nanoflower-like MoS_2@$CuCo_2O_4$ nanocomposite was meticulously designed. Under optimum conditions, the sensor had a high sensitivity of 1,303 μA mM^{-1} cm^{-2} over a broad range of 0.5-393.0 mol/L, with a low detection limit (0.5 mol/L) and a rapid response time (2.1 s) [115]. Common β-agonists like ractopamine (RAC) and clenbuterol (CLB) are added unlawfully to animal feed because they control sympathetic nerves and encourage lean meat. When ingested by humans through the food chain, β-agonists can cause hazardous effects such as muscle discomfort, tremors, and dizziness since they leave high residues in food-producing

animals like pigs, beef, and chicken. Since there are many exposed reactive sites of MoS_2 nanofibers and the efficient electron transfer rates of HPMo, the HPMo/MoS_2 sensor is employed for the concurrent analysis of CLB and RAC with outstanding sensing performances, such as the broad linear ranges: 1-1300 μM for CLB and 1-150 μM for RAC; LODs of CLB and RAC 0.153 μM and 0.029 μM, accordingly. The designed sensor also has remarkable sensitivity and stability for measuring CLB and RAC in pork samples. As a result, HPMo/MoS_2/GCE is anticipated to be a potential application as a cheap, simple-to-use screening approach for assessing food safety [116]. MoS_2-based nanocomposites can be further explored in the food processing industry for the electrochemical detection of Methyl Parathion, Chlorpyrifos, Carbaryl etc.,

1.4.2. (b) Explosion hazards

MoS_2 nanomaterials have expanded their utility for the detection of explosives. High levels of environmental contamination from the release of intense amounts of radiation, heat, noise, and pressure into the environment are among the explosion threats. TNT, also known as 2,4,6-trinitrotoluene, is one of the most dangerous explosive substances and is known to induce serious human ailments such as harmful cataracts, hepatitis, spleen enlargement and anemia. The homogeneous ZnO nanosheets were deposited on electrodes on pre-obtained MoS_2 using the CV technique in addition to a sensitive sensing setup to identify a few compounds with aromatic rings. SEM, powder XRD, and a few electrochemical techniques were used to examine the surface morphology and electrochemical performance of ZnO-MoS_2 nanosheets. Parallel tests were conducted to demonstrate that the homogeneous ZnO-MoS_2 nanosheet composite was a suitable electrochemical monitoring system for the sensing of the nitro-substituted aromatic explosive 2,4,6-trinitrotoluene (TNT). ZnO-MoS_2 demonstrated the most pronounced electrochemical response, the lowest detection limit, and a greater linear correlation in the lower concentration regime when compared to individual ZnO and individual MoS_2 [117]. Further, 2H–MoS_2/Co_3O_4 nanohybrids are used for particle-level detection of TNT. The microsensor demonstrated sensitive responsiveness from M to pM levels with an LOD of 1 pM while operating under optimal conditions [118]. Further, MoS_2-based electrode material can be explored for electrochemical detection of 2,4-dinitroanisole, 3,3',4,4'-tetrachlorobiphenyl etc.,

1.4.2. (c) Air Pollutants Detection

Routine environmental analysis often involves the detection of extremely low-level pollutants in complex samples. Additionally, environmental accidents can result in a sudden release of chemical compounds, requiring rapid and convenient field detection of pollutants. To address these needs, environmental analysis techniques must exhibit high sensitivity, selectivity, reproducibility, and portability [119]. The detection of toxic gasses in the atmosphere is a critical aspect of environmental pollution control. Due to its high surface-to-volume ratio, two-dimensional MoS_2 has shown significant potential as an electrical sensor. In a study, atomic-layered MoS_2 nanoflakes made by a hydrothermal technique were used to create a high-performance gas sensor. Studies on structure and morphology supported the growth of pure hexagonal MoS_2 nanoflakes. With a minimal NO detection limit of 0.1 ppm, the Pd-MoS_2 layers demonstrated a very high relative response to NO gas (70%) at a concentration of 2 ppm. On the other hand, the relative response to H_2S gas was shown to be 80% by Ni-MoS_2, with a limit of detection of 0.3 ppm and strong reproducibility and selectivity [120]. The MoS_2/MoO_3 composite material has promising sensing characteristics, specifically for detecting low levels of NH_3 at 25°C. The n-type behavior of the material suggests that it has an excess of electrons and can function as an electron donor. This property is useful for gas sensing because the adherence of gas molecules onto the surface of the material can alter its electrical properties, allowing for the detection of the gas. The faster response/recovery, reproducibility, and long-term durability of the sensor make it a good candidate for use in practical applications. Additionally, the stable and highly selective response to NH_3 under highly humid conditions (RH = 95%) is particularly noteworthy because many gas sensors struggle with maintaining selectivity in humid environments [121].

1.4.2. (d) Soil and Water Contaminants

Heavy metal ion pollution poses a significant environmental challenge as these ions are non-biodegradable and can pollute natural resources such as water. Heavy metals like lead, mercury, arsenic, chromium, and cadmium are highly poisonous and can be dangerous to human health even at particle levels. This highlights the necessity for quick, precise, and suitable methods for detecting heavy metal ions [122]. Several techniques are available for detecting heavy metal ions, including atomic absorption spectroscopy, inductively coupled plasma mass spectrometry, and electrochemical methods. These methods have varying levels of sensitivity, accuracy, and cost-effectiveness. In recent years, several nanomaterial-based sensors have been designed for sensing of heavy metal ions. These sensors utilize the distinct characteristics of

nanomaterials like high surface area, high reactivity, and strong affinity towards heavy metal ions. Nanomaterials such as graphene, carbon nanotubes, and metal oxides have been used to construct sensitive and selective sensors for detecting heavy metal ions [123]. The applications of nanomaterial-based sensors offer several advantages, including low cost, fast response time, high sensitivity, and selectivity. These sensors can also be seamlessly combined into portable devices, making them suitable for the instantaneous detection of heavy metal ions. Overall, the development of rapid, precise, and reliable methods for detecting heavy metal ions is essential for safeguarding human health and the environment. Nanomaterial-based sensors show great potential for meeting this need and may become an important tool in the fight against heavy metal ion pollution [124]. The sensing of mercury (II) ions in water is of great importance due to the potential health hazards associated with exposure to this heavy metal. In this study, a label-free ultra-low-level electrochemical detection method for Hg (II) ions in aqueous media is presented. The method involves the direct covalent functionalization of single-stranded DNA (ssDNA) with molybdenum disulfide (MoS_2) nanoflakes, which act as the sensing element for the Hg (II) ions. The electrochemical detection of Hg (II) ions was carried out utilizing DPV. The results indicated that the ssDNA-MoS_2 nanoflake-based sensor had a linear relationship over a broad range of Hg (II) ion concentrations, from 0.5 nM to 500 nM, with a detection limit (LOD) of 0.1 nM. The sensor also exhibited good selectivity for Hg (II) ions in the solution having other heavy metal ions such as Pb (II), Cd (II), and Cu (II). The sensitivity and selectivity of the sensor can be due to the specific binding of Hg (II) ions to the thymine bases in the ssDNA, as well as the elevated surface area and electrocatalytic properties of the MoS_2 nanoflakes. The sensor also demonstrated good stability and reproducibility over multiple measurements [125]. Further, solvent-exfoliated MoS_2 was also used for the electrochemical sensing of Hg^{2+}, and it can sense up to 10^{-15}M level and it also shows eminent selectivity for Hg^{2+}. MoS_2/GCE (Glassy Carbon Electrode) was able to sense Hg^{2+} even in seawater and tap water samples. The reason behind high sensitivity and selectivity was attributed to the interaction between the S^{2-} groups of MoS_2 and Hg^{2+} and the voluntary redox activities were ensured by different characterization techniques. The MoS_2/GCE sensor shows a remarkable 30 times enhanced peak current in comparison to a glassy carbon electrode (GCE). This suggests that the MoS_2 nanosheets on the GCE surface significantly enhance the electrochemical response, leading to improved sensitivity for detecting target species like Hg^{2+} [91]. A flexible electrochemical sensor for the detection of Cu^{2+} ions in water was fabricated using a MoS_2 modified screen-printed carbon electrode (SPCE). With a limit of detection (LOD) of 5.43 μM for Cu^{2+} ions in the detection range of 5 μM to 5 mM, the sensor

demonstrated an outstanding response. Electrochemical impedance spectroscopy (EIS) comparison experiments with a typical glassy carbon electrode modified with MoS_2 revealed improved linearity for the SPCE-based sensor [126]. Fe_3O_4/MoS_2 nanocomposite was used for the electrochemical detection of As (III) (arsenic). The valence modification of the Fe^{2+}/Fe^{3+} phase, which is responsible for the detection of heavy metal ions, was found to speed the electron transfer in the Fe_3O_4/MoS_2 nanocomposite. The study's findings demonstrated that the Fe_3O_4/MoS_2 nanocomposite surpassed commonly utilized noble-metal materials in its detection of As (III) with a sensitivity of 4.16 $\mu A \bullet ppb^{-1}$ [127].

1.4.2.(e) Medicinal Drugs

The medical device sector has grown quickly in recent years, and numerous medications are identified as potentially harmful chemicals. Antibiotics have been widely utilized to treat infectious infections in both animals and people. Thus, monitoring their content in bodily fluids or in the environment is crucial. Nanomaterials based on MoS_2 have been investigated for their possible application in the detection of medicines. In one study, an electrochemical sensor based on MoS_2 for the detection of metronidazole, a medication frequently used to treat bacterial and parasite illnesses, was developed. The sensor was prepared by depositing MoS_2 nanosheets onto a GCE surface, and the electrochemical performance of the sensor was characterized using CV and electrochemical impedance spectroscopy. The sensor was found to have improved sensitivity and selectivity towards metronidazole, with a detection limit of 0.36 µM (micromolar) [128]. Epinephrine is included in the category of medicines considered as alpha- and beta-adrenergic agonists. In addition to emergency medical treatment, epinephrine injections are utilized to treat fatal allergic reactions caused by edibles, medications, materials, stings, and other sources. Nitrogen-doped MoS_2/rGO was used for electrochemical detection of epinephrine. A combination of techniques, including sophisticated hummer and hydrothermal approaches, were used to create the MoS_2/N-rGO heterostructure. FE-SEM, EDX, HR-TEM, FTIR, and XRD methods were employed to characterize the produced heterostructure. The layout of MoS_2 nanorods on the exterior of 2D N-rGO nanosheets was validated by the results. The MoS_2/N-rGO modified GCE displayed a remarkable linear sensing range (2 µM-63 µM) and an outstanding detection limit (3.9 µM). Exceptional selectivity was displayed by MoS_2/N-rGO modified GCE when pharmaceuticals or similar compounds were present [129]. The electro-catalytic role of MoS_2 for the detection of Resorcinol is being demonstrated for the first time in this study endeavor. For the purpose of determining resorcinol, the MoS_2-modified glassy carbon electrode (MGC) was investigated. For the

purpose of determining resorcinol, the designed MGC sensor showed good sensitivity (0.79 μA μM-1 cm-2) and a detection limit (1.13 μM). Moreover, the fabricated MGC showed resorcinol detection with good stability and selectivity [141]. Even though it is often used as a painkiller and to treat fevers, paracetamol might cause liver issues if used excessively. The hybrid nanocomposites of CZTS/MoS_2/CNT are synthesized to combat this issue. The challenging determination of paracetamol from biological samples, including blood, stomach, small intestine, or gastrointestinal tract, has been resolved with the aid of this inquiry. Turnery CZTS/MoS_2/CNT sensor is being examined to detect paracetamol electrochemically for the first time. At a concentration of 10 ppm paracetamol, the sensitivity of the designed sensor is achieved up to 16 μA [130]. Neomine, also known as sulfamethoxazole (SMX), is a wide-spectrum antibiotic that is particularly effective against staphylococcus and E. coli. Sulfamethoxazole is an antibiotic that is used in veterinary medicine in contrast to other antibiotics. CuO/MoS_2 was used to detect Sulfamethoxazole (SMX). CuO/MoS_2 demonstrated outstanding electrochemical performance when compared to CuO, MoS_2, and bare Glassy carbon electrode (GCE), which indicated improved electrochemical conductivity for the detection of SMX by reducing the oxidation potential ranging from +0.18 V to +0.10 V. SMX was detected with a detection limit of 0.34 Pg/L [131]. Due to their distinctive physical and chemical characteristics, such as strong biocompatibility, exceptional chemical stability, multiple redox states, affordability, and special magnetic attributes, spinel ferrite compounds (MFe_2O_4) have recently attracted fresh interest. Various spinel ferrite-based nanohybrids are being built in an effort to improve their inherent properties and increase the variety of applications they can be used for, including biotechnology, biomedical, and environmental applications. The electrochemical studies and detection abilities of an electrode modified with $NiFe_2O_4$ (NFO), MoS_2, and MoS_2-NFO were fully examined using CV, EIS, DPV, and CA techniques. Compared to other suggested electrodes, MoS_2-NFO/SPE offered a greater sensing capability for the detection of clenbuterol (CLB). The current response measured at MoS_2-NFO/SPE after pH and accumulation time optimization rose linearly with an increase in CLB concentrations within the range of 1 to 50 μM, resulting in a LOD of 0.471 μM. Along with improving mass movement, ionic/charge diffusion, and absorbance ability, an external magnetic field also improved CLB's ability to electrocatalyze redox processes. Under the effect of external magnetic field, the linear detection range was expanded 0.5 to 50 μM with a LOD of 0.161 μM [132]. The electrochemical data obtained at the modified MoS_2/GCE and bare GCE were processed using chemometrics, which made it possible to estimate the quantities of hydroxyurea in human plasma. Multivariable partial least square regression and principal

component analysis are two mathematical methods used in chemometrics. A LOD of 22 nM and a sensitivity of 37 nA μM^{-1} cm^{-2} were determined that are suitable for medicinal and clinical applications [133].

1.4.2. (f) Pesticides

In modern agriculture, pesticides are frequently used to manage weeds and pests, monitor and improve plant growth, and increase food production. The traces of pesticides in food can endanger human health when they are used excessively or abusively. The remains of pesticides contain harmful chemicals that, even in extremely small quantities, can harm the environment and human health. In order to monitor food security and protect the public's health, efficient residue detection techniques were created [134]. Nitrates are produced naturally by the process of nitrogen cycling and are an essential component of the environment. Plant and aquatic vegetation development depend on nitrates in the soil and water. Drinking water and leafy vegetables are two major dietary sources of nitrates, essential for controlling various bodily processes. Nevertheless, too much nitrate in the soil and water could adversely affect a person's health. Pesticides, meat preservatives, and the chemical industry are the main contributors to the ecosystem's oversupply of nitrates. Ni/MoS_2 was prepared successfully and MoS_2 nanosheets were beautifully grown on nickel nanosheets which resulted in increased conductivity. The electrocatalytic oxidation of nitrite by the Ni/MoS_2 nanocomposite shows a strong current response. The designed electrochemical sensor displayed a linear sensing range of 5-800 µM and a LOD of 2.48 µM [135]. A Photoelectrochemical (PEC) aptasensor for the sensing of Carbendazim (CBZ) was developed. It entailed the specific interaction of an aptamer to the analyte on the surface of CdTe-PANI@MoS_2, which resulted in enhanced atomic interference for electron transfer and a "signal-off" detection mode. The aptasensor was successfully used to analyze tomato samples with a linear span of 0.523-5230 nM (0.1-100 ng mL^{-1}) and a detection limit of 1.74 10^{-10} M (0.033 ng mL^{-1}) for CBZ detection [136].

1.4.2. (g) Clinical Diagnosis

As the main source of energy for living cells, glucose is a crucial part of biological activities. It is an essential metabolic intermediate that organisms utilize for a variety of purposes. To keep normal body processes, however, the level of glucose in the blood must be controlled within a specific range. Increased insulin levels brought on by too much blood glucose can result in obesity and hyperglycemia. High blood sugar levels (>7 mM) are the hallmark of hyperglycemia, which can cause a variety of health issues, including cardiovascular illness,

nerve damage, and kidney damage. On the other hand, low blood glucose levels can produce hypoglycemia, which can result in insulin shock. Low blood sugar levels are a symptom of hypoglycemia. A diabetic coma is a severe case of hypoglycemia that, if untreated, can cause death and brain damage [137]. To promote good health and delay the emergence of many diseases and health issues, it is crucial to maintain a normal balance of glucose in the blood. The study centers on the construction of a glucose sensor using CNT/MoS_2/NiNPs nanocomposites. The findings demonstrated that the CNT/MoS_2/NiNPs nanocomposites had high sensitivity towards glucose detection, with a sensitivity value of 1212 μA $mM^{-1}cm^{-2}$, a broad linear range of 0.05-0.65 mM, a low detection limit of 0.197 μM, and a quick reaction time of 3s [138]. MoS_2 on aluminum foil has been employed for the non-enzymatic detection of Uric acid. Pictures obtained from FESEM disclosed MoS_2 has a structure similar to micro-flower consisting of interwoven nanosheets while chemical characterization of data verified the lucrative growth of 4 layered MoS_2 on Aluminum foil. The designed sensor demonstrated a LOD of 1.169 μM, selectivity, superb reproducibility, and a response time of 3 seconds towards uric acid over glucose. The sensor developed has detected uric acid in human urine as well [96]. Electrochemical testing on 30 patients with osteoporosis at Seoul National University Bundang Hospital was conducted. The designed MoS_2-Graphene sensor was used for the detection of parathyroid hormone concentration in the human body [139]. Monoclonal antibodies captured were confirmed by using electrochemical impedance spectroscopy. Test results obtained using a MoS2-Graphene electrochemical sensor were compared to Standard Electrochemical Immunoassay devices and it shows high correlation in the results obtained from two devices. MoS_2-Au NPs/GCE has been used for detection of cancer antigen 72-4 (CA72-4) [140]. For the detection of Glutathione which is associated with various human diseases like AIDS, HIV, Cancer, Liver damage etc., MoS2-based electrochemical sensor is used. It demonstrates superb potentiality for electrochemical detection due to its label free sensing capabilities. The designed sensor obtained LOD of 704 pA/μM and detection range of 10μM-500mM. The liquid phase exfoliation method is adopted for the synthesis of the MoS_2 due to good large-scale production. The repeatability and stability of the biosensor is assessed by carrying out three different measurements of the sample. It was found effective testing with real patient serum as well [142]. Dopamine (DA), a catecholamine neurotransmitter, affects key motor activities such as mental actions, brain plasticity, memory, and learning. It is abundantly prevalent in the body's nervous system. Additionally, it is frequently linked to a variety of neurological conditions like schizophrenia, Alzheimer's, and Parkinson's disease. For the correct diagnosis of any disease, direct and focused biomarker detection in complicated

biological samples like whole blood, urine, etc., is crucial. A substantial detection approach for DA analysis was created with this objective in mind. MoS_2-PANI/rGO nanocomposite is deployed for contemporaneous sensing of ascorbic acid (AA), dopamine (DA) and uric acid (UA). A one-pot hydrothermal synthesis method is used for synthesizing nanomaterial. It is observed that MoS_2-PANI/rGO unveils good performance, bio-affinity, and high electrochemical catalytic activities. The limits of detection for AA, DA, and UA are 22.20, 0.70 and 0.36 μM respectively [91]. A carbon paste electrode modified with MoS_2/Au was used as the foundation for the construction of an electrochemical sensor for the sensitive and accurate measurement of dopamine. Excellent analytical performances are demonstrated by the prepared electrochemical sensor, including extremely revamped sensitivity, broad linear relationship (0.5-300 M), and low detection thresholds (76 nM). Also, the designed sensor exhibits great selectivity, strong reproducibility, and stability, and it may be applied to the analysis of actual sample data [143]. The process for making the large-efficiency electrocatalysts and electrochemical sensors described in this paper serves as a useful guide for creating more operationalized nanocomposites and expanding the range of applicable practical uses. The integration of MoS_2-AuNPs (Gold nanoparticles) with an E-DNA sensor has resulted in a significantly enhanced sensitivity for the sensing of Polynucleotide Kinase (PNK), with a detection limit of 2.18×10^{-4} U/mL. The high sensitivity of this assay may be due to the unique properties of the MoS_2-AuNPs, which can increase the signal output of the E-DNA sensor. In addition to its high sensitivity, this assay also demonstrates high selectivity, as it can distinguish PNK from other enzymes and proteins. This selectivity is an important feature of any biosensor, as it ensures that the sensor responds specifically to the target analyte and minimizes false positive results. Furthermore, the ability of this assay to screen inhibitors is also noteworthy, as it could be useful for drug discovery or for studying the mechanisms of enzyme inhibition. Overall, the integration of MoS_2-AuNPs with an E-DNA sensor appears to be a promising approach for the detection of PNK, with potential applications in diverse fields, including biotechnology and medicine [144]. However, further research may be necessary to optimize the assay for specific applications and to evaluate its performance in different sample matrices. Another advantage of MoS_2-based electrochemical sensors is their ability to operate in complex biological matrices, such as blood, saliva, and urine. These sensors can be designed to be selective for specific biomolecules, which reduces the risk of false positives or false negatives.

1.5. Research motivation and gaps

MoS_2 has an excellent possibility of replacing other materials as the preferred option for electrochemical sensors in the future. MoS_2 can form nanohybrid structures with other materials such as Carbon-based materials, polymers, or metallic nanoparticles to enhance their sensing and chemical activity. MoS_2-based electrochemical sensors have demonstrated fast response times, enabling rapid detection and analysis. It enables portable and point-of-care sensing applications when incorporated into smaller devices. The compatibility of MoS_2 with microfabrication techniques makes it suitable for the fabrication of miniaturized and more sensitive sensing platforms MoS_2 is biocompatible, so it can be used for detecting biomarkers, pathogens, and other biological entities, opening up possibilities for medical diagnostics and healthcare applications. It's important to note that while MoS_2 shows great promise in electrochemical sensing, further additional research and development is required to fully maximize its potential. The optimization of fabrication techniques, enhancement of stability and selectivity, and exploration of new applications are ongoing areas of research in order to realize the full benefits of MoS_2 in electrochemical sensing.

In this review, a holistic picture regarding the detection capabilities of MoS_2 in regard to chemical bonding, electronic properties, and morphological structures has been portrayed in an elaborated manner. MoS_2-based nanocomposites exhibit promising potential for the electrochemical detection of various target molecules in the food industry, such as monosodium glutamate, thiabendazole, sunset yellow for coloring food, glucose, and β-agonists like ractopamine and clenbuterol. These sensors have demonstrated high sensitivity, selectivity, stability, and low detection limits for the respective target molecules. MoS_2-based nanocomposites can also be further explored for the electrochemical detection of other target molecules in the food industry, such as Methyl Parathion, Chlorpyrifos, Carbaryl, and more. MoS_2 nanomaterials have potential applications in detecting various explosive compounds and other chemicals. The use of ZnO-MoS_2 nanosheets as a sensitive sensing platform for the detection of 2,4,6-trinitrotoluene (TNT), with lower limits of detection and higher linear relationships in low concentration ranges, shows promising results. Additionally, the MoS_2-based electrode material can be explored for the electrochemical detection of other compounds such as 2,4-dinitroanisole and 3,3’,4,4’-tetrachlorobiphenyl. It will be interesting to see how these materials can be further developed and optimized for practical applications in detecting explosives and other hazardous compounds. MoS_2, a two-dimensional material with a high surface-to-volume ratio, has shown significant potential as an electrical sensor for the detection

of toxic gasses. Studies have demonstrated the high sensitivity, selectivity, reproducibility, and portability of MoS_2-based gas sensors. MoS_2-based gas sensors have the potential to address the needs of environmental analysis and can detect low-level pollutants in complex samples. The development of flexible electrochemical sensors for the detection of heavy metal ions such as Hg^{2+}, Cu^{2+} is an important area of research. In clinical diagnostics, electrochemical sensors based on MoS_2 have been used for the detection of various biomolecules, such as glucose, uric acid, and cancer. Compared to conventional diagnostic methods, these sensors provide a number of benefits, such as superior specificity, sensitivity, and reliability. They have already been used in several clinical diagnostic applications, including the detection of glucose for diabetes monitoring and the detection of cancer biomarkers. Further, research in this area is likely to lead to the development of more sensitive and selective sensing platforms for a range of diseases. This research holds multidisciplinary applications and offers significant potential to benefit society, which has inspired us to continue this valuable work. In this study, MoS_2, MoS_2/RGO, Mn-MoS_2/RGO, and Co-MoS_2/RGO are synthesized using a microwave-assisted method. This innovative synthesis approach allowed efficient production of these materials with controlled morphologies and enhanced properties. Using electrochemical techniques, we assessed the sensitivity and selectivity of these synthesized materials in detecting ascorbic acid, uric acid, and resorcinol. The results demonstrated remarkable performance, with each material exhibiting high sensitivity, low detection limits, and excellent repeatability. This study not only underscores the competence of MoS_2-based composites for advanced sensing applications but also highlights the effectiveness of the microwave-assisted synthesis method in producing high-performance sensing materials.

1.6 Research Objectives of the study:

1. Synthesis and optimization of Molybdenum disulfide by using a suitable technique, to obtain desirable morphology.
2. Preparation of Molybdenum disulfide-based nanocomposites and their characterization.
3. Assessing sensing properties of Molybdenum disulfide-based nanocomposite.

Chapter 2

Materials and synthesis details

The preceding chapter provided a glimpse into the historical background of MoS_2-based nanocomposites and their applications in the realm of electrochemical sensing. Selecting an appropriate synthesis method is paramount for the successful fabrication of MoS_2-based nanocomposites. Over the past decade, there has been growing inquisitiveness in MoS_2-based nanocomposites due to their broad range of practices, including healthcare diagnostics, energy storage, environmental monitoring, toxic gas detection, and the pharmaceutical industry. The catalytic properties of MoS_2-based nanocomposites are enhanced as their shape, size, and morphology deviate from those of bulk materials. They can be synthesized through various methods, including hydrothermal synthesis [150], exfoliation [151], mechanical exfoliation, chemical vapor deposition (CVD) [152], and microwave irradiation. However, microwave-assisted synthesis is an ideal method for creating biosensors because it allows electrochemists to design them directly without the need for chemical reductants or toxic compounds. This approach is cost-effective, energy-efficient, and minimizes the use of harmful substances [153]. After successful synthesis, characterization is crucial for ensuring that prepared particles are at the nanoscale. In material science, "characterization" encompasses the various methods used to examine the properties and structure of materials. This fundamental process is essential for scientifically understanding materials and involves a range of techniques that explore material properties and microscopic structures. As the field advances, newer techniques continuously emerge, complementing the traditional methods that have been practiced for centuries. Characterization allows for determining the composition and structure of materials and assessing the success of the preparation methods. Some techniques provide qualitative data, while others offer quantitative results. The chapter will cover the synthesis procedure of various MoS_2-based nanocomposites, chemicals used, characterization techniques, and the technical details of the instruments used for characterization. This chapter covers a range of analytical techniques, including XRD (abbreviated as X-Rays Diffraction), Raman spectroscopy, FESEM (abbreviated as field emission scanning electron microscopy), EDS (abbreviated as energy dispersive X-ray analysis), HRTEM (abbreviated as high-resolution transmission electron microscopy), FTIR (abbreviated as Fourier transform infrared spectroscopy), ultraviolet-visible spectrometry (UV-Vis), X-ray photoelectron spectroscopy (XPS), BET (abbreviated as Brunauer-Emmett-Teller) method, and various electrochemical studies such as CV (abbreviated as cyclic voltammetry), DPV (abbreviated as differential pulse voltammetry), and

EIS (abbreviated as electrochemical impedance spectroscopy). The fundamental principles and mechanisms underlying these techniques are thoroughly explained.

2.1 Materials and Synthesis

2.1.1 Materials used

All the chemicals used in this research are listed in Table 2.1, which includes their manufacturer details. Additionally, general information about these chemicals is provided to ensure their cautious use in the laboratory.

2.1.2 Synthesis of pristine MoS_2

Initially, solutions were prepared by mixing 1 gm of $MoCl_5$ in 3 ml of ethanol. These solutions were magnetically stirred for at least 30 mins to ensure thorough mixing. Following this, 0.632 gm of thiourea were added to each solution. Stirring continued until the solutions completely dried, resulting in a solid product. The dried product was then placed in a microwave. Under microwave irradiation, organic reactions can be significantly accelerated, and the desired amount can be fine-tuned by adjusting microwave parameters. This method offers several benefits over traditional heating, such as rapid, uniform, and selective heating. Microwave-assisted synthesis is known for its speed and efficiency. Recently, it has been suggested that the synthesis of nanomaterials, metal nanoparticles, and nanostructures whose growth is susceptible to reaction conditions can greatly benefit from the precise and efficient heating provided by microwave irradiation [154]. This approach ensures better control over reaction parameters, leading to high-quality nanomaterial production [155]. Microwaves facilitate the synthesis process by interacting with synthesis precursors and/or solvents through dipolar interactions, providing ample energy to overcome nucleation barriers [156]. This results in elevated super-saturation levels within the reaction mixture, prompting crystallization to occur. The product was subjected to 3–4 cycles of microwave irradiation, each lasting 45 seconds at a power level of 700 watts. This process facilitated the annealing of the product. Once annealed, the product was crushed into a fine powder to ensure uniformity. The resulting powder was then stored in an airtight container to preserve its integrity and prevent contamination from air and moisture.

2.1.3 Synthesis of GO

B.C. Brodie, a British Chemist was the pioneer in discovering the properties of graphite oxide, sparking significant interest among researchers due to its unique characteristics.

Table 2.1 Chemicals used in the present work.

Chemical Name	Chemical Formula	Procured from (Company)	General Information
1. Molybdenum (V) chloride	$MoCl_5$, (95% purity)	Sigma Aldrich Ltd. (India)	Highly oxidizing, non-flammable
2. Graphite powder	CH_4, (99.9% purity)	Sigma Aldrich Ltd. (India)	Inert, heat resistant
3. Hydrochloric acid	HCL, (35% purity)	LOBA Chemie (India)	Highly odorous, hazardous
4. Sulphuric acid	H_2SO_4	LOBA Chemie (India)	Hazardous, corrosive
5. Manganese (II) Acetate (Tetrahydrate)	$Mn(CH_3COOH)_2$ (98.5%, purity)	LOBA Chemie (India)	Non-corrosive, easily soluble in water
6. Thiourea	CH_4N_2S, (99% purity)	LOBA Chemie (India)	Reducing agent, hazardous
7. Ethanol	C_2H_5OH, (99.5% purity)	LOBA Chemie (India)	Highly flammable, organic solvent.
8. Hydrogen peroxide	H_2O_2, (30% purity)	LOBA Chemie (India)	Weak acid, mildly irritating to the skin.
9. Ascorbic acid	$C_6H_8O_6$ (99.5% purity)	LOBA Chemie (India)	Antioxidant, non-hazardous
10. Uric acid	$C_5H_4N_4O_3$ (99% purity)	LOBA Chemie (India)	Antioxidant, weak organic acid.
11. Resorcinol	$C_6H_6O_2$ (99% purity)	LOBA Chemie (India)	Toxic, easily adsorb in the skin.
12. Dimethylformamide	DMF, (99.8% purity)	LOBA Chemie (India)	Polar solvent, hard Lewis base.
13. Potassium Phosphate Dibasic Anhydrous	K_2HPO_4, (99% purity)	LOBA Chemie (India)	Water soluble salt, buffering agent.
14. Potassium Dihydrogen orthophosphate	KH_2PO_4, (99.5% purity)	LOBA Chemie (India)	Water soluble salt, buffering agent.
15. Potassium Chloride	KCl, (99% purity)	LOBA Chemie (India)	Non-flammable, safe
16. Potassium Permanganate	$KMnO_4$ (99% purity)	LOBA Chemie (India)	Strong oxidizing agent, versatile
17. Sodium Nitrate	$NaNO_3$	LOBA Chemie (India)	Oxidizing agent, water-soluble
18. Alumina Slurry Polishing	Al_2O_3 (99.9% purity)	Nanochemazone (India)	Highly stable, evenly dispersed.

Despite the extensive research, data limitations persist, and investigations into graphite oxide continue worldwide. Brodie's method involved mixing graphite and potassium chlorate ($KClO_3$) in a 1:3 ratio with fuming nitric acid (HNO_3) and heating the mixture at 60°C for three

to four days. In 1898, L. Staudenmaier enhanced Brodie's technique by substituting 2/3 of the fuming HNO_3 with sulfuric acid (H_2SO_4) and adding multiple portions of $KClO_3$. However, this modification posed hazards, including continuous bursts, and the reaction duration is extended to four days [157]. This method replaced $KClO_3$ with $KMnO_4$ to prevent spontaneous explosions and substituted $NaNO_3$ for fuming HNO_3 to avoid the generation of fog acid, significantly reducing the reaction time to a few hours and yielding high-quality graphite oxide [158]. Additionally, the Hummers method produced more oxygen compared to Brodie's method. In present work, GO was prepared using a Hummer's method. In a 1000 ml beaker, 2.0 gm of $NaNO_3$ and 1.2 gm of graphite powder were dissolved in 50 ml of H_2SO_4 and kept on a magnetic stirrer along with an ice bath maintaining the temperature at 10ºC. After that 6 gm of $KMnO_4$ was added and the solution was stirred for 2 hours. Then ice bath was removed and the solution temperature was maintained at 35ºC with continuous stirring until it turned into a thick brown slurry. Further, 100 ml of Deionized water was added with continuous stirring, and a sudden rise in the solution temperature was observed. When the temperature of the solution reached up to 90º C it was maintained for 15 minutes. Then, 8 ml H_2O_2 was added to halt the reaction, resulting in a yellow-colored solution. After this, the solution was rinsed with 8% HCl to remove metal impurities. Further, the solution was strained and the filtrate was kept in a vacuum-dried oven at 60º C for 1 day in order to obtain GO.

2.1.4 Synthesis of MoS_2/RGO

A pictorial representation of the preparation of the MoS_2/RGO composite material is depicted in Fig. 2.1. Specifically, 1 gm of $MoCl_5$ was dissolved in 3 ml of ethanol within a glove box to ensure a proper vacuum environment, given the highly oxidizing nature of $MoCl_5$. Upon dissolution, the solution turned a dark green color, accompanied by the release of HCl gas. Subsequently, 100 gm of GO was added to the solution and then stirred magnetically for 30 minutes. Following this, 0.632 gm of thiourea was added, causing the solution to shift to a brownish-green hue. The mixture was then maintained on the magnetic stirrer at a temperature of 40ºC, continuing until it thickened into a slurry. The resulting slurry was then placed in a microwave set at 700 watts, receiving 3-4 pulses of 45 seconds each. After microwave treatment, the composite was ground into a fine powder using a pestle and mortar and stored in an airtight container to maintain its integrity. This procedure was replicated with varying amounts of GO to synthesize different compositions, resulting in 1% doped MoS_2/RGO, 3% doped MoS_2/RGO, and 5% doped MoS_2/RGO nanocomposites.

2.1.5 Synthesis of Mn-MoS_2/RGO

Mn-MoS_2/RGO was prepared employing a two-step microwave-assisted synthesis technique. In the initial step, 1 gm of $MoCl_5$ was mixed in 3 ml of ethanol in a glove box to provide a sufficient vacuum for the reaction to take place as $MoCl_5$ is a strongly oxidizing substance by nature.

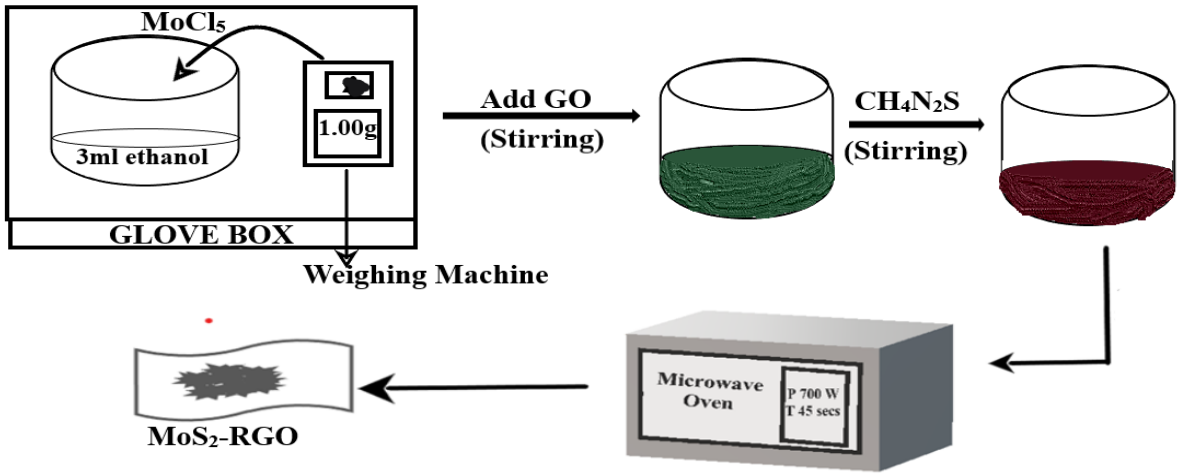

Fig. 2.1 Microwave-assisted synthesis of MoS_2-RGO nanocomposite.

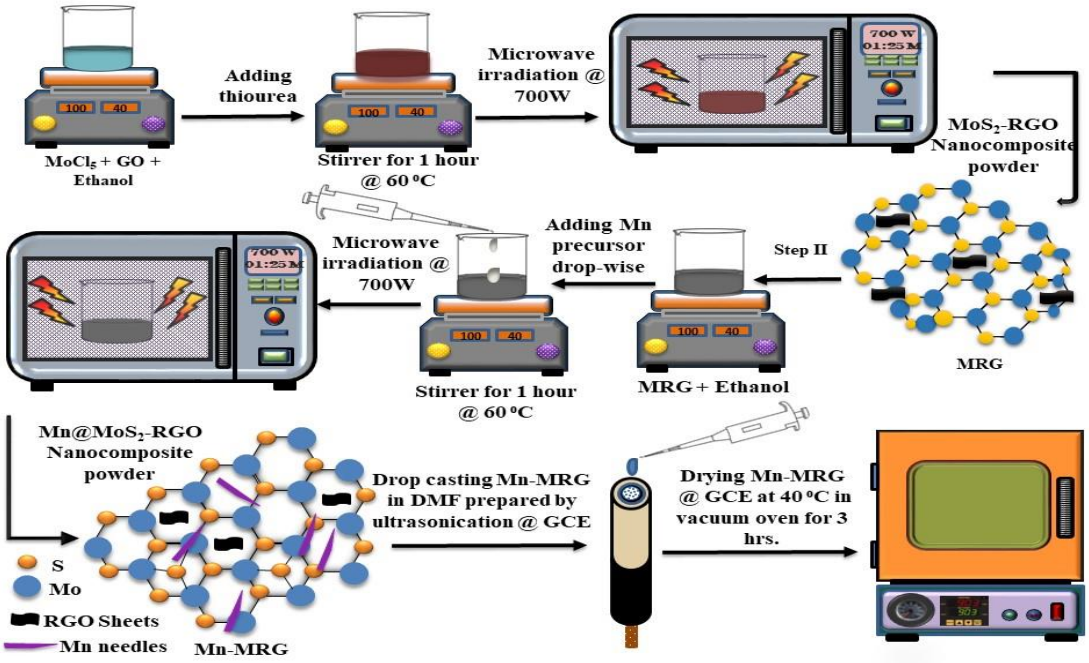

Fig. 2.2 Microwave-assisted synthesis process of the Mn-MRG composite and the fabrication of the Mn-MRG working electrode on the GCE.

The solution changed color to dark green while also emitting HCl gas. After adding the predetermined amount of GO, the mixture was magnetically stirred using a stirrer for half an hour before 0.632 g of thiourea was added, giving the mixture a brownish-green hue. The solution was then stirred until it thickened into a slurry. Additionally, it was heated in a microwave three or four times for 45-second bursts at a power level of 700 Watts. At this stage MoS_2/RGO is formed. The second step involves the addition of 50 mg of MoS_2/RGO and a predetermined amount of manganese acetate solution to 1 ml of ethanol, which is then agitated for a short period at 40ºC until the mixture is fully dry. Afterward, it was subjected to two 10-second bursts in a microwave oven set to 700 watts. After that, it was ground into a fine powder and stored in an airtight container. The same process was used to synthesize 3% Mn-MRG, 5% Mn-MRG, 7% Mn-MRG, and 9% Mn-MRG while varying the amount of Mn. Further, the suspensions were prepared for each composite in DMF and drop-casted on GCE to design different sensors as illustrated in Fig. 2.2.

2.1.6 Synthesis of Co-MoS_2/RGO

A two-step microwave-assisted synthesis technique was used to synthesize Co-MoS_2/RGO. In the first step, 1 gm of $MoCl_5$ was dissolved in 3ml of ethanol inside a glove box to maintain a vacuum, given $MoCl_5$'s strong oxidizing properties.

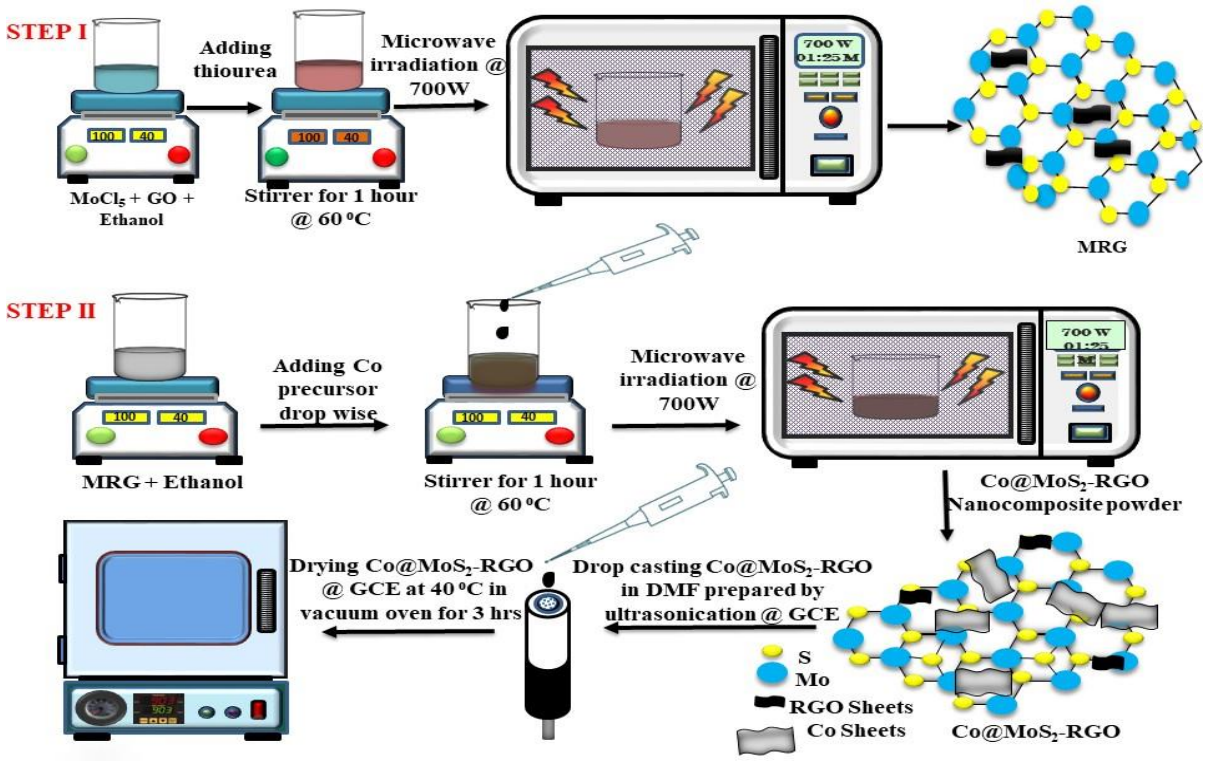

Fig. 2.3 Microwave-assisted synthesis process of the Co-MoS_2/RGO composite and the drop-casting of the Co-MoS_2/RGO on the GCE.

Table 2.2 Technical details of the microwave oven used in this study

Instrument Used	Available at	Operating frequency	Power range	Microwave absorbers	Microwave transmitter
1. GALANZ SOLO	Physics Lab, LPU, Punjab, India	2.47 GHz	100 to 1000 W.	Ethanol	Teflon beakers

This solution turned dark green and released HCl gas. After adding 300 mg of GO, the solutions were magnetically stirred for at least 30 mins to ensure thorough mixing. Following the addition of 0.632 gm of thiourea, the mixture became brownish-green. The solution was then stirred until it thickened into a slurry and subsequently heated in a microwave three to four times for 45-second intervals at 700 watts, forming MoS2/RGO. In the subsequent step, a predetermined amount of cobalt powder and 50 mg of MoS_2/RGO were added to 1 ml of ethanol, and the mixture was stirred at 40ºC until completely dry. The mixture was then subjected to two 10-second pulses in a microwave oven at 700 watts. Finally, the product was ground into a fine powder and stored in an airtight container. Following this, suspensions for each composite were made in DMF and deposited onto GCE via a drop-casting technique to design the sensor, as shown in Fig. 2.3. A household multimode cavity microwave oven is used in this work for synthesizing MoS_2, MoS_2/RGO, Mn-MoS_2/RGO, and Co-MoS_2/RGO. All the instrumentation details are given in Table 2.2.

2.2 Characterization techniques

2.2.1 X-Ray Diffraction (XRD)

Wilhelm Conrad Roentgen, a German physicist, is known for discovering X-rays. He first observed and recorded this phenomenon on November 8, 1895, while experimenting with cathode rays. He noticed a mysterious glow from a nearby chemically coated screen during his experiments. Roentgen discovered that these rays could penetrate most materials, including the soft tissues of the human body, but were blocked by denser substances such as bone and metal. This discovery led to the creation of the first X-ray images, including a famous one of his wife's hand, which clearly showed her bones and wedding ring. Roentgen's groundbreaking work transformed medical diagnostics and earned him the first Nobel Prize in Physics in 1901 [159]. X-rays constitute bundles of electromagnetic energy originating from electron clouds surrounding atoms. XRD is a widely utilized technique for characterizing samples, particularly for studying crystallographic changes such as phase identification in materials. This characterization procedure is applicable only to crystalline or semi-crystalline materials.

Consequently, if the sample under examination possesses a regular arrangement of atoms, the dispersed light is oriented in specific directions determined by the X-ray wavelength, crystal lattice dimensions, and orientation.

a) Principle: This characterization technique is founded on the principle of constructive interference occurring in a cathode ray tube, resulting in the production of a monochromatic beam of X-rays from the crystalline sample. XRD is a non-damaging method that involves the interaction of X-rays with matter. When a monochromatic X-ray beam interacts with an object, elastic scattering, also known as Rayleigh scattering, takes place, wherein the scattered X-rays disperse in random directions while retaining the same energy as the input photons.

b) Working: In the production of X-rays, a high-speed electron from the cathode strikes an atom of the anode. Upon bombardment, an electron from the cathode is ejected, inducing a vacancy. An electron present in a higher energy level then shifts to a lower energy level to fill the vacancy, releasing X-ray photons of specific energy during this transition. When the sample is introduced to these X-rays, they are diffracted by the atoms within in the material. Interacting with the regular array of electrons within the atom, arrays of spherical waves are generated. Due to destructive interference, a significant number of these waves cancel out in most directions. Conversely, in certain directions, some waves add up constructively, as elucidated by Bragg's law, expressed as follows:

$$2d \sin\theta = n\lambda \quad (1)$$

Where d represents the interplanar distance, λ signifies the wavelength of the X-ray, and θ corresponds to the angle of incidence. The attainable diffraction directions of the lattice are scanned by the angles 2θ. Consequently, XRD spectra are recorded in the form of diffraction peaks representing specific Miller indices values (hkl).

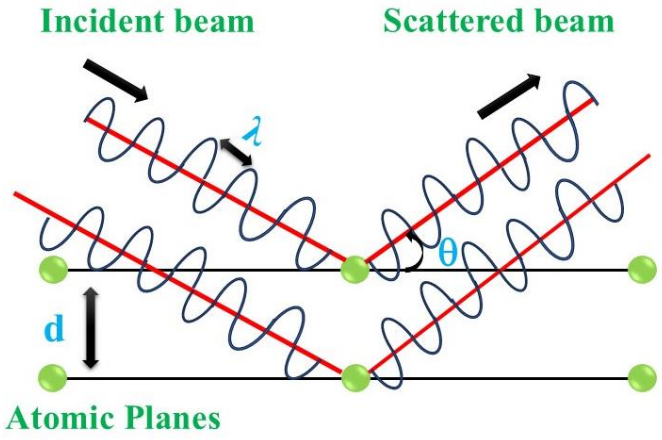

Fig. 2.4 Working principle of XRD.

Table 2.3 XRD instrumentation specification used in present work.

Instrument used	Available at	X-rays Wavelength	Scanning range 2θ (Degrees)
1. Bruker D8 Advance	CIF, Lovely Professional University, India.	Cu $K_{\alpha1}$ = 1.54 Å	20 - 80º
2. PANalytical EMPYREAN	CIF, IIT Jammu, India.	Cu $K_{\alpha1}$ = 1.54 Å	10 - 80º

c) Application: Sample identification is facilitated by utilizing diffraction peaks, which are then converted to d-spacing, with each material possessing its unique d-spacing. Additionally, applying the Scherrer equation, the average crystallite size can be calculated from the broadening of diffraction peaks:

$$D = K\lambda / \beta \cos\theta \quad (2)$$

where D represents the grain size, K denotes the shape factor (typically around 0.9), λ denotes the X-ray wavelength, β represent the full width at half maximum of the peak, and θ represents the Bragg angle. Furthermore, the microstrain within the crystal lattice can be determined from the peak broadening using Williamson-Hall analysis, which separates the contributions of crystallite size and strain to the peak broadening. Also, changes in the diffraction pattern with temperature or pressure can be used to study phase transitions and transformations in the material. By analyzing these parameters, XRD provides a comprehensive analysis of the crystalline material's structure, size, and properties, making it an essential tool in materials science and engineering [160]. In this study, we utilized XRD to confirm phase identification and determine the diffraction planes of the materials. Furthermore, the JCPDS (Joint Committee on Powder Diffraction Standards) mapping of the synthesized material was conducted to ensure accurate phase

2.2.2 Raman Spectroscopy

When Chandrasekhara Venkata Raman traveled to Calcutta in 1921 from Europe, he was drawn to the Mediterranean Sea's rich blue color. He subsequently discovered that the scattering of sunlight by water molecules was the source of this color. C.V. Raman won the Nobel Prize in 1930 for revealing that some of the dispersed radiation changes in wavelength when light travels through a transparent material. The Raman effect is the name given to this finding, and the word "Raman" has subsequently gained a lot of prominence in scholarly publications. Rayleigh scattering, in contrast, occurs when electromagnetic radiation is elastically scattered

by particles that are lesser than the wavelength of the incident radiation. Rayleigh scattering is the grounds for the sky's blue hue, in which sunlight is elastically scattered by air molecules. On the other hand, Raman scattering refers to the inelastic scattering of light in which a small portion of the scattered radiation has a frequency that differs from the frequency of the monochromatic radiation that was incident.

a) Principle: Upon impact, monochromatic electromagnetic radiation with energy $h\nu_o$ can disperse, reflect, or absorb in different directions. A tiny fraction of the scattered radiation is inelastic (approx 1 in 10^7 of the scattered light). It has a frequency that differs from the incident radiation ($h\nu_o \pm h\nu$), where $h\nu$ denotes the energy difference between the vibrational states. The scattered radiation with a lower frequency ($h\nu o - h\nu$), is known as Stokes lines, while the scattered radiation with a higher frequency ($h\nu o + h\nu$) is known as anti-Stokes lines. Changes in molecule polarizability cause a wavelength shift in the scattered photons that reveals structural details about the sample. The basic idea behind Raman spectroscopy is the light scattering that occurs when optical phonons are present in a substance. Raman scattering is a phenomenon that occurs when incident light interacts with the vibrational modes of molecules in the medium.

c) Working: The sample's surface is illuminated by a laser beam that acts as the excitation source and travels through a notch filter before entering the entrance slit. The Raman signal is divided into its component wavelengths using a monochromator by collecting the dispersed light through the use of a lens. A sensitive photomultiplier then picks up this signal. The signal is amplified, then processed and shown by a sensitive photomultiplier. After amplification, the signal is processed and displayed by a computer system [161].

c) Applications: Raman spectroscopy's ability to provide detailed molecular information makes it an indispensable tool in both research and industry such as explosives identification

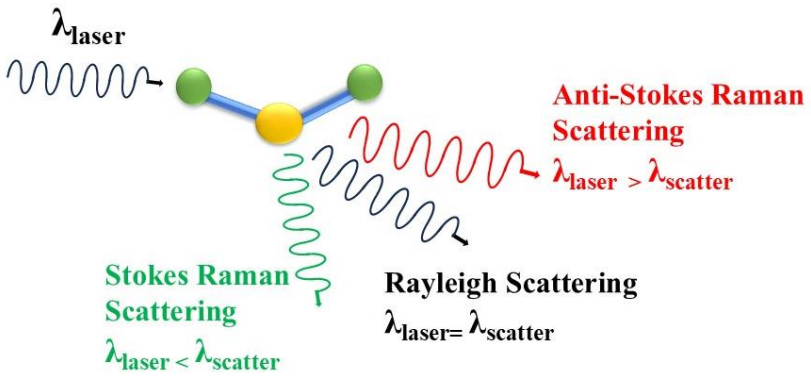

Fig. 2.5 Basic principle of Raman Scattering.

Table 2.4 Instrumentation details used for Raman in the present work.

Instrument Used	Available at	Laser used	Spectral Range
1. Renishaw-Invia-Reflex	USIF, AMU, Aligarh, India	532 nm	101.65-3202.7 cm^{-1}
2. Raman Spectrometer	MNIT MRC, Jaipur, India	532 nm	100-2000 cm^{-1}

[162], offering insights into the structural, chemical, and physical properties of materials.

In this study, Raman spectra were employed to validate the successful synthesis of the material. This analytical technique offers valuable insights into the molecular vibrations characteristic of the molecule. Additionally, further information regarding the instruments used is provided in Table 2.4.

2.2.3 Fourier transforms infrared spectroscopy (FTIR)

FTIR spectroscopy, a cutting-edge form of dispersive spectrometer, was employed to explore the interactions between infrared radiation and the sample. This technology stands out as the most recently developed and is preferred over its counterparts due to several advantageous features. Its exceptional precision, accuracy, speed, heightened sensitivity, ease of operation, and non-destructive nature all contribute to its widespread use and success in various fields [163]. *a) Principle:* The foundation of infrared spectroscopy is attributed to the atomic vibrations of molecules, which selectively absorb specific frequencies and energies of IR radiations. Since different compounds exhibit distinct infrared spectra, FTIR spectroscopy can effectively detect and classify these compounds. Its primary function is to probe the vibrational properties of molecules within a substance, aiding in the identification of various functional groups and residues present in a sample. The infrared region, spanning from (0.7-1) to (200-350) μm, is categorized into three ranges: near IR (13000 - 4000 cm^{-1}), intermediate IR (4000-400 cm^{-1}), and Far IR (400-10 cm^{-1}). Far-infrared radiation, characterized by its low energy, is utilized to study fundamental and rotational vibrations. Mid-infrared radiation, with moderate energy levels, is employed to investigate coupled rotational-vibrational structures. Far infrared, possessing higher energy, is used to excite overtone vibrations. For characterization purposes, the mid-infrared spectrum is typically utilized [164].

b) Working: During FTIR spectroscopy, infrared radiation is passed through the sample, where it is absorbed by the molecules present. For energy absorption to occur, the vibration

frequencies of the molecules must match those of the radiation. When light interacts with a sample, it is reflected, absorbed, or transmitted. The specific frequencies of energy absorbed by the specimen correspond to the vibrational energy of the functional groups within the sample. A detector captures the transmitted light, which contains valuable molecular information about the sample. In FTIR, mid-infrared frequencies are measured by an interferometer within a few seconds. The interferometer analyzes the energy transmitted through the material and comprises a beam splitter, fixed mirror, and oscillating mirror. The incoming IR radiation is split into two beams, with one beam maintaining a fixed path length and the other experiencing a variable path length due to the moving mirror. These two beams interfere constructively, resulting in an emitted beam known as an interferogram, which contains comprehensive information about the sample. Through mathematical techniques such as Fourier transformation, the individual frequency information is decoded [165].

c) Application: In molecules possessing a center of symmetry, vibrational transitions that are feasible in the infrared (IR) spectrum are typically inactive in the Raman spectrum, and the reverse is also true. For example, in CO_2, the symmetric stretching vibration is not active in the IR spectrum but is active in the Raman spectrum due to the change in bond polarizability. Conversely, the asymmetric stretching vibration induces a change in dipole moment, making it IR active but Raman inactive, as the polarizability changes in one bond offset those in the other.

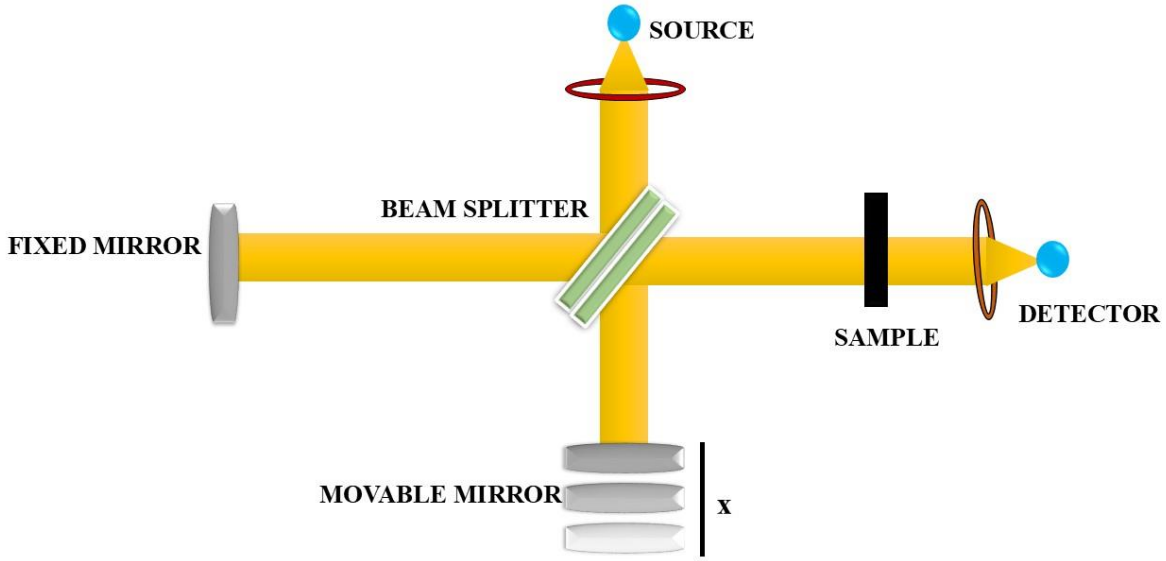

Fig. 2.6 Working of FTIR instrument.

Table 2.5 Instrumentation specifications used for FTIR in present study.

Instrument Used	Available at	Spectral Range
1. NICOLET iS50 FTIR Tridetector ThermoScientific)	CIF, IIT Jammu, India	Mid IR (4000-400 cm^{-1})

So, we can use FTIR for the molecules which are Raman inactive and IR active. In the present study, FTIR is employed to identify the functional groups found in the composite by measuring the transmittance of infrared radiation at various wavelengths, which correspond to specific molecular vibrations. Additional information about the instruments utilized for FTIR analysis can be found in Table 2.5.

2.2.4 UV-Vis Spectroscopy

This technique is primarily employed for the identification of chemical species within a sample, focusing on the electronic transitions of atoms. Typically, when atoms or molecules absorb ultraviolet (UV) and visible radiations, the transitioning of electrons from lower to higher energy states is observed. The discrete quantum energy levels of atoms dictate that only radiation with specific energy levels can induce transitions between these states.

a) Principle: The underlying principle of this spectroscopy aligns with Beer-Lambert's law, where absorbance (α) is proportionate to the path distance of the absorbing medium (b) and the concentration of the sample (c).

$$\alpha = Log10\ (I/I^{o}) = \varepsilon bc \quad (3)$$

In this equation, I^{o} denotes reference beam intensity, I denotes sample beam intensity, and ε is the proportionality constant.

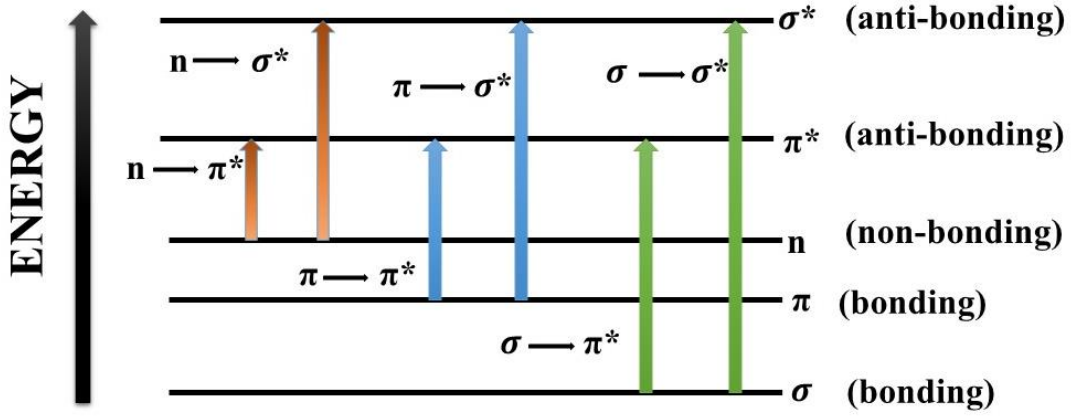

Fig. 2.7 All possible transitions in UV spectroscopy.

Table 2.6 Instrumentation details for UV.

Instrument Used	Available at	Spectral range	Solvent used
1. UV spectrometer	CIF, LPU, Punjab, India	200-800 nm	DMF

UV radiation typically ranges between 200 to 400 nm, possessing sufficient energy to induce electronic excitations within molecular orbitals (ΔE). ΔE refers to the difference in energy between the highest filled and the lowest vacant molecular orbitals. A smaller ΔE implies a lower energy requirement for electron excitation. For an incident photon to be absorbed and excite the electron, its energy must be greater than or equal to that of the excited electron [166].

b) Working: This method employs monochromatic radiation, which can be UV, visible, or near-infrared. Upon radiation exposure, molecules within the sample can undergo electronic transitions. The color of a material is intimately linked with its electronic structure. This spectroscopy facilitates the assessment of all electronic transitions and the determination of certain sample properties, such as band gap energy, which aids in classifying the sample as an insulator, semiconductor, or conductor. When light (energy) interacts with a sample, it is typically absorbed, prompting electrons to transition between the lowest energy state to excited or anti-bonding orbitals. Fig. 2.5 illustrates all possible transitions when a photon is absorbed (σ-σ*, π-π*, σ-π*, π-σ*, n-σ*, n-π*). However, in UV-vis spectroscopy, σ-σ*, π-π*, σ-π*, n-σ*, and n-π* transitions are feasible, with σ-σ* and n-σ* transitions requiring high energy, while π-π* and n-π* transitions demand less energy [167].

c) Application: UV spectroscopy is utilized to examine the electronic structure of molecules, allowing for the identification and analysis of chemical substances. It enables quantitative analysis by correlating the absorbance of light with the concentration of the analyte, facilitating accurate measurements of sample concentrations.

A UV spectrometer has been utilized in this study to calculate the bandgap of the various synthesized materials. Detailed information about the spectrometer is provided in Table 2.6

2.2.5 X-ray photoelectron spectroscopy

Electron spectroscopy for chemical structure examination, also known to as X-ray photoelectron spectroscopy (XPS), is a popular surface analysis method for analyzing the chemical analysis of surfaces. XPS is grounded in the photoelectric effect and was pioneered

in the middle of the 1960s by Dr. Kai Siegbahn and his team at the University of Uppsala in Sweden. Dr. Siegbahn received the Nobel Prize in 1981 for this groundbreaking project. The surface of solid exhibits distinct chemical compositions and physical properties compared to its interior. In XPS, an energetic beam of ultraviolet or X-ray radiation is used to ionize molecules or atoms. The energy of the light must be high enough to knock out electrons, from the topmost occupied energy level of the atoms. When hν is sufficiently large, electrons from deeper atomic levels can also be ejected. When photons with wavelengths in the lower energy X-ray region strike the surface of a crystal, core electrons are expelled from the atoms. By measuring the properties of these escaping electrons, a spectrum is obtained. The XPS method includes irradiating the material with small energy (~1.5 keV) X-rays to produce the photoelectric effect. An electron spectrometer with high magnification stores the energy spectrum of the photoemitters that are released. Maintaining the highest possible vacuum conditions is crucial for XPS experiments. A high vacuum keeps the clean sample from getting contaminated again and makes it easier for photoelectrons to be transported to the analyzer. Because of its sensitivity to surface composition and its usual sample depth of a few nanometers, contamination is a major problem in XPS. The ejected photoelectrons' kinetic energies allow for the direct identification of the sample's constituent elements, and the intensities of these photoelectrons can be used to calculate the elements' relative concentrations.

a) Principle: An electron can be ejected from an atom's K-shell when known energy photons, most commonly X-rays, collide with a surface. Afterward, spectroscopy is used to determine the kinetic energy (K.E.) of this expelled electron. Plotting binding energy against electron counting rate is how the resultant spectrum is shown. Every element possesses a particular binding energy that functions as an attribute. Since X-rays can only penetrate solids a few microns below the surface, photoelectrons are emitted predominantly due to interactions between incident photons and surface atoms. The following formula yields the kinetic energy of these released electrons:

$$K.E. = h\nu - B.E. - \Phi_S \quad (4)$$

where ΦS represents the spectrometer's work function, hv is the photon's energy, and B.E. is the atomic orbital's binding energy from which the electron is released. In an XPS spectrum, electrons from inner orbitals appear at higher binding energies compared to those from outer orbitals. According to an empirical formula, the binding energies of 1s orbitals rise proportionately with atomic number. A graph that displays the quantity of electrons found in relation to their kinetic energy is a typical XPS spectrum. The energy distribution of the electrons in an element is shown by this spectrum.

Table 2.7 XPS data of all the elements related to MoS_2-based nanocomposites from the International XPS database.

Element	Electronic level	Species	B.E (eV)
Mo	$3d_{5/2}$	MoS_2	229.4 ±0.46
Mo	$3d_{3/2}$	MoS_2	232.94 ±0.46
S	S2s	MoS_2	226.99 ±0.6
S	$Sp_{3/2}$	MoS_2	161.85 ±0.6
S	$Sp_{1/2}$	MoS_2	163.42 ±0.6
C	Csp^2	RGO	284.6 ±0.42
C	C1s	RGO	288 ±0.42
O	O1s	RGO	532.80 ±0.4
Mn	$2p_{3/2}$	MnS	644.42 ±1.0
Mn	$2p_{1/2}$	MnS	641.3 ±1.0
Co	$2p_{3/2}$	Co	778.2
Co	$2p_{1/2}$	Co	793

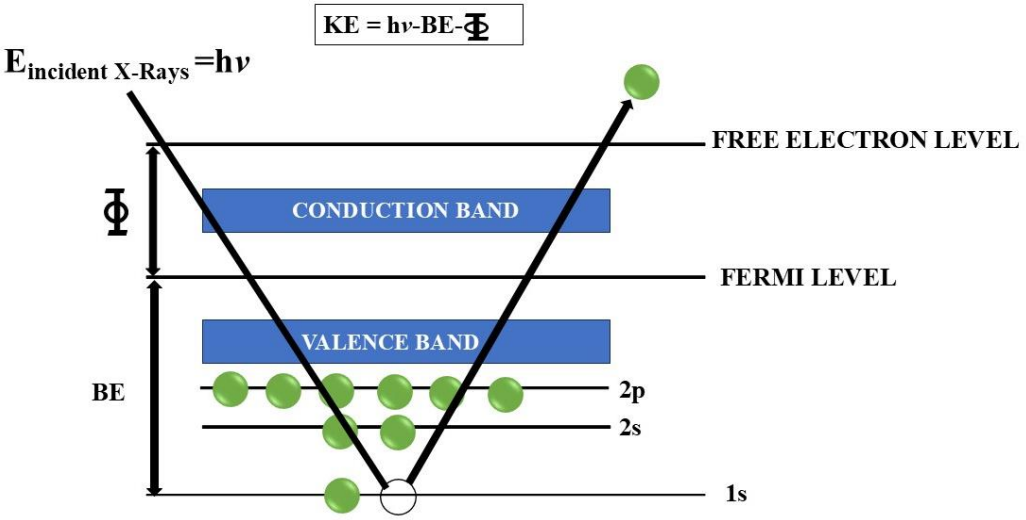

Fig. 2.8 Working Principle of XPS.

Table 2.8 Instrumentation details used for XPS in the present work.

Instrument Used	Available at	Range
1. ThermoScientific NEXA Surface analyzer	CIF, IIT Jammu	0- 1350 eV

In the process of data collection, the Fermi energy is used as the standard reference point for materials, serving as the "natural" zero. The elements that are present on or on the surface of the material under study may be identified directly since each element generates a distinct collection of XPS peaks at certain binding energy levels. These distinctive peaks line up with the electrons' electrical configurations in different atomic orbitals, including the 1s, 2s, 2p, 3s, and so on.

b) Working: In the experimental setup of X-ray photoelectron spectroscopy (XPS), a sample is situated within an ultra-high vacuum environment and exposed to low-energy X-rays with a photon energy represented by hν. When these photons interact with the core-level electrons of surface atoms, photoelectrons are emitted. This process can be elucidated in several steps: Firstly, a photon is absorbed by a bonded electron, which transforms some of the energy into kinetic energy. Subsequently, as the electron leaves the atom, it uses some of its energy to overcome the Coulombic attraction of the nucleus, thereby reducing its KE. The atom then readjusts its outer orbitals, which lowers the final state's energy and transfers the extra energy to the leaving electron. Lastly, the KE and the quantity of e^-s departing from the top 0 to 10 nm of the sample are measured in order to produce the XPS spectrum.

c) Application: Inorganic compounds, such as glasses, ion-modified materials, metal alloys, ion-modified materials, semiconductors, ceramics, and polymers are frequently analyzed using XPS. [168].

The standard binding energy values for each element related to this work are presented in Table 2.7, sourced from the International XPS database [169]. These standard binding energy values provide a standardized framework for comparison, ensuring consistency and reliability in the interpretation of experimental results. The fundamental makeup, chemical states, and electronic states of the elements included within the nanocomposites are all determined in this work using XPS. The device specifications used are detailed in Table 2.8.

2.2.6 Field Emission Scanning Electron Microscopy (FESEM)

FESEM presents a valuable electron microscopic approach for scrutinizing micrographs and delving into the structural details of micro-structured materials within high-resolution

specimens, ranging from nearly 10 to 300,000 times magnification, offering substantial depth. FESEM surpasses conventional Scanning Electron Microscopy (SEM) by providing three to six times superior resolution. Additionally, it enables the investigation of minute contamination spots through fine-tuned electron accelerating voltages, along with Energy Dispersive Spectroscopy (EDS). EDS facilitates the differentiation of characteristic X-rays emitted by various elements within the sample, allowing for their quantification through spectral analysis software.

a) Principle: Fundamentally, FESEM operates by scanning samples with electrons rather than light, relying on electron-matter interactions.

b) Working: The experimental setting of the FESEM instrumentations is shown in Fig. 2.5. Electrons, generated by an electron gun or field emission source, undergo acceleration via a field gradient before passing across electromagnetic lenses to direct the beam onto the material. Upon interaction, the sample emits diverse electrons, captured by a detector to construct an image of the surface based on the intensity contrast between secondary electrons and the primary electron beam [170].

Ultimately, this image is portrayed on a computer monitor. Notably, emitted electrons, including those from an X-ray tube, aid in assessing object size and morphology. Incident electrons produce a plethora of radiation upon striking the material's surface, encompassing backscattered and secondary electrons, X-rays, heat, and even transmitted electrons. However, backscattered and secondary electrons predominantly convey information regarding surface morphology. To prevent spatial charge accumulation, detrimental to FESEM micrographs, the test specimen is grounded.

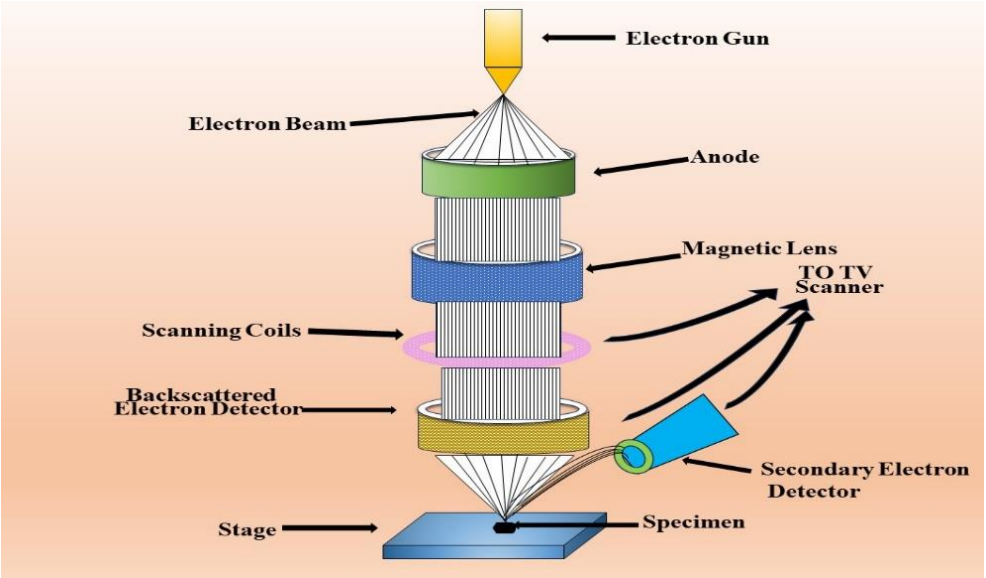

Fig. 2.9 Experimental setup for FESEM analysis

Table 2.9 Instrumentation specifications used for FESEM and EDS analysis in the current study.

Instrument Used	Available at	Magnifications
1. JEOL JSM-7610F Plus 2. EDS (OXFORD EDS LN2)	CIF, LPU, Punjab, India	100 µm- 100 nm

Table 2.10 Instrumentation specifications used for HRTEM in the present study.

Instrument Used	Available at	Magnifications	Software Used
1. Hitachi H-7500	CIL, PU, Punjab, India	10nm - 500 nm	ImageJ

The electron beam scans the surface, elucidating the embedded particles' reactions, thereby facilitating detailed analysis.

c) Application: By examining the FESEM images, researchers can obtain insightful knowledge about the structural characteristics and surface properties of the synthesized materials. This knowledge is essential for comprehending the links between morphology and characteristics and for streamlining the synthesis procedure to provide the right material qualities for a range of uses.

FESEM analysis along with EDS was conducted in this research to visualize the surface features of the synthesized materials with exceptional detail and clarity. This technique allowed us to examine various aspects of the material's surface, including particle size, shape, distribution, and surface roughness. Instruments used for both FESEM and EDS are mentioned in Table 2.9

2.2.7 HRTEM

High-resolution transmission electron microscopy (HRTEM) is a TEM imaging technique that enables visualization of the crystallographic structure of a sample at the atomic level. Unlike conventional microscopy, HRTEM does not rely on absorption to create images. Instead, it forms images through interference patterns in the image plane. In this process, electrons interact independently with the sample, and the electron wave undergoes phase changes as it passes through the imaging system, resulting in an image that does not directly represent the sample's structure.

a) Principle: The contrast in HRTEM images differs from that in light microscopy. In the case of HRTEM, diffraction takes place in place of absorption when the electron ray hits the material. The orientation of the sample plane with respect to the electron beam affects the

diffraction intensity. [171].

b) Working: The electron beam can be strongly diffracted from the axis at specific angles or transmitted at other angles. Specimen holders are designed to allow tilting of the specimen to achieve particular diffraction conditions. By blocking deflected electrons with an aperture and allowing unscattered electrons to pass through, a contrast image, known as a light field image, is obtained. Conversely, using the deflected electrons to form an image results in a dark field image. *c) Application:* This method is invaluable for studying nanoscale properties due to its high resolution, allowing for the imaging of crystal structures, crystal defects, and individual atoms [172].

In this work, the precise morphology and structure of materials at the atomic level are investigated using HRTEM. Additionally, ImageJ software was employed to calculate d-spacing. Details regarding the instruments used for this analysis are provided in Table 2.10.

2.2.8 Brunauer-Emmett-Teller (BET)

The BET abbreviated as (Brunauer-Emmett-Teller) theory, established during the early 20th century, holds a pivotal position within surface science and material characterization. It owes its name to its creators: Stephen Brunauer, Paul Hugh Emmett, and Edward Teller. The BET theory offers a robust framework for comprehending the process of gas adsorption onto solid surfaces, playing an essential role across a spectrum of scientific domains and industrial sectors.

a) Principle: Gas molecules adhering to a solid surface is the fundamental idea underlying the BET theory. To create a monolayer, gas molecules are first adhered onto the solid material's surface. The uniform distribution of gas molecules over the surface is a defining feature of this monolayer. The BET-specific surface area is calculated from a multipoint surface area curve between relative pressure (P/P^o) and $1 / [W((P/Po) - 1)]$ where P is equilibrium pressure, P^o is the saturation pressure and W is the amount of N_2 gas adsorbed at a given relative pressure.

b) Working: The BET theory provides insight into the physisorption of gas molecules onto an upper layer of the solid and is the basis for a crucial analytical method that measures a material's specific surface area. Based on observations of the nitrogen adsorption isotherm at 77 K, the BET method is frequently utilized to determine the specific surface area. For analysis, data points within the relative pressure span of 0.05 to 0.3 are usually deployed. Multilayer gas adsorption on the adsorbent's surface is assumed by the BET model. Consequently, data selection needs to be carefully considered, especially for materials with tiny orifices (2–3 nm in diameter) or those with poor ordering, where multiple-layer adsorption may not occur in the

pressure range stated above but rather capillary condensation. Data within the capillary condensation pressure range should be omitted from computations in order to avoid significantly overestimating specific surface area. To enable findings from multiple laboratories to be compared, the pressure range used in BET calculations must be included. If below relative pressure 0.01 data is accessible, the specific surface area can be determined by using comparable plotting techniques like t-plot or oh-plot. Plotting the quantity adsorbed for the material under investigation versus the quantity adsorbed for a suitable macroporous reference solid at the same values of pressure is used to create comparative graphs. Plots that are linear show comparable adsorption processes (monolayer-multilayer adsorption), whereas those that are nonlinear show variations in the adsorption. Because of their significant closeness in nitrogen adsorption characteristics at 77K, chromatographic grade macroporous silica gels and siliceous ordered mesoporous materials are frequently utilized as reference solids [173]. Furthermore, the mesopore and macropore total surface area may be calculated from the slope of the linear segment. In this work, we have studied the effective surface area of MoS_2 and MoS_2-based nanocomposites using the BET technique. The parameters that were employed are stated in Table 2.11.

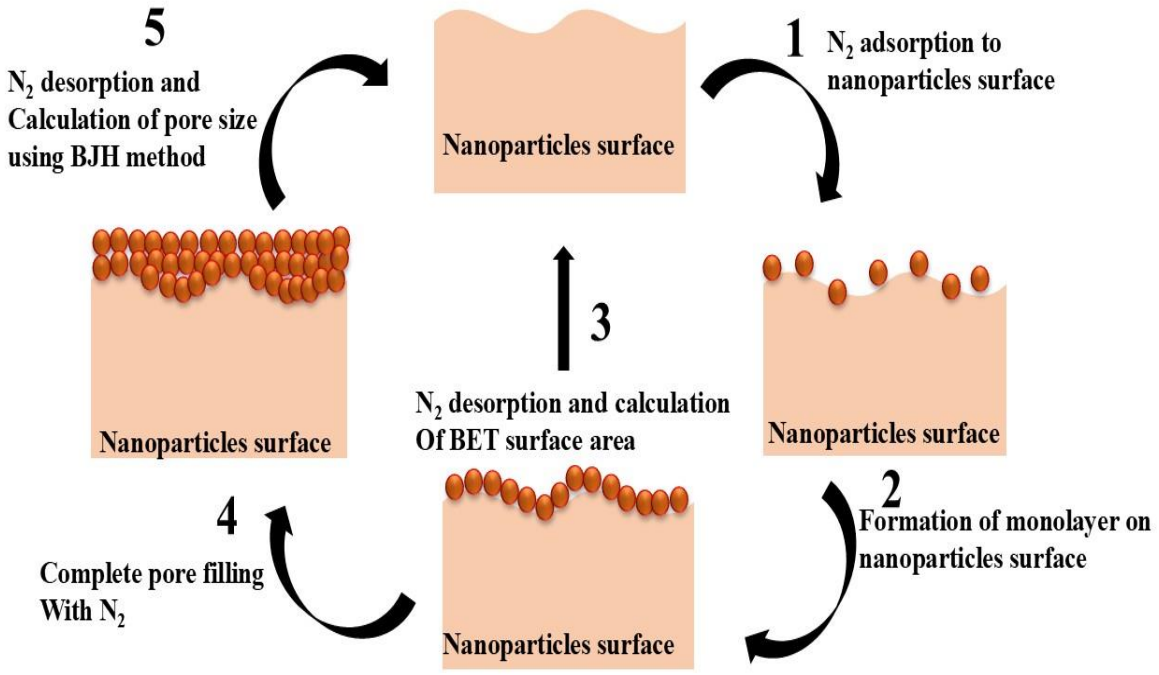

Fig. 2.10 Principle of BET and BJH method.

Table 2.11 Instrumentation specifications used for FTIR in the present study.

Instrument used	Available at	Degassing Temperature	Degassing Time	Pressure
1. Autosorb iQ Station 3	SAIF, Chandigarh, India	150º C	12 h	10^{-6} Torr

2.3 Electrochemical techniques

Electrochemical techniques are extensively utilized for detecting analytes because of their remarkable sensitivity, selectivity, and cost-effectiveness. These methods involve measuring electrical parameters such as current, voltage, or charge, which vary in response to specific analytes. Here are some prominent electrochemical techniques used in the current study for sensing various analytes:

2.3.1 Cyclic Voltammetry

In many different areas of chemistry, cyclic voltammetry (CV) is a crucial and extensively used electroanalytical method. It is mostly used to look into redox processes, examine electrochemical reactions between ions and atoms on the electrode surface, comprehend reaction intermediates, assess the stability of reaction products, and collect qualitative data on electrode reaction mechanisms. It also sheds light on the processes of charge transfer between electrode electrons and electrolyte ions. Consequently, CV is an effective method for studying redox processes, which are essential for understanding electrochemical sensing mechanisms [174].

a) Principle: Using a three-electrode electrochemical cell, cyclic voltammetry measures current by scanning a working electrode's potential in both forward and backward directions at a specific scan rate. Through cyclic and linear electrode potential variations within a preset potential frame, this technique tracks the current flow betwixt the working and counter electrodes. In CV, the WE's potential is raised in one direction, then reversed to return to its starting value. This cycle is frequently repeated several times. The cyclic graph between current versus applied potential results in a cyclic voltammogram.

b) Working: Charged species are involved in a chemical process that takes place in an electrochemical cell. These species' energy is connected to the potential of the phase in which they exist. The movement of ions or electrons across the interface between two nearby species is the basic stage in these reactions. An electrode reaction is a type of interfacial reaction that

involves the transfer of charge. The reaction possesses a predictable rate, and its overall rate is proportional to the unit area of the interface. Chemical reactions, adsorption, and structural rearrangement involving charge transfer are examples of interfacial or electrode reactions. Electrode processes, including electrode reactions and the mass transport process, encompass all changes and activities that occur at the electrode as current flows through the cell. Experiments using cyclic voltammetry are conducted on a solution within a cell that has tri-electrode system. An operational electrode, a reference, and an auxiliary electrode are often found in an electrochemical cell. The electrochemical process (oxidation or reduction) may be studied since the operational electrode is where the voltage is regulated and the current is observed. It functions as the basis for the electrochemical process. The reference electrode determines the potential of the operational electrode. It must maintain a steady electrochemical potential when no current runs through it. The counter electrode, also known as the auxiliary electrode, operates as an electron source or sink, allowing current to pass from the external circuit to the cell. It completes the cell circuit, with current entering the solution through the working electrode and exiting through the counter electrode. This electrode should be inert with a large surface area, such as platinum or carbon. These three electrodes are dipped in an electrolyte, and the electrochemical cell consists of the electrodes, the solution, and the container in which the solution is stored. The electrolyte provides sufficient conductivity. The solvent, electrolyte, and working electrode material determine the potential range available during a cyclic voltammetry experiment [175].

c) Analysis from Cyclic Voltammogram: Cyclic voltammetry serves as a versatile tool for understanding various electrochemical parameters.

(i) Redox potential (E°): An electroactive species' redox potential can be determined via cyclic voltammetry. The standard potential, E^o, may be easily estimated for a reversible system by measuring the midway potential between the two peaks, which is the point at which the quantities of the oxidized and reduced species are balanced.

(ii) Electrochemical reversibility: The cyclic voltammetry's form can reveal the redox process's nature, whether it is quasi-reversible, irreversible, or reversible. An irreversible reaction will have an asymmetrical peak, whereas a reversible reaction will display a clearly defined, symmetrical peak.

Table 2.12 Instrumentation specifications used for CV in the present study.

Instrument used	Available at	Parameters used
1. Metrohm: Multi-Channel Autolab	CIF, LPU, Punjab, India	Scan rate: Ranging from 10 – 100 mVs-1 pH: 7 PBS: 0.1 M Potential window: -0.2 – 0.8 V

(iii) Diffusion coefficient (D): By conducting a number of tests at various scan rates, cyclic voltammetry may offer information regarding the diffusion coefficient of electroactive molecules. Because of the thinner diffusion layer at faster scan speeds, there are stronger currents. The peak current is directly proportionate to the under root of the scan rate, as stated by the Randles-Sevcik equation, which also links the peak current to the scan rate. This is how an electroactive species that diffuses freely acts. An alteration in behavior is noted if the electroactive species is adhered to or adsorbed onto the electrode surface. In this case, the correlation between the peak current and the scan rate is linear. This is a crucial method to determine whether your reactant is adsorbed at the electrode surface.

(iv) Double layer capacitance: To calculate double-layer capacitance (C_{dl}) from cyclic voltammetry (CV) data, the peak current vs scan rate at multiple scan rate is plotted. The slope of the linear fit in the figure equals the double-layer capacitance, which represents the coefficient of proportionality between the current and the scan rate. The capacitive current is proportional to the scan rate.

(v) Electroactive Surface area: The electrochemical surface area (ECSA) can be calculated as follows:

$$ECSA = C_{dl}/C_A, \quad (5)$$

Where C_A is the areal capacitance of the nanocomposite.

In our research, we have determined the redox potential, assessed electrochemical reversibility, and analyzed the shape and size of peaks. This has provided insights into reaction kinetics, electron transfer rates, and reaction mechanisms. Additionally, we have estimated the surface area of the electrodes from multiscan CV curves. Further experimental details are presented in Table 2.12

2.3.2 Differential Pulse Voltammetry:

Differential Pulse Voltammetry (DPV), proposed by Barker and Gardner, is an effective electroanalytical method known for its improved sensitivity and resolution in the detection and

quantification of various species, including drugs and biomolecules. This technique stands out among other pulse methods due to its unique approach to measuring current, which significantly reduces capacitive and background currents, thereby improving the detection of analytes.

a) Principle: Every pulse in DPV has two measurements of the current: one right before the potential step and one right after the step. To build the voltammogram, the difference between these two current values is utilized.

b) Working: In DPV experiments, the electrochemical cell comprises three electrodes: a WE, a RE, and a CE, which are used to measure both current and potential. The reaction of interest happens at the working electrode. It must be made of redox-inert material within the potential range of interest. Different types of working electrodes can provide various potential windows and are chosen based on the specific requirements of the experiment. Common materials include mercury, gold, platinum, and various forms of carbon. Mercury electrodes offer a broad negative potential range due to the surface reduction of hydrogen ions or water. Platinum is durable and suitable for use in anhydrous organic solvents, providing a broad potential window. Gold is less commonly used due to surface oxidation at positive potentials. Carbon electrodes are valued for their wide potential window, high conductivity, affordability, and structural stability. The reference electrode serves as a standard to control the potential of the working electrode in voltammetry experiments. It should facilitate a reversible half-reaction with Nernstian behavior and is often insulated from the sample solution to prevent contamination, typically using a bridge or a frit. Common reference electrodes include saturated calomel, silver chloride, and mercury sulfate electrodes. The counter electrode provides an alternative path for current flow to prevent it from passing through the reference electrode, thus minimizing changes in the concentration of reactants and products. Inert conducting materials like platinum wire and graphite rod are typically used. The electrochemical cell can also function as an auxiliary electrode if it is metallic. This trio of electrodes is connected to a device known as a potentiostat. The potentiostat is the central component in voltammetric instrumentation. Its main function is to precisely regulate the applied potential and monitor the resulting current changes within the system. Modern potentiostats include converters, electrometer circuits, a microprocessor with internal memory, and an amplifier. Most voltammetric techniques require dynamic potential modulation according to predefined waveforms, and the potentiostat is crucial for delivering accurate and adaptable potential control. Advances in digital electronics have enabled potentiostats to operate digitally, facilitating the execution of rapid experiments and enhancing sensitivity through advanced pulse voltammetry techniques. When using

computer-controlled instruments, waveform modulation and properties are managed by software, allowing further operator control. In DPV we used a differential pulse waveform as shown in Fig. 2.6. The potentiostat regulates the applied potential at the interface between the electrolyte and the working electrode based on the reference electrode potential [176].

The electrolytic solution must be liquid at room temperature, capable of dissolving ionic substances to form an electrolyte, and must dissolve the electroactive species of interest. It should have a broad potential range to avoid solvent oxidation or reduction during the redox process. Water is the most common solvent, but other solvents and solvent mixtures are also used. Organic solvents often use salts like tetraalkylammonium. Buffers such as phosphate, acetate, citrate, and Britton-Robinson are used when maintaining pH is necessary, although they are less common in quantitative determinations. The oxidation or reduction of the analyte occurs when current passes through the working electrode as a result of a potential being applied to it, causing it to rotate around the formal potential. The analyte's concentration in the solution is directly correlated with the current value. Additionally, computerized processing of analytical data has facilitated the development of these techniques. c) Analysis from DPV: DPV is a crucial technique in electroanalysis, offering superior sensitivity and resolution by effectively reducing background noise and enhancing signal clarity.

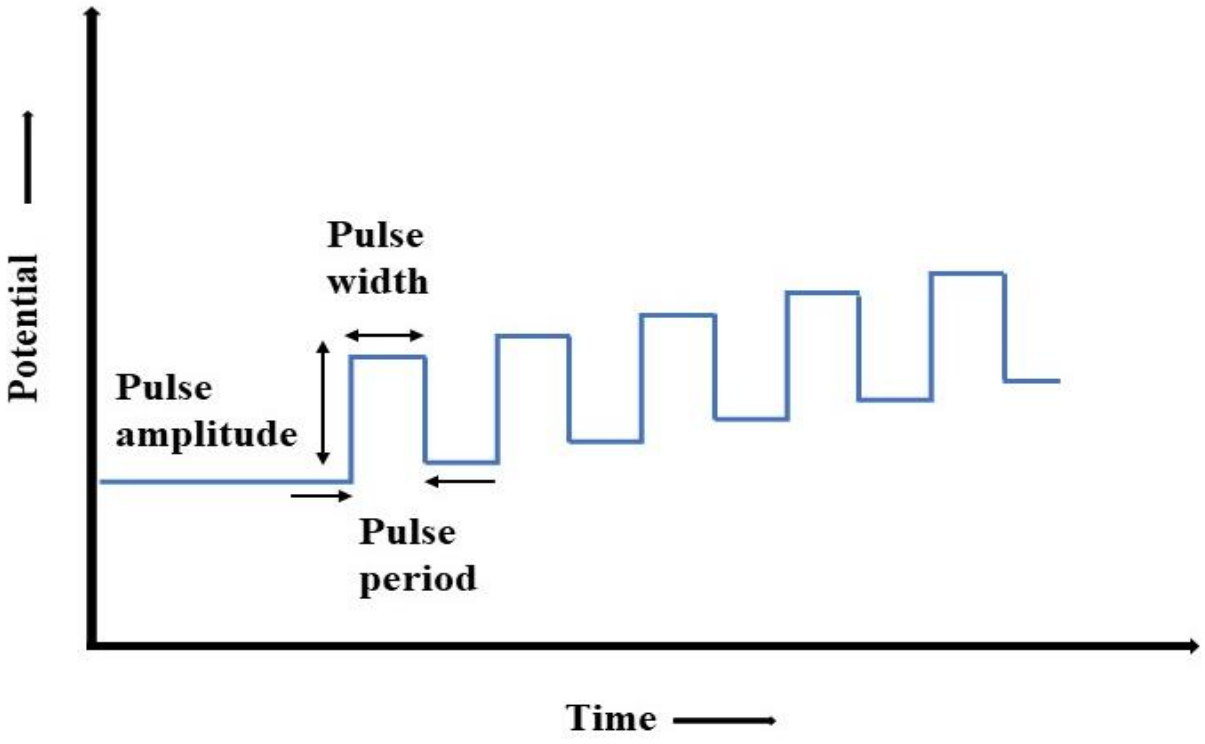

Fig. 2.11 Potential Waveform used in DPV

Its practical applications, particularly in clinical settings, underscore its importance in analytical chemistry. We can extract the following information from DPV:

(i) Linear range: The concentration range where the linear response between the observed signal and the analyte concentration is constant is referred to as the linear range. From DPV we can find the linear range of various analytes.

(ii) Limit of detection (LOD): The detection limit measures the slightest amount of an analyte that can be reliably detected. From DPV we can plot a curve between concentrations vs peak current. Then linearly fitted data will provide a linear regression equation. Further, three times the standard deviation of the data is divided by the slope of the calibration curve. Mathematically it is expressed as below:

$$LOD = 3\times\sigma/slope \quad (6)$$

(iii) Sensitivity: Sensitivity in analytical chemistry denotes the capability of an analytical method to consistently and precisely detect minute variations in the concentration of an analyte. Sensitivity is calculated as follows:

$$Sensitivity = Slope/ ECSA \quad (7)$$

(iv) Selectivity: The term "selectivity" describes an analytical method's capability to precisely identify and measure a target analyte surrounded by additional interfering species or matrix elements. DPV facilitates the separation of analyte peaks based on their oxidation or reduction potentials. This capability is fundamental in assessing the selectivity of a designed sensor. By analyzing the DPV voltammograms, distinct peaks corresponding to the target analyte and potentially interfering species can be observed. If the sensor exhibits well-defined and separate peaks for the target analyte surrounded by interfering substances, it suggests good selectivity. Conversely, overlapping or indistinguishable peaks may indicate poor selectivity and potential interference issues. Therefore, DPV provides valuable information regarding the selectivity of the designed sensor. In this research, a thorough evaluation of the designed sensor's performance parameters, including LOD, sensitivity, selectivity, stability, and reproducibility, using DPV is done. Further experimental details, including instrument details and measurement procedures, are provided in Table 2.13.

2.3.3 Electrochemical Impedance Spectroscopy

EIS abbreviated as (Electrochemical Impedance Spectroscopy) is an electrochemical method that is employed for the examination of various electrochemical phenomena occurring at the electrode/electrolyte interface. In this method, the recognition and calculation of the variables are based on the frequency signal of the electrochemical system under observation.

Table 2.13 Instrumentation specifications used for DPV in the present study.

Instrument used	Available at	Parameters
1. Metrohm: Multi-Channel Autolab	CIF, LPU, Punjab, India	Scan rate = 60 mVs^{-1} WE = (MoS_2, MoS_2/RGO, Mn-MoS_2/RGO, Co-MoS_2/RGO) modified GCE. Area of GCE= 0.07 cm^2 CE = Pt wires RE = Ag/AgCl PBS = 0.1 M

Its special attributes make it surpasses other electrochemical methods. Operating in an equilibrium state, EIS employs minimal signal analysis, enabling it to explore signal relaxations across a broad frequency spectrum, spanning from less than 1 mHz to beyond 1 MHz. This versatility is facilitated by the accessibility of commercial electrochemical workstations, commonly known as potentiostats. EIS makes it feasible to explore intrinsic material properties or particular processes that could impact an electrochemical system's capacitance, resistance, or conductance.

a) Principle: The electrochemical cell responds in a pseudo-linear manner to an applied sinusoidal potential, which is characterized by a phase shift between the current response and the excitation signal. The equation represents the excitation potential with respect to time is written below:

$$E(t) = E_o \cdot sin(\omega t) \quad (9)$$

Here, Eo indicates the applied signal's amplitude, while ω indicates the radial frequency parameter. E(t) is the system's potential at a particular time t.

b) Working: The expression of impedance delineates into a real part (I_{real}) and an imaginary part (I_{imag}). By plotting I_{real} on the X-axis and I_{imag} on the Y-axis, a "Nyquist Plot" emerges. Each point on this plot corresponds to an impedance value at a specific frequency point, typically with negative I_{imag} values. On the X-axis, impedance shifts from low to high frequencies, reflecting a right-to-left progression. Additionally, impedance on a Nyquist plot can be illustrated as a line vector |I|, and the angle between this vector and the horizontal axis is termed the "phase angle." One more common representation of impedance results is the Bode plot, prevalent in engineering circles. Unlike the Nyquist plot, the Bode plot is comprised of two logarithmic graphical representations: phase vs frequency and magnitude versus

frequency. Impedance measurement practically entails exposing the working electrode to a potential wave and recording the current wave that occurs. Parameters such as I, Φ, I_{real}, and I_{imag} are obtained and shown from these recorded waves.

c) Working: In the experimental setup a frequency signal analyzer is conjoined with an electrochemical system to measure the current of the response of the EIS system which is subjected to change in the frequency of an input sinusoidal wave. These factors are measured across possible waves with different frequencies to create this spectrum. Conducting an EIS experiment with a three-electrode setup requires keeping the applied voltage constant. Nyquist plots are then used to gather and represent the resulting solution resistance (Rs), charge transfer resistance (Rct), and Warburg impedance (W).

d) Analysis from EIS: Electrochemical phenomena seen at the electrolyte/interface and during redox reactions are commonly represented as an equivalent circuit, which is an electric circuit made up of resistors, capacitors, and inductors, among other electrical components. This comparable circuit is built and used to analyze and comprehend the various components of the EIS system. Components such as Rs abbreviated as (solution resistance), Cdl abbreviated as (double layer capacitance at the electrode surface), Rct abbreviated as (charge transfer resistance), and Zw abbreviated as (Warburg resistance) are combined and simplified inside the Randles equivalent circuits. Warburg resistance is caused by diffusion at the electrode-electrolyte contact. To imitate or model this non-ideal capacitance behavior, a constant phase element (CPE) is included, as an ideal capacitor is seldom discovered experimentally. Surface imperfections, material non-homogeneity, and surface porosity found in the materials under investigation make this inclusion necessary [177]. It is generally employed to investigate the thin films deposited on the electrode surface as it can easily differentiate the conductivity phenomena occurring at the surface. Using an amplitude of 5 mV, the EIS curves were recorded in this work within the frequency range of 0.01 Hz to 100 kHz. Table 2.14 contains a tabulation of the experimental parameters and instrument specifications. The buffer-analyte solution or other non-capacitive series phenomena caused a series resistance (Rs) in the suggested circuit, which was comprised up of two impedances. The first impedance consists of charge-transfer resistance (RCT), Warburg (W), inductor (L), and a constant phase element (CPE) and the other one carries a resister (R) and a double-layer capacitor (C). The impedance of CPE was derived by using, $ZCPE = A^{-1}(\omega)^{-N}$. Here, ω is the imaginary component of angular frequency and N is a distribution factor with a value between 0 and 1 [216]. The parameters of the equivalent circuit at different analyte concentrations were estimated after fitting.

Table 2.14 Instrumentation specifications used for EIS.

Instrument used	Available at	Parameters
1. Metrohm: Multi-Channel Autolab	CIF, LPU, Punjab, India	WE = (MoS_2, MoS_2/RGO, Mn-MoS_2/RGO, Co-MoS_2/RGO) modified GCE. Area of GCE= 0.07 cm^2 CE = Pt wires RE = Ag/AgCl PBS = 0.1 M

2. 4 Conclusion

This chapter offers a detailed outline of the synthesis methods, chemicals used, and several characterization techniques, including XRD, Raman spectroscopy, FESEM, EDX, HRTEM, FTIR, UV-Vis, XPS, BET, and electrochemical studies like CV, DPV, and EIS. The principles and mechanisms behind these techniques are comprehensively explained, aiming to offer both theoretical and practical insights into the preparation and analysis of MoS_2-based nanocomposites. In the next chapter, we will discuss the electrochemical sensing of ascorbic acid using pristine MoS_2 and MoS_2-RGO.

Chapter 3

Hierarchical granular morphology of MoS_2-RGO nanocomposite for electrochemical sensing of ascorbic acid

Ascorbic acid is a vital molecule found in the human body. Recognized as l-ascorbic acid, Vitamin C plays a critical role in the construction of skin structure, the healing of damaged tissues, the prevention of scurvy, and the actinic synthesis of perceptible neurotransmitters. Vitamin C deficiency can result in internal bleeding, fatigue, connective tissue abnormalities, delayed wound healing, etc., [179,180] There are many scientific methods including chromatography[181], surface Plasmon resonance spectroscopy[182] chemical luminescence[183], fluorescence[184], electrochemical analysis, etc., for sensing different bio-molecules. Compared to other techniques, the electrochemical analysis is favored because it is more sensitive, doesn't change the surface characteristics, is economical, and enhances our understanding of the lepton transfer process[185-188]. As a result, electrochemical sensors are extremely selective toward diverse chemical processes and effective in detecting multiple molecular species with lower detection limits[4]. Although graphene is the strongest, lightest, thinnest, and greatest electrical and thermal conductor at ambient temperature, it has some limits in terms of sensing. Because graphene lacks a bandgap, its sensitivity is compromised. This limitation prompted researchers to look at other materials such as transition-metal-dichalcogenides (TMDs) which exhibit indirect band gaps in the range of 1.0-2.0 eV and have unique electro-catalytic, electronic, and optical properties, and thus attracted new interests to design new sensing platforms. Among TMDs, MoS_2 has gained maximum attention due to its exceptional electronic, structural, and optical properties[189,190]can be chemically exfoliated from multilayer to monolayer, which is extremely beneficial to tune its properties as per the application[191]. The MoS_2 possesses three switchable different crystal phases *i.e.*, 1T[192, 193], 2H[47], and 3R[194], and hence its electronic behavior can be modified from insulating to metallic[195]. Its morphology can be altered under a controlled synthesis process[52], which facilitates effective sensing[196]. Even though MoS_2's large surface area provides enough reactive sites for electro-active species to react, its conductivity and aggregation are concerning. Because of its remarkable qualities, RGO is the best option discovered in the literature for producing nanocomposites with MoS_2[197]. MoS_2 can be prepared by hydrothermal, chemical exfoliation, microwave-assisted synthesis, co-precipitation, and mechanical exfoliation techniques[62]. On comparing, it was realized that insitu microwave-assisted synthesis is more advantageous as it involves uniform heating, forms uniform particle

size, is cost-effective, facile and above all it is time and energy-saving[198, 199]. For detection of glutathione which is associated with various human diseases like AIDS, HIV, cancer, liver damage, etc., MoS_2-based electrochemical sensors demonstrated superb potentiality due to its label-free sensing capabilities with a limit of detection (LOD) of 704 $pA\mu M^{-1}$ in a detection range of 10µM-500mM[139]. The MoS_2-based nanocomposites are potential candidates for the detection of various molecular species such as uric acid, dopamine, ascorbic acid[89], glutathione, Hg^{2+}[81], cardiac troponin-I[84], valproic acid[88], *etc.* It shows good compatibility with RGO[200], PANI[201], Au particles[143], diamond nanoparticles[82], aluminum foil[202], *etc.*, for enhancing sensing properties. The MoS_2-PANI/rGO synthesized by the one-pot hydrothermal process was used for concurrent detection of ascorbic acid had given LoD of 22.0 µM[180], 0.7 µM[203] and a decent sensitivity of 0.12 $\mu A\mu M^{-1}cm^{-2}$[203]. It is realized that still there is a scarcity of quantitative information related to the sensing of ascorbic acid by MoS_2-RGO based nanomaterials. Further, the ascorbic-acid sensing by MoS_2-RGO synthesized *via* microwave-assisted technique has not been thoroughly studied yet. This motivated us to carry forward this work. We adopted a microwave-assisted technique to synthesize MoS_2-RGO nanocomposites for the detection of ascorbic acid. By varying the percentage ratio of RGO in MoS_2, the sensitivity of the designed sensor towards ascorbic acid is reported and discussed in this work. Further, the selectivity of the sensor in the solution having uric acid toward ascorbic acid is discussed.

3.1 Structural studies

The XRD-patterns were recorded to reveal the identity of the chemical composition and crystalline phases of the synthesized material. Fig. 3.1(a), 3.1(b) and 3.1(c) typically show the XRD pattern of RGO, Pristine MoS_2 and 3% MoS_2-RGO nanocomposite. Fig. 3.1(a) the observed peak belongs to RGO. From Fig. 3.1(b) it can be seen that MoS_2 is successfully synthesized as all the identified peaks are well in accordance with the JCPDS data (no. 37-1492) corresponding to hexagonal MoS_2. The XRD pattern peaks for 3% MoS_2-RGO appeared at 22.8°, 32.59°, 39.55°, 49.29°, 58.5° and 69.2° corresponding to the crystalline planes (002), (100), (103), (105), (110) and (201), respectively. The synthesized-material exhibited hexagonal crystal-structure with lattice parameters a=3.15Å and c=12.3Å and the crystal plane (100) had a maximum intense peak indicating the excess orientation of atomic arrangements towards this particular plane. No extra peaks other than MoS_2/RGO are observed, which confirmed the absence of any impurity.

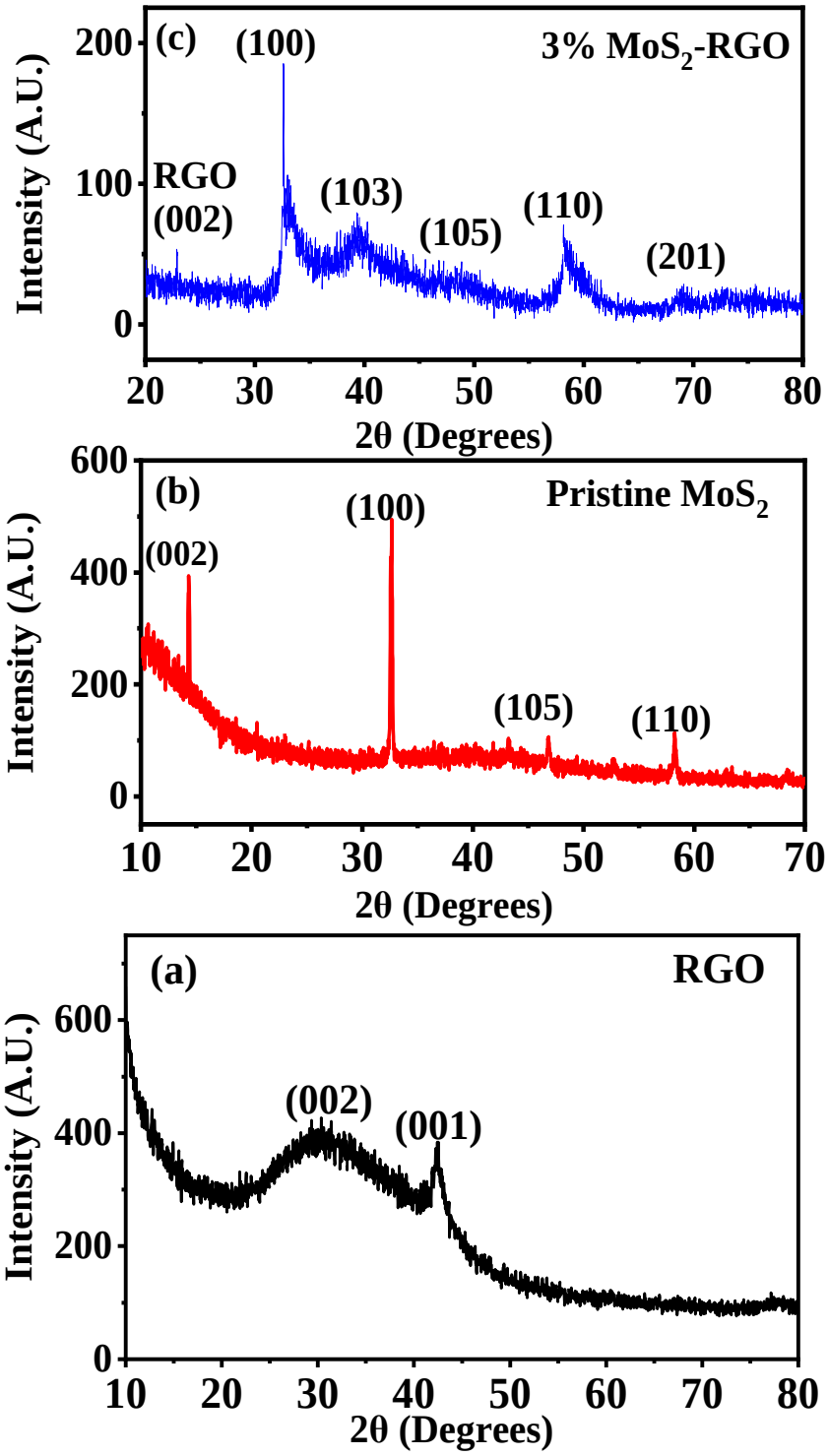

Fig. 3.1 (a) The XRD pattern of RGO, (b) pristine MoS_2, and (c) 3% MoS_2-RGO.

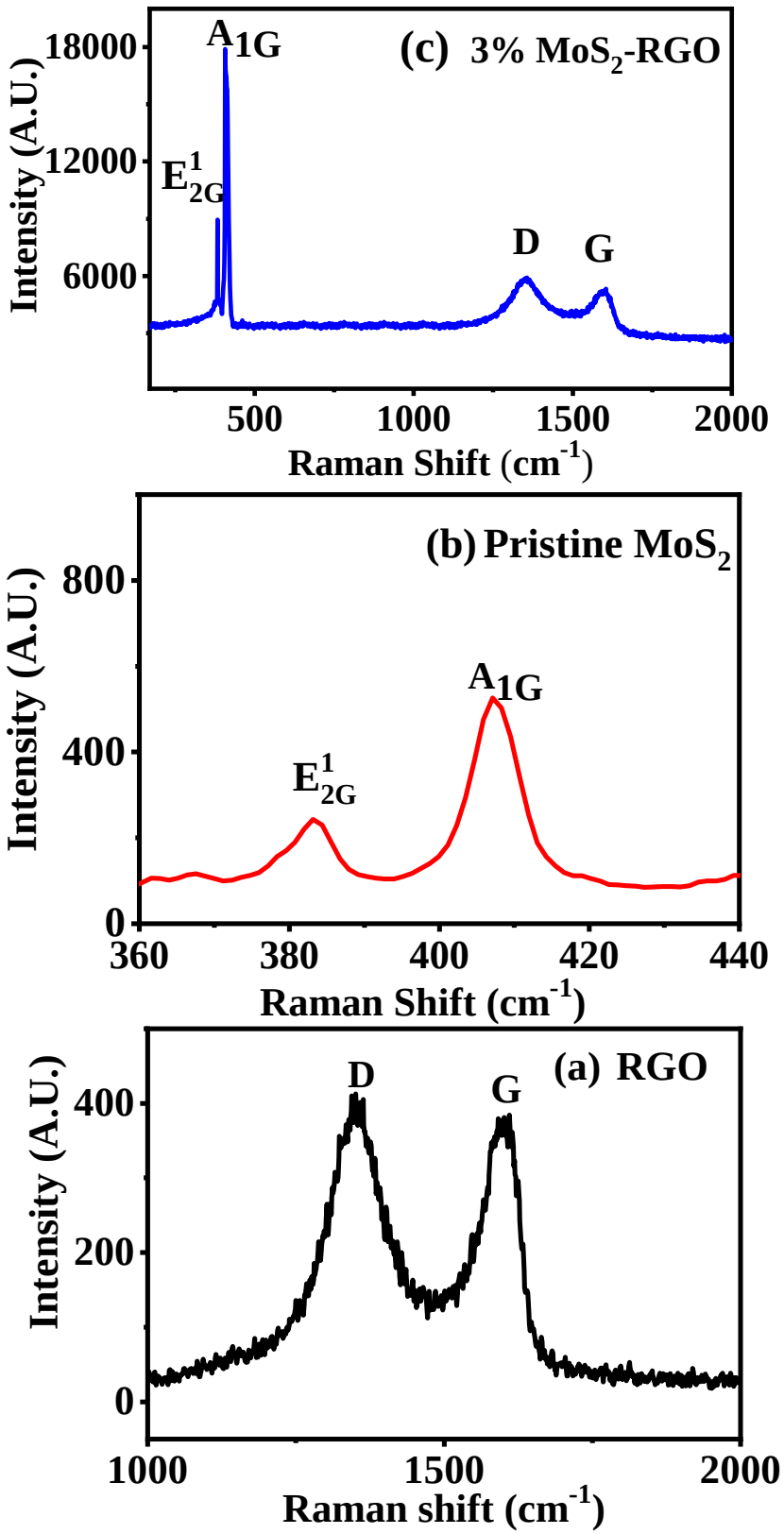

Fig. 3.2 (a) Raman spectra of (a) Pristine MoS_2, (b) RGO and (c) 3%MoS_2-RGO nanocomposite.

The Raman-spectrum of pristine MoS_2, RGO and 3% MoS_2-RGO nanocomposite is shown in Fig. 3.2 (a), (b) and (c) respectively. From Fig. 3.2(a) and 3.2(b) shows the characteristics peaks of synthesized MoS_2 and RGO alone. In Fig. 3(c) for 3% MoS_2-RGO nanocomposite the characteristic A_{1G} and E^1_{2G} peaks of MoS_2, were observed at 382.9 cm^{-1} and 407.5 cm^{-1}, respectively, whereas the characteristic D and G peaks of graphene, were observed at 1356 cm^{-1} and 1604 cm^{-1}, respectively. The wavenumber difference between E^1_{2G} and A_{1G} modes were measured as ~25 cm^{-1}, which confirmed the formation of a few layered MoS_2[204]. It is noticed that intensity of D band is greater than G band (*i.e.*$I_D/I_G \approx 1.109$) indicating the existence of more defects, which may be due to excess sp^2 to sp^3 transitions of electrons[205, 206].

3.2 Morphological and Topographical Characteristics:

Fig. 3.3 displays 3%MoS_2-RGO nanocomposite's SEM images at different magnifications. From micrographs, hierarchical-granular morphology of MoS_2-RGO nanocomposites is evident[207].

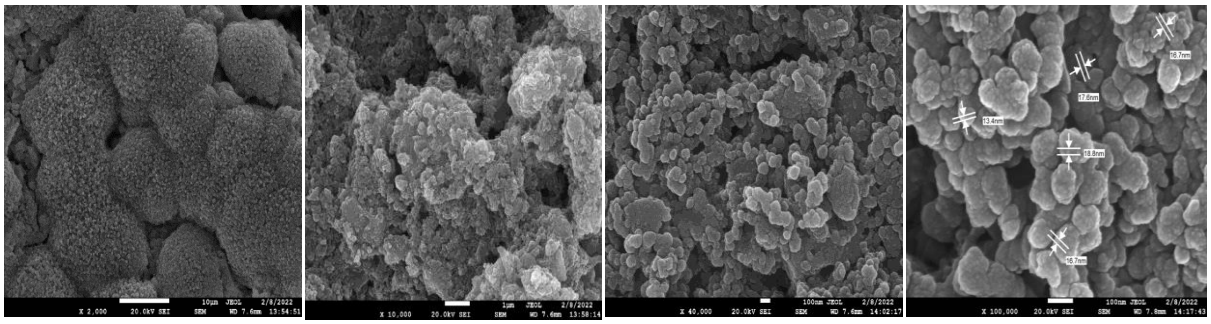

Fig. 3.3 The FESEM images of 3%MoS_2-RGO nanocomposite at different magnifications.

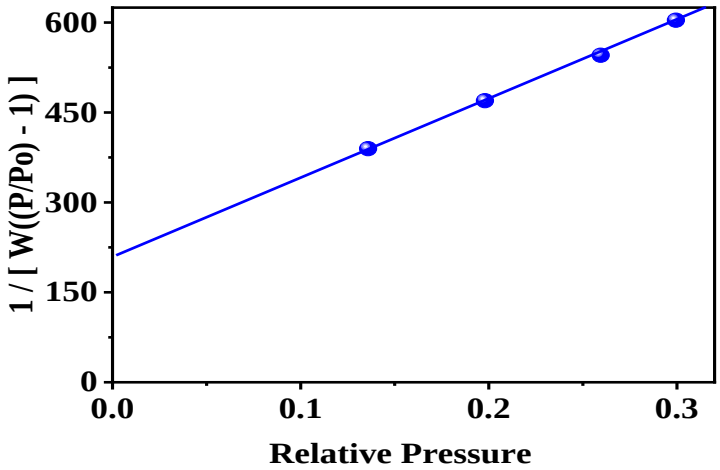

Fig. 3.4 Shows multipoint BET surface area plot for 3% MoS_2-RGO

It can be inferred that MoS_2-RGO nanocomposites synthesized *via* microwave assisted technique can be suitable material for electrochemical sensing as hierarchical granular morphology is having large-surface-area to interact with the analyte and can facilitates the propagation of electrons/ions through its well-connected lamellar network. For effective sensing, specific surface area plays vital role. In present work, for ensuring the specific surface area and porosity of MoS_2-RGO nanocomposite BET analysis is done. Prior to measurement, nanocomposite was degassed in a vacuum of 10^{-6} Torr at 150ºC for 14 h to remove moisture in the sample. For calculating the BET specific surface area is calculated from multipoint surface area curve between relative pressure (P/P^o) and 1 / [W((P/Po) - 1)] where P is equilibrium pressure, P^o is the saturation pressure and W is amount of N_2 gas adsorbed at a given relative pressure. The specific surface area of bare MoS_2 is reported as 8.6 m^2g^{-1} [208]whereas from Fig. 3.4 BET specific surface area of MoS_2-RGO is calculated as 18.4 m^2g^{-1} using BET calculations. Further, the average pore radius is found to be 6.24 nm which discloses that synthesized MoS_2-RGO is mesoporous. This reveals that the introduction of RGO in MoS_2-RGO gives sufficient reactive sites for ascorbic acid to react and produce a better sensing response.

3. 3Electrochemical studies

In Fig. 3.5(a) the CV curves of MoS_2@GCE, 1%, 3% and 5% MoS_2-RGO@GCE in 0.1 M PBS at a scan-rate of 100 $mVs^{-1}$are shown. It is noticed that the maximum area of the loop was grabbed by 3%MoS_2-RGO@GCE, which suggests that a 3% addition of RGO in MoS_2 is most suitable among all prepared compositions. Under similar conditions, the CV curves of 3%MoS_2-RGO@GCE at varying concentrations of analyte are displayed in Fig. 3.5(b). It was inferred that the area of the loop was increasing with the addition of ascorbic-acid concentration in the buffer-analyte solution, which is advocating the sensing capability of the MoS_2-RGO nanocomposites. The maximum area of the loop was swayed at 80µM ascorbic-acid concentration.

The sensing behavior of working electrodes i.e., MoS_2@GCE, 1%, 3% and 5% MoS_2-RGO@GCE was further probed by DPV as shown in Fig. 3.6(a). It was observed that for all electrodes, the detection peaks of ascorbic acid were observed at ~0.2V and the maximum current was found to be 1.74 µA corresponding to 3%MoS_2-RGO@GCE and with further addition of RGO, the current reduced to 1.08 µA.

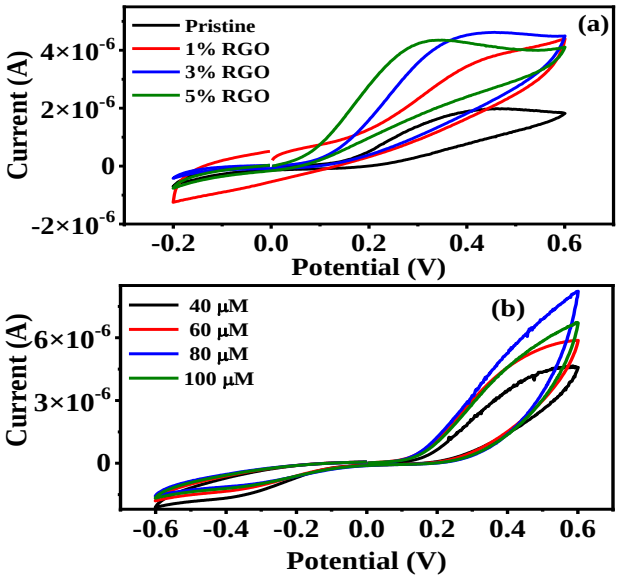

Fig. 3.5 The CV curves of MoS_2-RGO nanocomposites (a) with different composition of RGO at a specific concentration of ascorbic-acid, (b) for best composition*i.e.*3%MoS_2-RGO@GCE, at different concentration of ascorbic-acid.

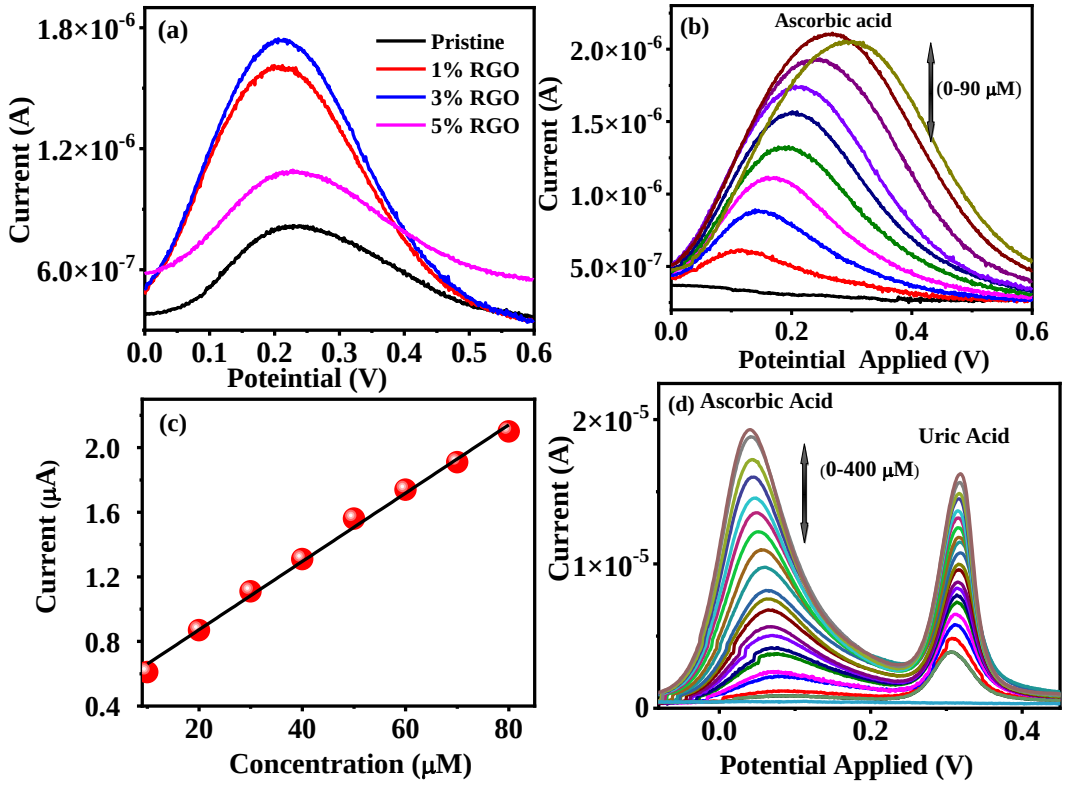

Fig. 3.6 The DPV curves (a) of different composition of RGO in MoS_2-RGO nanocomposite at a specific concentration of ascorbic-acid, (b) for 3%MoS_2-RGO@GCE at different concentration of ascorbic-acid. (c) The variation of current with the concentration of ascorbic-acid and the fitted line with linear regression equation I_p (µA)=0.487+0.020C(µM). (d) DPV curves for different concentration of Ascorbic acid in the solution having 30 µM Uric acid in 0.1 M PBS at 3% MoS_2-RGO modified glassy carbon electrode.

This result supported the findings of the CV analysis and confirmed that 3%MoS_2-RGO@GCE is the most optimized electrode among the prepared ones, for the sensing of ascorbic-acid. The synergistic effect of MoS_2 and RGO i.e., hierarchical-granular morphology, might be responsible for the distinguished behaviour of the designed electrode. The detection of varying concentrations of ascorbic-acid ranging from 10 μM to 90 μM by 3%MoS_2-RGO@GCE is depicted in Fig. 3.6(b). The designed sensor has shown a linear raise of peak-current (I_p) with the addition of concentration of ascorbic-acid till 80μM and afterwards, it starts decreasing with further addition of analyte in buffer solution. The variation of I_p with the ascorbic-acid concentration (C) and its linear fit is plotted in Fig. 3.6(c). The linear regression equation of the fitted line was $\boldsymbol{I_p(\mu A)= 0.487 + 0.020C(\mu M)}$ with coefficient of determination *i.e.,* $R^2 = 0.9985$. In order to calculate sensitivity of the designed sensor, electroactive surface area (ECSA) of the working electrode was calculated from CV analysis by plotting the graph between peak current and scan rate[209]. The measured value of ECSA was 0.00698 cm^{-2}. Then the slope of the calibration curve is divided with ECSA to compute the value of sensitivity *i.e.,*2.9 μA $\mu M^{-1}cm^{-2}$ of the designed electrode. The calculated values of limit of detection and limit of quantitation (LoQ) by using the standard relations were 0.43 μM and 1.45 μM, respectively[210]. These values of sensitivity and LoD were compared in Table 3.1 with those reported on the nanomaterial developed with MoS_2 or similar compositions and it was found that the 3%MoS_2-RGO prepared by microwave-assisted technique is one the most sensitive material towards ascorbic-acid. This may be attributed to the synergistic effect of MoS_2 and RGO, which is providing the enlarged-surface-area for interaction with analyte and is also facilitating the charge propagation process by providing well-connected conducting networks through hierarchical granular morphology. The peak in the DPV curves was also shown to be migrating towards a higher voltage, which might be related to the disruption in the mass-transport mechanism. This disruption may have resulted from the analyte's addition creating a concentration gradient in the buffer solution. In general, in any solution, the mass-transport mechanism is disrupted in the higher concentration zone due to random particle migrations from higher to lower concentration regions during the diffusion process. As a result, in order to counteract this impact, the electrochemical system expends more potential, which leads to the observed peak shift. Fig. 3.6(d) shows selective detection of ascorbic acid. Besides individual sensing of ascorbic acid, 3% MoS_2-RGO@GCE displays remarkably selective sensing of ascorbic acid in the solution having uric acid.

Table 3.1 Comparison of MoS_2 based sensors for detection of Ascorbic-acid.

Nanocomposite used	**Sensing Method**	**LOD (μM)**	**Sensitivity**	**Linear Range**	**Ref.**
MoS_2-PANI/rGO	DPV	22.2	Not mentioned	50μM- 8mM	[180]
AuNPs@MoS_2/GCE	DPV	100	Not mentioned	1mM-70mM	[213]
MoS_2/RGO/GCE	DPV	0.72	$0.12\mu A\mu M^{-1}cm^{-2}$	12 μM-5402μM	[203]
MoS_2-AuNPs/GCE	DPV	2.1	Not mentioned	710μM-2.7mM	[211]
MoS_2 modified electrode	DPV	8.1	Not Mentioned	27μM-1.1mM	[212]
AuNPs@MoS_2-NSs/GCE	DPV	3	Not Mentioned	20μM-300μM	[196]
MoS_2-rGO/GCE	DPV	0.09	$8nA\mu M^{-1}cm^{-2}$	300μM-3.3mM	[213]
MoS_2-OCu	CV	0.0222	Not mentioned	0.05-100mM	[188]
MoS_2-RGO@GCE	DPV/EIS	0.43μM/ 0.16μM	$2.9\mu A\mu M^{-1}cm^{-2}$/ $1508\Omega\mu M^{-1}cm^{-2}$	10μM- 80μM	This Work

DPV curves from Fig. 3.6(d) shows different concentration of ascorbic acid ranging from 0 μM to 400 μM ascorbic acid in the solution having 30μM uric acid in 0.1 M of 7 PBS. There exist two well-distinguishable peaks of ascorbic acid and uric acid. From DPV it can be observed that in addition of ascorbic acid, there is an increase in the current detection peak of ascorbic acid as well as in the current detection peak of uric acid which is well supported in the literature[213]. The considerable increase in the peak current of ascorbic acid could be credited to the electrocatalytic oxidation of ascorbic acid at the electrode-electrolyte interface.

The charge-kinetics of the prepared working electrodes was further explored by EIS. The impedance-spectra of MoS_2@GCE, 1%, 3% and 5% MoS_2-RGO@GCEs at specific and varying concentrations of ascorbic-acid were recorded in the frequency range from 0.01Hz to 100kHz and are displayed in Fig. 3.7 and 3.8(a), respectively. It is perceived that the impedance curves become steepest for 3%MoS_2-RGO@GCE at 80 μM of ascorbic-acid in PBS, which is specifying its better sensitivity among the all investigated electrodes. The interesting phenomenon associated with inductive-effect was noticed while investigating the impact of molar-concentration of ascorbic-acid on the EIS responses of 3%MoS_2-RGO@GCE, as shown in the Fig. 3.8(b)[214]. In the fourth-quadrant of the impedance graph, specifically at the high frequency end, there was a formation of semicircle after the addition of ascorbic acid in the buffer-solution and its size was increasing with the concentration of the analyte. This increasing trend was observed till 80μM of analyte was supplemented in the

buffer-analyte solution and with its further addition, the size of the semicircle was reduced. In the absence of ascorbic acid, no such formation was observed in the impedance curve of the same electrode, which firmly suggests the cause of inductive behavior is associated only with the interaction between ascorbic acid and the working electrode.

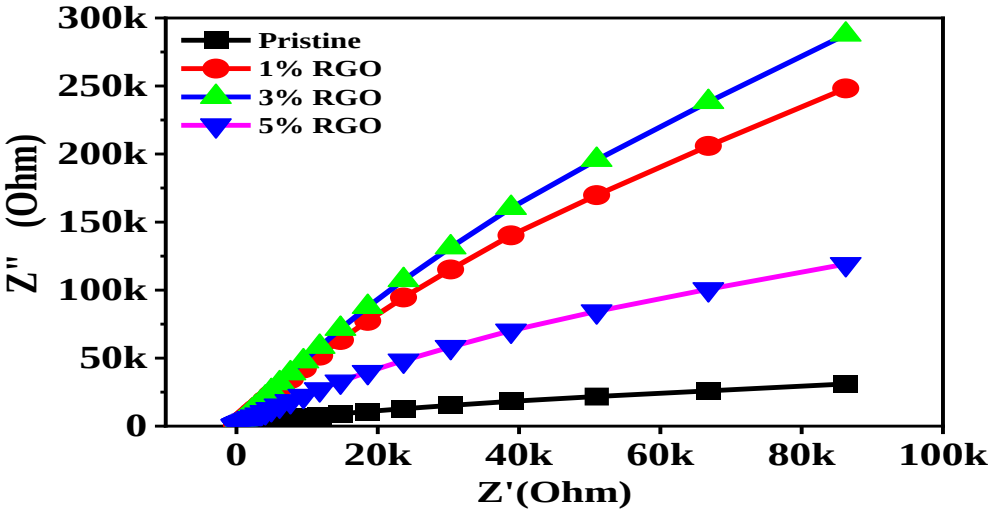

Fig. 3.7 The EIS curves of MoS_2-RGO@GCE with different compositions of RGO, at specific concentration of ascorbic-acid.

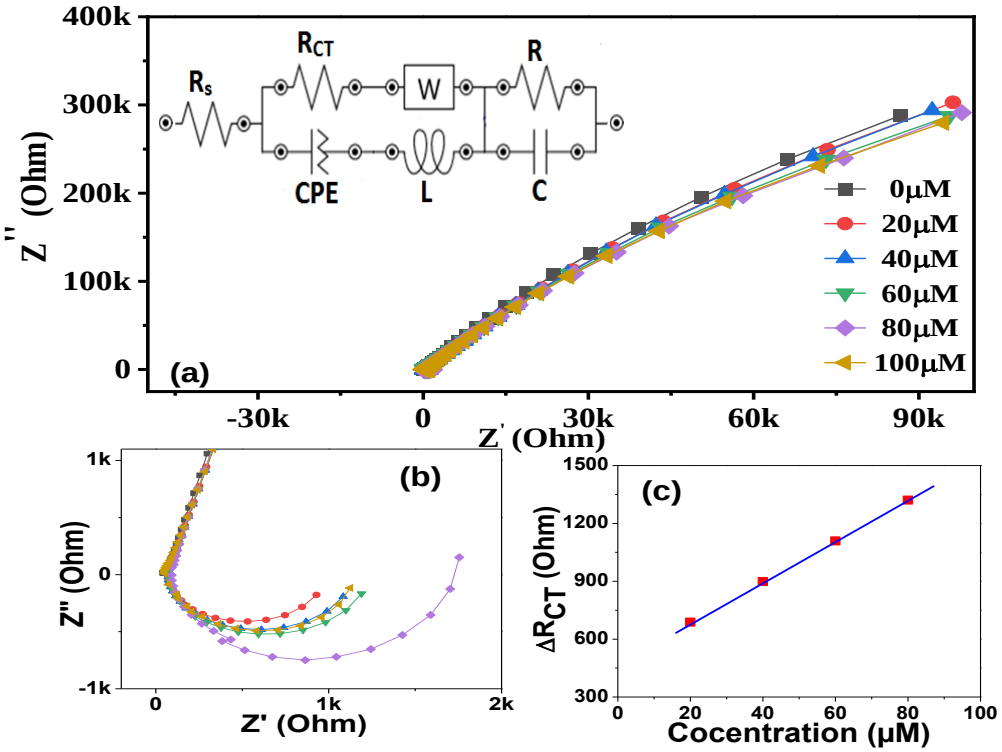

Fig. 3.8 The EIS curves of 3%MoS_2-RGO@GCE (a) at different concentrations of ascorbic-acid with their equivalent circuit and(b) the magnified view of a specific range. (c) The variation of charge transfer resistance with concentration of analyte and the fitted line with linear regression equation ΔR_{CT} (Ω)= 477.2 + 10.53C(μM).

Table 3.2 The computed values of different elements of the equivalent circuit at different analyte concentrations.

Concentration ***(of analyte in 0.1 M PBH)***	**R_S** ***(Ω)***	**R_{CT}** ***(Ω)***	**CPE/N** ***($\mu\Omega^{-1}s^N$)***	**W** ***($\mu\Omega^{-1}s^{1/2}$)***	**L** ***(mH)***	**R** ***(MΩ)***	**C** ***(μF)***
20 μM	68.4	709.7	5.0/0.89	22.3	3.91	0.99	5.38
40 μM	66.1	920.2	6.4/0.86	16.6	4.19	1.00	5.91
60 μM	74.7	1130.4	4.9/0.90	24.7	5.90	0.90	5.53
80 μM	83.2	1342.2	6.1/0.87	21.0	11.34	0.88	5.58
100 μM	19.0	534.0	15.6/0.65	14.1	3.32	0.75	5.42

The observed inductive behavior at high-frequency end of the Nyquist plots is primarily ascribed to the intercalation of hydrogen ions in the lamellar-nanostructures of MoS_2-RGO nanocomposite during the reduction process. These hydrogen ions were formed during the dissociation of the ascorbic-acid to ascorbate ions. The diffusion process associated with the splitting of ascorbic acid in the buffer-solution, itself can be a secondary cause behind the above-mentioned effect. Generally, the EIS plot is controlled by the diffusion-process at lower-frequencies but at the higher-frequencies, the contribution of the impedance of the intercalation process becomes visible[215]. An equivalent-circuit, as portrayed in the inset of Fig. 3.8(a), was used to fit the Nyquist plots of 3%MoS_2-RGO@GCE at different concentrations of analyte in PBS. The proposed circuit was composed of a series resistance (R_s) due to buffer-analyte solution or other non-capacitive series phenomena and two impedances. The first impedance-element is consisting of charge-transfer resistance (R_{CT}), Warburg (W), inductor (L), and a constant phase element (CPE) and the other one is carrying a resister (R) and a double-layer capacitor (C). The impedance of CPE was derived by using, $Z_{CPE} = A^{-1}(\omega)^{-N}$. Here, ω is the imaginary component of angular frequency and N is a distribution factor with a value between 0 and 1 [216]. The values of all elements of the equivalent-circuit at different analyte concentrations were computed after fitting and presented in Table 3.2 The diameter of the above-mentioned semicircles represents the charge-transfer resistances of redox-conversion on the electrode[217]. The escalation of the R_{CT} values is may be attributed to the difficulty raised for diffusion of ions/charges due to the formation of excess large-sized ascorbate ions and 1,3-diketones at the electrode-buffer-solution interface.

In addition to this, the occupancy of the active sites on the electrode surface due to intercalation activity could also be equally responsible for the constrained propagation of the ions/charges. The increasing value of inductance with the addition of analyte is further justifying the

assumption of intercalation and interruption in the diffusion process in the 0.1M PBS. The significant raise of R_{CT} and L was ascribed to the specific-recognition capability of hierarchical-granular morphology of MoS_2-RGO to sense ascorbic acid. The peak-shifting of DPV curves towards higher voltage on addition of analyte in the buffer-analyte solution is also supporting the existence of inductive effect. No significant variation in the values of R, C, W and CPE was noticed, however, the fitted values of the exponent N is suggesting the capacitive nature of CPE impedance at all studied concentrations of analyte except at the highest one, where the resistive character of the CPE impedance was found. When 100 μM of ascorbic acid was added to the buffer solution, substantial decrease in the values of R_{CT} and L was observed owing to the existence of the excess charged species in the buffer-analyte solution and on the surface of electrode leading to the enhanced charge transportation *via* hopping mechanism.

The quantifiable response of the designed biosensor was evaluated by assessing the dependence of ΔR_{CT} $\{= R_{CT(\text{with analyte})} - R_{CT(\text{without analyte})}\}$ on the analyte concentration (C). Here, we measured 21.6 Ω as the value of $R_{CT(\text{without analyte})}$ after fitting the relevant EIS plot without using the inductor-element. The graph between ΔR_{CT} and C was plotted in the range 10 μM to 80 μM. The fitted linear regression equation was $\boldsymbol{\Delta R_{CT}(\Omega) = 10.53C(\mu M) + 477.2}$ as shown in the Fig. 3.8(c), with R^2= 0.9978. The calculated value of LoD, LoQ and sensitivity were 0.16 μM, 0.55 μM and 1508 $\Omega\mu M^{-1}cm^{-2}$, respectively. To the best of our knowledge, such analysis has not been reported so far on any MoS_2-based biosensors. The inferences drawn from EIS analysis are further reconfirming the findings of CV and DPV analysis.

3.4 Conclusion: An effective and highly sensitive MoS_2-RGO nanocomposite based electrochemical sensor is fabricated using an insitu-microwave assisted technique. The hierarchical granular morphology of MoS_2-RGO nanocomposite is suitable to provide sufficient surface area and well-connected conducting networks for the detection of ascorbic-acid. The optimized MoS_2-RGO@GCE has proven its potential candidature as a highly sensitive biosensor by displaying remarkable sensitivity of 2.9 $\mu A\mu M^{-1}cm^{-2}$/1508 $\Omega\mu M^{-1}cm^{-2}$ and a very precise LOD of ~0.43 μM/0.16 μM between the linear detection range 10 μM to 80 μM. The unique sensing behavior of MoS_2-RGO@GCE towards ascorbic acid was found to be caused by an inductive behavior brought on by the intercalation process on the electrode surface and the dissociation of the analyte in the buffer solution. While the MoS_2-RGO nanocomposite shows strong potential for highly sensitive and selective electrochemical sensing of ascorbic acid, achieving a practical device based on this study presents several challenges. Stability and durability of the sensor material, optimization of the nanocomposite composition, and

scalability of the microwave-assisted synthesis method are critical areas that require further exploration. Additionally, ensuring selectivity in complex biological media, integration with portable diagnostic platforms, fast response and recovery times, and cost-effectiveness for commercial deployment are vital hurdles to address. By tackling these challenges, the MoS2-RGO nanocomposite can advance toward becoming a robust and reliable platform for practical sensing applications in healthcare and beyond.

Chapter 4

A Noval Co-MoS_2/RGO-Based Highly Sensitive Sensor for Simultaneous Detection of Ascorbic Acid and Uric Acid

In ancient times, individuals experienced the painful effects of gout without comprehending its origins. It wasn't until the late 17th century that a deeper understanding started to take shape. This advancement was attributed to Carl Wilhelm Scheele's identification of uric acid (UA, $C_5H_4N_4O_3$), as he successfully extracted a crystalline substance from gout-afflicted kidney nodules[218,219]. UA is the terminal product of purine catabolism processes, found in both urine and blood. In both lifeblood and urine, the standard levels of UA typically fall within the range of 0.14 to 0.4 mmol dm^{-3} and 1.5 to 4.5 mmol dm^{-3}[220]. Elevated UA levels are linked with various health conditions, including gout, hyperuricemia[221], Lesch-Nyhan syndrome[222], and renal disease. Conversely, low UA levels are responsible for multiple sclerosis, Parkinson's disease, and Alzheimer's disease[223]. These conditions can be attributed to the accumulation of uric acid, highlighting the significance of monitoring and managing UA levels in the body. UA and AA are two prevalent antioxidants that often exist in food and biospecimens[224, 225]. Vitamin C, also known as AA, is commonly added to a wide variety of foods and beverages due to its powerful antioxidant properties, which help enhance the appearance and extend the shelf life of preserved items[226]. Additionally, it serves as a color and flavor stabilizer and inhibits browning[227]. Vitamin C is essential in the human body for the biosynthesis of levocarnitine, protein, and neurotransmitters. The European Food Safety Authority states that healthy adults typically consume about 90 mg of vitamin C daily from their diet[228]. Consuming high amounts of vitamin C can result in undesirable digestive and kidney effects, due to irritant reactions and the discharging of oxalate in the urine[229]. Conversely, a low intake of vitamin C can cause scurvy, an ailment associated with collagen synthesis[230]. Furthermore, vitamin C deficiency can adversely impact immunity, iron absorption, as well as high-density lipoprotein and protein breakdown processes[231]. Even minor deviations in their concentrations, typically within the range observed in human physiology and food items, can give rise to diverse health complications and impact the overall quality of food products. For a comprehensive assessment, it is crucial to analyze the concentrations of UA and AA in both edibles and vital human fluids. Various methodologies have been utilized to quantify UA and AA, including titration[232], capillary cataphoresis[233], solvent chromatography[234], and spectrophotometric analysis[235]. However, these approaches have inherent limitations, such as the potential for overestimating

acid concentration[236]. Moreover, they are reliant on laboratory-based procedures, necessitating highly skilled personnel, costly equipment, and reagents, and are not amenable to real-time or in situ analysis[237]. Given the susceptibility of UA and AA to electrochemical oxidation in aqueous solutions, their detection through electrochemical techniques such as CV and DPV represents a valid, expeditious, straightforward, sensitive, and selective method. Numerous advanced sensors have been meticulously designed to detect UA and AA employing a diverse range of sensing materials to significantly enhance selectivity[238–241]. MoS_2's distinctive two-dimensional nanostructure and specific energy gap have made it a highly sought-after material across a broad range of applications such as supercapacitors, solar cells, catalysis, electrochemical sensing, and optoelectronic devices.[242–244]. Despite MoS_2's slightly lower electronic conductivity in comparison to graphene, it has been the subject of limited exploration in sensors[245]. To address this limitation, several innovative processes have been proposed, including the amalgamation of MoS_2 with more conductive nanomaterials, metal oxides, benevolent metal nanoparticles, and hydrocarbons, to create novel nanocomposites. Additionally, MoS_2 nanohybrids featuring graphene oxides, CNTs (carbon nanotubes), Acetylene black, and noble metal nanocrystals (such as Pd, Pt, Au, and Ag NCs) have demonstrated exceptional conductivity, rendering them highly suitable for deployment in electrochemical sensors[246,247]. In a previous study[92], we presented initial findings regarding the development of an electrochemical sensor utilizing MoS_2 and RGO for the sensing of AA. Our research demonstrated that microwave-assisted synthesis of MoS_2/RGO proved to be a viable method for achieving favorable sensor characteristics. However, our observations revealed a simultaneous rise in the peak current of UA upon successive addition of AA, thereby posing a challenge to the sensor's selectivity. This study involved the application of a microwave irradiation synthesis method for the fabrication of Co-MoS_2/RGO nanohybrids, meticulously designed for the specific and simultaneous electrochemical sensing of UA and AA.

4.1 Structural Characteristics

Fig. 4.1(a-c) presents the XRD structures for pristine MoS_2, MoS_2/RGO, and Co-MoS_2/RGO nanostructures, within a 2θ range of 10 to 70 degrees. This analysis was conducted to verify the synthesis of MoS_2, MoS_2/RGO, and Co-MoS_2/RGO nanocomposites. In Fig. 4.1(a), the XRD data demonstrate the 2H phase of MoS_2, with diffraction peaks at 13.13º, 32.57º, 39.53º, and 58.46º, corresponding to the (002), (100), (105), and (110) planes respectively, as per PDF 37-1492. In MoS_2/RGO a diffraction peak at 23.0º, related to the (002) plane, confirms the

existence of RGO in MoS_2/RGO (shown in Fig. 4.1(b)). Further, one additional peak at 33.5º corresponds to the (103) plane of 2H MoS_2 along with the four characteristic peaks of 2H MoS_2, indicating enhanced crystallinity of the material due to the incorporation of RGO sheets. Fig. 4.1(c) depicts the XRD pattern of Co-MoS_2/RGO. Peak broadening observed in the (002) plane of 2H MoS_2 in Co-MoS_2/RGO suggests a transition from multilayered to few-layered composites.

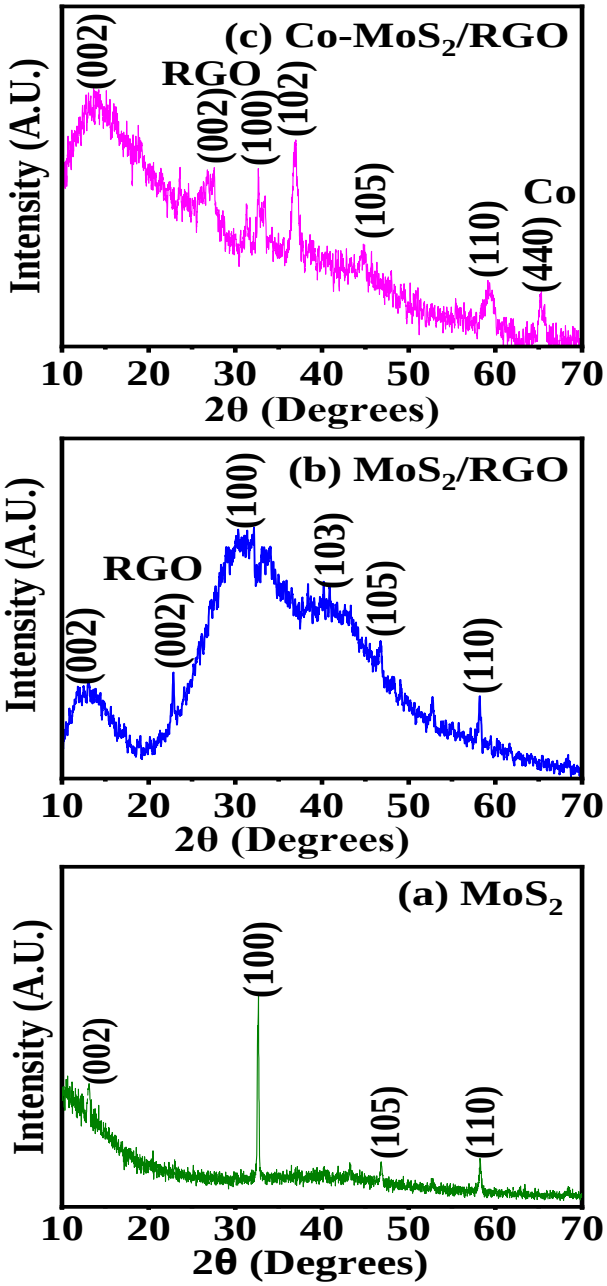

Fig. 4.1(a-c) XRD patterns of MoS_2, MoS_2/RGO and Co-MoS_2/RGO

Additionally, the peak broadening and shifting towards the right of the (002) plane of RGO points to the existence of amorphous carbon in the Co-MoS_2/RGO nanocomposite. An additional peak at 36.9º Corresponding to the (102) plane of 2H MoS_2 is seen in Co-MoS_2/RGO. Further, the diffraction peak at 65.5º relates to the (440) plane of Cobalt, confirming the existence of Co in the composite[248]. Fig. 4.2(a-c) displays the Raman spectra for MoS_2, MoS_2/RGO, and Co-MoS_2/RGO. For both MoS_2 and MoS_2/RGO, peaks at 384 and 407 cm^{-1} are associated with the E^1_{2g} and A^1_g modes of 2H MoS_2 nanocomposites [242].

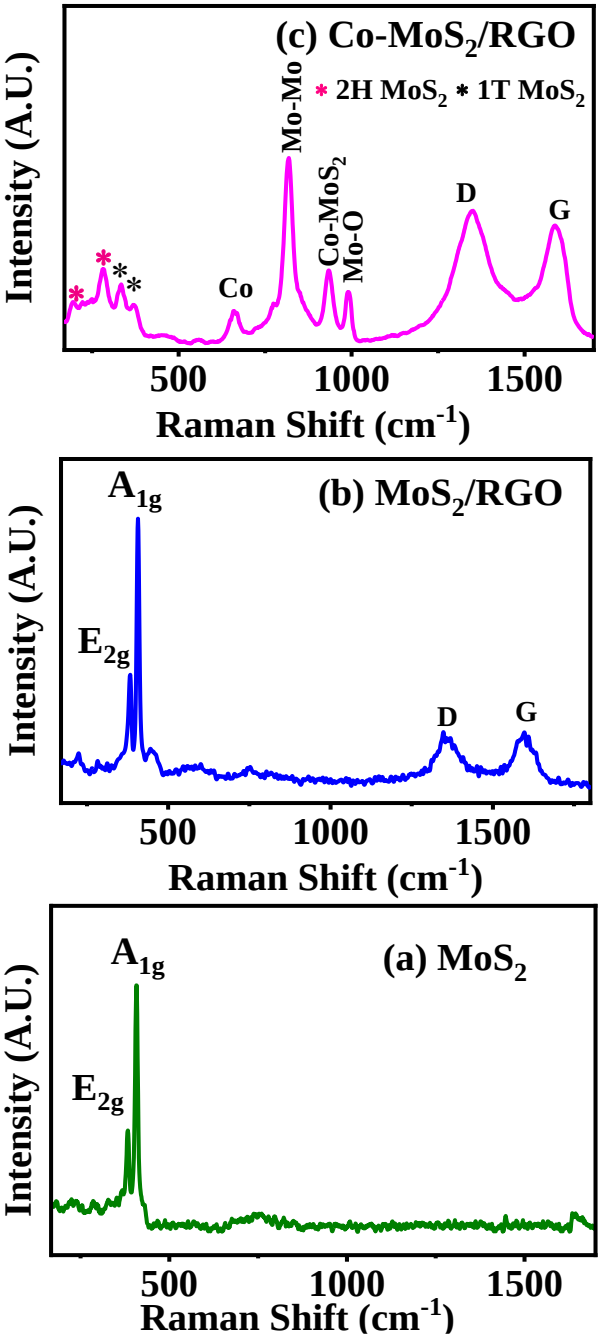

Fig. 4.2 (a-c) Raman spectra of MoS_2. MoS_2/RGO and Co-MoS_2/RGO.

Additionally, Raman peaks at 1388 cm^{-1} (D-band) and 1596 cm^{-1} (G-band) confirm the effective integration of RGO sheets within the MoS_2/RGO nanocomposite, as depicted in Fig. 4.2(b) [243]. The calculated I_D/I_G ratio is 0.91, suggesting a high order of crystallinity in the material. In Fig. 4.2(c), the peaks appearing at 191, 283, and 384 cm^{-1} are linked with the longitudinal acoustic phonon modes (LA), E^1_g, and E^1_{2g} modes of 2H-MoS_2. A peak at 333 cm^{-1} suggests the existence of the 1T-phase of MoS_2, suggesting a mix of 2H and 1T phases in the Co-MoS_2/RGO composite. Moreover, new peaks at 669 and 932 cm^{-1} in the Co-MoS_2/RGO spectra correspond to Co and Co-MoS_2 vibrations [250]. The peak at 815 cm^{-1} is related to the second harmonic resonance of a few layers of pure Mo-Mo bond interactions. This might be due to the two-step synthesis of Co-MoS_2/RGO, the sample is subjected to microwave irradiation twice at 700 watts. This might cause the development of a metallic Mo layer on the MoS_2 surface, which causes the appearance of a distinct peak for Mo-Mo interaction in the Raman spectra[251]. The peak at 991 cm^{-1} suggests partial oxidation of MoS_2 upon air exposure. In Co-MoS_2/RGO, the D and G bands of RGO are observed at 1345 cm^{-1} and 1587 cm^{-1}, respectively, with an I_D/I_G ratio of 1.08, indicating structural defects that may enhance the composite's selectivity. Co-doping leads to a decrease in the E^1_{2g} and A^1_g vibration modes, attributed to tensile strain within the lattice due to Co doping at the Mo sites.

4.2 Morphological Characteristic

FESEM images were used to confirm the morphological structure of the synthesized materials. RGO exhibits a slender, lamellar structure with folds, as shown in Fig. 4.3(a).

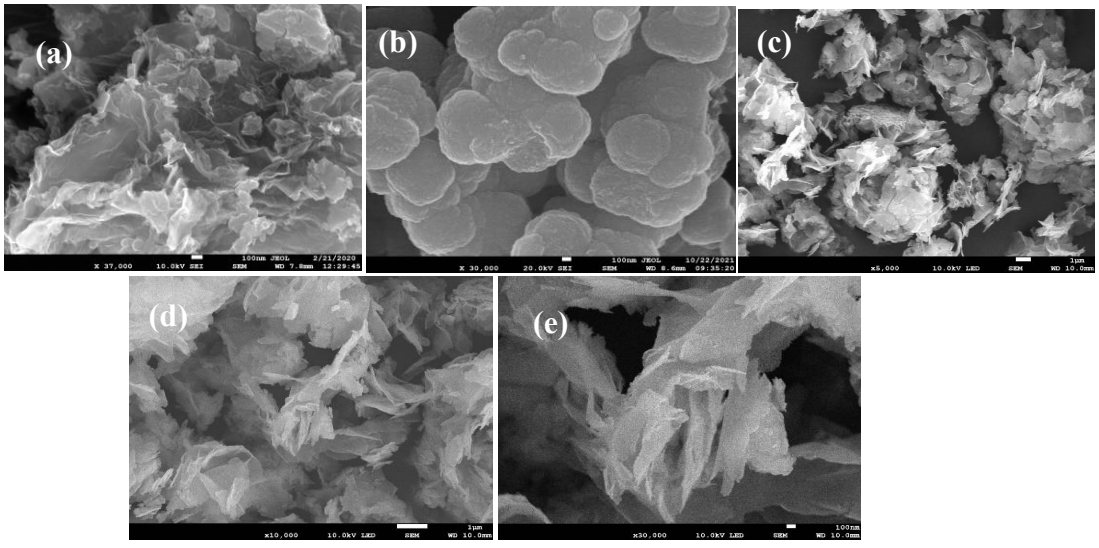

Fig. 4.3 FESEM images of (a) RGO nanosheets, (b) MoS_2, (c-e) Co-MoS_2/RGO nanosheets at different magnifications.

In contrast, MoS_2 appears as aggregated hierarchical granular morphology in Fig. 4.3(b), which may lead to reduced conductivity. Fig. 4.3(c-e) presents FESEM images of Co-MoS_2/RGO at various magnifications, showing the successful formation of open, flower-like 3D ultrathin nanosheets through two-step microwave irradiation synthesis. No distinct morphology for Cobalt is observed in the composite, likely because of the higher Fermi level of the MoS_2/RGO heterojunction[252] compared to the standard reduction potential of Co^{3+} ions facilitates spontaneous electron transfer. This electron transfer reduces Co^{3+} ions, leading to the formation of Co-MoS_2/RGO nanosheets. These 3D nanosheets offer a large surface area and numerous reactive sites, enhancing sensitivity and efficiency in detecting electrochemical signals, and potentially improving electron transfer and interactions with analytes.

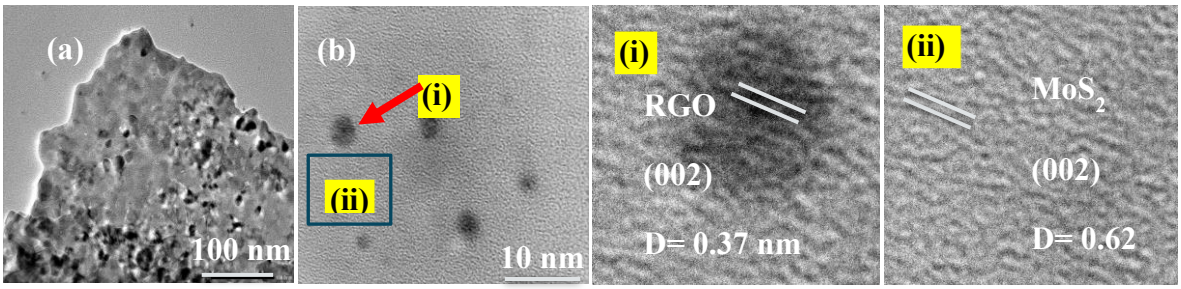

Fig. 4.4 HRTEM images of (a, b) Co-MoS_2/RGO. (b(i & ii)) are the magnified views of the marked area in (b).

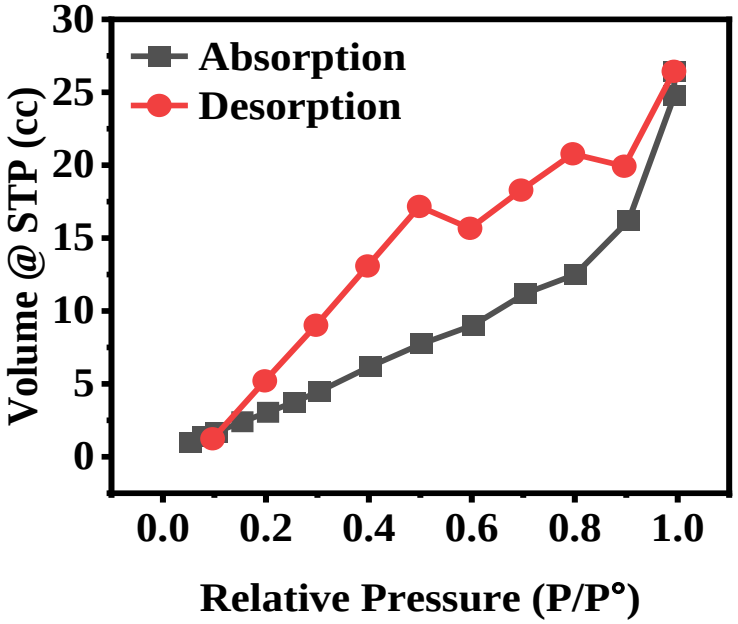

Fig. 4.5 (a) BET adsorption-desorption isotherm of Co-MoS_2/RGO

Further, the HRTEM image of Co-MoS_2/RGO is shown in Fig. 4.4(a,b). Fig. 6.4(b) has two marked areas which are further magnified and marked as (i) and (ii). Fig. 4.4(b(i)) shows the (002) plane of well-stacked RGO sheets having an interplanar distance of 0.385 nm. In Fig. 4.4(b(ii)), the measured interplanar distance is 0.62 nm aligns with XRD results and corresponds to the (002) plane of MoS_2 [253]. The surface area and porosity of the Co-MoS_2/RGO 3D nanosheets were determined through BET analysis. The nitrogen adsorption-desorption analysis revealed a gradual increase in the adhered volume in the BET isotherm within the P/P° range of 0.049–0.3 (refer to Fig. 4.5) whereas, saturation pressure and equilibrium pressures are denoted by P° and P respectively. The calculated BET-specific surface area of Co-MoS_2-RGO is 20.5 m^2g^{-1}, significantly higher than the proclaimed specific surface area of pristine MoS_2 (8.6 m^2g^{-1}) and MoS_2/RGO (18.4 m^2g^{-1}) [254]. The BJH technique, which uses the Kelvin equation and DH techniques to compute the pore size distribution, was deployed to compute the pore volume data. The composite has pore diameters of 2.3 nm, making it mesoporous. The material has a pore volume of 0.067 cm^3. This substantial pore volume indicates that the Co-MoS_2/RGO nanosheets probably possess a significant capacity to accommodate adsorbates, making them highly effective for applications that require the detection of a large number of analytes. The mesoporous structure provides numerous active sites and facilitates efficient mass transport, which may enhance the material's sensitivity and responsiveness.

4.3 Chemical and Compositional Analysis

The FTIR spectra presented in Fig. 4.6 illustrate the distinctive peaks of the Co-MoS_2/RGO composites. Two peaks observed at 544 and 654 cm^{-1} correlated to the S-S and Mo-S stretching vibrations, affirming the existence of MoS_2 within the composites [255, 256]. Furthermore, the peak at 1068 cm^{-1} in the Co-MoS_2/RGO spectrum is indicative of Co-S vibrations, signifying the effective incorporation of cobalt. Regarding RGO, the peaks at 1407, 1506, 1638, 1737, 3035, and 3145 cm^{-1} are associated with distinct chemical groups, such as C-H stretching of aromatic carbon, C=C stretching related to the non-oxidized graphitic domain, C-O (alkoxy) stretching vibrations, C-H elongation, and =C-H alkenes or C-H aromatics of the carboxyl group [257]. Additionally, the small peak around 3321 cm^{-1} corresponds to O-H stretching of ethanol absorbed during the microwave synthesis process. These spectral characteristics collectively confirm the combined existence of Co-doped MoS_2 and RGO within the synthesized composites. Based on the XPS results, an extensive analysis is done to determine the chemical states and bonding inside the Co-MoS_2/RGO composite material, including the

oxidation states of molybdenum, sulfur, carbon, oxygen, and cobalt, as seen in Fig. 4.7(a). The deconvolution of the Mo3d spectrum (Fig. 4.7(b)) into 2 peaks lies on energy values 229.88 and 233.07 eV, accredited to Mo^{4+} $3d_{5/2}$ and Mo^{4+} $3d_{3/2}$, respectively, indicating that Mo^{4+} is the molybdenum's oxidation state in the composite. Furthermore, Fig. 5(b) shows a peak at 227.3 eV that is attributed to the S2s of MoS_2.

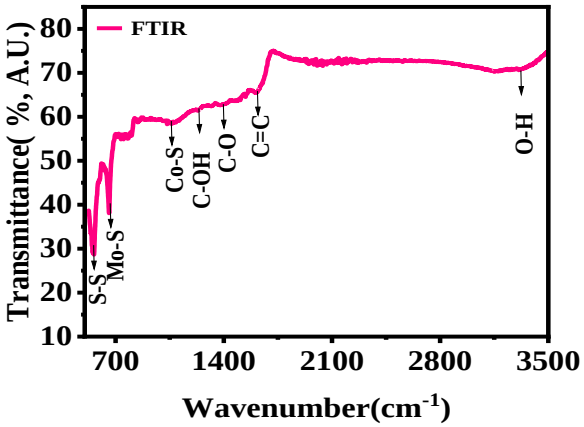

Fig. 4.6 FTIR spectrum of Co-MoS_2/RGO.

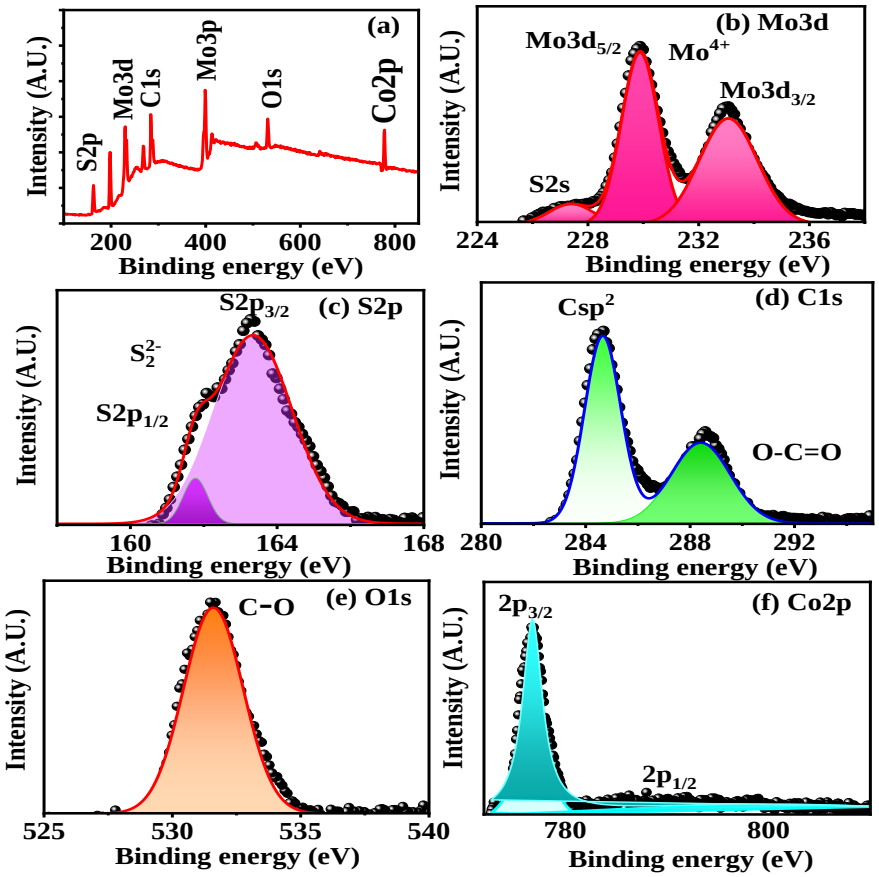

Fig. 4.7 XPS pattern of Co-MoS_2/RGO (a) full scan spectrum (b-f) high-resolution spectra of, (b) Mo3d, (c) S2p, (d) C1s, (e) O1s and (f) Co2p.

The two peaks in the S2p spectra seen in Fig. 4.7(c) at 161.16 and 163.03 eV were ascribed to the $S2p_{3/2}$ and $S2p_{1/2}$ of the S^{2-} and S_2^{2-} charged states in the composites. These findings provide light on the distinct chemical state of sulfur, which may be linked to MoS_2 [25]. The C1s spectra is shown in Fig. 4.7(d); two peaks with binding energy values corresponding to the Carbon-Carbon and C=O functional groups are seen at 284.6 and 288.4 eV, respectively. The existence of RGO in the composite is confirmed by the occurrence of a peak at 531.03 eV, which can be observed in O1s in Fig. 4.7(e) [258]. Moreover, the Co 2p core level spectra, Co $2p_{3/2}$, and Co $2p_{1/2}$ [259] are correlated with the binding energy values of 776.8 and 800.54 eV in Fig. 4.7(f). This implies the successful doping of Co in MoS_2/RGO nanocomposite.

4.4 Electrochemical studies

The cyclic voltammetry (CV) data has been utilized to elucidate the electrochemical behavior of the glassy carbon electrodes designed with Co-MoS_2/RGO.

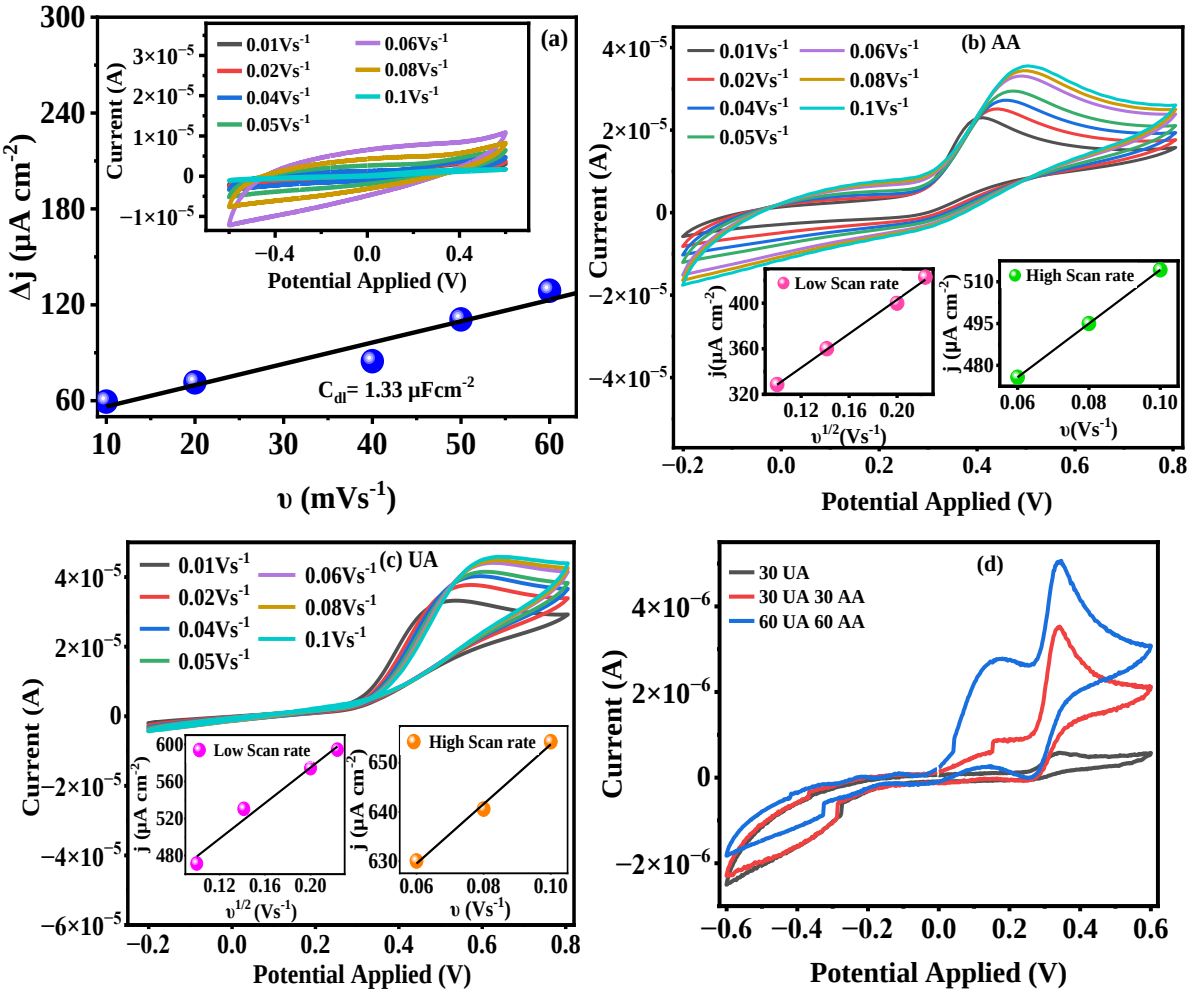

Fig. 4.8 Multiscan CV curves for (a) devoid solution, (b) 150 µM AA in 0.1 M PBS (pH=7), (c) 500 µM UA in 0.1 M PBS (pH=7), and (d) CV curves for varied concentrations of AA and UA.

Through the use of CVs at varying scan rates, the double-layer capacitance (C_{dL}) was calculated to explore the impact of Cobalt doping on the electrochemical response of the sensors (refer to Fig. 4.8(a) inset). The experiments were conducted in a pH 7 phosphate-buffered saline (PBS) solution devoid of UA and AA. From the CV curves, it can be inferred that the optimum current is observed at a scan rate of 60 mVs^{-1}. Further, the plot of the differential double-layer charging current density (Δj), where ($\Delta i = i_a - i_c$), exhibited a linear increase proportionate to the scan rate, the slope of this relationship is correlated to C_{dL} (refer Fig. 4.8(a). The Co-MoS_2/RGO exhibited a noticeably higher double-layer capacitance of 1.33 $\mu F\ cm^{-2}$ as compared to 0.007 $\mu F\ cm^{-2}$ and 0.69 $\mu F\ cm^{-2}$ of bare MoS_2 and MoS_2/RGO, respectively, [260]. This implies a significant enhancement in the material's capacity for storing electrical charge, possibly resulting from the combined influence of Co-doping and the existence of RGO. Since C_{dL} is associated with the electrochemical active surface area of the electrode (ESCA), these findings indicate that incorporating Co and RGO into MoS_2 as an effective strategy for electrode modification. This approach entails a large active surface area, thereby significantly boosting the electroactivity of the fabricated sensor[261].

AA and UA's electrochemical oxidation was investigated employing the Co-MoS_2/RGO modified glassy carbon electrode via CV across scan rates spanning from 10 to 100 mVs^{-1} in a pH 7 PBS solution containing 150 µM AA (see Fig. 4.8(b)) and 500 µM UA (Fig. 4.8(c)). For both UA and AA at low scan rates (Fig. 4.8(b,c) insets), a proportional rise in peak current density (j) with the under root of the scan rate suggests a diffusion-controlled process. Conversely, at high scan rates, there is a linear rise in peak current density with the scan rate, indicative of an adsorption-controlled process. This implies for both AA and UA at low scan rates there is sufficient time to diffuse to the upper layer of the electrode, causing an increase in the observed current density. Whereas, at high scan rates AA and UA have less time to diffuse to the electrode surface, so the primary factor influencing the current density becomes the rate at which both of them adsorb upon the surface of Co-MoS_2/RGO-modified GCE. Furthermore, the oxidation process of AA and UA can be deemed irreversible since there is no reduction peak evident in the CV curves.

The electrochemical response of AA and UA was scrutinized via CV as depicted in Fig 4.8(d). The experiments were conducted for the solution containing 30 µM UA, and a combination of 30 µM AA and 30 µM UA, as well as a solution consisting of both 60 µM AA and UA, in a 0.1 M phosphate buffer (pH = 7). In the absence of AA, a single oxidation peak was discerned for UA at 0.33 V. Upon examination of a solution containing 30 µM AA and UA, a distinct peak

for UA was solely observed at 0.34 V. Subsequently, upon the addition of 60 μM AA and UA, separate oxidation peaks were detected for AA and UA at 0.17 V and 0.34 V, respectively. Moreover, the peak-to-peak separation potential (ΔEp) between AA and UA was quantified at 0.17 V. This suggests that Co-MoS_2/RGO nanocomposite exhibited the capability to oxidize AA and UA with higher potential resolution of 0.17 V. This observation underscores the efficacy of the Co-MoS_2/RGO nanocomposite in discerning the oxidation processes of AA and UA. The electrochemical sensing mechanism for AA and uric acid UA was elucidated based on the scan-rate studies. The results demonstrate that the electrochemical sensing of AA and UA is predominantly governed by a diffusion-controlled process. CV data, presented in Fig. 4.8(d), reveal oxidation potentials of 0.17 V for AA and 0.34 V for UA, which delineate their specific oxidation behaviors. Fig. 4.9 demonstrates the proposed electrochemical sensing mechanism for AA and UA utilizing a Co-MoS_2/RGO composite electrode. The oxidation of AA is primarily associated with the intercalation of protons (H^+ ions) into the 3D layered nanostructures of the Co-MoS_2/RGO composite in the course of the reduction process. These protons are generated via the dissociation of AA into ascorbate ions (AA^-) in pH 7 buffer solution. The intercalation of these protons into the Co-MoS_2/RGO nanostructures facilitates the oxidation process of AA. For UA, the oxidation process involves its conversion into uric acid imine.

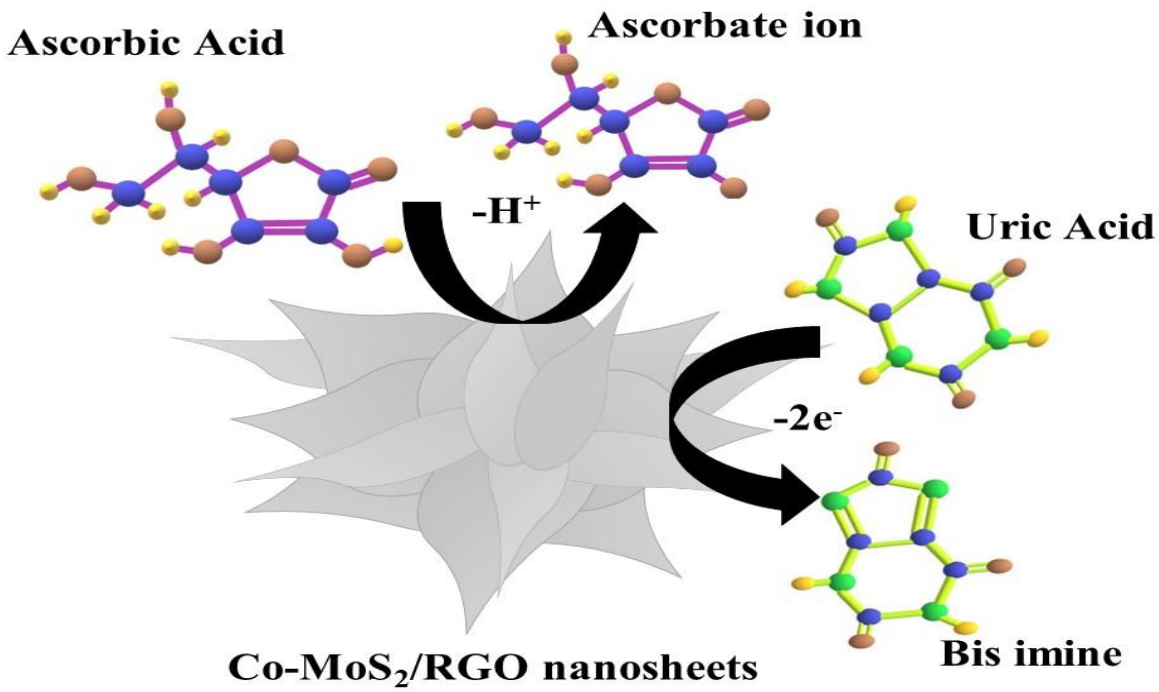

Fig. 4.9 Sensing mechanism of detection of both AA and UA.

During this electrochemical oxidation, UA undergoes a $2e^-$, $2H^+$ transfer reaction, resulting in the formation of the imine derivative. The specific interaction of UA with the Co-MoS_2/RGO composite facilitates this transformation, which is critical for the detection mechanism. This detailed mechanism underscores the pivotal role of the Co-MoS_2/RGO nanocomposite in enhancing the electrochemical response and selectivity for AA and UA through its unique structural and catalytic properties. The single and concurrent quantification of AA and UA at the Co-MoS_2/RGO@GCE electrode was conducted using the differential pulse voltammetry (DPV) technique. As observed in Figure 4.10(a), it is noteworthy that the peak potential of AA shifted to the right with increasing AA concentration, suggesting the participation of protons in the electro-oxidation process of AA. Moreover, the widening of the peak shape of AA, as noted in previous studies, suggests a potential relationship with excessive AA concentration. The AA on the electrode surface was rapidly catalyzed at lower AA levels, resulting in a quick response.

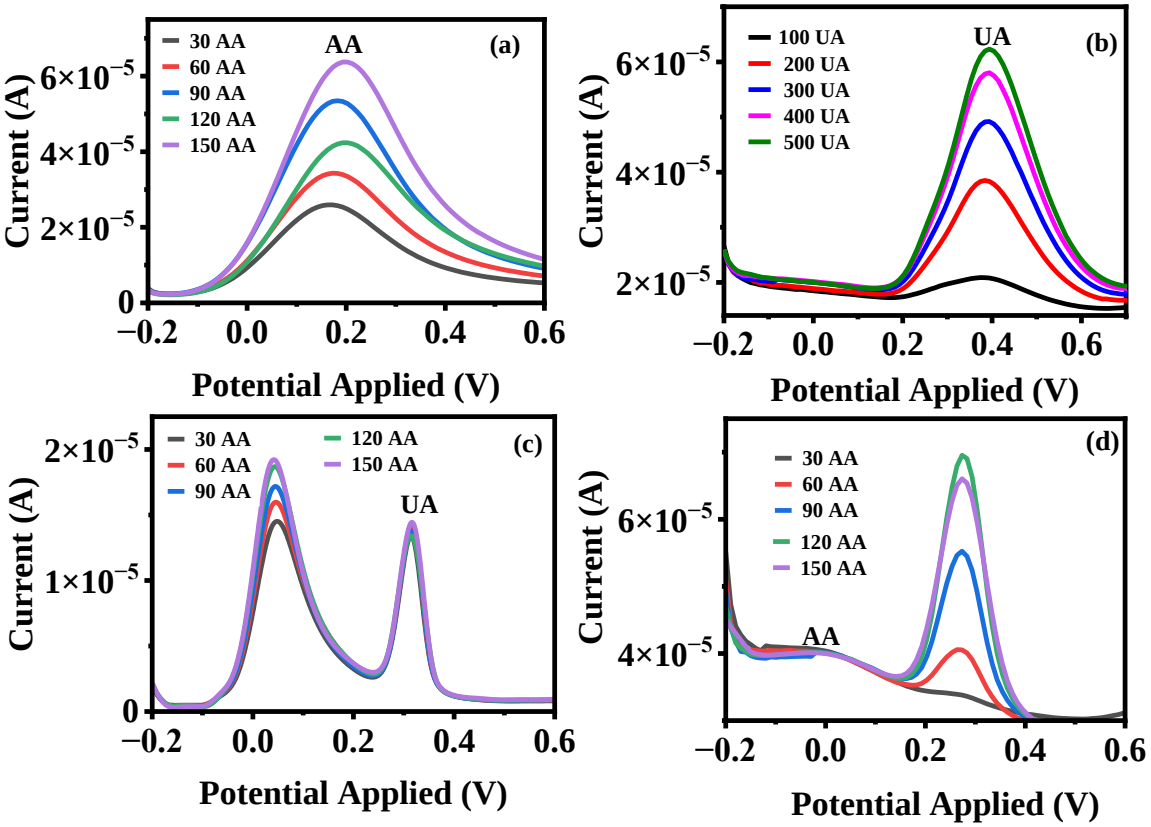

Fig. 4.10 DPV curves for (a)30-150 µM AA (b) (100-500) µM UA (c) varied AA concentration in the solution having 30 µM UA and (d) varied UA concentrations in the solution having 30 µM AA in 0.1 M PBS (pH=7).

Conversely, at higher AA concentrations, a significant amount of AA was adsorbed on the electrode surface, reducing active sites and prolonging the catalytic time of Co-MoS_2/RGO@GCE for AA. This phenomenon of slowing down of the catalytic process results in the widening of the peak shape. However, in the case of DPV of UA (refer Fig. 4.10(b)), sharp peaks are observed with a gradual increase in peak current up to 500 µM, revealing the equal participation of electrons and protons in the electro-oxidation process of UA. In the binary mixture, the concentration of one analyte was increased while maintaining the other at a constant level to facilitate selective detection at the Co-MoS_2/RGO@GCE electrode. In Fig. 4.10(c), the concentration of AA was raised from 30 to 150 µM keeping 30 µM UA constant. The existence of UA did not affect the current signal of AA. Likewise, the oxidation peak currents for UA showed a linear rise across its concentration range of 30 to 150 µM, as depicted in Fig. 4.10(d). The results demonstrate that Co-MoS_2/RGO@GCE exhibits excellent separation capability for AA and UA, as evidenced by the distinct potential peaks corresponding to each analyte. Fig. 4.11(a-d) illustrates the logarithmic correlation between peak current and various concentrations of AA and UA. The graph includes fitted lines obtained from linear regression equations for AA, UA, AA in the solution having UA, and UA in the solution having AA, respectively. Moreover, the detection limits for AA, UA, AA with UA, and UA with AA are 0.07, 0.2, 0.27, and 0.47 µM, respectively.

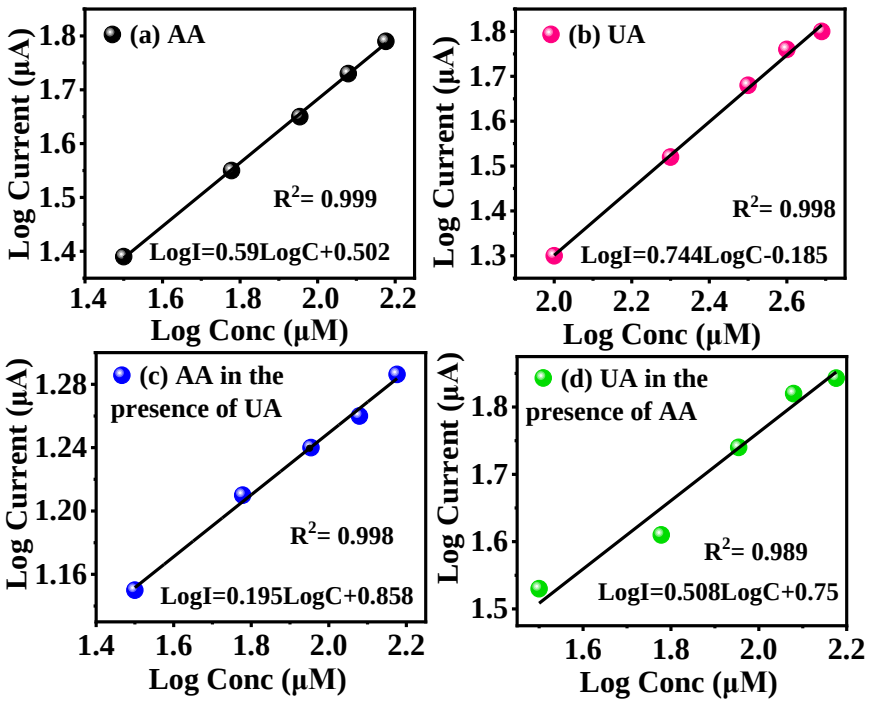

Fig. 4.11 Linear fitted plot for logarithmic variation of concentration vs current for (a) AA (b) UA (c) AA in the solution having UA and (d) UA in the solution having AA in 0.1 M PBS at pH 7.

These findings underscore the robustness of the Co-MoS_2/RGO nanocomposite in distinguishing and accurately measuring concentrations of AA and UA, both separately and together. Notably, in our previous work, the detection limit for AA using MoS_2/RGO was found to be 0.43 μM[92]. The incorporation of Co markedly hauls down the sensor's limit of detection by up to 15-fold and addresses the selectivity challenges encountered with MoS_2/RGO, demonstrating the improved performance of the Co-MoS_2/RGO nanocomposite. The detection limits and linear detection ranges were further compared with those from studies focused on the selective and individual detection of UA and AA, as summarized in Table 4.1. The Co-MoS_2/RGO sensor exhibits outstanding selectivity and a significantly lower limit of detection for ascorbic acid AA and UA when compared to the other studies presented in Table 4.1. The ability to maintain relatively low detection limits, even in mixed samples, is particularly valuable for applications requiring precise and reliable detection in complex biological or chemical environments. Moreover, in our previous research, we found that the sensitivity of MoS_2/RGO in detecting AA was 2.9 μA μM^{-1} cm^{-2}. Upon utilizing Co-MoS_2/RGO for AA detection, the sensor's sensitivity was measured at 8.42 μA μM^{-1} cm^{-2}, indicating a 2.9-fold enhancement. Additionally, the sensitivity of Co-MoS_2/RGO towards UA was estimated to be 10.628 μA μM^{-1} cm^{-2}. Further, the selective sensitivities of Co-MoS_2/RGO towards AA and UA were calculated as 2.786 and7.25 μA μM^{-1} cm^{-2} respectively. These results suggest that Co-MoS_2/RGO is more sensitive towards UA. Overall, these findings demonstrate the exceptional sensitivity of the designed sensor towards both analytes, highlighting its potential efficacy in electrochemical sensing applications. Both AA and resorcinol (RS) were held at a consistent concentration of 60 μM, while the concentration of UA was adjusted from 100 μM to 300 μM, as depicted in Figure 4.12(a). It was observed that the sensor exhibited an increase in peak current specifically corresponding to UA. This indicates the sensor's excellent selectivity, as it can distinguish UA from RS and AA, even when these substances are present at fixed concentrations. The sensor's ability to accurately detect changes in UA concentration without interference from AA or RS is crucial for reliable and precise measurements in complex mixtures where multiple analytes coexist. Additionally, the Co-MoS_2/RGO sensor exhibits exceptional sensitivity and selectivity while maintaining outstanding stability in ambient air. Over a period of 15 days, the DPV response of the sensor to a mixed solution of 30 μM AA and 100 μM UA was recorded approximately every 5 days, with the results depicted in a bar graph (refer to Fig. 4.12(b)).

Table 4.1 Comparison of Electrochemical Detection of AA and UA with Other Reported Studies.

Electrode material	AA		UA		Ref.
	LOD (µM)	**Linear Range (µM)**	**LOD (µM)**	**Linear Range (µM)**	
1. PdNPs/rGO/GCE	100	30–7000	16.67	0.05–1000	[261]
2. GQDs-IL-SPCE	6.64	25–400	0.03	0.5–20	[262]
3. PVP-GR/GCE	0.8	4.0–1000	0.02	0.04–100	[263]
4. AuNPs@MoS_2/GCE	100	50 – 100 000	10	50 –40000	[217]
5. 3D-MoS_2/rGO/Au@GCE	0.93 *(Individual)* & 1. 46 *(Simultaneous)*	2.0 - 5400	0.74*(Individual)* & 0.29*(Simultaneous)*	5.0 to 2215	[264]
6. MoS_2/PEDOT/GCE	5.83	20–140	0.95	2–25	[265]
7. Pt@g-C_3N_4/N-CNTs	29.44	100–3,000	0.21	1–100	[266]
8. Co-MoS_2/RGO	0.07*(Individual)* & 0.27*(Simultaneous)*	30-150	0.22*(Individual)* & 0.47 *(Simultaneous)*	100-500	This work

Despite this extended duration, only 2 and 3% degradation in peak current of AA and UA were observed. This minimal decline underscores the sensor's excellent stability in ambient conditions, as well as its reproducibility and repeatability, emphasizing its suitability for consistent and reliable sensing of AA and UA in practical applications. The sensor's robustness and minimal performance degradation over time make it a promising tool for accurate monitoring of AA and UA in various settings.

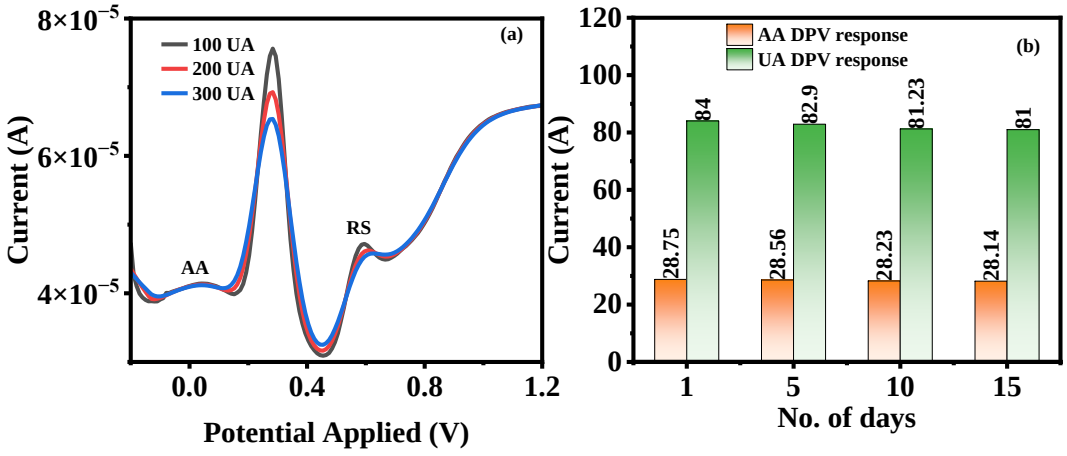

Fig. 4.12(a) Anti-interference response of Co-MoS_2/RGO towards UA in the solution having 60 µM AA and 60 µM resorcinol, (b) bar graph representing the DPV response of simultaneous and selective detection of AA (30 µM) and UA (100 µM) for 15 days in 0.1 M PBS at pH 7.

Conclusion: In conclusion, the Co-MoS_2/RGO composite was successfully synthesized using a two-step microwave-assisted method. Comprehensive characterization confirmed its structural integrity and 3D flower-like nanosheet morphology. Electrochemical analysis revealed the composite's exceptional sensitivity and selectivity. Specifically, the individual and selective limits of detection for ascorbic acid were determined to be 0.07 μM and 0.27 μM, respectively, while for uric acid, they were 0.22 μM and 0.47 μM. Furthermore, the Co-MoS_2/RGO composite demonstrated remarkable individual and selective sensitivities for ascorbic acid, measuring 8.42 and 2.786 μA μM^{-1} cm^{-2}, respectively. For uric acid, the corresponding values were 10.628 and 7.25 μA μM^{-1} cm^{-2}. Additionally, the sensor exhibited excellent stability under ambient conditions and high reproducibility, underscoring its reliability and effectiveness for the electrochemical sensing of ascorbic acid and uric acid, both individually and simultaneously. These results underscore the potential of Co-MoS_2/RGO as a highly promising material for practical applications in complex analytical environments.

Chapter 5

Microwave-assisted incorporation and optimization of Mn doping in MoS_2/RGO for application in multi-detection to single-detection electrochemical biosensing: Uric acid

Electroactive moieties, including ascorbic acid (AA) and uric acid (UA), co-occur within the human nervous system and serum, exerting pivotal roles in human metabolic processes [267, 268]. Uric acid (7,9-dihydro-1H-purine2,6,8(3 H)-trione), the terminal by-product of purine catabolism in humans, has garnered attention for its neuroprotective attributes attributed to potent antioxidant capacities [269]. Various pathologies, including osteoarthritis, hyperuricemia, gout, Lesch–Nyhan syndrome, Type 2 diabetes, elevated cholesterol levels, kidney, neurological, and cardiovascular problems., among others, can be discerned through the measurement of aberrant uric acid levels [270]. Precisely detecting UA levels in human bodily fluids is critical in diagnosing diverse diseases. The typical UA levels in human blood serum should range from 0.13 to 0.46 mM, while in urine, they should range from 1.49 to 4.46 mM [271]. The detection of uric acid (UA) can indeed be carried out using various methods, including mass spectrometry, liquid chromatography, and electrochemical detection [272]. UA has a high redox activity, making electrochemical sensing a natural option for its detection. Electrochemical techniques offer multiple advantages, such as enhanced sensitivity, rapid response, and the potential for miniaturization and automation. Electrochemical detection of uric acid has found implementations in diverse fields, including clinical testing, food analysis, and environmental regulation [273]. It offers a reliable and efficient means of quantifying uric acid levels, aiding in disease diagnosis, treatment monitoring, and research investigations related to uric acid metabolism and associated disorders [274]. Some previous reports have demonstrated the capability of electrochemical sensors to detect low concentrations of UA. However, some of these reports have used expensive metals or sophisticated biological immobilized molecules (e.g., nucleic acids, aptamers, or enzymes) to achieve this level of sensitivity [275, 276]. Using such materials can add to the manufacturing complexity, increase overall costs, and limit large-scale production, which is a concern when developing low-cost point-of-care diagnostic tools. To overcome these challenges, ongoing research focuses on finding alternative materials and simpler sensor designs to achieve highly responsive and selective detection of UA without compromising on cost-effectiveness and scalability. 2D materials have become a promising building block for flexible and ultrasensitive sensors. High surface-to- volume ratio, scaling down to a monolayer capability, durable covalent bonding

inside the layer, and tunable electrical and optical properties are just a few of the beneficial characteristics of 2D materials [277]. Graphene has attracted the most attention as a promising UA sensor [278]. However, pristine graphene has some limitations, such as being a zero-bandgap material and lacking dangling bonds on its surface, which can affect its interaction with certain analytes. To overcome this restriction, graphene is often offered defects to widen a bandgap and improve its sensing abilities. Transition metal dichalcogenides (TMDs) have a wide spectrum of electronic characteristics, including insulators, semiconductors, semimetals, and metals, making them flexible for a variety of applications. Molybdenum disulfide (MoS_2) is an excellent material for UA detection among TMDs. So, the hybrid of MoS_2 and reduced graphene oxide (MoS_2/RGO) is suitable for the sensitive detection of UA [279]. As previously discussed, employing MoS_2/RGO for selectively determining the electrochemical levels of UA in the solution having ascorbic acid (AA) poses a challenge due to the proximity of their oxidation potentials and the deposition of oxidation byproducts on the electrode surface, resulting in electrode poisoning [280]. This, in turn, hampers the reusability, selectivity, and reproducibility of these electrode surfaces. To overcome this interference, researchers and scientists have explored several strategies and methods to selectively detect uric acid in the solution having ascorbic acid. Modifying the electrode surface with selective materials can improve the discrimination between uric acid and ascorbic acid. In this case, doping MoS_2/RGO with heteroatoms allows you to alter and functionalize the material's surface. Localized gap states created by heteroatom doping can change electronic characteristics and improve molecule adsorption. Metal particles, like gold (Au), are frequently employed to form nanohybrids with MoS_2 for UA detection. However, because of their scarcity and cost, it is desirable to find lower-cost substitutes. Manganese (Mn) has been regarded as a competent catalytic site for the oxidation of UA via redox cycling between Mn (II) and Mn (III). Therefore, it is hypothesized in the present work that by incorporating Mn into MoS_2/RGO, the selectivity of UA detection can be significantly improved.

5.1 Structural studies

The XRD analysis of the crystal structures of MoS_2, MRG, and 7% Mn- MRG composites is presented in Fig. 5.1 MoS_2 MRG, & 7% Mn-MRG composites exhibit XRD patterns that are similar to the peaks appearing at 2θ = 13.6, 32.63, 40.27, and 58.3°, which are ascribed to the (002), (100), (103), and (110) planes of the hexagonal MoS_2 phase (as per JCPDS No. 00-037-1492), accordingly. A well-ordered crystal structure of MoS_2 in the material is revealed by the prominent peak at 2θ = 32.63° (100), which corresponds to a d-spacing of 0.27

nm. Here, it is crucial to consider that the existence of the characteristic diffraction peak at 2θ =22.98 caused by RGO in 7% Mn-MRG composites indicates that RGO is stacked in 7% Mn-MRG. Mn may be effectively incorporated into the MoS_2 matrix, as suggested by the absence of peaks corresponding to MnS. In particular, when the Mn is doped, the peak intensity of the resulting nanocomposites drops. The Shannon ionic radius is a useful reference for understanding the relative sizes of ions in a crystal lattice. As seen in Fig. 5.1 the expansion of the 2θ range of 11–15° reveals a minor shift of the (002) peak to the lower-angle area, indicating an augmentation in the spacing between layers of the doped samples. At a coordination number of 6, Shannon's ionic radius indicates that the greater ionic radius of Mn^{2+} (0.067 nm) compared to the Mo^{4+} (0.065 nm) could account for this growth [281, 282]. When Mn^{2+} ions are embodied into the crystal structure, they may occupy the Mo^{4+} sites, and their larger ionic radius can push the neighboring layers slightly further apart.

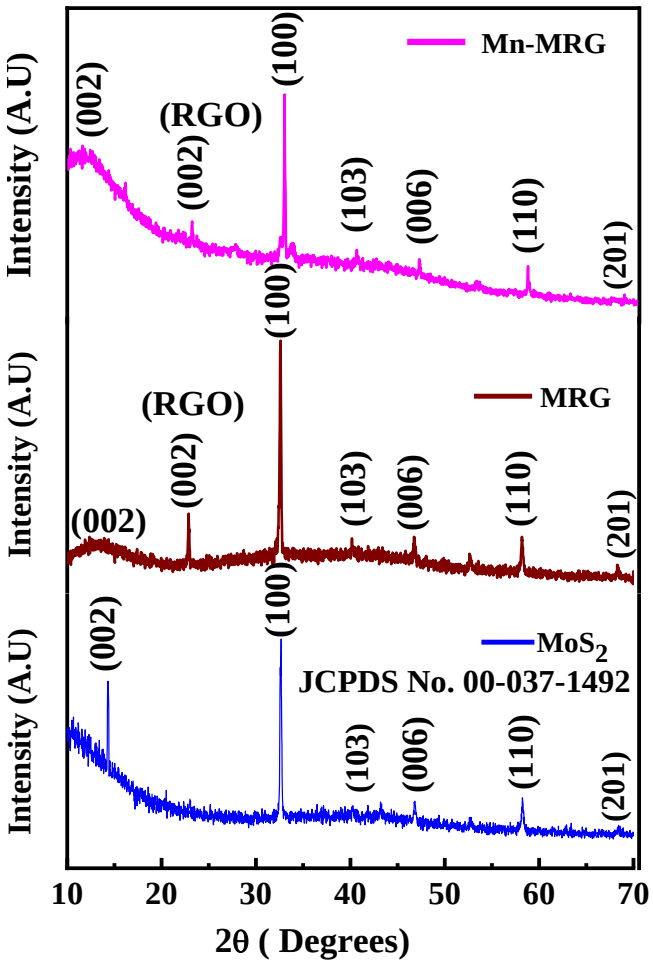

Fig. 5.1 the XRD patterns for MoS_2, MRG, and Mn-MRG

This results in an increase in the interlayer spacing, which is reflected in the XRD pattern as a shift in the (002) peak to lower 2θ angles. The synthesis of Mn-MRG was further characterized using Raman spectroscopy, as illustrated in Fig. 5.2. The Raman spectrum of MoS_2, MRG, and the Mn-MRG nanocomposite reveals distinct peaks associated with specific vibrational modes. For MoS_2 and MRG the peaks appearing at 381 and 407 cm^{-1} correspond to the characteristic E^1_{2g} and A_{1g} modes of the hexagonal (2H) MoS_2 nanocomposite. Additionally, Raman peaks of reduced graphene oxide at 1355 (D-band) and 1605 (G-band) cm^{-1} show the existence and good integration of RGO sheets in MRG nanocomposite. In Mn-MRG, distinctive spectral bands located at 376 cm^{-1} and 403 cm^{-1} coincide with the (2H) MoS_2 vibration modes (E^1_{2g} and A_{1g}), both in-plane and out-of-plane.

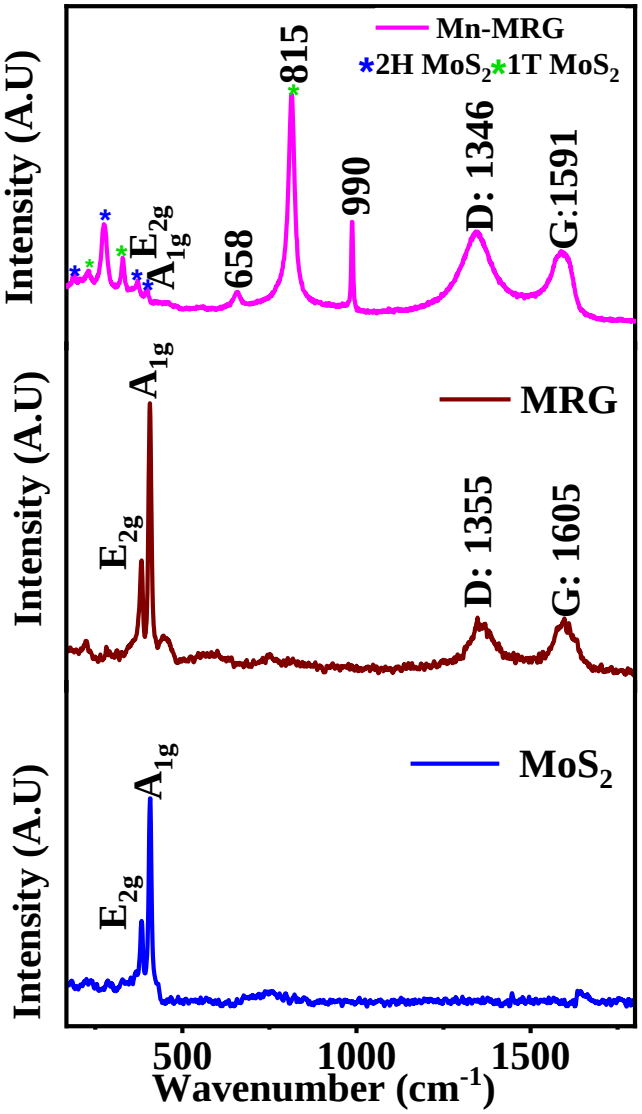

Fig. 5.2 Raman spectra of MoS_2, MRG, and Mn-MRG.

The peaks at 192 cm^{-1} and 280 cm^{-1} are attributed to A_{1g}-longitudinal acoustic phonon modes (LA) and E_{1g} transverse mode (T), which are consistent with the 2H-MoS_2 structure. Additionally, two small peaks at 231 cm^{-1} and 334 cm^{-1} correspond to the 1T phase of molybdenum disulfide, resulting from structural changes induced during the two-step microwave irradiation reaction. The existence of coexisting 2H and 1T phases of MoS_2 in the Mn-MRG composite suggests an optimized structure for enhanced stability [283]. The peak at 815 cm^{-1} is correlated to the second harmonic peak of a few layers of pure Mo-Mo bond interaction [251]. The Raman peak at 658 cm^{-1} indicates the stretching vibration of Mn–O, confirming the existence of manganese in the composite [284]. The formation of oxides noticed at the peak at 990 cm^{-1}, is probably a result of undergoing partial oxidation of MoS_2 upon exposure to air during synthesis. The D and G bands of RGO in Mn-MRG emerge at 1346 cm^{-1} and 1591 cm^{-1}, respectively, with an I_D/I_G ratio of 1.194 indicating the existence of structural defects that may contribute to enhanced selectivity in the composite.

5.2 Morphological and textural studies

The FESEM images depicted in Fig. 5.3(a-d) reveal distinct morphological structures for each constituent of the Mn-doped MRG composite. In Fig. 5.3(a), the RGO sheets are distinctly visible, while 5.3(b) displays a spherical morphology of MoS_2. Meanwhile, 5.3(c) emphasizes the existence of manganese needles within the composite. Notably, Fig. 5.3 (c,d) collectively depict the three morphologies: spherical MoS_2, nanosheet-like RGO structures, and acicular manganese morphology. The combination of these morphologies indicates a complex nanocomposite material where each component likely contributes to the overall effectiveness of the designed electrochemical sensor. The spherical MoS_2 nanoparticles possess a high surface area and exhibit a more homogeneous size and shape distribution, which can contribute to consistent electrochemical performance.

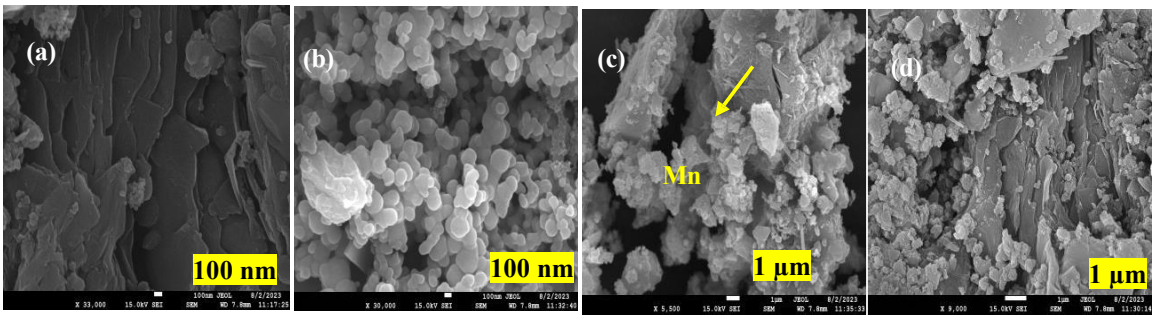

Fig. 5.3 FESEM (a) images of RGO (b) images of MoS_2 and (c,d) images of Mn-MRG.

The existence of sheets in FESEM images indicates the reduction process of GO to form graphene layers, known for their high surface area and electrical conductivity. The elongated, needle-shaped Mn structure facilitates efficient electron transport of reactants and products, enhancing the kinetics of catalytic reactions.

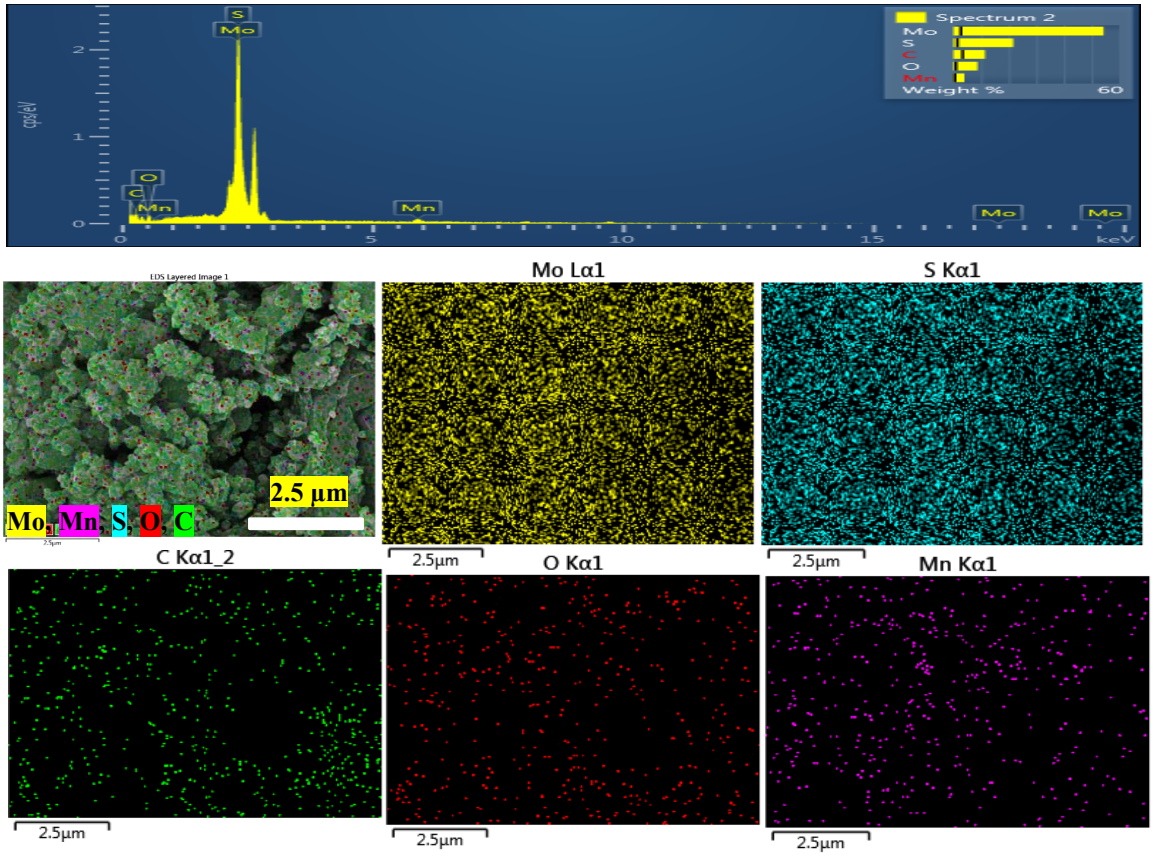

Fig. 5.4 EDS analysis of FESEM images of Mn-MRG.

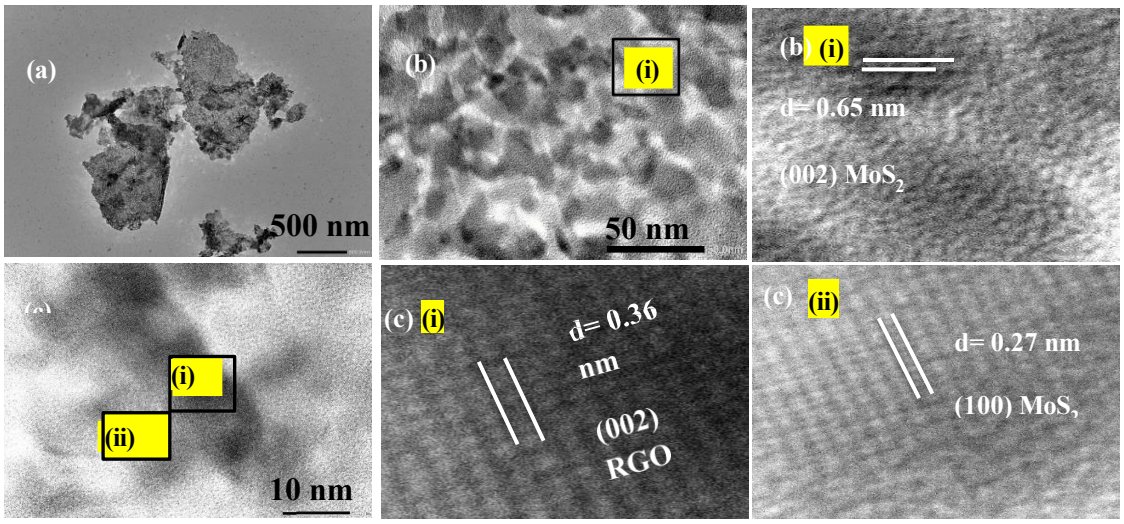

Fig. 5.5 HRTEM (a,c) images of Mn-MRG composite at different magnifications and (b(i)) zoomed view of the marked area in (b) and (c(i),c(ii)) zoomed view of the marked area in (c).

Moreover, the directional orientation of needle-shaped Mn structures allows for the preferred accessibility of active sites to target molecules. The energy-dispersive X-ray spectroscopy (EDS) analysis of FESEM images verifies the successful doping of Mn in MRG, as illustrated in Fig. 5.4. Fig. 5.5 (a,c) depict the HRTEM of the Mn-MRG nanocomposite. Fig. 5.5(b(i)) presents a zoomed-in view of the marked area in Fig. 5.5(b), while Fig. 5.5(c(i)) and Fig. 5.5(c(ii)) provide magnified views of Fig. 5.5(c). The measured d-spacing from the fringes are 0.65 nm, 0.27 nm, and 0.36 nm corresponding to the (002) plane of MoS_2 (illustrated in Fig. 5.5(b(i)), the (100) plane of MoS_2 (Fig. 5.5(c(ii)), and the (002) plane of RGO (Fig. 5.5(c(i)), respectively. These observations are consistent with prior investigations [253] and are in agreement with the outcomes obtained from XRD.

Using BET analysis, we examined the surface area and porosity of the Mn-MoS_2/RGO nanohybrids. Nitrogen adsorption-desorption analysis reveals a gradual increase in the adhered volume in the BET isotherm within the range of P/P^o = 0.049– 0.1535 (Fig. 5.6(a)). The Mn-MRG demonstrates a remarkable BET surface area of 14.804 m^2g^{-1} and a high pore volume of 0.092 cm^3g^{-1}. The observed pore size distribution of Mn-MRG, as illustrated in Fig. 5.6(b), reveals that the material is mesoporous, with predominant pore sizes of 6.15 nm. This feature renders it a highly promising electrochemical sensing platform, capable of accommodating a broad range of molecular sizes. The abundant edges and defects resulting from the elevated specific surface area and porous structure of Mn-MRG play a crucial role. These features assisted electrolyte perforation and transportation while providing the target analyte with a have a high likelihood of contact with the active sites.

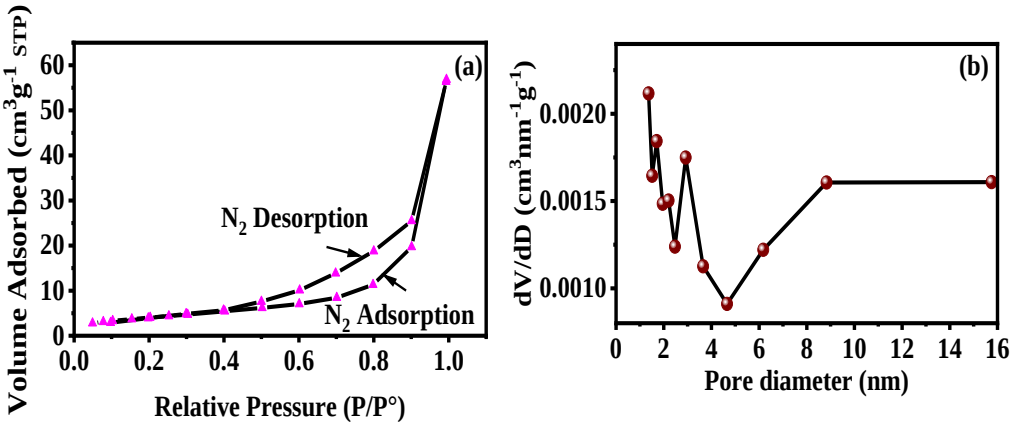

Fig. 5.6 (a) Nitrogen adsorption-desorption isotherm for Mn-MRG, inset (b) pore distribution curve for Mn-MRG.

This may contribute to the efficiency of redox reactions [285], ultimately improving electrochemical catalysis and sensitivity [286].

5.3 Compositional studies

Fig. 5.7(a) presents a comprehensive analysis of the XPS data revealing the chemical states and bonds within the 7% Mn-MRG composite material, including the oxidation states of manganese and the chemical environment of molybdenum, sulfur, and carbon.

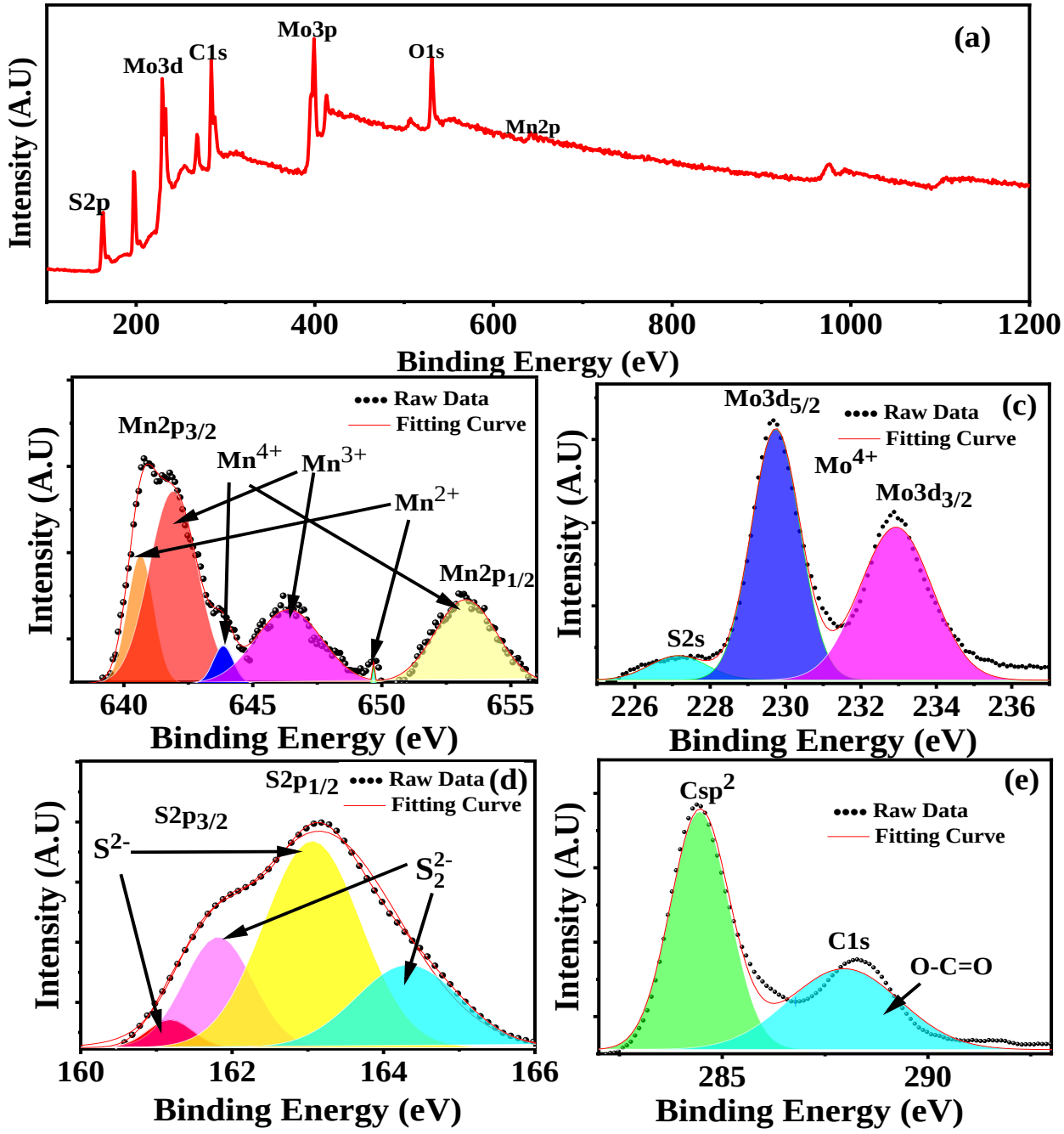

Fig. 5.7 XPS pattern Mn-MRG (a) full scan spectrum of Mn-MRG (b-e) high resolution spectra of (b) Mn2p, (c) Mo3d, (d) S2p and (e) C1s.

In Fig. 5.7(b), the Mn2p spectrum was deconvoluted into six peaks representing different oxidation states of manganese: Mn^{2+} at binding energies of 640.81 and 650.48 eV, Mn^{3+} at 641.8 and 646.50 eV, and Mn^{4+} at 643.83 and 653 eV. This indicates the concurrence of Mn^{2+}, Mn^{3+}, and Mn^{4+} ions on the sample surface, highlighting the multiple oxidation states of manganese within the composite material [286, 287]. The Mo3d spectrum in Fig. 5.7(c) displayed two peaks at 229.73 and 232.88 eV, equivalent to the binding energy values of Mo^{4+} $3d_{5/2}$ and Mo^{4+} $3d_{3/2}$, respectively, indicating the oxidation state of molybdenum as Mo^{4+} in the sample. Furthermore, Fig. 5.7(d) shows a peak at 226.9 eV ascribed to the S2s of MoS_2. The S2p spectrum in the same figure exhibited four peaks at 161.16, 161.8, 163.08, and 164.33 eV, imputed to the $S2p_{3/2}$ and $S2p_{1/2}$ of S^{2-} and S_2^{2-} charged states of sulfur in the composites, indicating the specific chemical state of sulfur, likely associated with MoS_2 [288]. In Fig. 5.7(e), the C1s spectrum revealed four peaks corresponding to different carbon-containing functional groups in the RGO component. Peaks at 284.36 and 285.7 eV represent C-C and C=C bonds, indicating the existence of carbon-carbon double bonds. The peak at 288.29 eV is attributed to C=O and O-C=O bonds, suggesting the existence of carbonyl and carboxyl functional groups within the composite material [255]. Fig.5.8 illustrates the FTIR spectra of MoS_2, MRG, and 7% Mn-MRG composites. In all the materials, the peaks observed at 544, and 654 cm^{-1} correspond to S-S and Mo-S stretching vibrations [254, 255], confirming the existence of MoS_2 in the materials. A peak observed at 2084 cm^{-1} in 7% Mn-MRG corresponds to Mn-O vibrations confirming the successful doping of Manganese.

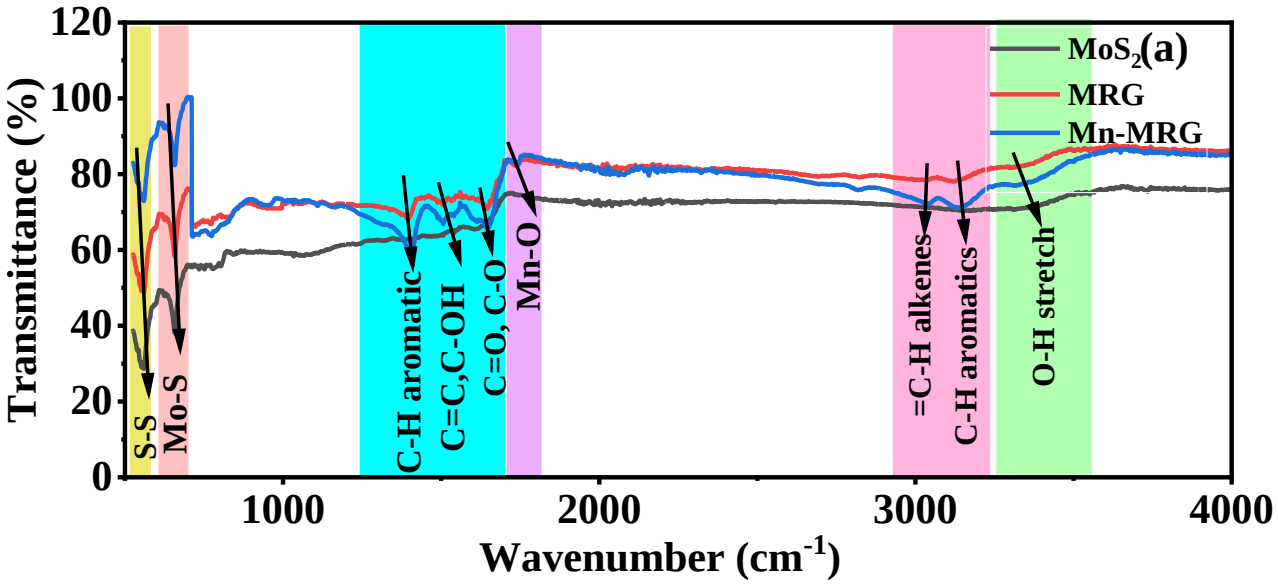

Fig. 5.8 FTIR spectra of MoS_2, MRG and Mn-MRG

Regarding RGO, the peaks at 1407, 1506, 1638, 1737, 3035, and 3145 cm^{-1} are accredited to C-H stretching of aromatic carbon, C=C stretches from the unoxidized graphitic domain, C-O (alkoxy) stretching vibrations [289.290], C-H elongation and =C-H Alkenes or C-H aromatics of the carboxyl group [291]. Additionally, the vibration band around 3321 cm^{-1} can be attributed to the O-H stretching of ethanol absorbed by the composites during microwave synthesis. The bonding nature revealed by the IR spectra serves as further affirmation of the concurrence of Mn doped MoS_2 and RGO in the synthesized composites.

5.4 Optical characteristics

The UV-Vis analysis of MoS_2, MRG, and Mn-MRG composites is done to reveal their absorption characteristics. Compared to pristine MoS_2, the absorption intensity across the entire wavelength range is notably enhanced and red-shifted in Mn-MRG composites, likely due to the inherent light absorption properties of RGO. In Fig. 5.9(a), the specific absorption edges are observed at 265, 274 and 294 nm for pristine MoS_2, MRG and Mn-MRG, respectively.

Notably, the absorption edge of ascorbic acid is reported at 265 nm [292], while uric acid shows an absorption at 294.46 nm [293]. This finding suggests that uric acid possesses an absorption peak similar to that of 7% Mn-MRG, indicating potential for selective detection using Mn-MRG. The calculated band gap energies from the Tauc plot in Fig. 5.9(b) are 1.78 eV for MoS_2, 1.63 eV for MRG, and 2.16 eV for Mn-MRG. These values align well with the reported direct band gap of MoS_2 (1.8 eV), validating the synthesis of the material [294].

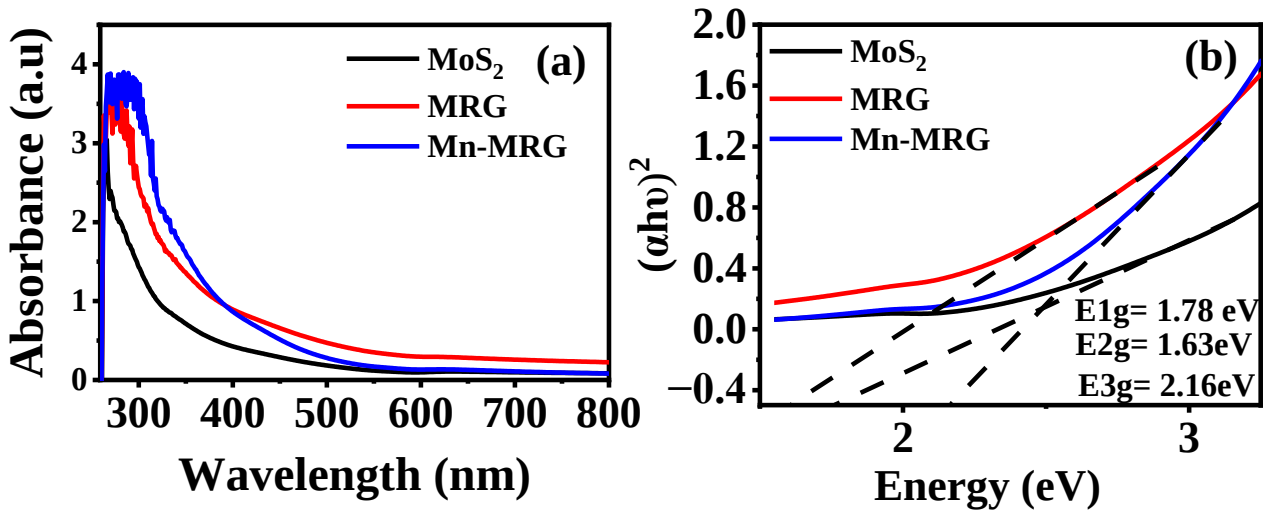

Fig. 5.9(a) UV and (b) Tauc plot of MoS_2, MRG and Mn-MRG.

5.5 Electrochemical measurements

To investigate the impact of substrate modification on the electrochemical performance of the sensors, the double-layer capacitance (C_{dL}) was assessed through cyclovoltammetry tests (CVs) conducted at various scan rates (see Fig. 5.10). These tests were performed in a blank solution of phosphate-buffered saline (PBS) at pH 7, devoid of ascorbic acid (AA) or uric acid (UA) [260,295]. For a more meaningful comparison of results, this evaluation was executed using electrodes with MRG, 3%, 5%, 7% and 9%Mn-MRG as shown in Fig. 5.10(a). The plot depicting the oxidation peak current displayed a linear response with the under root of the scan rate, and the slope of this relationship was correlated with C_{dL} as shown in Fig. 5.12(a). The analysis discloses that the double-layer capacitance (C_{dL}) of the unmodified MRG is notably low at 0.0283 mF.

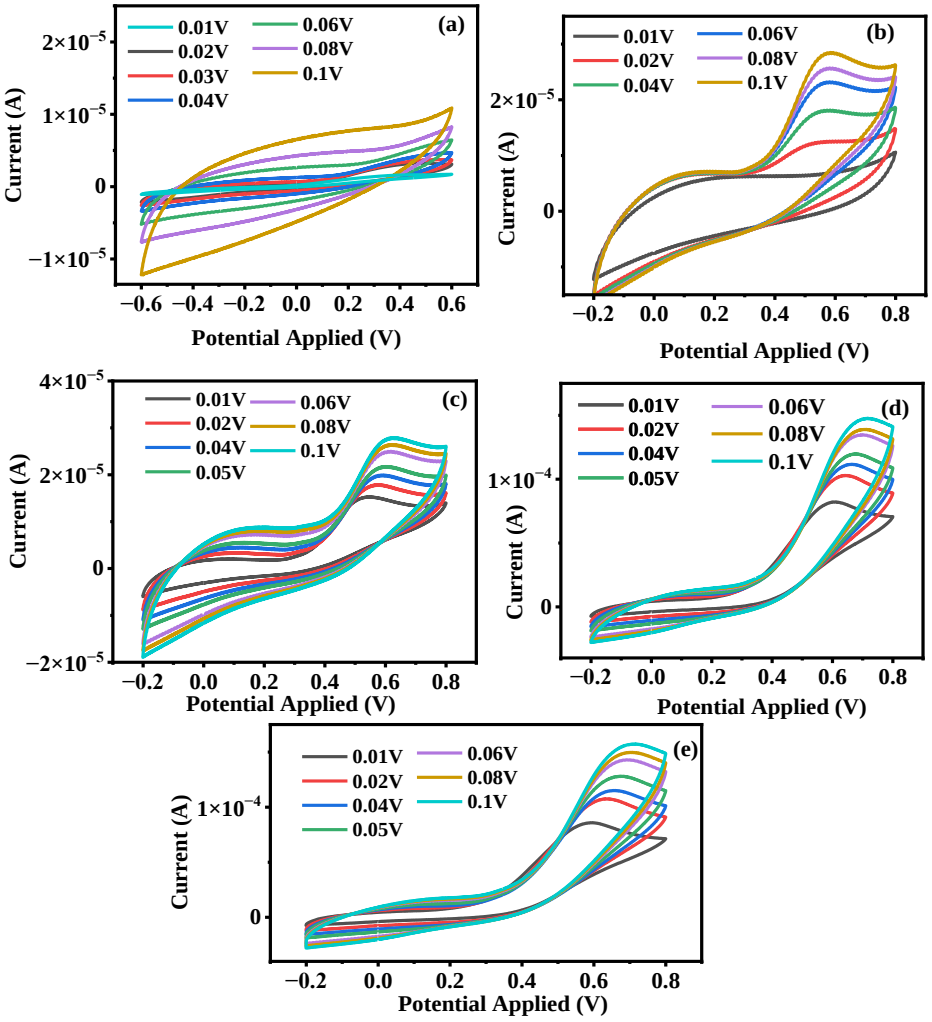

Fig. 5.10 Multiscan CV curves for devoid buffer solution (a) MRG (b) 3% Mn-MRG (c) 5% Mn-MRG (d) 7% Mn-MRG and (e) 9% Mn-MRG.

Introducing modifications to the MRG by doping 3%, 5%, 7%, and 9% Manganese, results in a substantial increase in C_{dL} by approximately 0.0467, 0.067, 0.238, and 0.205 mF, respectively. This trend indicates that increasing the Mn doping up to 7% boosts the material's ability to store electrical charge at its interface and after that, it declines. Interestingly, when MRG is modified with Mn, the highest C_{dL} value is observed at 0.238 mF for 7% Mn-MRG. This represents a remarkable increase of approximately 10 times compared to the C_{dL} for undoped MRG. Notably, the blend of spherical-shaped nanoparticles, nanosheets, and nanoneedles contributes to a more significant enhancement in C_{dL} compared to the hierarchical morphology of MRG [92]. Given that C_{dL} is linked to the real electrochemical active surface area (ECSA). The ECSA values for the MRG, 3% Mn-MRG, 5% Mn-MRG,7% Mn-MRG, and 9% Mn-MRG were 2.93, 6.5, 8.1, 5.37, and 4.3cm^2, respectively. This indicates that 5% mn-MRG results in the highest ECSA value 8.1cm^2, indicating the largest accessible surface area for electrochemical reactions among the tested variations. The additional note about the decrease in ECSA at higher doping levels, such as 7% and 9%, suggests that there might be a mechanism hindering ECSA beyond a certain threshold of Mn doping.

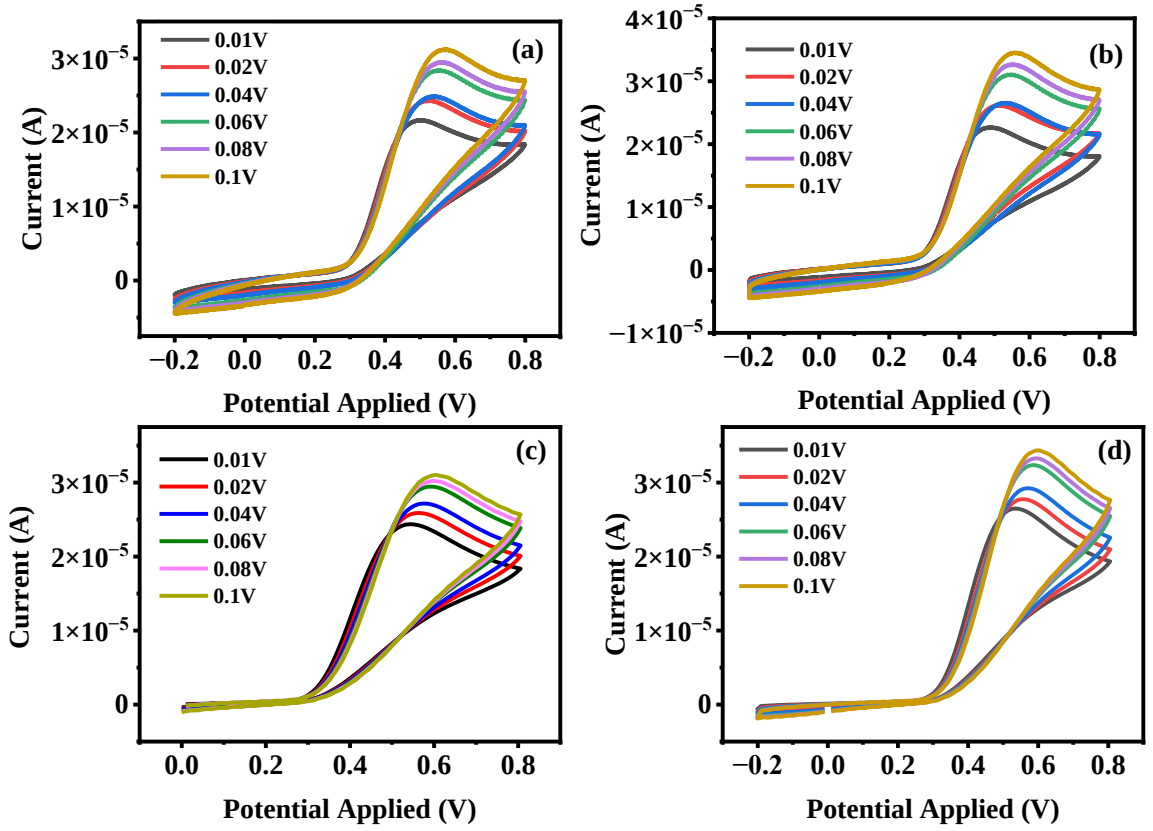

Fig. 5.11 Multiscan Curves at various scan rate in the solution having 30 µM AA and 500 µM UA.

The hypothesis put forth is that the stacking of manganese needles on the surface of MRG could be a contributing factor. This stacking could potentially limit the available surface area for electrochemical reactions, leading to a decrease in ECSA despite the increased Mn concentration. Notably, the ECSA of 5% Mn-MRG 3 folds larger than undoped MRG. This increase in ECSA is attributed to the incorporation of manganese needles within the MRG composites, enhancing the conductivity of Mn-doped MRG. These findings underscore that Mn doping serves as an excellent strategy for electrode modification, causing to a substantial increase in the active surface area and promoting high electroactivity. The electrochemical oxidation of UA utilizing the Mn-MRG modified glassy carbon electrodes was examined through CVs conducted at varied scan rates (v) ranging from 10 to 100 mV/s, employing 7 pH PBS containing 500 µM UA in the solution having 30µM AA (refer Fig. 5.11). The electrochemical oxidation of UA is consistent with previous reports [152], the oxidation process is diffusion- controlled at varied scan rates, evidenced by a direct proportionality between peak current density and the square root of scan rate (See Fig. 5.12(a). The logarithm of current density (log(j)) plotted against the logarithm of scan rate (log(v)) for each Mn-MRG composition, depicted in Fig. 5.12(b), aligns with the concept of the heterogeneous charge transfer coefficient (α) [296]. For UA, the computed α value is 0.153, 0.188, 0.10894, and 0.11715 for 3% Mn-MRG, 5% Mn-MRG, 7% Mn-MRG and 9% Mn-MRG respectively. This α value is utilized to determine the number of electrons (n) involved in the oxidation of UA using the equation [297]

$$E_p - E_{p/2} = 47.7/\alpha n \quad - (I)$$

where E_p represents the peak potential, and $E_{p/2}$ is the half-peak potential.

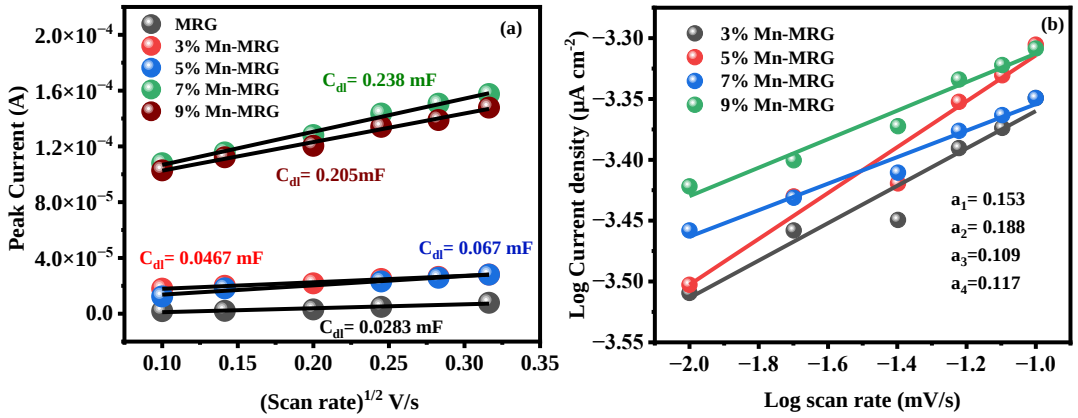

Fig. 5.12 (a) Scan rate versus peak current linear fit plots for MRG, 3% Mn-MRG, 5% Mn-MRG, 7% Mn-MRG and 9% Mn-MRG; (b) Log of scan rate versus peak current density plots for 7% Mn-MRG.

Employing this equation, the estimated number of electrons for UA oxidation was found to be 2 (with estimated values of 2.1, 1.8, 2.76, 2.5), in accordance with the mechanism suggested by Kannan et al. [241]. In Fig. 5.13(a), CV curves of MRG, 3% Mn-MRG, 5% Mn-MRG, 7% Mn-MRG, and 9 % Mn-MRG in 0.1 M PBS at a scan rate of 60 mVs^{-1} are presented. It was observed that the 7 % Mn-MRG exhibited the maximum loop area, indicating that a 7% doping of Mn to MRG is the most optimal among the prepared compositions. Furthermore, under the same conditions, the CV curves of MRG, 3% Mn-MRG, 5% Mn-MRG, 7% Mn-MRG, and 9% Mn-MRG at varying analyte concentrations are depicted in Fig. 5.13(b-e).

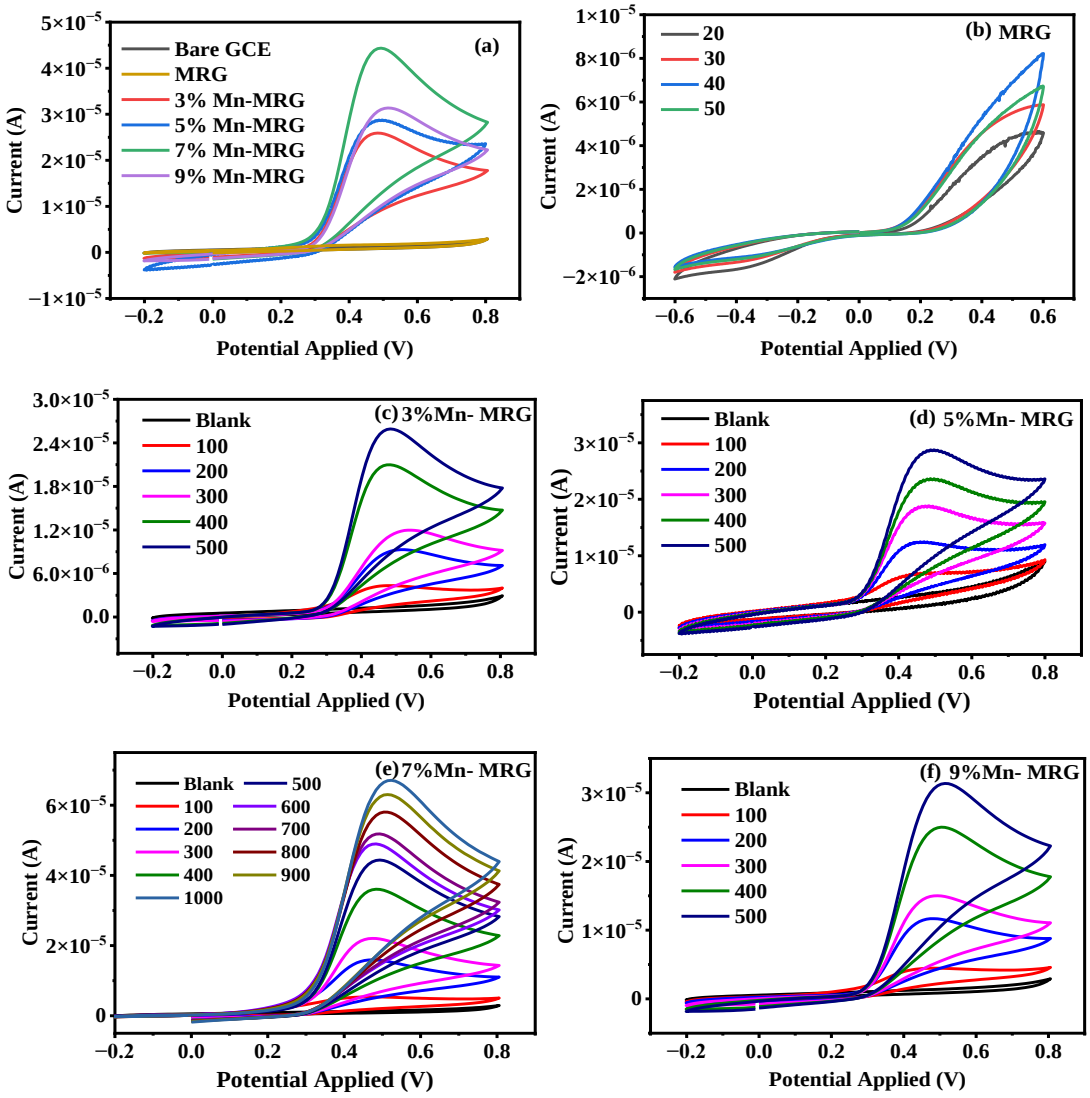

Fig. 5.13 (a) The CV curves of bare GCE, MRG, and MRG nanocomposites with various compositions of Mn at a specific concentration of AA and UA; the CV data for (b) MRG, (c) 3% Mn-MRG, (d) 5% Mn-MRG, (e) 7% Mn-MRG and (f) 9% Mn-MRG shows different concentrations of UA in the solution having 30 µM AA in a PBS solution with a pH of 7. All the measurements are done at a scan rate of 60mV/s.

It was noted that the loop area increased with the rising concentration of UA in the buffer-analyte solution, highlighting the sensing capabilities of the Mn-MRG nanocomposites. The CV data shows varying concentrations of UA in MRG, 3% Mn-MRG, 5% Mn-MRG, 7% Mn-MRG, and 9% Mn-MRG in the solution having 30 µM AA. The 7% Mn-MRG displayed the greatest linear detection range. The results of the CV experiment indicated the absence of distinct peaks for ascorbic acid (AA). Consequently, a more precise evaluation of the sensing performance was conducted using differential pulse voltammetry (DPV). This method allowed for a more refined assessment of the sensor performance, which was otherwise limited by the CV experiment.

The performance of the Mn-MRG nanocomposite-based electrodes was evaluated using CV, differential pulse voltammetry (DPV) techniques. DPV is a widely utilized electrochemical sensing method, employing square pulses during a linear potential sweep. The efficacy of DPV in achieving high sensitivity lies in its ability to "filter" non-Faradaic current through the sampling of current before and after each pulse. Firstly, a DPV response study was carried out using Mn-MRG solely with ascorbic acid to identify the most effective concentration of AA that generates the peak current. As illustrated in Fig. 5.14, the DPV response revealed that a concentration of 30 µM AA results in the highest current. Therefore, this concentration was maintained for all subsequent experiments. Additionally, the Mn-MRG was observed to have a limit of detection (LoD) of 5.69 µM for ascorbic acid.

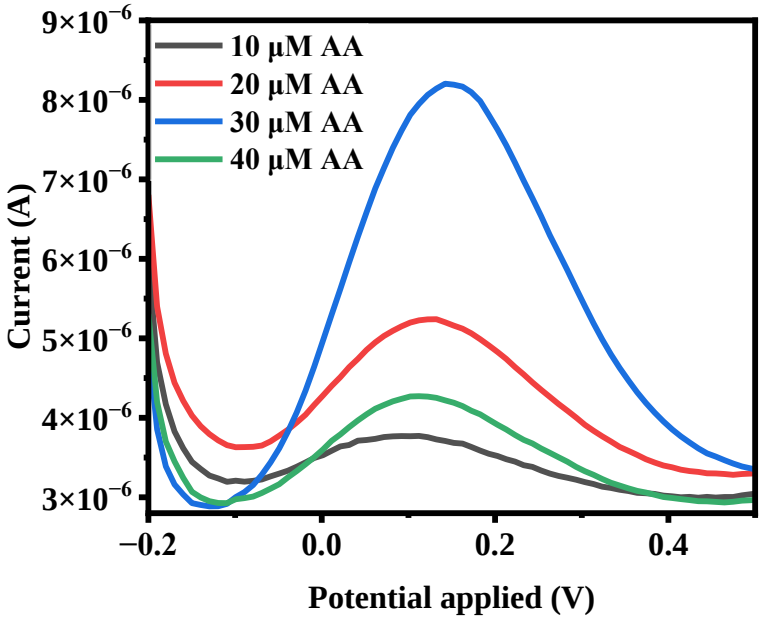

Fig. 5.14 Mn-MRG DPV for various concentration of AA.

A comparative DPV response for 30 µM AA and 500µM UA in 0.1M PBS is shown in Fig. 5.15(a). The graph provides a clear and detailed visual representation of the response current obtained from each sample.

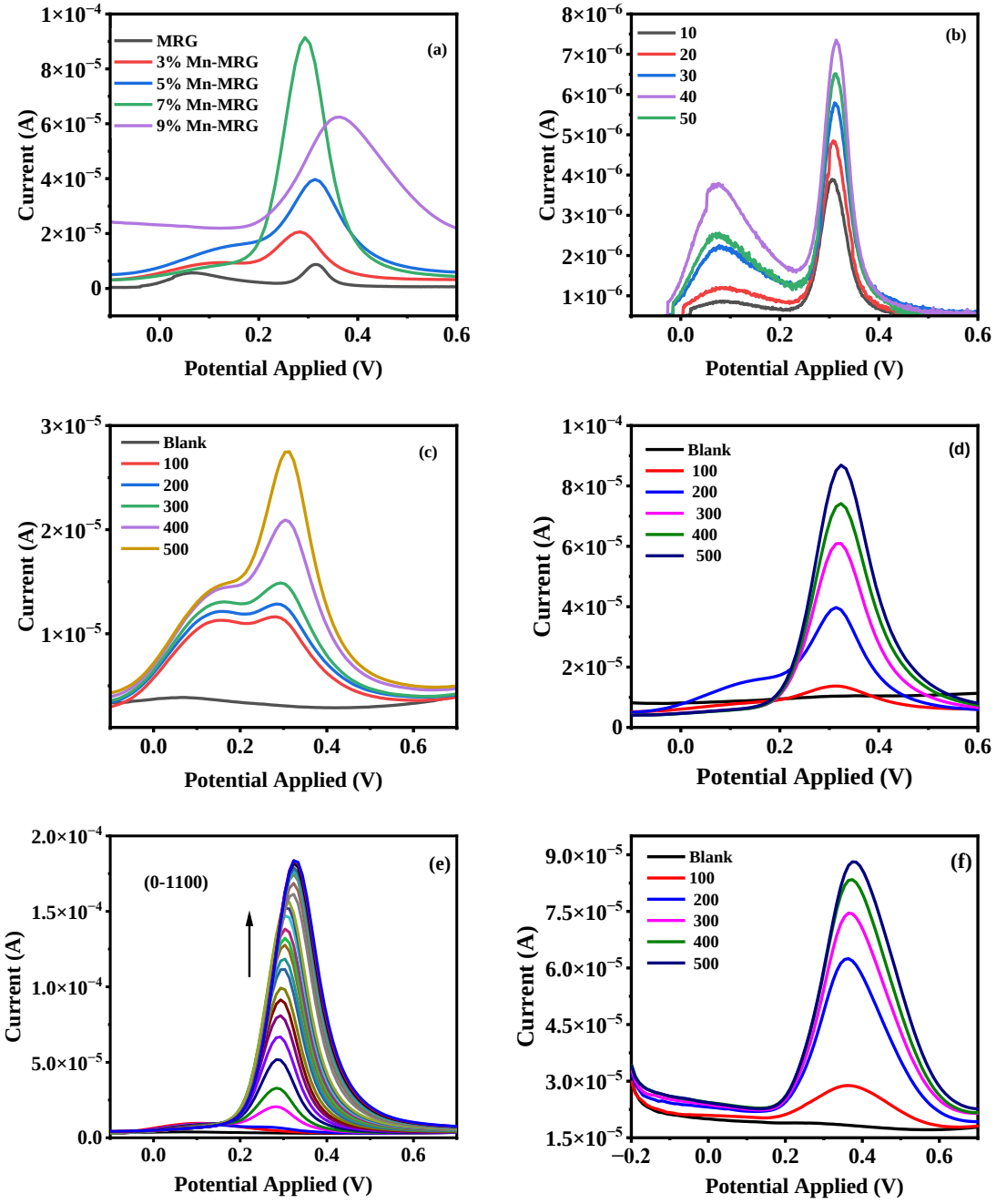

Fig. 5.15 (a) the DPV curves of bare GCE, MRG, and MRG nanocomposites with various compositions of Mn at a specific concentration of AA and UA; (b) the DPV data for MRG, 3% Mn-MRG, 5% Mn-MRG, 7% Mn-MRG and 9% Mn-MRG shows different concentrations of UA ranging from 0 µM to 330 µM, 0 µM to 500 µM, 0 µM to 500 µM, 0 µM to 1100 µM and 0 µM to 500 µM respectively in the solution having 30 µM AA in a PBS solution with a pH of 7.

It is evident from the graph that the 7% Mn-MRG sample demonstrates the highest response current when compared to other samples tested. In the case of undoped MRG, it was noted that the addition of uric acid to the buffer solution in the solution having ascorbic acid resulted in the appearance of two distinct peaks as shown in Fig. 5.15(b). However, with the gradual increase in the concentration of uric acid, there was a concurrent rise in the peak current of ascorbic acid, thereby impacting the sensitivity and selectivity of the sensor. To address this issue, Mn doping is introduced into the composite material. DPV data for MRG and its various Mn-doped variants (3%, 5%, 7%, and 9% Mn-MRG) are depicted in Fig. 5.15(b-f). The dataset encompasses a range of linear concentrations of UA in the solution having 30 µM AA within a pH 7 PBS solution. The purpose of Mn doping is to modify the material's properties in such a way that it enhances the differentiation between AA and UA. As the percentage of Mn doping increases from 3% to 7%, the peak current corresponding to AA decreases, while the peak current for UA rises. This pattern suggests that the introduction of Mn doping is altering the material's response to the analytes, making it more sensitive towards UA over AA. This finding suggests that the 7% Mn-MRG sample has a higher sensitivity towards the analytes as compared to other samples. Observing the DPV data in Fig. 5.15(e), an increase in the concentration of UA from 0 µM to 500 µM induces a shift in the DPV peak towards more positive values. Further increases to 1100 µM result in an almost 45 mV shift. These shifts are generally attributed to a diminished diffusion coefficient, necessitating a more positive potential to overcome the kinetic barrier as concentration increases. Higher concentrations may also induce peak shifts due to surface fouling from by-products of UA oxidation. At 9% Mn-MRG, the absence of a peak for AA indeed reinforces the idea that the material has become highly selective and sensitive for sensing UA only as illustrated in Fig. 5.15(f). In contrast, when the concentration of AA was varied while maintaining a constant UA concentration, it was observed (See Fig. 5.16) that there was no discernible peak separation. This suggests that Mn-MRG exhibits selectivity towards UA as opposed to AA. This makes Mn-MRG a promising candidate for the selective detection and quantification of UA in the solution having AA. Additionally, the concentration versus the current plot for 3%, 5%, 7%, and 9% Mn-MRG is depicted in Fig. 5.17(a-d). Observing Fig. 5.17(a, b), it's apparent that initially, there exists only a single linear region for 3% and 5% Mn-MRG. However, as the doping concentration progresses towards 7% Mn-MRG, the plot exhibits two distinct linear regions shown in Fig. 10(c). The existence of Mn needles within the MRG could align between the layers of the composites and on the upper layer, resulting in the observation of two distinct dynamic regions

in the calibration curve [152]. In the first linear region spanning from 30 to 210 µM, characterized by low concentrations of UA, physisorption predominates.

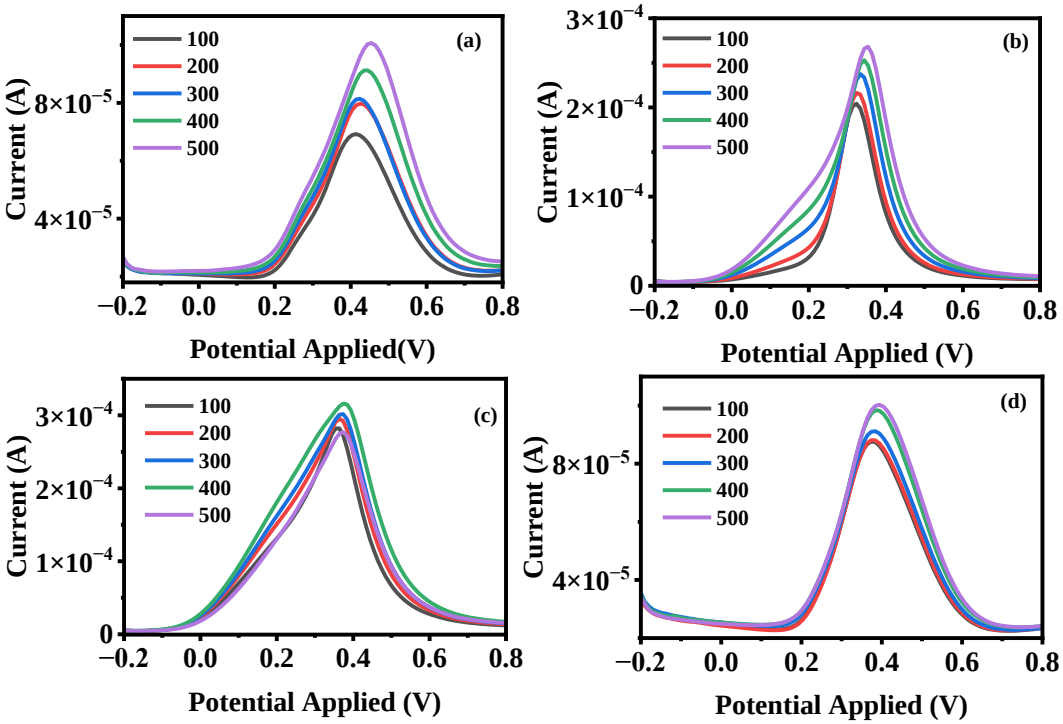

Fig. 5.16 DPV curves of (a) 3% Mn-MRG, (b) 5% Mn-MRG, (c) 7% Mn-MRG and (d) 9% Mn-MRG with a varying concentration of AA at 500 µM UA.

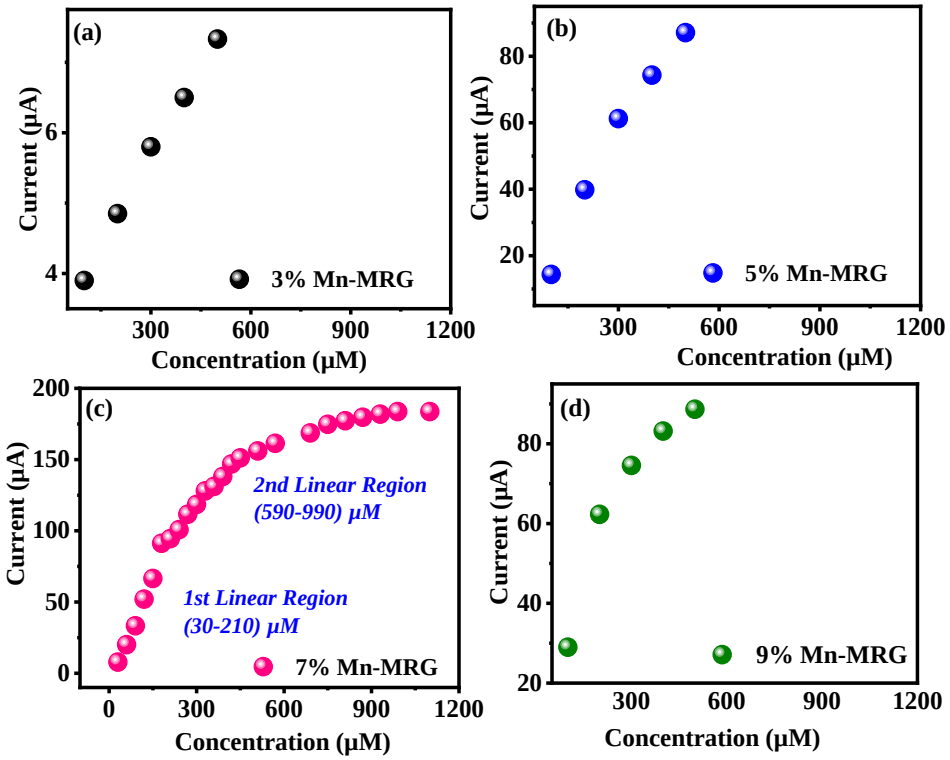

Fig. 5.17(a) Concentration vs current plot for 3% Mn-MRG, (b) 5% mn-MRG, (c) 7% Mn-MRG and (d) 9% Mn-MRG.

This process entails the analyte's interaction primarily occurring at the composite surface, leading to the oxidation of both UA and AA. In the second linear region, ranging from 590 to 990 µM where UA concentrations are notably high, chemisorption becomes prominent. Here, the analyte establishes chemical bonds at the composite surface, resulting in the oxidation of UA exclusively. Fig. 5.17(d) indicates that the 9% Mn-MRG composite also displays a linear region, attributed to the chemical interaction of UA at the surface of Mn-MRG, leading to the oxidation of UA alone. In Fig. 5.18(a-f), the logarithmic change in current concerning the concentration of UA is depicted alongside maintaining the concentration of AA at 30 µM.

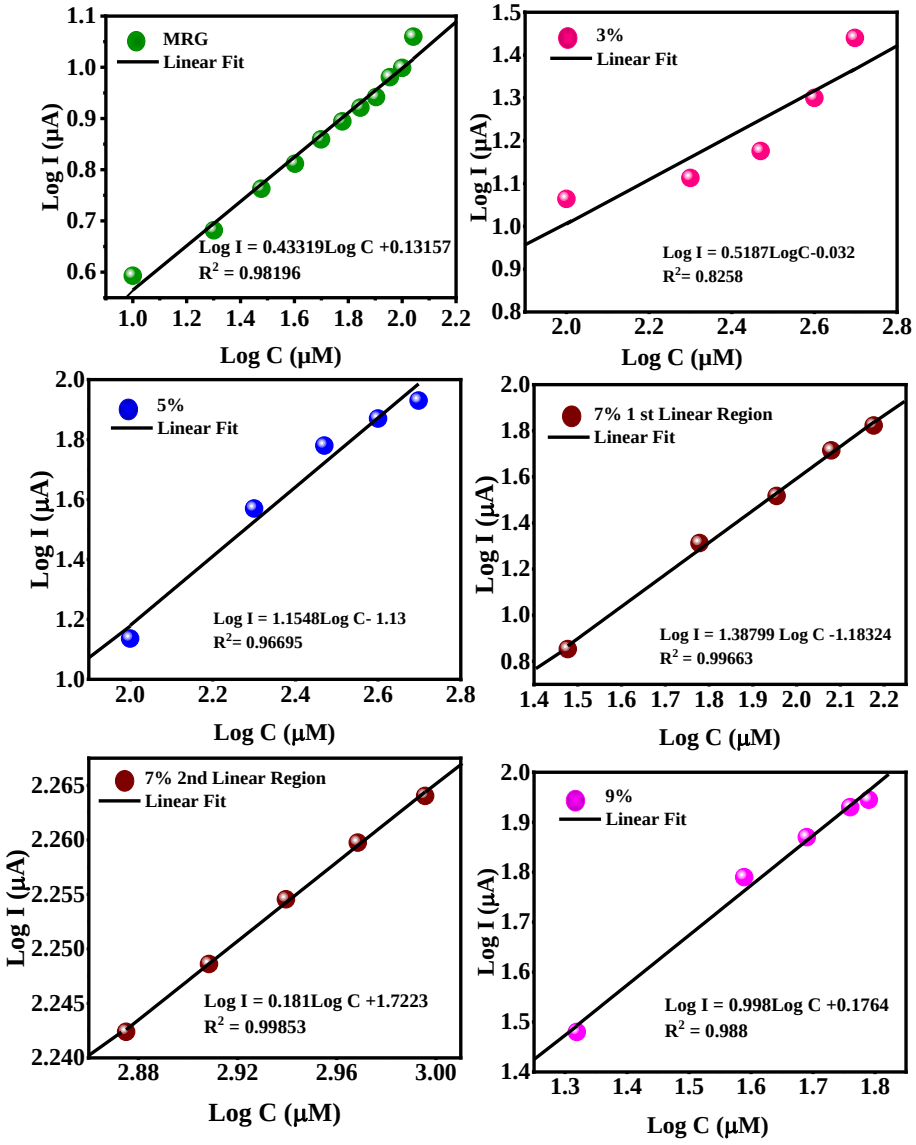

Fig. 5.18(a) the logarithmic variation of current with the concentration of UA in the solution having 30 µM AA and the fitted line with linear regression equation for MRG, 3% Mn-MRG, 5% Mn-MRG, 7% Mn- MRG and 9% Mn-MRG.

The graph includes fitted lines using linear regression equations for MRG, 3%, 5%, 7%(1st &2nd region), and 9% Mn-MRG. Notably, the oxidation peak currents of UA exhibit an increase with concentration, showcasing an LoD of approximately 1911, 670, 80, 379, and 270 nM for, 3%, 5%, 7% (1st linear region), 7% (2nd linear region), and 9% Mn-MRG respectively. The 7% Mn-MRG composition exhibits the lowest LoD, indicating the highest sensitivity among the tested compositions. Specifically, the 7% Mn-MRG exhibits two distinct linear regions, each with its own LoD value, indicating different sensitivities within the same composite material. This suggests that the concentration and composition of Mn-MRG play a significant role in determining the sensitivity and effectiveness of the detection method for UA. As compared to 7% Mn-MRG, the LoD for undoped MRG is significantly higher, around 911 nM. This substantial enhancement in the detection limit aligns with the improved charge transfer resistance of 7% Mn-MRG in comparison to the other samples. Further, the sensitivities observed for MRG, 3%, 5%,7% (1^{st} region), 7% (2^{nd} region), and 9% Mn-MRG are determined to be 148, 80, 143, 258, 33, and 232 nA M^{-1} cm^{-2} respectively. The Mn-MRG with a 7% concentration in the first linear region has shown a remarkably high sensitivity when compared to other compositions. This could be attributed to the involvement of Mn, which may act as a catalyst or participate in redox reactions, thereby increasing the signal produced during UA oxidation. An interesting observation can be made from the DPV responses presented in Fig. 5.15(b-f) and Fig. 5.20(a). The information has been plotted as a bar graph to analyze the effects of Mn doping as shown in Fig. 5.19(a). It compares the peak currents of 30 µM AA in the absence of UA with 30 µM AA in the solution having 500 µM UA for each composite.

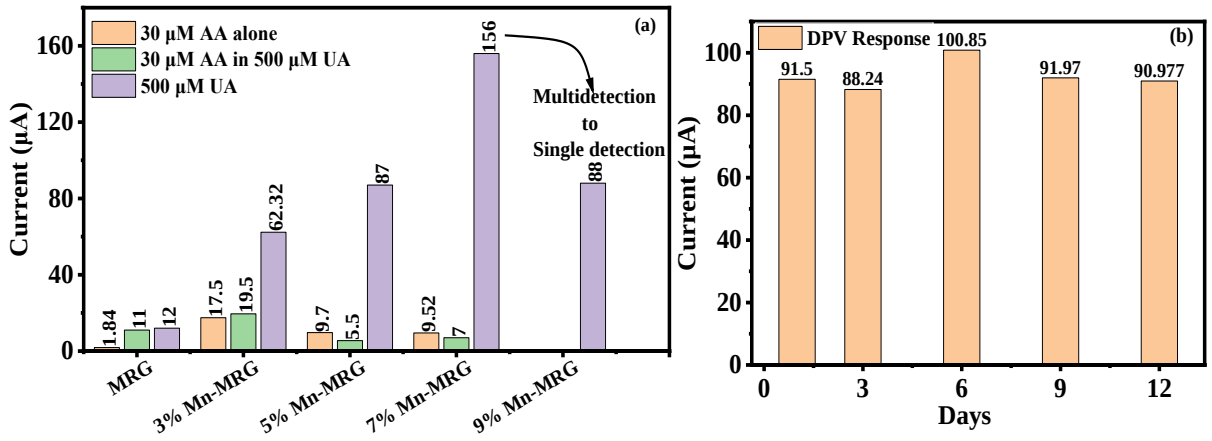

Fig. 5.19(a) Bar graph depicting the enhancement of selectivity through Mn doping in MRG, transitioning from multi-detection selectivity to single-detection selectivity (b) Bar graph showing the stability of the 7% Mn-MRG sensor.

This comparison demonstrates that 7% Mn-MRG has a more significant response to UA compared to AA. This heightened response suggests the favorable adsorption of UA on the surface of 7% Mn-MRG over AA under the same conditions. No peak for AA oxidation is detected in 9% Mn-MRG, indicating that doping MRG with 9% Mn shifts the sensor's functionality from multi-detection to single detection and indicates that this sensor is solely designed for UA detection. This selective behavior can be attributed to the existence of Mn in the system, which inhibits the oxidation of AA as shown in Fig. 5.20. Fig. 5.20(a) and (b) display DPV and CV curves of 3%, 5%, 7%, and 9% Mn-MRG respectively in the solution having 30 µM AA in PBS at pH7.

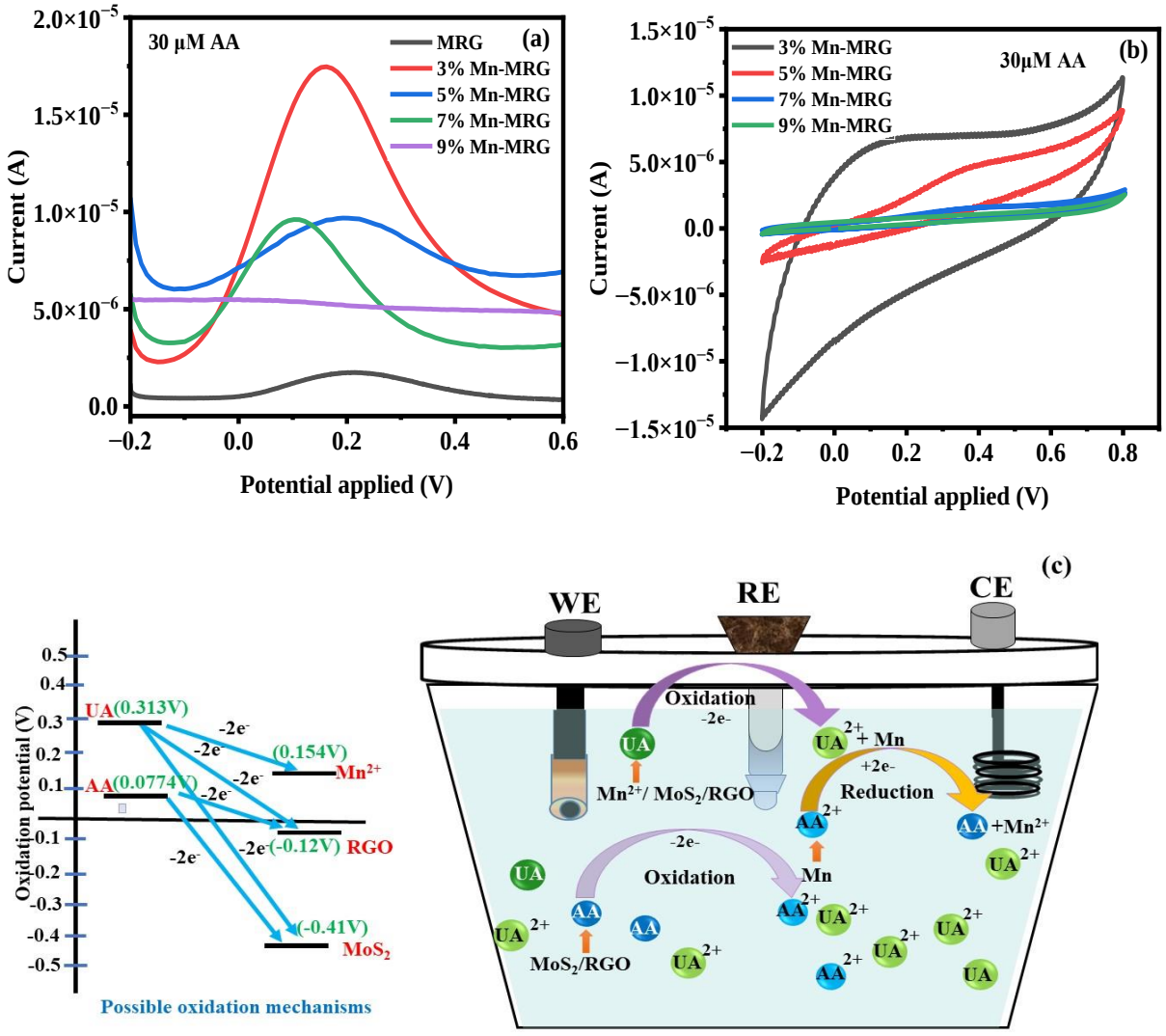

Fig. 5.20(a) DPV curve of AA detection by different doping concentrations of Mn in MRG (b) CV curves of AA detection by different doping concentrations of Mn in MRG (c) an oxidation plot with proposed with sensing mechanism.

This study is exclusively done to see the interaction of Mn with AA. The chemistry of ascorbic acid is complicated; it usually reduces an electron by one to generate the comparatively inert ascorbate radical. Its oxidized form, dehydroascorbic acid (DHA), is essential to comprehending its oxidation processes. A disproportionation process involving two ascorbate radicals can produce DHA, the completely oxidized form of ascorbic acid, as can the two-electron oxidation of ascorbic acid and the one-electron oxidation of the ascorbate radical. Using pulse radiolysis, Bielski et al.'s study found that two ascorbate radicals can unite to create an unidentified dimer in the solution having protons. This dimer then proceeds through disproportionation, resulting in fully oxidized DHA and reduced ascorbic acid. In Mn-MRG Mn, an increase in Mn doping is influencing the surface interactions of MRG with both AA and UA. Mn doping enhances adsorption controlled process and facilitates the chemical interaction with UA, leading to its selective detection. Mn ions on the surface of the electrode are acting as a proton donor for ascorbate free radical forming an unidentified dimer, resulting in decreased AA sensitivity as Mn doping rises. The same information can be extracted from the CV curve shown in Fig. 5.20(b). In order to gain a deeper understanding of this mechanism, it is imperative that we take into account the significance of oxidation potential in the oxidation and reduction of analytes. Fig. 5.20(c), provides information regarding the oxidation potential of AA, UA, Mn ions, RGO, and MoS_2. Specifically, AA has an average oxidation potential of +0.0774 V, while UA has an oxidation potential of +0.313 V can be seen from the DPV curve shown in Fig 10. Mn ions have a redox potential of +0.154 V [298], while RGO and MoS_2 have oxidation potentials of -0.12 V [299] and -0.41 V [300], respectively. After analyzing Fig. 5.20(c), it becomes clear that UA can undergo oxidation through three possible pathways. The first pathway is via Mn ions, the second pathway is via RGO, and the third pathway is via MoS_2. On the other hand, AA can undergo oxidation through two pathways only, either via MoS_2 or RGO. It is worth noting that both MoS_2 and RGO contribute to the oxidation of both UA and AA. However, Manganese behaves differently. It acts as an oxidizing agent for UA and a reducing agent for AA. Furthermore, as the doping level increases, Mn accelerates its role as a redox agent, simultaneously contributing to the oxidation of UA and the reduction of AA. Additionally in Fig. 5.20(c), a fascinating phenomenon is explained where undoped MRG exhibits a concurrent increase in current when UA is added to a buffer solution that has a constant concentration of AA as shown in DPV Fig. 5.15(b). This occurs because both RGO and MoS_2 act as oxidizing agents for both UA and AA due to their negative oxidation potential. As a result, each time UA is added, the peak current of ascorbic acid is enhanced. However,

when MRG is doped with Mn, the process changes, making the composite highly selective and sensitive. With the introduction of Mn, UA is oxidized, and AA is reduced, leading to a shift in the sensing mechanism. At 9% doping of Mn, the composite switches from multidetection sensing to single detection sensing as all dehydro-ascorbic acid ions are converted to AA. Beyond sensitivity and selectivity, the Mn-MRG sensor demonstrates environmental stability in the air. The DPV response (see Fig. 5.21) of the 7% Mn-MRG sensor to 240 µM UA is recorded approximately every 3 days. A bar graph is plotted for the observed data (refer to Fig. 5.19(b)). After 12 days, only a 1% degradation in the peak current is observed, indicating commendable ambient stability, reproducibility and repeatability. The minimal degradation in performance over time implies that the sensor can reliably and consistently detect UA in real-world scenarios.UA and AA typically coexist in the human body and share nearly identical redox potentials. Consequently, simultaneous detection is of significant interest to researchers and holds paramount importance compared to individual detection. Over the past few years, numerous materials have been developed by researchers to achieve this objective, as outlined in Table 5.1. Table 5.1. provides an overview of the latest electrochemical biosensors for the detection of uric acid using MoS_2-based nanocomposites. "Sun et al. modified an electrode with AuNPs@MoS_2 nanocomposite film and used it to create an ultrasensitive biosensor for AA, DA, and UA detection. AuNPs@MoS_2/GCE demonstrates efficient electrocatalytic oxidation towards AA, DA, and UA, allowing them to be determined concurrently. The fabricated AuNPs/MoS_2 sensor exhibited a LOD of 10 µM, and a detection range from 10 to 7000 µM [240]. In the present work, we have achieved 80 nM LOD using 7% Mn-MRG which is comparatively very low. Ma et al. specified PtNi NPs adorned MoS_2 for UA identification, with PtNi@MoS_2 formed through a co-reduction process.

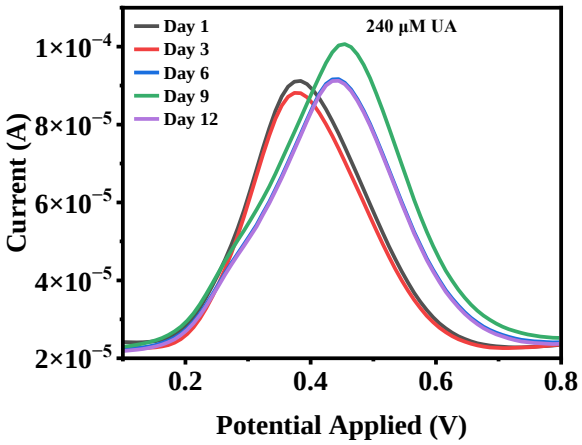

Fig. 5.21 DPV response for 7% Mn-MRG for every 3 days.

Table 5.1 MoS_2 based detection of UA in the solution having AA.

Reference	Nanocomposite	LOD (μM)	Sensitivity (μA μM^{-1} cm^{-2})	Detection Range
[240]	AuNPs/MoS_2	10	-	10-7000 μM
[265]	MoS_2-PEDOT/GCE	0.95	-	2-25 μM
[249]	MoS_2/ rGO modified GCE	0.46	1.59 μA μM^{-1} cm^{-2}	25–2745 μM
[238]	AuNPs/MoS_2-NSs	0.5	-	5-260 μM
[303]	MoS_2-catalyzed TMB-H_2O_2	0.3	-	0.5-100 μM
[86]	MoS_2 on aluminium foil	1.169	98.3 nA μM^{-1}	10–400 μM
[301]	PtNi NPs -MoS_2	0.1 μM	-	0.5–1800 μM
[302]	Au NPs–MoS_2	0.0182	-	0.033–10.0 μM
[304]	Ppy-α-Fe_2O_3-MoS_2	0.061	1.26 μA μM^{-1} cm^{-2}	300 nM-1 mM
[10] Present work	7% Mn-MRG/GCE	80 nM	258 nA $\mu M^{-1}cm^{-2}$	30 μM-1.1Mm

The designed sensor demonstrated a sensitivity of 7.6 nA μM^{-1} (R^2 = 0.9876) in the detection span of 0.5-1800 μM UA, with good repeatability, stability, and selectivity [301]. The sensitivity achieved in the present work is 258 nA $\mu M^{-1}cm^{-2}$ which is significantly high as compared to the work reported. In comparison with other nanocomposites outlined in Table 5.1, the 7% Mn-MRG nanocomposite possesses the potential to serve as a promising candidate for the detection of UA in the solution having AA, owing to its ultra-high sensitivity and low detection limit. Notably, this nanocomposite is also cost-effective, thus offering an efficient solution for the detection of UA in such conditions.

5.6 Conclusion:

This study presents the successful development of an electrochemical sensor employing the Mn-MRG nanocomposite for the selective detection of uric acid. Utilizing various characterization techniques, including scanning electron microscopy and electrochemical analysis revealed the formation of Mn nanoneedles encapsulating MoS_2 and RGO nanosheets, resulting in a high surface area conducive to efficient sensing. Comparative analysis with existing uric acid sensors highlights the superior performance of the 7% Mn-MRG sensor,

exhibiting a lower detection limit (0.08 µM) and a broad linear range (0-1100 µM). The transition observed from multi-detection to single-detection sensing between 7% and 9% Mn doping levels suggests the influence of Mn needles' interaction with the analyte, promoting a redox mechanism within the composite. This phenomenon arises due to Mn doping acting as both an oxidizing agent for uric acid and a reducing agent for interfering species like ascorbic acid (AA). At 9% Mn doping, complete elimination of AA interference is achieved, enabling the sensor's switch from multi-detection to single-detection sensing mode. Rigorous assessments of stability and reproducibility underscore the highly favorable characteristics of the developed sensor.

Chapter 6

Resorcinol Sensing with Co-Doped MoS_2/RGO Nanocomposite: Unveiling Nano-Detection

Resorcinol, chemically known as 1,3-dihydroxybenzene with CAS Registry Number 108-46-3, fulfills several roles across various industries. Resorcinol finds extensive use in the manufacturing of rubber-based compounds, including tires, as it acts as a crosslinking agent for rubber. Furthermore, it is employed in photography, using it as a developer in black and white photographic film and paper. In the leather industry, resorcinol is used as a tanning agent for leather processing. Apart from its industrial applications, resorcinol is also utilized in cosmetics and personalized products, such as hair dyes, scalp treatments, and skin-lightening products [305]. It is used in these products due to its ability to penetrate the skin and hair and its effectiveness in treating various skin conditions such as acne, psoriasis, and eczema. Currently, resorcinol is predominantly used as a peeling agent to treat acne vulgaris; however, its original use was treating leg ulcers [306]. Literature provides us with several instances of systemic toxicity caused by percutaneous absorption [307], which can lead to dire consequences [308]. Resorcinol intoxication can cause various signs and symptoms, such as dizziness, cold sweats, collapse, tremors, methemoglobinemia, pallor, hemolytic anemia, hemoglobinuria, violet-black urine, maculopapular eruptions, and hypothyroidism. Recognizing these symptoms is crucial for prompt identification and treatment of the condition [309]. Therefore, a quick detection of resorcinol is very important. A range of analytical methods has recently been utilized for determining resorcinol. These methods encompass flow injection chemiluminescence, surface plasmon resonance, quartz crystal microbalance, spectrophotometric, fluorescence [310], spectrometry spectrofluorimetric methods, and gas chromatography/mass all extensively documented in the literature [311]. These methodologies require prior treatment procedures for samples, involving extraction, adsorption, and separation, rendering them both expensive and time-intensive. In addition, the chemiluminescence signal does not currently allow for the identification of adverse effects of RS [312]. Electrochemical techniques, renowned for their exceptional sensitivity, accuracy, effectiveness, minimal upkeep expenses, ease of handling, broad linear analysis range, adaptability, and simplicity, have garnered significant attention in research [313]. Moreover, their reproducibility, suitability for analyzing low quantities of analytes, time efficiency, and

stability further highlight their advantages. To ensure accurate detection, the standard electrode should be modified with potent nanomaterials, thereby validating its efficacy [314]. Various nanoparticles find widespread use due to their advanced catalytic properties, distinct morphologies, and applications in opto-electrochemical sensing platforms. In current times, there has been considerable interest in two-dimensional (2D) materials, including carbon compounds, phosphides, halogens, oxyhalides, chalcogenides, nitrides, and stratified silicate materials, because of their outstanding optoelectronic and physiochemical characteristics. TMDs have appeared as noteworthy 2D-layered materials with extremely thin characteristics [315]. The properties of TMDs, specifically MoS_2, are greatly influenced by factors like the stacking sequences, level of crystallinity, and number of layers within their crystal structure [92]. MoS_2, in particular, has garnered significant interest from the scientific community because of its remarkable optical attributes, distinct crystal structure, and electrical characteristics [242]. The Mo atoms layers are ordered in a hexagonal pattern, wedged between layers of sulfur (S) [243]. The Mo-S bonds are covalently strong, whereas van der Waals interactions take place between the S layers. MoS_2 currently holds a distinctive position, and MoS_2-modified electrodes show considerable potential for the development of electrochemical sensing devices of the future generation. Whereas pristine MoS_2's electrochemical performance is hindered by its low electrical conductivity [304]. To address this, researchers have explored metal doping as a method to perk up the properties of metal oxides and sulfides. Metal doping facilitates charge transfer between the dopant metal and the host material, manipulating the electronic environment to lower resistance in charge transfer and improve efficiency [316]. Cobalt, being an efficient transition metal, is particularly effective for improving the redox reversibility of electrode materials. MoS_2 electrodes' electrical conductivity is further improved by cobalt doping. Recent research has revealed that altering MoS_2 with carbon can affect its electronic characteristics, whether by heteroatom doping, defect creation, or composite production. These carbon materials, with their huge specific surface area, are well suited to electrochemical sensing applications, either by providing structural support or improving electron transport. In the following chapter, we present the development of a Co-doped MoS_2/RGO nanomaterial using a microwave-assisted synthesis method, which demonstrates remarkable sensitivity and selectivity in comparison to pristine MoS_2 and MoS_2/RGO. The enhanced electrochemical characteristics of the Co-doped MoS_2/RGO electrode likely stem from the combined faradic and non-faradic processes of the MoS_2 layers in conjunction with Cobalt and the highly conducting reduced GO layers.

6.1 Structural studies

The XRD structures depicted in Fig. 6.1(a-c) were captured for MoS_2, MoS_2/RGO, and Co-doped MoS_2/RGO nanostructures, spanning a 2θ range from 10 to 70 degrees. This analysis aimed to confirm the synthesis of MoS_2, MoS_2/RGO, and Co-MoS_2/RGO nanocomposite. In Fig. 6.1(a) the XRD data illustrates the existence of the 2H phase of MoS_2, evidenced by diffraction peaks occurring at 13.13º, 32.57º, 39.53º, and 58.46º corresponding to (002), (100), (103), and (110) respectively (according to PDF 37-1492). A diffraction peak at 22.7º, referring to the (002) plane, confirms the existence of RGO in MoS_2/RGO (refer Fig. 6.1(b)). Fig. 6.1(c) displays the XRD pattern of Co-MoS_2/RGO. The peak broadening can be observed in the (002) plane of 2H MoS_2 in Co-MoS_2/RGO. This is indicative of a few layered composites from multilayered. Further, the existence of amorphous carbon in the Co-MoS_2/RGO composite is suggested by the peak widening in the RGO's (002) peak. The cobalt-containing species identified are as follows: CoS_2 (JCPDS card No. 01-089-3056), $CoMoS_2$ (JCPDS card No. 00-016-0439), and $CoMoO_4$ (JCPDS card No. 00-021-0868) [248].

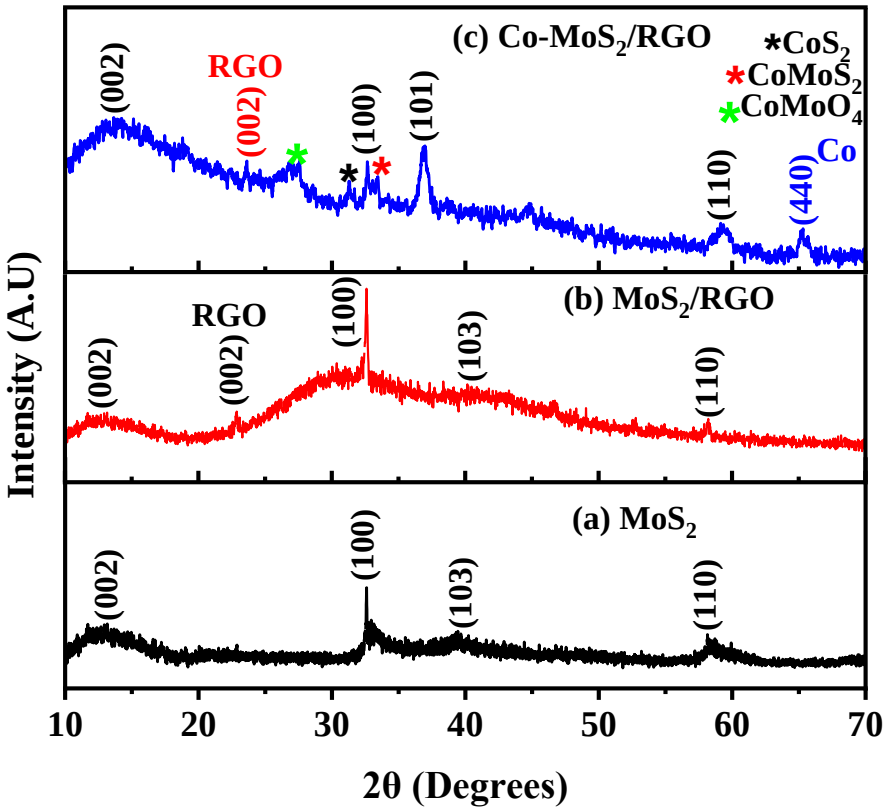

Fig. 6.1 The XRD patterns for MoS_2, MoS_2/RGO, Co-MoS_2/RGO.

The (006) plane, which first appears in MoS_2/RGO at 46.5º, further shifts to 44.7º in Co-MoS_2/RGO. This shift towards a lower angle implies a larger interplanar spacing in the composite, indicative of lattice strain induced by the bigger ionic radius of Co^{2+} (0.074 nm) compared to Mo^{4+} (0.065 nm). Furthermore, the diffraction peak at 65.45º corresponds to the (440) plane of Cobalt, thus confirming the doping of Co in the composite.

The Raman spectra recorded for MoS_2, MoS_2/RGO and Co-MoS_2/RGO are illustrated in Fig. 6.2(a-c). For MoS_2 and MoS_2/RGO, the peaks observed at 384 and 407 cm^{-1} align with the characteristic E^1_{2g} and A^1_g modes of the 2H MoS_2 nanocomposite [249]. Furthermore, the Raman peaks detected at 1388 (D-band) and 1596 (G-band) cm^{-1} for reduced graphene oxide confirm the existence and effective integration of RGO sheets within the MoS_2/RGO nanocomposite as shown in Fig. 6.2(b) [92]. In Fig. 6.2(c) the particulars peaks at 191, 283, and 384 cm^{-1} are associated with the longitudinal acoustic phonon modes (LA), E^1_g, and E^1_{2g}, modes of 2H-MoS_2. Additionally, a peak indicative of the 1T-phase of MoS_2 is detected at 333 cm^{-1}, suggesting that the synthesized Co-MoS_2/RGO composite comprises a combination of 2H and 1T phases of MoS_2 [248].

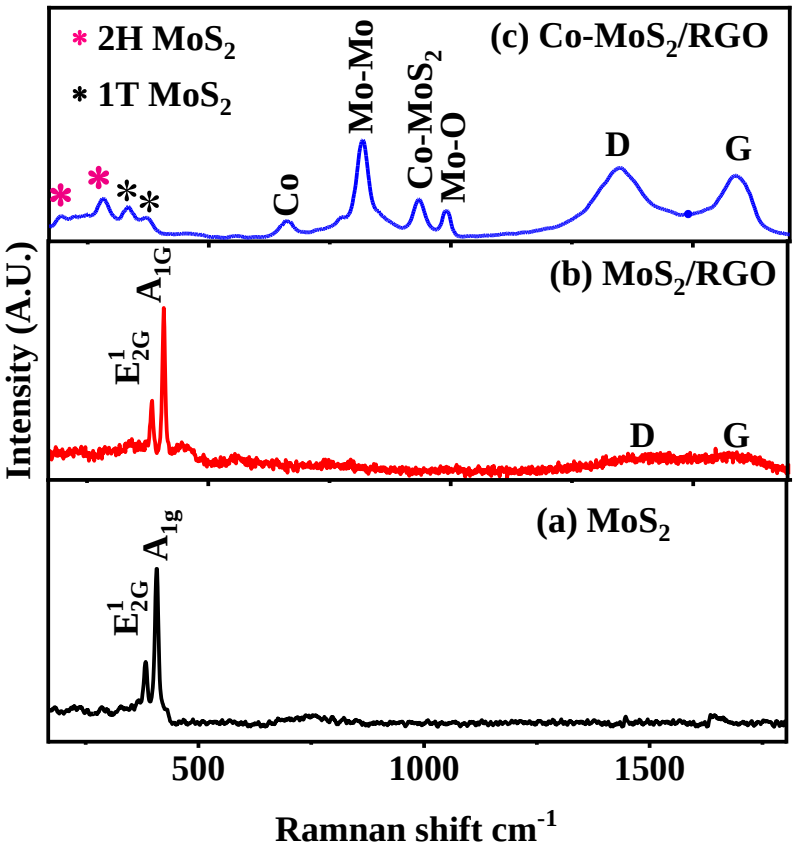

Fig. 6.2 Raman spectra of MoS_2, MoS_2/RGO, and Co-MoS_2/RGO.

Furthermore, two new peaks emerge at 669 and 932 cm^{-1} for Co-MoS_2/RGO nanostructures corresponding to the Co and Co-MoS_2 [250] vibrations. The 815 cm^{-1} peak is ascribed to the second harmonic resonance of a few layers exhibiting pure Mo-Mo bond interaction [251]. The observation of oxides, identified by the peak at 991 cm^{-1}, in the synthesized MoS_2 can be attributed to its partial oxidation during exposure to air. In Co-MoS_2/RGO, the D and G bands of RGO appear at 1345 cm^{-1} and 1587 cm^{-1}, accordingly, yielding an I_D/I_G ratio of 1.08. This ratio signifies the existence of structural defects, which could potentially augment the selectivity of the composite. Observations indicate that increased cobalt doping decreases the E^1_{2g} vibration mode while the A^1_g vibration mode diminishes. These changes are attributed to tensile strain within the matrix due to cobalt doping in the Mo site and the number of layers in MoS_2. The A^1_g and E^1_{2g} peaks exhibit a redshift, indicating that enhanced interlayer van der Waals force plays little part compared to stacking-induced structural defects or long-range Coulombic interlayer interactions within the layers of MoS_2.

6.2 Morphological and textural studies

The surface morphological structure of the synthesized materials was corroborated by the FESEM and HRTEM images. RGO appears slender and displays lamellar folds, as shown in Fig. 6.3(a). In contrast, aggregated and irregular spheres of pristine MoS_2 are observed in Fig. 6.3(b). This aggregation in pure MoS_2 might contribute to the material's reduced conductivity. Further, MoS_2/RGO possesses aggregated nanosheets as shown in Fig. 6.3(c). In Fig. 6.3(d-f) the FESEM images of Co-MoS_2/RGO are shown at different resolutions.

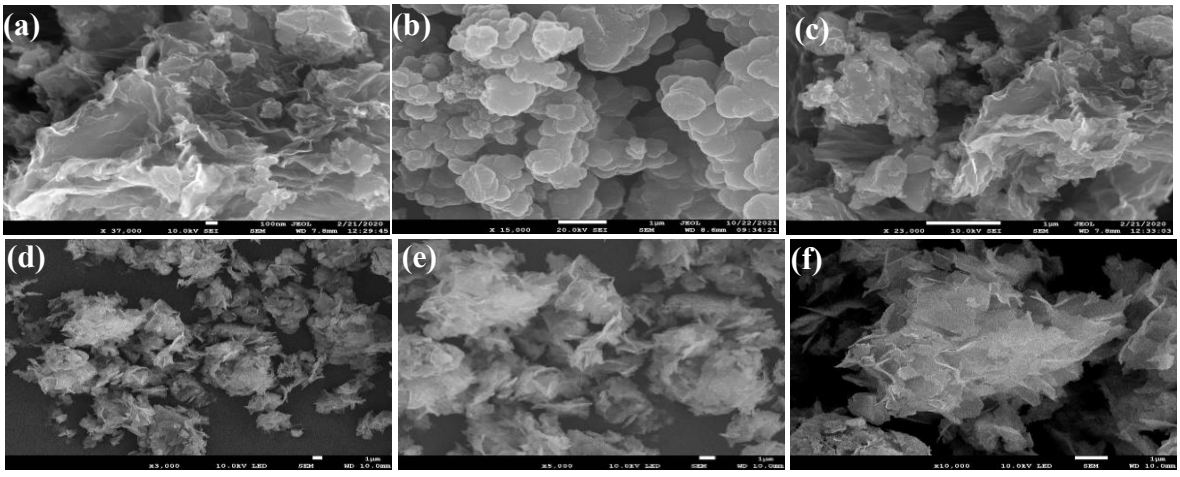

Fig. 6.3 FESEM (a) images of RGO (b) images of MoS_2, (c) images of MoS_2/RGO, (d-f) images of Co-MoS_2/RGO.

This integration likely alters the electronic properties without causing significant changes to the physical structure. The 3D nanosheets provide a large surface area and more active sites, probably may enhance the material's sensitivity and efficiency in detecting electrochemical signals. This structure may facilitate better electron transfer and improved interaction with analytes.

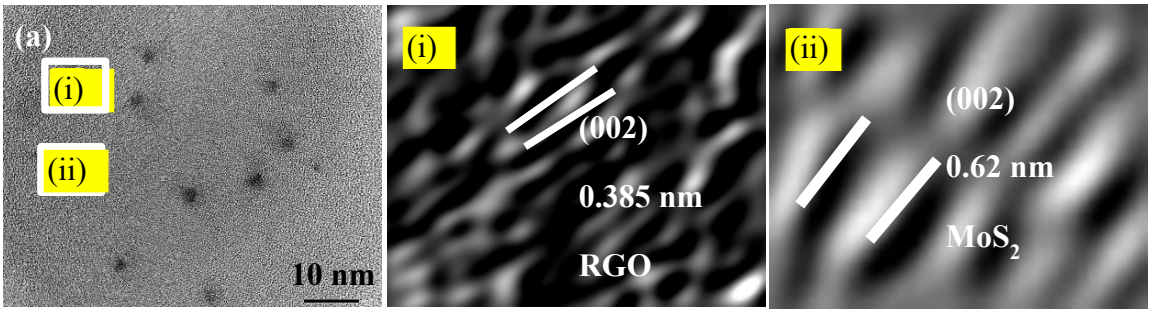

Fig. 6.4 HRTEM (a) images of Co-MoS_2/RGO composite and (a(i)) zoomed view of the marked area in (a) and (a(ii)) zoomed view of the marked area in (a).

Further, the HRTEM image of Co-MoS_2/RGO is shown in Fig. 6.4(a). Fig. 6.4(a) has two marked areas which are further magnified and marked as (i) and (ii). Fig. 6.4(a(i)) shows (002) plane corresponds to the well-stacked RGO sheets, with an interlayer distance of 0.385 nm. In Fig. 6.4(a(ii)) the calculated d-spacing is 0.62 nm which is in agreement with the XRD results and corresponds to the (002) plane of MoS_2 [253].

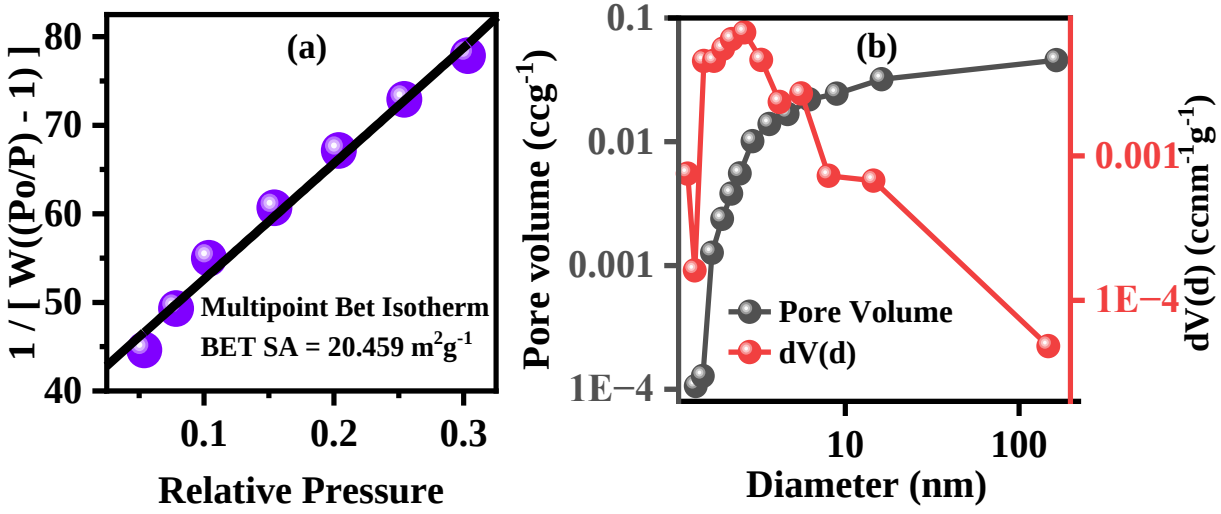

Fig. 6.5 BET results of Co-MoS_2/RGO (a) Multipoint BET N_2 adsorption-desorption isotherm and (b) BJH pore size distribution curve.

The surface area and the porosity of the Co-MoS_2/RGO 3D nanosheets were examined using BET analysis. The nanocomposite was degassed at 150 ºC and 10^{-6} Torr of vacuum for 12 hours before measurement. The multipoint surface area curve shown in Fig. 6.5(a) between relative pressure (P/Po) and 1/[W((P/Po) − 1)] is used to calculate the BET-specific surface area, where W is the quantity of N_2 gas adhered at a specific relative pressure, P^o is the saturation pressure, and P is the equilibrium pressure. The BET-specific surface area of Co-MoS_2-RGO is computed to be 20.459 m^2 g^{-1}, which is significantly higher than our reported specific surface area of bare MoS_2 and MoS_2/RGO which is 8.6 m^2 g^{-1} and 18.4 m^2g^{-1} respectively [92]. Further, the porosity of the material was calculated using the pore size distribution curve shown in Fig. 6.5(b). The BJH technique, which uses the Kelvin equation and DH techniques to compute the pore size distribution, was employed to calculate the pore volume data. The composite has pore diameters of 2.314 nm, making it microporous. The material has a pore volume of 0.067 cm^3. This implies that Co-MoS_2/RGO nanosheets have a high surface-to-volume ratio. This expanded surface area in relation to volume results in a larger number of active sites available for electrochemical reactions, thereby heightening the sensor's sensitivity to detect lower concentrations of analytes.

6.3 Compositional studies

The chemical states and bonding inside the Co-MoS_2/RGO composite material, including the oxidation states of the molybdenum, sulfur, carbon, oxygen, and cobalt are extensively analyzed based on the XPS data, as shown in Fig. 6.6(a). The Mo3d spectrum (see Fig. 6.6(b)) is discerned into two peaks at 229.88 and 233.07 eV, corresponding to Mo $3d_{5/2}$ and Mo $3d_{3/2}$, respectively, suggesting the molybdenum's oxidation state in the composite is Mo^{4+}. In addition, a peak at 227.3 eV in Fig. 6.6(b) is ascribed to the S2s of MoS_2. The S2p spectrum in Fig. 6.6(c) exhibited two peaks at 161.16 and 163.03 eV, accredited to the $S2p_{3/2}$ and $S2p_{1/2}$ of S^{2-} and S_2^{2-} species in the composites, revealing the unique chemical state of sulfur that is possibly related to MoS_2 [288]. The C1s spectrum is depicted in Fig. 6.6(d); two peaks can be seen at 284.6 and 288.4 eV, respectively, with binding energy values corresponding to the C-C and C=O functional groups. The existence of a peak at 531.03 eV, which is seen in O1s in Fig. 6.6(e), confirms the existence of RGO in the composite [255].

Further, in Fig. 6.6(f), the binding energy values of 776.8 and 800.54 eV correlate with the Co 2p core level spectra, Co $2p_{3/2}$, and Co $2p_{1/2}$ [257]. This suggests the successful doping of Cobalt in MoS_2/RGO nanocomposite.

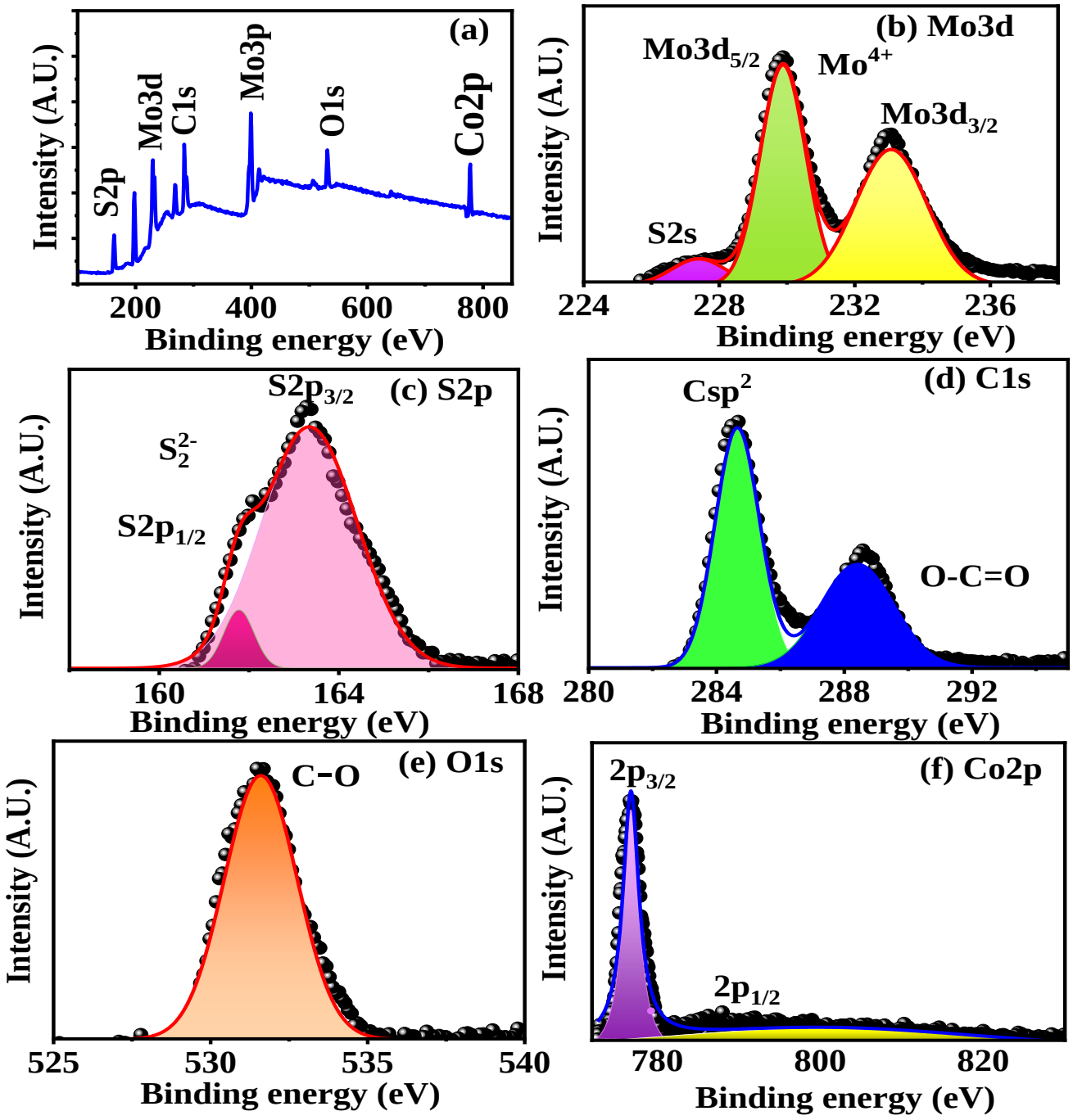

Fig. 6.6 XPS pattern of Co-MoS_2/RGO (a) full scan spectrum (b-f) high-resolution spectra of, (b) Mo3d, (c) S2p, (d) C1s, (e) O1s and (f) Co2p.

6.4 Electrochemical Studies

The electrochemical behavior of the MoS_2, MoS_2/RGO, and Co-MoS_2/RGO designed glassy carbon electrodes is depicted using the cyclic voltammetry (CV) data. Using CVs at different scan rates, the double-layer capacitance (C_{dL}) was measured to examine the combined effect of Cobalt and RGO doping on the electrochemical behavior of the MoS_2(refer to Fig. 6.7(a-c)). Phosphate-buffered saline (PBS) blank solution, pH 7, was used for these experiments. The oxidation peak current from multiscan CVs is used to determine the C_{dl} for each designed electrochemical sensor. In Fig. 6.7(d) the plot of the oxidation peak current showed a linear rise with the square root of the scan rate, and the slope of this relationship was linked to C_{dL}. The oxidation process at the surface of all three electrodes is governed by diffusion at different scan rates, as indicated by a direct proportional relationship between the oxidation peak current and the under root of the scan rate. The analysis indicates that the C_{dL} of the MoS_2 is significantly low, measured at 2.998 µF. MoS_2/RGO and Co-MoS_2/RGO significantly upsurged the C_{dL} to 5.5, and 26.3 µF, respectively.

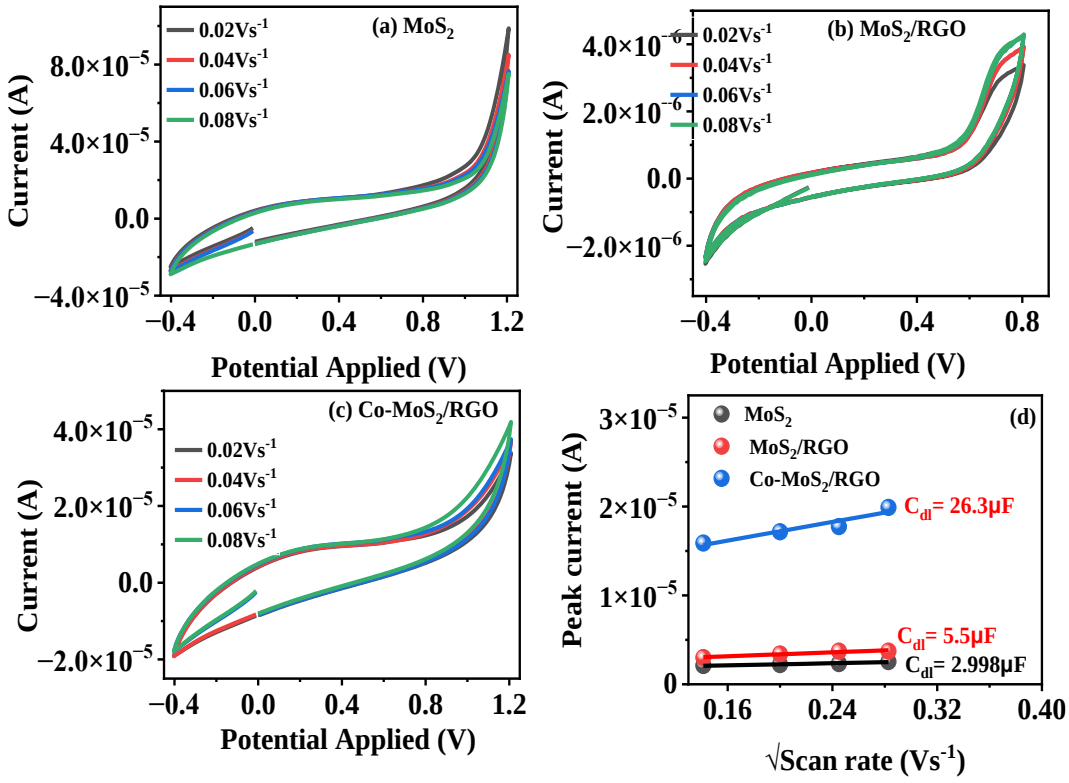

Fig. 6.7 Multiscan curves (a) MoS_2, (b) MoS_2/RGO and (c) Co-MoS_2/RGO. (d) oxidation peak current vs square root of scan rate plots for MoS_2, MoS_2/RGO and Co-MoS_2/RGO.

This suggests a substantial improvement in the material's ability to store electrical charge, likely due to the combined effects of Co-doping and the presence of RGO, which together improve the electrical conductivity and structural integrity of the Co-MoS_2/RGO. As we know C_{dl} is directly proportional to the electroactive surface area (ECSA) of the electrode. ECSA is calculated by dividing the double-layer capacitance of the electrode by the theoretical value of the areal capacitance of the material. As per the literature, the areal capacitance of MoS_2 is 1.35 μFcm^{-2} [318]. Thus, ECSA for MoS_2, MoS_2/RGO, and Co-MoS_2/RGO is calculated as 2.22cm^2, 4.07cm^2, and 19.48cm^2 respectively. The ECSA of MoS_2/RGO and Co-MoS_2/RGO is approximately two times and ten times respectively larger than that of undoped MoS_2. This significant increase in ECSA in Co-MoS_2/RGO is due to the open flower-like 3D nanosheets of the composites, which increases the active surface area and conductivity of the Co-MoS_2/RGO. These findings highlight that Co and RGO doping is an excellent strategy for electrode modification, causing a considerable increase in the active surface area and promoting high electroactivity.

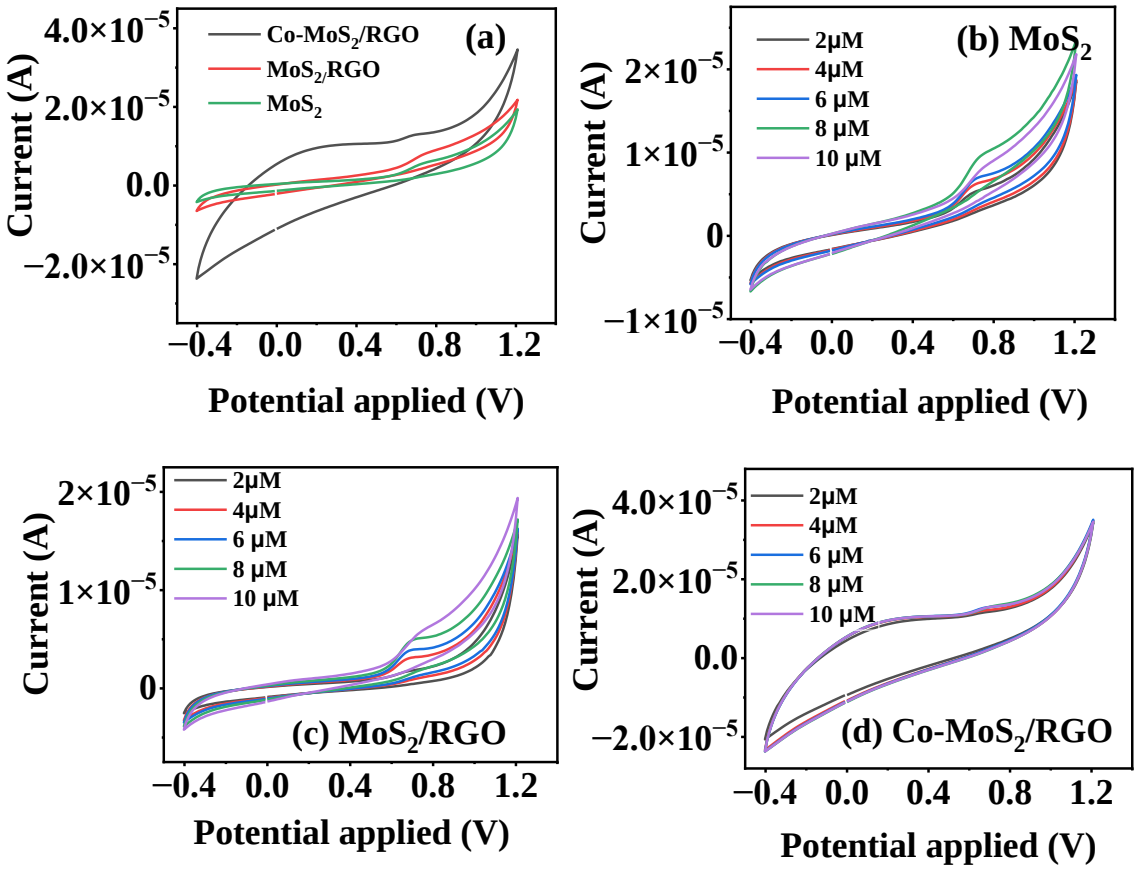

Fig. 6.8(a) The CV curves of MoS_2, MoS_2/RGO and Co-MoS_2/RGO nanocomposites at a specific concentration RS; the CV data for (b) MoS_2, (c) MoS_2/RGO, and (d) Co-MoS_2/RGO shows different concentrations of RS.

After examining the electrochemical behavior of MoS_2, MoS_2/RGO, and Co-MoS_2/RGO in a blank buffer solution, the electrochemical behavior of all three fabricated sensors was further studied in the solution having RS. Fig. 6.8(a) presents the CV of MoS_2, MoS_2/RGO and Co-MoS_2/RGO in 0.1 M PBS at a scan rate of 60 mV/s. The anodic peak potential (E_{pa}) for the pristine MoS_2 is estimated as 0.725 V. Upon subsequent modifications with Co and RGO, the E_{pa} shifts negatively to 0.694 V. This significant negative shift in E_{pa} suggests the enhanced electrocatalytic activity on the surface of the electrode by incorporation of Co in MoS_2/RGO. However, the anodic peak current (I_{pa}) for the Co-MoS_2/RGO is notably higher at 13.2 µA, representing a 2.1-fold increase compared to the pristine MoS_2 (6.2 µA) and a 1.6-fold increase compared to the MoS_2/RGO (8.17 µA). This suggests that Co-MoS_2/RGO impregnation enhances the electrical conductivity of the sensor. Furthermore, in addition to the well-defined redox peaks, the non-redox/pseudocapacitive currents in the Co-MoS_2/RGO CV curves are greatly improved within the potential window of -0.4-1.2 V, which can be credited to the existence of high-valence Co redox centers. Additionally, Fig. 6.8(b-d) displays the CV curves of MoS_2, MoS_2/RGO, and Co-MoS_2/RGO at various RS concentrations under the same conditions. CV scans show that when our nanocomposites interact with RS, an electrochemically inert compound settles on the electrode surface. There is no cathodic peak in the voltammetry because the system is extremely stable once the low-energy dimer is formed and does not experience a backward reduction process. It was observed that the loop area increased with the rising concentration of RS in the buffer-analyte solution, demonstrating the sensing capabilities of the nanocomposites. In CV, the change in oxidation peak current with the successive addition of resorcinol is minimal, making it challenging to use as the primary sensing technique. Consequently, differential pulse voltammetry (DPV) was used to examine the material's sensing properties.

The electrochemical sensing performance of various modified electrodes is discussed in detail using DPV. In contrast to CV, the DPV method amplified the oxidative responses of RS oxidation by reducing the capacitive (background) currents to a minimum as shown in Fig. 6.9. As depicted in Fig. 6.9(a,b), the enhanced conductivity of RGO nanosheets is elucidated through DPV, as evidenced by the higher redox peak current of the electrode following modification with the synthesized nanocomposite compared to the pristine MoS_2. Fig. 6.9(b) reveals that the MoS_2/RGO sensor exhibits overlapping DPV curves when resorcinol is added. The sensor might have a limited number of active sites available for redox reactions due to aggregated morphology. Upon the addition of resorcinol, these sites could become saturated,

leading to a plateau in the current response, which manifests as overlapping DPV curves. Furthermore, the incorporation of Co alongside MoS_2/RGO could potentially enhance the electrode's electrochemical behavior by facilitating necessary conduction pathways on its surface as Co-MoS_2/RGO has 3D nanosheet morphology. Fig. 6.9(c-f) presents the DPV data for Co-doped variants (5%, 7%, 9%, and 11% Co-MoS_2/RGO). This dataset includes a range of linear

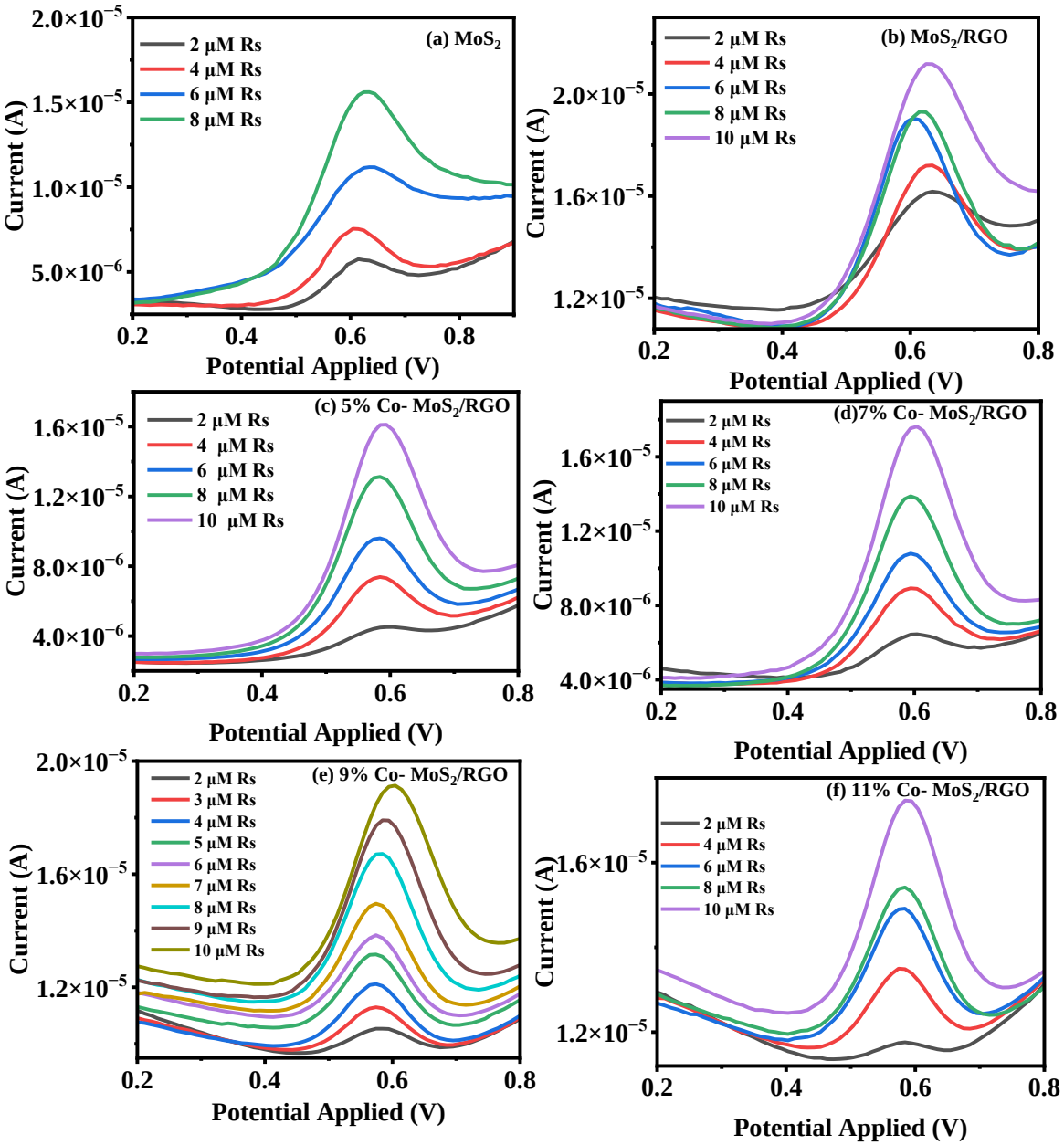

Fig. 6.9 DPV data for (a) MoS_2, (b) MoS_2/RGO, (c) 5% Co-MoS_2/RGO, (d) 7% Co-MoS_2/RGO, (e) 9% Co-MoS_2/RGO and (f)11% Co-MoS_2/RGO for varying concentration of RS in a PBS solution with a pH of 7 at 60 mVs^{-1}.

concentrations of RS within a pH 7 PBS. Among all the Co-doped variants, the 9% Co-MoS_2/RGO exhibits the highest peak current with discerning DPV peaks. The observed heightened redox peaks upon surface modification with Co-doped MoS_2/RGO nanosheets suggest a heightened direct electron transport across the electrode. From the DPV data, it can be inferred that it was successfully immobilized onto the electrode surface. The logarithmic variation between peak current and varied RS concentration is depicted in Fig. 6.10(a-f). The graph includes fitted lines obtained through linear regression equations for MoS_2, MoS_2/RGO, 5%, 7%, 9%, and 11% Co-MoS_2/RGO respectively.

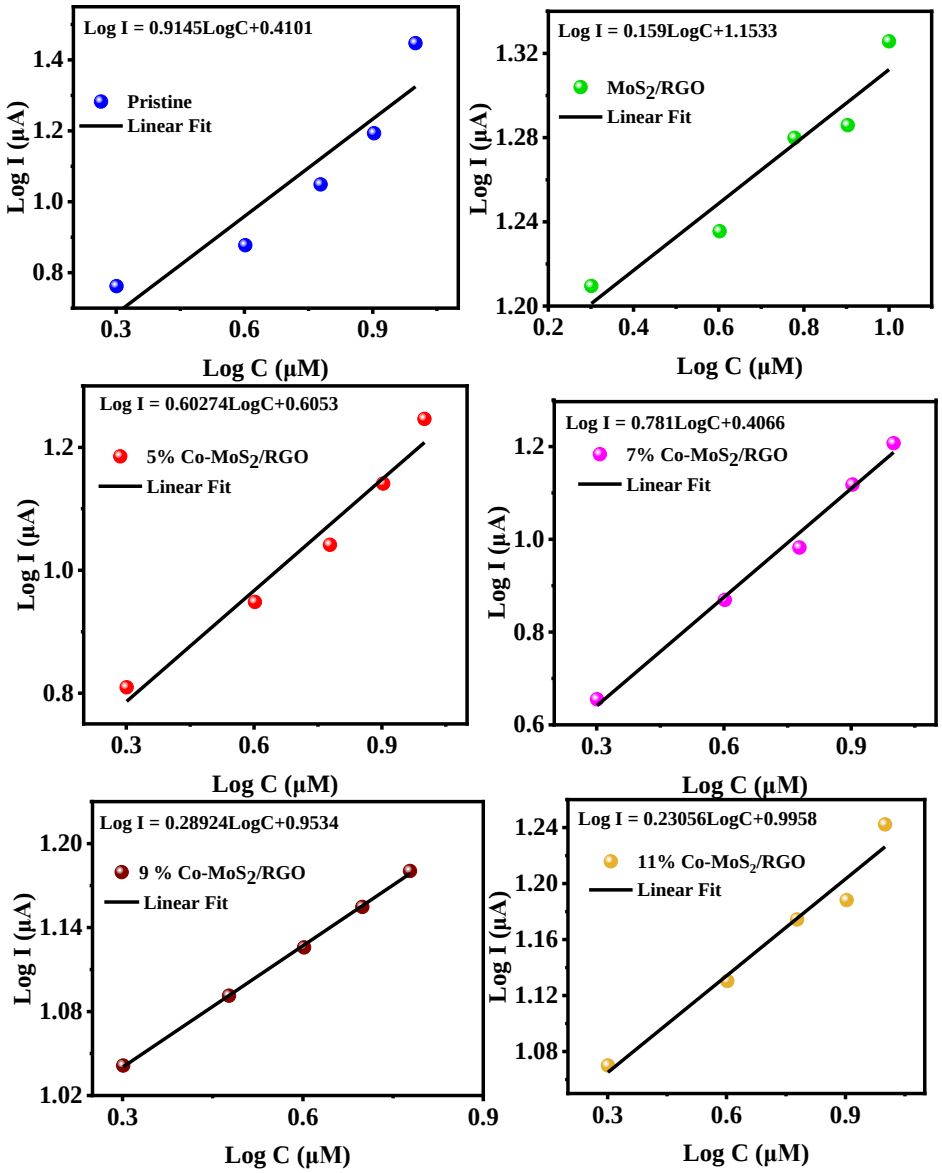

Fig. 6.10 Logarithmic linear fitted data of concentration vs current along with the linear regression equations, for (a) MoS_2, (b) MoS_2/RGO, (c) 5% Co-MoS_2/RGO, (d) 7% Co-MoS_2/RGO, (e) 9% Co-MoS_2/RGO and (f)11% Co-MoS_2/RGO.

Table 6.1 Comparison of the proposed electrochemical sensors with other reported work.

Electrode Material	Detection limit	Linear Range (μM)	Reference
Cd–Glutathione	0.3 μM	100-400	[318]
carbon microfiber	0.03 μM	0-120	[327]
boron-doped diamond	19.23 μM	50-100	[320]
MoS_2/GC	1.13 μM	2-125	[319]
C-ZnO NSs	5.89 μM	0.03-300	[321]
Porous RGO	2.62 μM	5-90	[141]
Graphene-CS/GCE	0.75 μM	1–550	[322]
MWCNTs/GCE	1 μM	5–80	[323]
WS_2-Gr/GCE	0.1 μM	1-100	[324]
MoS_2, MoS_2/RGO, Co-MoS_2/RGO	0.49 μM, 0.35 μM, 20 nM	2-8 2-10 1-10	Present work

The linearity is evidenced by the correlation coefficient (R^2). The value of R^2 for MoS_2, MoS_2/RGO, 5%, 7%, 9%, and 11% Co-MoS_2/RGO are of 0.873, 0.9321,0.9691,0.991,0.999, and 0.9674. Among these, the 9% Co-MoS_2/RGO exhibits the highest R^2 value of 0.999, indicating the most accurate linear correlation between the sensor response and the concentration of RS. This exceptional linearity makes 9% Co-MoS_2/RGO the most promising candidate for the electrochemical detection of RS, as it ensures reliable and precise measurements across different concentrations. Further, the detection limits of MoS_2, MoS_2/RGO, 5%, 7%, 9%, and 11% Co-MoS_2/RGO are determined to be 490, 350, 230, 130, 20 and 180 nM, respectively. Notably, 9% Co-MoS_2/RGO exhibits the lowest detection limit of 20 nM, which is 25-fold lower than that of pristine MoS_2, highlighting its superior sensitivity. This heightened sensitivity is accredited to the incorporation of Co in MoS_2/RGO. The substitution of Mo atoms by Co within a lattice is more likely due to its energetic favorability, supported by its relatively low formation energy. This substitution results in the transition of the monolayer to a half-metallic state, accompanied by the emergence of defect levels within the MoS_2 band gap, setting it apart from the pristine monolayer [325]. This is corroborated by Raman spectroscopy results, which indicate the existence of the 1T phase of MoS_2 in the Co-

MoS_2/RGO nanocomposite. Moreover, Co-MoS_2/RGO nanosheets provide active sites that aid electron transfer via redox cycling. These values are then compared with findings from previous studies, as presented in Table 6.1. The Co-MoS_2/RGO sensor exhibits the lowest detection limit (20 nM) among all the compared sensors, indicating its superior sensitivity. Its linear detection range (1-10 μM) is also competitive, making it highly effective for detecting low concentrations of RS.

In our investigation, we explored the oxidation of RS at the electrode surface using CV and DPV techniques. To grasp the sensing mechanism of resorcinol, it's essential to delve into its oxidation process. The schematic illustration of the sensing mechanism is shown in Fig. 6.11. At pH 7, the formation of the oxidized monomer 4-cyclohexene-1,3-dione is energetically more favorable when the RS reactant first loses a proton (H^+) before undergoing oxidation. Specifically, these findings suggest that in the initial step, the abstraction of a proton requires notably less energy (2.15 eV) compared to the energy demanded for direct oxidation (5.76 eV). Subsequently, the resulting intermediate prefers to lose another proton, requiring 2.60 eV, rather than proceeding directly to oxidation. This stepwise loss of protons before oxidation emerges as a more energetically favorable pathway for the formation of the oxidized product [327]. Given this insight, when Co-MoS_2/RGO interacts with RS, it is conceivable that the initial interaction involves the Co-MoS_2/RGO material gaining a proton from the resorcinol molecule.

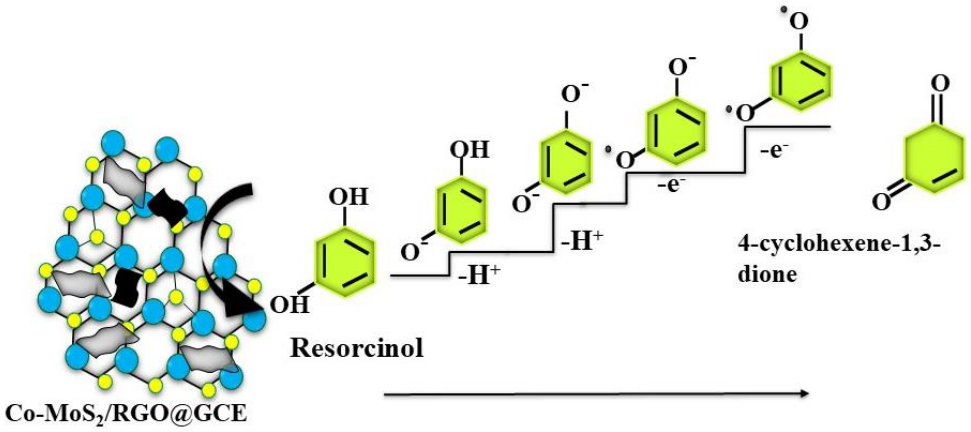

Fig. 6.11 Sensing mechanism of resorcinol.

Compared to MoS_2 and MoS_2/RGO, the DPV response of Co-MoS_2/RGO indicates that Co has higher reversible electron transfer performance and structural stability, which makes it more favorable for enhancing electrochemical activity in sensing applications. This proton transfer could facilitate subsequent steps in the oxidation process, influencing the electrochemical behavior observed at the electrode surface. This understanding underscores the importance of considering proton transfer dynamics in the design and optimization of sensing platforms for resorcinol and similar analytes. The primary challenge in concurrent detection is the potential for one analyte to obstruct the detection of another. As a result, by keeping one analyte at a high concentration and changing the concentration of the other, an interference investigation was carried out for the Co-MoS_2/RGO.

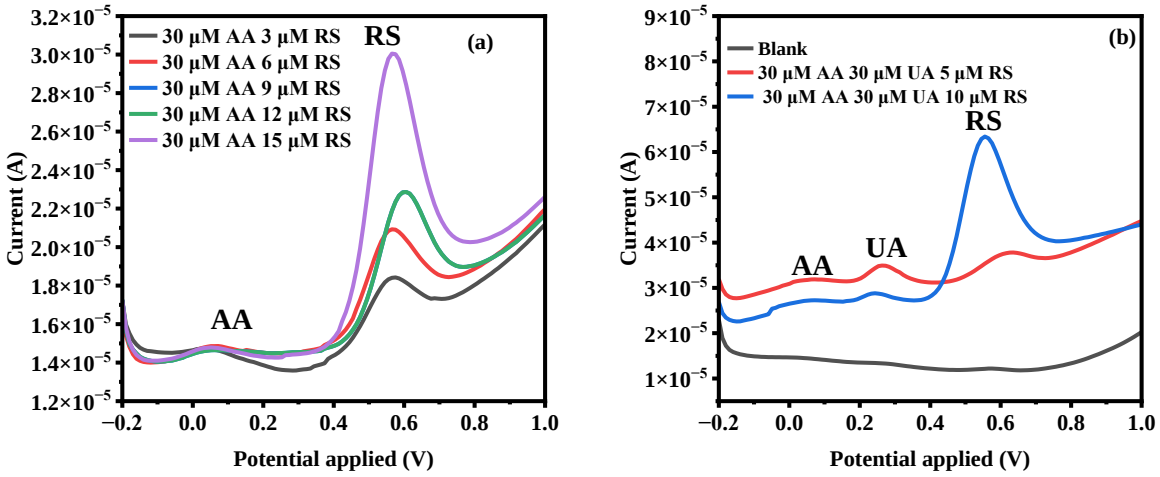

Fig. 6.12 DPV data of 9% Co-MoS_2/RGO for (a) varying concentration of RS in the solution having 30 µM AA, (b) varying concentration of RS in the solution having 30 µM AA, 30 µM UA.

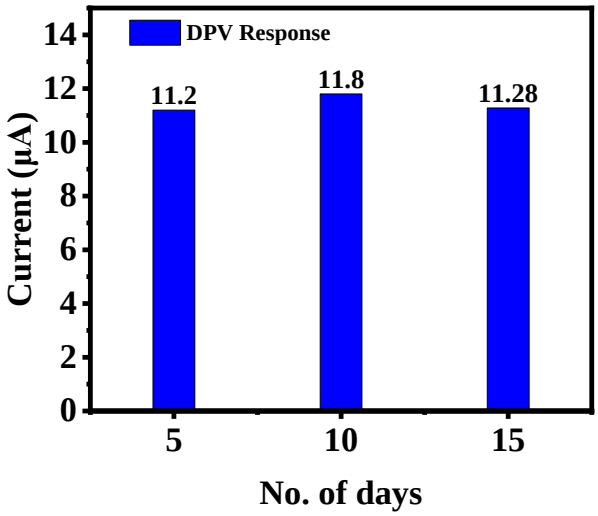

Fig. 6.13 Bar graph showing the stability of the Co-MoS_2/RGO sensor

First, the ascorbic acid (AA) concentration was held constant at 30 μM, meanwhile, the RS concentration was progressively raised from 3 to 15 μM. Peak current increased as RS concentration increased, as seen in Fig. 6.12(a), suggesting that AA existence didn't hamper in the oxidation of RS. Subsequently, both uric acid (UA) and AA were kept constant at 30 μM, while the concentration of RS was varied from 5 μM to 10 μM as shown in Fig. 6.12(b). It was noted that the sensor exhibited a rise in the peak current corresponding solely to RS, highlighting the excellent selectivity of the designed sensor. This suggests that the sensor is capable of distinguishing RS from UA and AA despite their existence at constant concentrations, and can accurately detect changes in RS concentration without interference from UA or AA. This selectivity is crucial for reliable and precise measurements in complex mixtures where multiple analytes are present. The 9% Co-MoS_2/RGO sensor not only demonstrates sensitivity and selectivity but also exhibits remarkable environmental durability in ambient air. Over a period of 12 days, the DPV response of the 9% Co-MoS_2/RGO sensor to 4 μM RS was recorded approximately every 5 days, with the observed data presented in a bar graph (refer to Fig. 6.13). Despite this extended duration, only a 0.7% degradation in peak current was observed, showcasing the sensor's exceptional ambient stability, reproducibility, and repeatability. This minimal decline in performance over time highlights the sensor's potential for reliable and consistent detection of RS in real-world scenarios.

6.5 Conclusion:

A microwave-assisted synthesis technique was used to successfully design MoS_2, MoS_2/RGO, and Co-MoS_2/RGO-based electrochemical sensing platforms. The synthesized nanocomposite was extensively characterized using XRD, FESEM, and HRTEM to examine nanostructure and surface morphology, and Raman spectroscopy to analyze vibrational modes. The characterization results, including XRD, Raman spectroscopy, FESEM, and HRTEM, confirmed the successful synthesis of Co-MoS_2/RGO composites with an open flower-like 3D nanosheet structure and effective integration of cobalt. This unique structure provides an extensive surface area and abundant active sites as evidenced by the BET, facilitating enhanced electron transfer. The electrochemical measurements (CV and DPV) revealed that these structural features significantly improve the sensitivity and selectivity of the sensor towards resorcinol detection, demonstrated by a low detection limit of 20 nM and high selectivity in the presence of common interfering substances such as AA and UA did not affect the sensor's performance, underscoring its high selectivity for RS. Further, the electrochemical oxidation mechanism of RS at the Co-MoS_2/RGO interface was also investigated using CV and DPV.

This investigation revealed a stepwise electro-oxidation process rather than a direct oxidation pathway. Additionally, the Co-MoS_2/RGO sensor exhibited excellent repeatability and reproducibility, maintaining consistent performance even when the electrode was replaced. Therefore, the developed Co-MoS_2/RGO electrochemical sensor not only provides high sensitivity and selectivity for RS detection but also ensures reliable and consistent results. This makes it a promising candidate for practical applications, including real-time sample analysis.

Chapter 7

Summary and Future Scope

An extensive review of the literature has been undertaken at the onset of this investigation, which has elucidated the remarkable sensing capabilities of MoS_2 with respect to its chemical bonding, electronic properties, and morphological structures. This two-dimensional material has been shown to be particularly adept at detecting various molecules prevalent in the food sector, including monosodium glutamate, thiabendazole, and sunset yellow, which are commonly utilized as food colorants. Moreover, MoS_2-based nanocomposites have demonstrated potential for the sensitive and selective detection of glucose and β-agonists such as ractopamine and clenbuterol. These sensors exhibit enhanced sensitivity, selectivity, and stability, with significantly lower limits of detection across a range of target molecules. Further exploration of the electrochemical detection potential of MoS_2-based nanocomposites suggests that these materials could be extended to detect additional food-related substances, such as Methyl Parathion, Chlorpyrifos, and Carbaryl. This sensing capability can be transposed to the realm of explosive detection, facilitating a more sensitive platform for the identification of 2,4,6-trinitrotoluene, which is characterized by lower detection limits and superior linearity at low concentrations. Furthermore, the versatility of these materials extends to the detection of other chemical species, such as 2,4-dinitroanisole and 3,3',4,4'-tetrachlorobiphen. The synthesis of MoS2 in this study was performed via a microwave-assisted methodology. This approach offers several advantages over alternative techniques, such as hydrothermal synthesis, exfoliation, mechanical exfoliation, and chemical vapor deposition, as it minimizes the use of toxic substances and chemical reductants, thereby reducing potential environmental and health hazards. The synthesized MoS_2 was initially employed for the identification of ascorbic acid; however, the observed sensitivity was found to be suboptimal. To surmount this limitation, RGO doping was implemented in concentrations of 1%, 3%, and 5%. It was observed that a 3% RGO doping significantly improved the sensor's performance, as evidenced by differential pulse voltammetry (DPV), cyclic voltammetry (CV), and electrochemical impedance spectroscopy (EIS). The EIS spectra of the 3% MoS_2/RGO nanocomposite revealed inductive behavior upon exposure to ascorbic acid in a phosphate-buffered saline (PBS) solution at pH 7, a phenomenon not previously reported in the previous studies. The selectivity of the sensor was then assessed in the presence of a fixed concentration of uric acid. However, the addition of ascorbic acid resulted in a concurrent increase in the peak current of uric acid, thereby questioning the sensor's selectivity. To address this issue, metal ion doping was pursued

as a subsequent modification. A Co-MoS_2/RGO sensor was synthesized through a two-step microwave irradiation process and was successfully utilized for the selective and simultaneous detection of uric acid and ascorbic acid. This sensor presented exceptional sensitivity and stability, surpassing the performance of those previously reported. Following this, the influence of Mn doping on the MoS_2/RGO matrix was scrutinized. The results indicated that a 7% Mn-MRG doping level conferred the highest sensitivity toward uric acid in the presence of ascorbic acid. However, upon increasing the Mn doping to 9%, the sensor's functionality transitioned from multi-detection to single detection, exclusively detecting uric acid. This remarkable shift in capability was ascribed to Mn's dual role as an oxidizing agent for uric acid and a reducing agent for ascorbic acid. At 9% doping, Mn effectively reduced ascorbic acid, thereby altering the sensor's detection profile. Finally, considering the limited utilization of MoS_2-based sensors for resorcinol detection, a novel Co-MoS_2/RGO sensor was developed for this purpose. By varying the cobalt doping concentration, we achieved nanomolar detection of resorcinol, demonstrating remarkable sensing performance relative to existing studies.

The development of advanced electrochemical sensors using nanocomposites such as MoS_2-RGO, Mn-MRG, and Co-MoS_2/RGO heralds significant opportunities in biosensing and environmental monitoring. Future research in this field can explore several promising directions. Firstly, the development of integrated sensor arrays capable of simultaneous multi-analyte detection can greatly benefit clinical diagnostics and health monitoring. By leveraging the unique properties of each nanocomposite, such as the selective redox behavior of Mn-MRG, researchers can create precise multi-analyte sensing platforms. Secondly, enhancing sensitivity and selectivity remains a critical goal. This can be achieved by optimizing nanostructures, such as fine-tuning the doping levels of metals like Mn in Mn-MRG, to achieve lower detection limits and broader detection ranges. Investigating other dopants and their synergistic effects on sensor performance, along with selective surface functionalization using elements like aptamers or molecularly imprinted polymers, can further reduce interference from other substances in complex samples. Real-time and in-situ monitoring represents another significant future implication. The fabrication of portable and wearable electrochemical sensors based on these nanocomposites can facilitate real-time monitoring of health markers or environmental pollutants. Integrating these sensors with wireless communication technologies would enable remote monitoring and data analysis, thereby broadening their applications. Additionally, extending these sensors to environmental applications, such as detecting trace levels of pollutants or heavy metals in water and soil, can contribute to environmental protection and

public health. In-depth mechanistic studies and computational modeling will be vital for advancing this technology. Understanding the electrochemical mechanisms at the nanoscale, such as the stepwise electro-oxidation processes observed in Co-MoS_2/RGO sensors, can provide insights into sensor performance and guide the design of more efficient sensors. Developing scalable and cost-effective synthesis methods, such as the in-situ microwave-assisted techniques used for MoS_2-RGO, Co-MoS_2/RGO and Mn-MRG will facilitate large-scale production. Ensuring consistency and reliability in mass production is essential for commercialization. Establishing regulatory approvals and standards for the performance and safety of these nanocomposite sensors will also be critical. Collaborations with industry and regulatory bodies can help drive this process forward.

In conclusion, the promising results obtained from MoS_2-RGO, Mn-MRG, and Co-MoS_2/RGO nanocomposite-based electrochemical sensors demonstrate their potential as highly sensitive and selective detection platforms. Future research should focus on enhancing their multi-analyte detection capabilities, optimizing nanostructures, expanding real-time monitoring applications, and ensuring scalability for commercial use. These advancements will pave the way for innovative solutions in healthcare, environmental monitoring, and beyond, ultimately contributing to improved healthcare facilities and safety.

7.1 List of Publications

1. Seema Sharma, Prashant Kumar, and Kawaljeet Singh Samra, “Molybdenum disulfide as a propitious electrochemical sensing material: a mini review” J Solid State Electrochem 28, 337–356 (2024). https://doi.org/10.1007/s10008-023-05618-3.

2. Seema Sharma, Prashant Kumar, Shakra Jabeen and Kawaljeet Singh Samra, “Hierarchical granular morphology of MoS2-RGO nanocomposite for electrochemical sensing of ascorbic-acid” J Mater Sci: Mater Electron 33, 21048–21059 (2022). https://doi.org/10.1007/s10854-022-08909-z.

Communicated Papers

1. Seema Sharma, Prashant Kumar, and Kawaljeet Singh Samra, “A Noval Co-MoS_2/RGO-Based Highly Sensitive Sensor for Simultaneous Detection of Ascorbic Acid and Uric Acid”.

2. Seema Sharma, Prashant Kumar, and Kawaljeet Singh Samra, “Microwave-assisted incorporation and optimization of Mn doping in MoS_2/RGO for application in multi-detection to single-detection electrochemical biosensing: Uric acid”.

3. Seema Sharma, Prashant Kumar, and Kawaljeet Singh Samra, “Resorcinol Sensing with Co-Doped MoS_2/RGO Nanocomposite: Unveiling Nano-Detection”.

Other Publications

1. Sandeep Sheokand, Prashant Kumar, Seema Sharma, Kawaljeet Singh Samra, “Augmented Electrochemical Capacities of Microporous MoS2@NiO Heterostructures”, Electrochimica Acta, 2024, https://doi.org/10.1016/j.electacta.2024.144521.

2. Shakra Jabeen, Prashant Kumar, Seema Sharma, Kawaljeet Singh Samra, “Binder-free MnMoO4 nanoribbons on Ni-foam for high performance electrochemical energy storage devices”, Materials Letters, 324, 2022. https://doi.org/10.1016/j.matlet.2022.132741.

3. Prashant Kumar, Seema Sharma, Shakra Jabeen, Kawaljeet Singh Samra,“Hybrid microwave annealing assisted synthesis of MoS_2-RGO nanostructures: Optimization and characterization for application in supercapacitors”, Electrochimica Acta, 426, 2022, https://doi.org/10.1016/j.electacta.2022.140738.

7.2 Certificates of Conferences and workshops attended

International Conference on New Horizons and Trends in Chemical Sciences (ICNHTCS-2022)

CERTIFICATE

This is to certify that

Mrs. Seema Sharma

presented paper (ORAL) in an International Conference on New Horizons and Trends in Chemical Sciences (ICNHTCS-2022) organized by Department of Chemistry, Dada Ramchand Bakhru Sindhu Mahavidyalaya, Nagpur in Association with the Indian Society of Analytical Scientists, Nagpur Chapter during 25th - 26th March, 2022.

Dr. P. P. Chandrachoodan	Dr. A. V. Bharati	Dr. C. P. Pandhurnekar	Dr. S. A. Mandavgane	Dr. R. D. Sarkar	Dr. V. Pendsey
National President ISAS	Chairman ISAS Nagpur Chapter	Secretary ISAS Nagpur Chapter	Convenor ICNHTCS-22	Convenor ICNHTCS-22	Principal DRB Sindhu Mahavidyalya

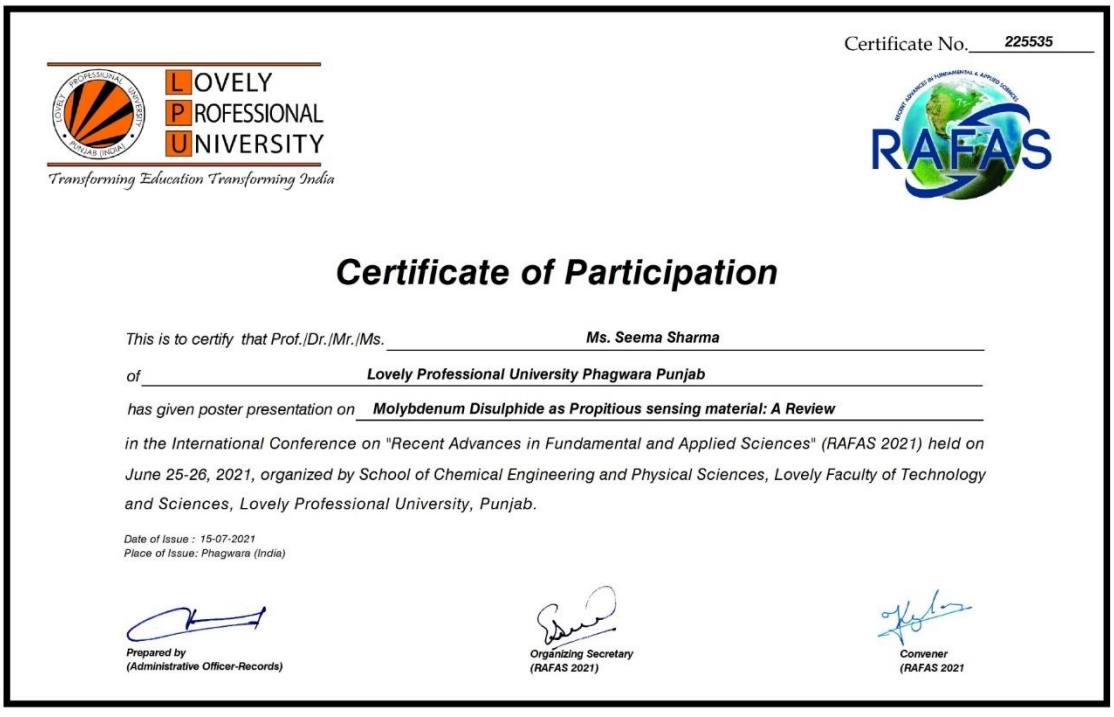

Certificate No. 225535

LOVELY PROFESSIONAL UNIVERSITY
Transforming Education Transforming India

RAFAS

Certificate of Participation

This is to certify that Prof./Dr./Mr./Ms. Ms. Seema Sharma

of Lovely Professional University Phagwara Punjab

has given poster presentation on Molybdenum Disulphide as Propitious sensing material: A Review

in the International Conference on "Recent Advances in Fundamental and Applied Sciences" (RAFAS 2021) held on June 25-26, 2021, organized by School of Chemical Engineering and Physical Sciences, Lovely Faculty of Technology and Sciences, Lovely Professional University, Punjab.

Date of Issue : 15-07-2021
Place of Issue: Phagwara (India)

Prepared by (Administrative Officer-Records)	Organizing Secretary (RAFAS 2021)	Convener (RAFAS 2021

CHITKARA UNIVERSITY

Certificate of Participation

This is to certify that Dr. / Mr. / Ms. ***Seema Sharma***
of ***Lovely Professional University, Jalandhar*** has attended two days Online Workshop on **Material Characterization Techniques** from 20th to 22nd July, 2020 organized by **Chitkara University Research and Innovation Network (CURIN)** Chitkara University, Punjab.

Dr. Malkit Singh
Professor
Chitkara University Research and Innovation Network (CURIN)

Dr. Ankush Kumar Bedyal
Assistant Professor
Chitkara University Research and Innovation Network (CURIN)

Dr. Jasminder Kaur Sandhu
Assistant Professor
Chitkara University Research and Innovation Network (CURIN)

VIGNAN'S INSTITUTE OF MANAGEMENT AND TECHNOLOGY FOR WOMEN
Ghatkesar, Hyderabad, Telangana 501301
Approved by AICTE, New Delhi and Affiliated to JNTUH Hyderabad

Accredited by NBA NATIONAL BOARD OF ACCREDITATION CSE & ECE

Certificate of Participation

Seema Sharma
of
Lovely Professional University

for his/her participation in the webinar on **"Journey to Mars and Moon"** conducted on 03-09-2020, organised by Department of Basic Sciences & Humanities, Vignan's Institute of Management & Technology for Women, Hyderabad.

Dr. T.Srinivasulu
HoD, BS & H

Dr. G. APPARAO NAIDU
Principal

Certificate ID: QSAYXU-CE000143

http://www.vmtw.in/

7.3 Bibliography

1. Javaid M, Haleem A, Rab S, Pratap Singh RP, Suman R (2021) Sens Int 2:100121. https://doi.org/10.1016/j.sintl.2021.100121
2. Global Health Estimates (2020) World Health Organization, Geneva. https://www.who.int/docs/default-source/ghodocuments/global-health estimates/ghe2019_cod_methods.pdf. Accessed 30 May 2023
3. Barua S, Dutta HS, Gogoi S, Devi R, Khan R (2018) ACS Appl Nano Mater 1:2–25. https://doi.org/10.1021/acsanm.7b00157
4. Sinha A, Dhanjai BT, Tan B, Huang Y, Zhao H, Dang X (2018) TrAC Trends Anal Chem 102:75–90. https://doi.org/10.1016/j. trac.2018.01.008
5. Bakker E, Martin TD (2002) ACS Appl Nano Mater 74:2781– 2800. https://doi.org/10.1021/ac0202278
6. Betancourt T, Peppas LB (2006) Int J Nanomedicine 4:483–495. https://doi.org/10.2147/nano.2006.1.4.483
7. Hanrahan G, Patil DG, Wang (2004) J Environ Monit 6:657–664. https://doi.org/10.1039/b403975k
8. Das S, Kim M, Lee J-W, Choi W (2014) Crit Rev Solid State Mater Sci 39:231–252. https://doi.org/10.1080/10408436.2013. 836075
9. Allen MJ, Tung VC, Kaner RB (2009) Chem Rev 110:132–145. https://doi.org/10.1021/cr900070d
10. Zhu C, Zeng Z, Li H, Li F, Fan C, Zhang H (2013) J Am Chem Soc 135:5998–6001. https://doi.org/10.1021/ja4019572
11. Bolotsky A, Butler D, Dong C, Gerace K, Glavin NR, Muratore C (2019) ACS Nano 13:9781–9810. https://doi.org/10.1021/ acsnano.9b03632
12. Wilson JA, Yoffe AD (1969) Adv Phys 18:193–335. https://doi. org/10.1080/00018736900101307
13. Samy O, Zeng S, Birowosuto MD, El Moutaouakil AE (2021) Crystals 11:355. https://doi.org/10.3390/cryst11040355
14. Jiang JW (2015) Front Phys 10:287–302. https://doi.org/10.1007/ s11467-015-0459-z
15. Rahman MT, Kumar R, Kumar M, Qiao Q (2021) Sens Actuators A Phys 318:112517. https://doi.org/10.1016/j.sna.2020.112517
16. Muratore C, Hu JJ, Wang B, Haque MA, Bultman JE (2014) Appl Phys Lett 26:261604. https://doi.org/10.1063/1.4885391
17. Hong S, Sheng C, Krishnamoorthy A, Rajak P, Tiwari S, Nomura K (2018) J Phys Chem C 122:7494–7503. https://doi.org/10. 1021/acs.jpcc.7b12035
18. Venkata Subbaiah YPV, Saji KJ, Tiwari A (2016) Adv Funct Mater 26:2046–2069. https://doi.org/10.1002/adfm.201504202
19. Elfadil D, Lamaoui A, Della Pelle FD, Amine A, Compag- none D (2021) Molecules 26:4607. https://doi.org/10.3390/ molecules26154607
20. Hu C, Hu S (2009) J Sens 2009:1–40. https://doi.org/10.1155/2009/187615
21. Al Hamrashdi HA, Monk SD, Cheneler D (2019) Sensors 19:2638. https://doi.org/10.3390/s19112638
22. Cavalcanti A, Shirinzadeh B, Zhang M, Kretly LC (2008) Sen- sors 8:2932–2958. https://doi.org/10.3390/s8052932
23. Kumar R, Zheng W, Liu X, Zhang J, Kumar M (2020) Adv Mater Technol 5:1901062. https://doi.org/10.1002/admt.201901062
24. Mandal S, Song G (2014) Text Res J 85:101–112. https://doi.org/ 10.1177/0040517514542864

25. Islam MM, Rony JH, Akhtar MN, Shakil SUP, Uddin J (2023) In: Marques G, González-Briones A (ed) Internet of Things for Smart Environments, Springer Cham, Switzerland. https://doi.org/10.1007/978-3-031-09729-4_4
26. Xu F, Li X, Shi Y, Li L, Wang W, He L (2018) Micromachines 9:580. https://doi.org/10.3390/mi9110580
27. Bai Y, Lu L, Cheng J, Liu J, Chen Y, Yu J (2020) Comput Netw 181:107447. https://doi.org/10.1016/j.comnet.2020.107447
28. Bertrand A (2011) In: 18th IEEE Symposium on Communica- tions and Vehicular Technology in the Benelux (SCVT), IEEE 1–6. https://doi.org/10.1109/SCVT.2011.6101302
29. Wang W, Pei Y, Ye L, Song K (2020) Sensors 20:6422. https:// doi.org/10.3390/s20226422
30. Guler U, Tufan TB, Chakravarti A, Jin Y, Ghovanloo M (2023) In: Mehmet R Y (ed) Encyclopedia of Sensors and Biosensors, 1st edn, Elsevier, United States. https://doi.org/10.1016/B978-0- 12-822548-6.00072-8
31. Ripka P, Závěta K (2009) In: Handbook of Magnetic Materials, Elsevier 18:347–420. https://doi.org/10.1016/S1567-2719(09) 01803-4
32. Battersby BJ, Chen A, Kozak D, Trau M (2012) In: Séamus Higson (ed) Biosensors for Medical Applications, 1st edn. Woodhead Publishing Series in Biomaterials, Australia. https:// doi.org/10.1533/9780857097187.2.191
33. Norman T (2014) Integrated security systems design. Elsevier, Boston. https://doi.org/10.1016/B978-0-12-800022-9.09997-6
34. Mehrotra P (2016) J Oral Biol Craniofac Res 6:153–159. https://doi.org/10.1016/j.jobcr.2015.12.002
35. Gaudin V (2020) Biosensors 10:21. https://doi.org/10.3390/ bios10030021
36. Saxena R, Srivastava S (2019) Mater Today Proc 18:1351– 1357. https://doi.org/10.1016/j.matpr.2019.06.600.18
37. Erden PE, Kılıç E (2013) Talanta 107:312–323. https://doi.org/ 10.1016/j.talanta.2013.01.043
38. Yoo EH, Lee SY (2010) Sensors 10:4558–4576. https://doi. org/10.3390/s100504558
39. Jung TH (2022) ACS Sensors 7:912–913. https://doi.org/10. 1021/acssensors.2c00688
40. Feng S, Farha F, Li Q, Wan Y, Xu Y, Zhang T (2019) Sensors 19:3760. https://doi.org/10.3390/s19173760
41. Feng L, Wang J, Chen Y, Ding C (2021) J Sens 2021:1–11. https://doi.org/10.1155/2021/6988676
42. Suma V, Shekar RR, Akshay KA (2019) In: 3rd International Confer- ence on Electronics, Communication and Aerospace Technology (ICECA) 2019. https://doi.org/10.1109/ICECA.2019.8822055
43. Francioso A, Baseggio Conrado AB, Mosca L, Fontana M (2020) Oxid Med Cell Longev 2020:1–27. https://doi.org/10. 1155/2020/8294158
44. Ravikumar A, Panneerselvam P, Radhakrishnan K, Christus AAB, Sivanesan S (2018) Appl Surf Sci 449:31–38. https:// doi.org/10.1016/j.apsusc.2017.12.098
45. Kumar NA, Dar MA, Gul R, Baek JB (2015) Mater Today 18:286–298. https://doi.org/10.1016/j.mattod.2015.01.016
46. Sebenik RF, Burkin AR, Dorfler RR, Laferty JM, Leichtfried G, Meyer-Grünow H (2000) Ullmann's encyclopedia of indus- trial chemistry.Wiley-VCH Verlag GmbH & Co. KGaA, Berlin. https://doi.org/10.1002/14356007
47. El-Mahalawy SH, Evans BL (1976) J Appl Crystallogr 9:403– 406. https://doi.org/10.1107/S0021889876011709
48. Arif Khalil RM, Hussain F, Manzoor Rana A, Imran M, Murtaza G (2019) Phys E Low Dimensional Syst Nanostruct 106:338–345. https://doi.org/10.1016/j.physe.2018.07.003

49. Wypych F, Schöllhorn R (1992) J Chem Soc 1992:1386–1388. https://doi.org/10.1039/C39920001386
50. Radisavljevic B (2011) Radenovic A Brivio, J Giacometti V, Kis A. Nat Nanotechnol 6:147–150. https://doi.org/10.1038/ nnano.2010.279
51. Somoano R, Hadek V, Rembaum A, Wolfe HC, Douglass DH (1971) Phys Rev Lett 27:402–404. https://doi.org/10.1103/ PhysRevLett.27.402
52. Chen F, Su W, Zhao S, Lv Y, Ding S, Fu L (2020) CrystEng- Comm 22:4174–4179. https://doi.org/10.1039/D0CE00558D
53. Neetika AK, Kumar A, Chandra R, Malik VK (2021) Thin Solid Films 725. https://doi.org/10.1016/j.tsf.2021.138625
54. Chithaiah P, Ghosh S, Idelevich A, Rovinsky L, Livneh T, Zak A (2020) ACS Nano 14:3004–3016. https://doi.org/10.1021/ acsnano.9b07866
55. Kobayashi K, Yamauchi J (1995) Phys Rev B Condens Matter 51:17085–17095. https://doi.org/10.1103/physrevb.51.17085
56. Tan X, Kang W, Liu J, Zhang C (2019) Nanoscale Res Lett 14:317. https://doi.org/10.1186/s11671-019-3126-4
57. Sahoo D, Kumar B, Sinha J, Ghosh S, Roy SS, Kaviraj B (2020) Sci Rep 10:10759. https://doi.org/10.1038/s41598-020-67683-2
58. Adilbekova B, Lin Y, Yengel E, Faber H, Harrison G, Firdaus Y (2020) J Mater Chem C 8:5259–5264. https://doi.org/10. 1039/D0TC00659A
59. Yadav S, Chaudhary P, Uttam KN, Varma A, Vashistha M, Yadav BC (2019) Nanotechnology 30:29550. https://doi.org/ 10.1088/1361-6528/ab1569
60. Kandhasamy DM, Muthu Mareeswaran PM, Chellappan S, Namasivayam D, Aldahish A, Chidambaram K (2021) ACS Omega 7:629–637. https://doi.org/10.1021/acsomega.1c05250
61. Rajbanshi B, Sarkar S, Sarkar P (2015) RSC Phys Chem Chem Phys 17:26166–26174. https://doi.org/10.1039/c5cp04653j
62. Gupta D, Chauhan V, Kumar R (2020) Inorg Chem Commun 121:108200. https://doi.org/10.1016/j.inoche.2020.108200
63. Ryou J, Kim YS, Kc S, Cho K (2016) Sci Rep 6:29184. https:// doi.org/10.1038/srep29184
64. Chu T, Ilatikhameneh H, Klimeck G, Rahman R, Chen Z (2015) Nano Lett 15:8000–8007. https://doi.org/10.1021/acs. nanolett.5b03218
65. Kamrun S, Jannati NN, Conrad R, Hasan HMdH (2019) Con- dens Matter 4:11. https://doi.org/10.3390/condmat4020049
66. Lopez-Sanchez OL, Lembke D, Kayci M, Radenovic A, Kis A (2013) Nat Nanotechnol 8:497–501. https://doi.org/10.1038/ nnano.2013.100
67. Zhang W, Chuu CP, Huang JK, Chen CH, Tsai ML, Chang YH (2014) Sci Rep 4:3826. https://doi.org/10.1038/srep03826
68. Li X, Zhu H (2015) J Materiomics 1:33–44. https://doi.org/10. 1016/j.jmat.2015.03.003
69. Gan X, Lee LYS, Wong K, Lo TW, Ho KH, Lei DY (2018) ACS Appl Energy Mater 1:4754–4765. https://doi.org/10.1021/ acsaem.8b00875
70. Cooper RC, Lee C, Marianetti CA, Wei X, Hone J, Kysar JW (2013) APS Phys Rev B 87:035423
71. Bertolazzi S, Brivio J, Kis A (2011) ACS Nano 5:9703–9709. https://doi.org/10.1021/nn203879f
72. Askari MB, Kalourazi AF, Seifi M, Shahangian SS, Askari N, Manjili TJ (2018) Optik 174:154–162. https://doi.org/10. 1016/j.ijleo.2018.08.035
73. Jiang JW, Park HS, Rabczuk T (2014) Nanoscale 6:3618. https://doi.org/10.1039/c3nr05991j
74. Jiang JW, Qi Z, Park HS, Rabczuk T (2013) Nanotechnol 24:435705. https://doi.org/10.1088/0957-4484/24/43/435705

75. Ali L, Subhan F, Ayaz M, Hassan SSU, Byeon CC, Kim JS (2022) Nanomaterials 12:3465. https://doi.org/10.3390/ nano12193465
76. Reshmi S, Akshaya MV, Satpati B, Roy A, Kumar Basu PK, Bhattacharjee K (2017) Mater Res Express 4:115012. https:// doi.org/10.1088/2053-1591/aa949c
77. Pyeon JJ, Kim SH, Jeong DS, Baek SH, Kang CY, Kim JS (2016) Nanoscale 8:10792–10798. https://doi.org/10.1039/c6nr01346e
78. Li H, Wu J, Yin Z, Zhang H (2014) Acc Chem Res 47:1067– 1075. https://doi.org/10.1021/ar4002312
79. Li D, Liu X, Yi R, Zhang J, Su Z, Wei G (2018) Inorg Chem Front 5:112–119. https://doi.org/10.1039/C7QI00542C
80. Li S, Ma Y, Liu Y, Xin G, Wang M, Zhang Z (2019) RSC Adv 9:2997–3003. https://doi.org/10.1039/c8ra09511f
81. Aswathi R, Sandhya KY (2018) J Mater Chem A 6:14602–14613. https://doi.org/10.1039/C8TA00476E
82. Petit-Domínguez MD, Quintana C, Vázquez L, del Pozo M, Cuadrado I, Parra-Alfambra AM (2018) Microchim Acta 185:334. https://doi.org/10.1007/s00604-018-2793-7
83. Gupta A, Neal C, Das S, Seal S (2016) IEEE Sens J 1–3. https:// doi.org/10.1109/ICSENS.2016.7808467
84. Qiao X, Li K, Xu J, Cheng N, Sheng Q, Cao W (2018) Biosens Bioelectron 113:142–147. https://doi.org/10.1016/j.bios.2018. 05.003
85. Huang M (2021) Int J Electrochem Sci 151014. https://doi.org/ 10.20964/2021.01.24
86. Sha R, Vishnu N, Badhulika S (2019) Sens Actuators B: Chem 279:53–60. https://doi.org/10.1016/j.snb.2018.09.106
87. Huang KJ, Wang L, Li J, Liu YM (2013) Sens Actuators B: Chem 178:671–677. https://doi.org/10.1016/j.snb.2013.01.028
88. Park SY, Lee JE, Kim YH, Kim JJ, Shim Y-S, Kim SY (2018) Sens Actuators B: Chem 258:775–782. https://doi.org/10.1016/j. snb.2017.11.176
89. Gawande MB, Shelke SN, Zboril R, Varma RS (2014) Acc Chem Res 47:1338–1348. https://doi.org/10.1021/ar400309b
90. Reeja-Jayan B, Harrison KL, Yang K, Wang CL, Yilmaz AE, Manthiram A (2012) Sci Rep 2:1003. https://doi.org/10.1038/ srep01003
91. Fathy M, Hassan H, Hafez H, Soliman M, Abulfotuh F, Kashyout AEHB (2022) ACS Omega 7:16757–16765. https://doi.org/10. 1021/acsomega.2c01455
92. Sharma S, Kumar P, Jabeen S, Samra KS (2022) J Mater Sci Mater Electron 33:21048–21059. https:// doi. org/ 10. 1007/ s10854-022-08909-z
93. Zhang W, Zhang P, Su Z, Wei G (2015) Nanoscale 7:18364– 18378. https://doi.org/10.1039/c5nr06121k
94. Feng SH, Li GH (2017) In: Xu R, Xu Y (ed) Modern inorganic synthetic chemistry, 2nd edn. Elsevier, China. https://doi.org/10. 1016/B978-0-444-63591-4.00004-5
95. Rafiq MKSB, Akhtaruzzaman M (2022) In: Akhtaruzzaman M, Selvanathan V (ed) Comprehensive Guide on Organic and Inor- ganic Solar Cells, Academic Press, Malaysia. https://doi.org/10. 1016/B978-0-323-85529-7.00012-8
96. Hussain CM, Keçili R (2020) Modern environmental analysis techniques for pollutants. Elsevier, US. https://doi.org/10.1016/ C2018-0-01639-4
97. Wang Y, Zeng S, Humbert G, Ho AHP (2023) In: Wing C M, Ho APH (ed) Microfluidic Biosensors, Academic Press, Hong Kong. https://doi.org/10.1016/B978-0-12-823846-2.00003-1
98. Curulli A (2020) Molecules 25:5759. https://doi.org/10.3390/ molecules25235759

99. Grieshaber D, MacKenzie R, Vörös J, Reimhult E (2008) Sensors 8:1400–1458. https://doi.org/10.3390/s80314000
100. Kumar A, Malinee M, Dhiman A, Kumar A, Sharma TK (2019) In: Inamuddin, Khan R, Ali M, Abdullah AM (ed) Advanced Biosensors for Health Care Applications, Elsevier, US. https:// doi.org/10.1016/B978-0j-12-815743-5.00002-0
101. Ju L (2021) Int J Electrochem Sci 16:2021. https://doi.org/10. 20964/2021.07.36
102. Arfin T (2021) Functionalized nanomaterials based devices for environmental applications, Elsevier 199–218. https://doi.org/ 10.1016/B978-0-12-822245-4.00008-8
103. Venton BJ, DiScenza DJ (2020) Electrochemistry for bioanalysis, Elsevier 27–50. https://doi.org/10.1016/B978-0-12-821203-5. 00004-X
104. Aoki K, Honda K, Tokuda K, Matsuda H (1985) J Electroanal Chem Interfacial Electrochem 182:267–279. https://doi.org/10. 1016/0368-1874(85)87005-2
105. Cobb SJ, Macpherson JV (2019) Anal Chem 91:7935–7942. https://doi.org/10.1021/acs.analchem.9b01857
106. Honeychurch MJ, Díaz-Cruz JM, Serrano N, Ariño C, Esteban M (2018) In: Paul W, Colin P, Alan T, Maneul M (ed) Reference module in chemistry, molecular sciences and chemical engineer- ing, 3rd edn. Elsevier, UK. https://doi.org/10.1016/B978-0-12- 409547-2.14432-4
107. Zhang W, Xiahou C, Ji X, Zhang Y, Zhang H, Song S (2022) Int J Electrochem Sci 17. https://doi.org/10.20964/2022.09.29
108. Guo C, Wang C, Sun H, Dai D, Gao H (2021) RSC Adv 11:29590–29597. https://doi.org/10.1039/d1ra05350g
109. Hu J, Zhang C, Li X, Du X (2020) Sensors 20:6817. https://doi. org/10.3390/s20236817
110. Zribi R, Foti A, Donato MG, Gucciardi PG, Neri G (2021) Sen- sors 21:1371. https://doi.org/10.3390/s21041371
111. Lin J, Mei Q, Duan Y, Yu C, Ding Y, Li L (2020) ECS Meet- ing Abstracts MA2020-01:1941–1941. https://doi.org/10.1149/ MA2020-01271941mtgabs
112. Devi R, Gogoi S, Barua S, Sankar Dutta HS, Bordoloi M, Khan R (2019) Food Chem 276:350–357. https://doi.org/10.1016/j. foodchem.2018.10.024
113. Huang KJ, Wang L, Li J, Liu YM (2013) Sens Actuators B Chem 178:671–677. https://doi.org/10.1016/j.snb.2013.01.028
114. Mahobiya SK, Balayan S, Chauhan N, Kuchhal NK, Islam SS, Jain U (2022) Biointerface Res Appl Chem 13:352. https://doi. org/10.33263/BRIAC134.352
115. Yan Q, Wu R, Chen H, Nan W (2023) J Saudi Chem Soc 27:101612. https://doi.org/10.1016/j.jscs.2023.101612
116. Wang Q, Wang M, Zhang N, Huang X, Wang X, Wang S (2022) Microchem J 189:108434. https://doi.org/10.1016/j.microc.2023. 108434
117. Kumar S, Singh D, Pathania D, Awasthi A, Singh K (2023) Mater Chem Phys 297:127446. https://doi.org/10.1016/j.matchemphys. 2023.127446
118. Ramya M, Kumar PS, Rangasamy G, Shankar VU, Rajesh G, Nirmala K (2023) Environ Res 216:114463. https://doi.org/10. 1016/j.envres.2022.114463
119. Qiao Z, Jiang X (2017) Org Biomol Chem 15:1942–1946. https://doi.org/10.1039/c6ob02833k
120. Kumar S, Awasthi A, Sharma MD, Singh K, Singh D (2022) Mater Chem Phys 290:126656. https://doi.org/10.1016/j.match emphys.2022.126656
121. Neethipathi DK, Ganguly P, Beniwal A, Scott M, Bass A, Dahiya R (2022) IEEE International Conference on Flexible and Print- able Sensors and Systems (FLEPS) 2022. https://doi.org/10. 1109/FLEPS53764.2022.9781564
122. Mekonnen ML, Mola AM, Abda EM (2023) ACS Agri Sci Tech- nol 3:82–89. https://doi.org/10.1021/acsagscitech.2c00241

123. Jahani PM (2022) J Electrochem Sci Eng 12:1099–1109. https://doi. org/10.5599/jese.1413
124. Wang H, Zhu W, Xu T, Zhang Y, Tian Y, Liu X (2022) Food Chem 396:133630. https://doi.org/10.1016/j.foodchem.2022. 133630
125. Yang T, Cui Y, Chen M, Yu R, Luo S, Li W (2017) ACS Sus- tainable Chem Eng 5:1332–1338. https://doi.org/10.1021/acssu schemeng.6b01699
126. Ma Y, Deng M, Wang X, Gao X, Song H, Zhu Y (2022) Anal Chim Acta 1221:340078. https://doi.org/10.1016/j.aca.2022. 340078
127. Chacko L, Massera E, Aneesh PM (2020) J Electrochem Soc 167:106506. https://doi.org/10.1149/1945-7111/ab992c
128. Lu Y, Liang X, Niyungeko C, Zhou J, Xu J, Tian G (2018) Talanta 178:324–338. https://doi.org/10.1016/j.talanta.2017. 08.033
129. Zhou G, Chang J, Pu H, Shi K, Mao S, Sui X, Ren R, Cui S, Chen J (2016) J ACS Sens 1:295–302. https://doi.org/10.1021/acsse nsors.5b00241
130. Gao C, Yu XY, Xiong SQ, Liu JH, Huang XJ (2013) Anal Chem 85:2673–2680. https://doi.org/10.1021/ac303143x
131. Chen HY, Wang J, Meng L, Yang T, Jiao K (2016) Chem Lett 27:231–234. https://doi.org/10.1016/j.cclet.2015.09.018
132. Chetana S, Kumar N, Choudhary P, Amulya G, Anandakumar CS, Kumar KGB (2023) Mater Chem Phys 294:126869. https:// doi.org/10.1016/j.matchemphys.2022.126869
133. Tien VM, Ong VH, Pham TN, Quang Hoa N, Nguyen TL, Thang PD (2023) RSC Adv 13:10577–10591. https://doi.org/10.1039/ d3ra01136d
134. Cazelles R, Shukla RP, Ware RE, Vinks AA, Ben-Yoav H (2020) Biomedicines 9:6. https://doi.org/10.3390/biomedicines9010006
135. Yang Y, Zhang J, Li YW, Shan Q, Wu W (2021) Colloids Surf A Physicochem Eng Asp 625:126865. https://doi.org/10.1016/j. colsurfa.2021.126865
136. Liu D, Gong Q, Xu X, Meng S, Li Y, You T (2023) J Electroa- nal Chem 930:117143. https://doi.org/10.1016/j.jelechem.2023. 117143
137. Fall B, Sall DD, Hémadi M, Diaw AKD, Fall M, Randriama- hazaka H (2023) Sens Actuators Rep 5:100136. https://doi.org/ 10.1016/j.snr.2022.100136
138. Kim HU, Kim HY, Kulkarni A, Ahn C, Jin Y, Kim Y (2016) Sci Rep 6:34587. https://doi.org/10.1038/srep345876
139. Rawat B, Mishra KK, Barman U, Arora L, Pal D, Paily RP (2020) IEEE Sens J 20:6937–6944. https://doi.org/10.1109/JSEN.2020. 2978275
140. Chen C, Chen, Hong (2019) Catalysts 9:653. https://doi.org/10. 3390/catal9080653
141. Alsaeedi H, Alsalme A (2023) Mater 16:1180. https://doi.org/10. 3390/ma16031180
142. Lin M, Wan H, Zhang J, Wang Q, Hu X, Xia F (2020) ACS Appl Mater Interfaces 12:45814–45821. https://doi.org/10.1021/ acsami.0c13385
143. Adeloju SB (2005) Encyclopedia of analytical science. Elsevier, UK. https://doi.org/10.1016/B0-12-369397-7/00012-1
144. Li DW, Zhai WL, Li YT, Long YT (2013) Microchim Acta 181:23–43. https://doi.org/10.1007/s00604-013-1115-3
145. Gumpu MB, Sethuraman S, Krishnan UM, Rayappan JBB (2015) Sens Actuators B Chem 213:515–533. https://doi.org/10.1016/j. snb.2015.02.122
146. Xu X, Yang S, Wang Y, Qian K (2022) Green Anal Chem 2:100020. https://doi.org/10.1016/j.greeac.2022.100020
147. Arduini F, Cinti S, Scognamiglio V, Moscone D (2020) Hand- book of nanomaterials in analytical chemistry. Elsevier, US. https://doi.org/10.1016/B978-0-12-816699-4.00013-X

148. Ghosh S, AlKafaas SS, Bornman C, Apollon W, Hussien AM, Badawy AE (2022) J Basic Appl Sci 11:73. https://doi.org/10. 1186/s43088-022-00248-6
149. Revenis M, Wong ECC (2021) In: Dietzen D, Bennett M, Wong E, Haymond S (ed) Biochemical and Molecular Basis of Pediatric Disease, 5th edn. Elsevier, US. https://doi.org/10.1016/B978- 0-12-817962-8.00006-8
150. Zhang X, Ma G, Wang J (2019) Tungsten 1:59–79. https://doi.org/10.1007/s42864-019-00014-9
151. Ma H, Shen Z, Ben S (2018) J Colloid Interface Sci 517:204–212. https://doi.org/10.1016/j.jcis.2017.11.013
152. Lei Y, Butler D, Lucking MC, et al (2020) Sci Adv 6: https://doi.org/10.1126/sciadv.abc4250
153. Leadbeater NE, Torenius HM (2002) J Org Chem 67:3145–3148. https://doi.org/10.1021/jo016297g
154. Kumar A, Kuang Y, Liang Z, Sun X (2020) Mater Today Nano 11:100076. https://doi.org/10.1016/j.mtnano.2020.100076
155. de la Hoz A, Díaz-Ortiz Á, Moreno A (2005) Chem Soc Rev 34:164–178. https://doi.org/10.1039/B411438H
156. Krishnan R, Shibu SN, Poelman D, et al (2022) Mater Today Commun 32:103890. https://doi.org/10.1016/j.mtcomm.2022.103890
157. Staudenmaier L (1898) Verfahren zur Darstellung der Graphitsäure. Berichte der deutschen chemischen Gesellschaft 31:1481–1487. https://doi.org/10.1002/cber.18980310237
158. Hummers WS, Offeman RE (1958) J Am Chem Soc 80:1339–1339. https://doi.org/10.1021/ja01539a017
159. KAYE GWC (1934) Nature 133:511–513. https://doi.org/10.1038/133511a0
160. Bunaciu AA, Udriştioiu E gabriela, Aboul-Enein HY (2015) Crit Rev Anal Chem 45:289–299. https://doi.org/10.1080/10408347.2014.949616
161. Bumbrah GS, Sharma RM (2016) Egypt J Forensic Sci 6:209–215. https://doi.org/10.1016/j.ejfs.2015.06.001
162. López-López M, García-Ruiz C (2014) Infrared and Raman spectroscopy techniques applied to identification of explosives. TrAC Trends in Analytical Chemistry 54:36–44. https://doi.org/10.1016/j.trac.2013.10.011
163. Costa-Fernandez JM, Redondo-Fernandez G, Fernandez-Arguelles MT, Soldado AB (2022) In: Luminescent Metal Nanoclusters. Elsevier, pp 57–88
164. Khan SA, Khan SB, Khan LU, et al (2018) In: Handbook of Materials Characterization. Springer International Publishing, Cham, pp 317–344
165. Herrero YR, Camas KL, Ullah A (2023) In: Advanced Applications of Biobased Materials. Elsevier, pp 111–143
166. Yang Z, Zhu M (2023) Case Studies: Ultraviolet-Visible (UV-Vis) Spectroscopy. pp 265–283
167. Vogt C, Wondergem CS, Weckhuysen BM (2023) Ultraviolet-Visible (UV-Vis) Spectroscopy. pp 237–264
168. Simon P, Baldovino-Medrano VG, Wojcieszak R (2022) Springer, pp 249–271. https://doi.org/10.1007/978-3-030-63713-2_10
169. Crist BV (2019) J Electron Spectros Relat Phenomena 231:75–87. https://doi.org/10.1016/j.elspec.2018.02.005
170. Ahmad A, Ahmad I, Ramzan S, et al (2021) In: Nanomedicine Manufacturing and Applications. Elsevier, pp 73–85
171. Zavašnik J, Šestan A, Shvalya V (2021) Microscopic techniques for the characterisation of metal-based nanoparticles. pp 241–284
172. Agrawal S (2022) In: Rare-Earth-Activated Phosphors. Elsevier, pp 147–175

173. Jaroniec M, Kruk M, Sayari A (1998) Adsorption methods for characterization of surface and structural properties of mesoporous molecular sieves. pp 325–332
174. P.S. J, Sutrave DS (2018) Int J Chemtech Res 11:77–88. https://doi.org/10.20902/IJCTR.2018.110911
175. Chooto P (2019) In: Voltammetry. IntechOpen
176. Mendoza S, Bustos E, Manríquez J, Godínez LA (2015) In: Agricultural and Food Electroanalysis. Wiley, pp 21–48
177. Li X, Qin Z, Fu H, et al (2021) Biosens Bioelectron 177:112672. https://doi.org/10.1016/j.bios.2020.112672
178. Magar HS, Hassan RYA, Mulchandani A (2021) Sensors 21:6578. https://doi.org/10.3390/s21196578
179. Bilal S, Akbar A, Shah A-HA (2019) Polymers (Basel) 11:1346. https://doi.org/10.3390/polym11081346
180. Li S, Ma Y, Liu Y, et al (2019) RSC Adv 9:2997–3003. https://doi.org/10.1039/C8RA09511F
181. Barui AK, Sharma R, Rajput YS, Singh S (2013) J Food Sci Technol 50:826–829. https://doi.org/10.1007/s13197-013-0934-x
182. Dostálek J, Přibyl J, Homola J, Skládal P (2007) Anal Bioanal Chem 389:1841–1847. https://doi.org/10.1007/s00216-007-1536-0
183. Ibañez GA, Escandar GM (2011) Sensors 11:11081–11102. https://doi.org/10.3390/s111211081
184. Mishra A, Dheepika R, Parvathy PA, et al (2021) Sci Rep 11:19324. https://doi.org/10.1038/s41598-021-97832-0
185. Zhang X, Cao Y, Yu S, et al (2013) Biosens Bioelectron 44:183–190. https://doi.org/10.1016/j.bios.2013.01.020
186. Wei Y, Liu Y, Xu Z, et al (2020) Int J Anal Chem 2020:1–13. https://doi.org/10.1155/2020/8812443
187. Zhou C, Li S, Zhu W, et al (2013) Electrochim Acta 113:454–463. https://doi.org/10.1016/j.electacta.2013.09.109
188. Li D, Liu X, Yi R, et al (2018) Inorg Chem Front 5:112–119. https://doi.org/10.1039/C7QI00542C
189. Akbari E, Jahanbin K, Afroozeh A, et al (2018) Physica B Condens Matter 545:510–518. https://doi.org/10.1016/j.physb.2018.06.033
190. Jiang J-W (2015) Graphene versus MoS2: Front Phys (Beijing) 10:287–302. https://doi.org/10.1007/s11467-015-0459-z
191. Kumar NA, Dar MA, Gul R, Baek J-B (2015) Materials Today 18:286–298. https://doi.org/10.1016/j.mattod.2015.01.016
192. Wypych F, Weber Th, Prins R (1997) Surf Sci 380:L474–L478. https://doi.org/10.1016/S0039-6028(97)00015-0
193. Gan X, Lee LYS, Wong K, et al (2018) ACS Appl Energy Mater 1:4754–4765. https://doi.org/10.1021/acsaem.8b00875
194. Arif Khalil RM, Hussain F, Manzoor Rana A, et al (2019) Physica E Low Dimens Syst Nanostruct 106:338–345. https://doi.org/10.1016/j.physe.2018.07.003
195. Tokura Y, Nagaosa N (2000) Science (1979) 288:462–468. https://doi.org/10.1126/science.288.5465.462
196. Gómez-Pozos H, González-Vidal J, Torres G, et al (2013) Sensors 14:403–415. https://doi.org/10.3390/s140100403
197. Gautam AK, Faraz M, Khare N (2020) J Alloys Compd 838:155673. https://doi.org/10.1016/j.jallcom.2020.155673
198. Solomon G, Mazzaro R, Morandi V, et al (2020) Crystals (Basel) 10:1040. https://doi.org/10.3390/cryst10111040
199. Kudr J, Adam V, Zitka O (2019) Molecules 24:3374. https://doi.org/10.3390/molecules24183374

200. Park SY, Lee JE, Kim YH, et al (2018) Sens Actuators B Chem 258:775–782. https://doi.org/10.1016/j.snb.2017.11.176
201. Chen H-Y, Wang J, Meng L, et al (2016) Chinese Chemical Letters 27:231–234. https://doi.org/10.1016/j.cclet.2015.09.018
202. Yang Y, Lei Q, Li J, et al (2022) Microchemical Journal 172:106904. https://doi.org/10.1016/j.microc.2021.106904
203. Xing L, Ma Z (2016) Microchimica Acta 183:257–263. https://doi.org/10.1007/s00604-015-1648-8
204. Lee C, Yan H, Brus LE, et al (2010) ACS Nano 4:2695–2700. https://doi.org/10.1021/nn1003937
205. Kudin KN, Ozbas B, Schniepp HC, et al (2008) Nano Lett 8:36–41. https://doi.org/10.1021/nl071822y
206. Stankovich S, Dikin DA, Piner RD, et al (2007) Carbon N Y 45:1558–1565. https://doi.org/10.1016/j.carbon.2007.02.034
207. He H-Y (2017) Sci Rep 7:45608. https://doi.org/10.1038/srep45608
208. Wang R, Gao S, Wang K, et al (2017) Sci Rep 7:7963. https://doi.org/10.1038/s41598-017-08341-y
209. Karikalan N, Karthik R, Chen S-M, Chen H-A (2017) Sci Rep 7:45924. https://doi.org/10.1038/srep45924
210. Odeh AA, Al-Douri Y, Voon CH, et al (2017) Microchimica Acta 184:2211–2218. https://doi.org/10.1007/s00604-017-2249-5
211. Huang M, Tian H, Zhou P, et al (2021) Int J Electrochem Sci 16:151014. https://doi.org/10.20964/2021.01.24
212. ASAN G, Çelikkan H (2017) Gazi Üniversitesi Mühendislik-Mimarlık Fakültesi Dergisi 32:. https://doi.org/10.17341/gazimmfd.337608
213. Saraf M, Natarajan K, Saini AK, Mobin SM (2017) Dalton Transactions 46:15848–15858. https://doi.org/10.1039/C7DT03888G
214. Wei Y, Liu Y, Xu Z, et al (2020) Int J Anal Chem 2020:1–13. https://doi.org/10.1155/2020/8812443
215. Bisquert J, Randriamahazaka H, Garcia-Belmonte G (2005) Electrochim Acta 51:627–640. https://doi.org/10.1016/j.electacta.2005.05.025
216. Fan X, Li Z, Wang S, et al (2019) J Braz Chem Soc. https://doi.org/10.21577/0103-5053.20190081
217. Sun H, Chao J, Zuo X, et al (2014) RSC Adv 4:27625. https://doi.org/10.1039/c4ra04046e
218. MacKenzie CR (2015) Curr Treatm Opt Rheumatol 1:119–130. https://doi.org/10.1007/s40674-015-0012-9
219. Wang Q, Wen X, Kong J (2020) Crit Rev Anal Chem 50:359–375. https://doi.org/10.1080/10408347.2019.1637711
220. Yazdani M, Yazdani A, Noori-Mahdavi K, et al (2015) Shiraz E Med J 16:. https://doi.org/10.17795/semj26470
221. Kuwabara M (2015) Pulse 3:242–252. https://doi.org/10.1159/000443769
222. Nyhan WL (2007) Tzu Chi Med J 19:105–108. https://doi.org/10.1016/S1016-3190(10)60001-8
223. Jin Jun Luo XL (2013) Brain Disord Ther 02: https://doi.org/10.4172/2168-975X.1000109
224. Hediger (2004) Therapeutische Umschau 61:541–545. https://doi.org/10.1024/0040-5930.61.9.541
225. Jiang L-L, Gong X, Ji M-Y, et al (2020) Foods 9:973. https://doi.org/10.3390/foods9080973
226. Naidu KA (2003) Nutr J 2:7. https://doi.org/10.1186/1475-2891-2-7
227. Varvara M, Bozzo G, Disanto C, et al (2016) Ital J Food Saf 5:. https://doi.org/10.4081/ijfs.2016.4313
228. (2013) EFSA Journal 11:. https://doi.org/10.2903/j.efsa.2013.3418

229. Carr AC, Rosengrave PC, Bayer S, et al (2017) Crit Care 21:300. https://doi.org/10.1186/s13054-017-1891-y
230. Liebling EJ, Sze RW, Behrens EM (2020) Pediatric Rheumatology 18:45. https://doi.org/10.1186/s12969-020-00439-4
231. Sabatier M, Rytz A, Husny J, et al (2020) nutrients 12:2776. https://doi.org/10.3390/nu12092776
232. Bitziou E, Snowden ME, Joseph MB, et al (2013) J Electroanal Chem 692:72–79. https://doi.org/10.1016/j.jelechem.2012.12.014
233. Zinellu A, Sotgia S, Deiana L, Carru C (2006) J Biochem Biophys Methods 67:95–105. https://doi.org/10.1016/j.jbbm.2006.01.006
234. Kanďár R, Drábková P, Hampl R (2011) J Chromatography B 879:2834–2839. https://doi.org/10.1016/j.jchromb.2011.08.007
235. Moghadam MR, Dadfarnia S, Shabani AMH, Shahbazikhah P (2011) Anal Biochem 410:289–295. https://doi.org/10.1016/j.ab.2010.11.007
236. Okiei W, Ogunlesi M, Azeez L, et al (2009) Int J Electrochem Sci 4:276–287. https://doi.org/10.1016/S1452-3981(23)15128-5
237. Patella B, Sunseri C, Inguanta R (2019) J Nanosci Nanotechnol 19:3459–3470. https://doi.org/10.1166/jnn.2019.16110
238. Zou HL, Li BL, Luo HQ, Li NB (2017) Sens Actuators B Chem 253:352–360. https://doi.org/10.1016/j.snb.2017.06.158
239. Li Y, Lin H, Peng H, et al (2016) Microchimica Acta 183:2517–2523. https://doi.org/10.1007/s00604-016-1897-1
240. Sun H, Chao J, Zuo X, et al (2014) RSC Adv 4:27625. https://doi.org/10.1039/c4ra04046e
241. Kannan A, Sivanesan A, Kalaivani G, et al (2016) RSC Adv 6:96898–96907. https://doi.org/10.1039/C6RA18440E
242. Sharma S, Kumar P, Samra KS (2024) J Solid State Electrochem 28:. https://doi.org/10.1007/s10008-023-05618-3
243. Kumar P, Sharma S, Jabeen S, Samra KS (2022) Electrochim Acta 426:. https://doi.org/10.1016/j.electacta.2022.140738
244. Al-Ghiffari AD, Ludin NA, Davies ML, et al (2022) Mater Today Commun 32:104078. https://doi.org/10.1016/j.mtcomm.2022.104078
245. Shen M, Yan Z, Yang L, et al (2014) Chem Commun 50:15447–15449. https://doi.org/10.1039/C4CC07351G
246. Li Z, Wong SL (2017) Mat Sci Eng: C 70:1095–1106. https://doi.org/10.1016/j.msec.2016.03.039
247. Sarkar D, Liu W, Xie X, et al (2014) ACS Nano 8:3992–4003. https://doi.org/10.1021/nn5009148
248. Xi X, Zeng F, Cao H, et al (2020) Appl Catal B 272:118950. https://doi.org/10.1016/j.apcatb.2020.118950
249. Xing L, Ma Z (2016) Microchimica Acta 183:257–263. https://doi.org/10.1007/s00604-015-1648-8
250. Wu M, Chen S, Soomro A, et al (2019) Environ Sci Pollut Res 26:12123–12135. https://doi.org/10.1007/s11356-019-04672-7
251. Sahu TK, Kumar N, Chahal S, et al (2023) Nat Nanotechnol 18:1430–1438. https://doi.org/10.1038/s41565-023-01484-2
252. Liu C, Zou L, Wang L, et al (2020) J Mater Sci 55:6915–6927. https://doi.org/10.1007/s10853-020-04440-w
253. Zhou S, Ma W, Anjum U, et al (2023) Nat Commun 14:5872. https://doi.org/10.1038/s41467-023-41362-y
254. Zhang J, Xu Y, Liu Z, et al (2015) RSC Adv 5:54275–54282. https://doi.org/10.1039/C5RA07857A

255. Li S, Wang H, Cao K, Huo P (2019) J Taiwan Inst Chem Eng 104:177–186. https://doi.org/10.1016/j.jtice.2019.09.004
256. Guo H-L, Wang X-F, Qian Q-Y, et al (2009) ACS Nano 3:2653–2659. https://doi.org/10.1021/nn900227d
257. Liu C, Zou L, Wang L, et al (2020) J Mater Sci 55:6915–6927. https://doi.org/10.1007/s10853-020-04440-w
258. Wang K, Wu C, Wang F, et al (2020) Biosens Bioelectron 150:111869. https://doi.org/10.1016/j.bios.2019.111869
259. Mazzara F, Patella B, Aiello G, et al (2021) Electrochim Acta 388:138652. https://doi.org/10.1016/j.electacta.2021.138652
260. Anantharaj S, Ede SR, Karthick K, et al (2018) Energy Environ Sci 11:744–771. https://doi.org/10.1039/C7EE03457A
261. Wei Y, Liu Y, Xu Z, et al (2020) Int J Anal Chem 2020:1–13. https://doi.org/10.1155/2020/8812443
262. Kunpatee K, Traipop S, Chailapakul O, Chuanuwatanakul S (2020) Sens Actuators B Chem 314:128059. https://doi.org/10.1016/j.snb.2020.128059
263. Wu Y, Deng P, Tian Y, et al (2020) Simultaneous and sensitive determination of ascorbic acid, dopamine and uric acid via an electrochemical sensor based on PVP-graphene composite. J Nanobiotechnology 18:112. https://doi.org/10.1186/s12951-020-00672-9
264. Zhao Y, Zhou J, Jia Z, et al (2019) Microchimica Acta 186:92. https://doi.org/10.1007/s00604-018-3222-7
265. Li Y, Lin H, Peng H, et al (2016) Microchimica Acta 183:2517–2523. https://doi.org/10.1007/s00604-016-1897-1
266. Zhang L, Yu L, Peng J, et al (2024) iScience 27:109241. https://doi.org/10.1016/j.isci.2024.109241
267. Arrigoni O, De Tullio MC (2002) Biochimica et Biophysica Acta (BBA) - General Subjects 1569:1–9. https://doi.org/10.1016/S0304-4165(01)00235-5
268. Li Y, Chen S, Shao X, et al (2014) Int J Environ Res Public Health 11:2899–2910. https://doi.org/10.3390/ijerph110302899
269. Black CN, Bot M, Scheffer PG, et al (2018). J Affect Disord 225:684–690. https://doi.org/10.1016/j.jad.2017.09.003
270. Rana L, Gupta R, Tomar M, Gupta V (2018) Sens Actuators B Chem 261:169–177. https://doi.org/10.1016/j.snb.2018.01.122
271. Xu X, Zhang H, Li C-H, Guo X-M (2022) Microchem J 175:107198. https://doi.org/10.1016/j.microc.2022.107198
272. INOUE K, NAMIKI T, IWASAKI Y, et al (2003) J Chromatography B 785:57–63. https://doi.org/10.1016/S1570-0232(02)00850-4
273. Aafria S, Kumari P, Sharma S, et al (2022) Microchem J 182:107945. https://doi.org/10.1016/j.microc.2022.107945
274. Han SH, Ha Y-J, Kang EH, et al (2022) Sci Rep 12:12033. https://doi.org/10.1038/s41598-022-16176-5
275. Shahamirifard SA, Ghaedi M, Razmi Z, Hajati S (2018) Biosens Bioelectron 114:30–36. https://doi.org/10.1016/j.bios.2018.05.009
276. Liu Y, Liu J (2022) Analysis & Sensing 2:. https://doi.org/10.1002/anse.202200010
277. Lee CW, Suh JM, Jang HW (2019) Front Chem 7:. https://doi.org/10.3389/fchem.2019.00708
278. Wang Y, Huang Y, Wang B, et al (2016) J Electroanal Chem 782:76–83. https://doi.org/10.1016/j.jelechem.2016.09.050
279. Zhao Y, Zhou J, Jia Z, et al (2019) Microchimica Acta 186:92. https://doi.org/10.1007/s00604-018-3222-7

280. Mazzara F, Patella B, Aiello G, et al (2021) Electrochim Acta 388:138652. https://doi.org/10.1016/j.electacta.2021.138652
281. Shannon RD (1976) Acta Crystallographica Section A 32:751–767. https://doi.org/10.1107/S0567739476001551
282. Wang J, Sun F, Yang S, et al (2016) Appl Phys Lett 109:. https://doi.org/10.1063/1.4961883
283. Yao Y, Ao K, Lv P, Wei Q (2019). Nanomaterials 9:844. https://doi.org/10.3390/nano9060844
284. Diallo A, Tandjigora N, Ndiaye S, et al (2021) SN Appl Sci 3:562. https://doi.org/10.1007/s42452-021-04550-3
285. Gao S, Li X, Li L, Wei X (2017) Nano Energy 33:334–342. https://doi.org/10.1016/j.nanoen.2017.01.045
286. Wang L, Zhang Q, Chen S, et al (2014) Anal Chem 86:1414–1421. https://doi.org/10.1021/ac401563m
287. Chen K, Wang M, Li G, et al (2018) Materials 11:601. https://doi.org/10.3390/ma11040601
288. Hiremath V, Cho M, Seo JG (2018) New Journal of Chemistry 42:19608–19614. https://doi.org/10.1039/C8NJ04850A
289. Tronganh N, Yang Y, Chen F, et al (2016) RSC Adv 6:74436–74444. https://doi.org/10.1039/C6RA15944C
290. Yin X-L, Li L-L, Li D-C, Dou J-M (2018) Int J Hydrogen Energy 43:20382–20391. https://doi.org/10.1016/j.ijhydene.2018.09.047
291. Kumar S, Sharma V, Bhattacharyya K, Krishnan V (2016) New Journal of Chemistry 40:5185–5197. https://doi.org/10.1039/C5NJ03595C
292. Toth M (2002) Mol Hum Reprod 8:271–280. https://doi.org/10.1093/molehr/8.3.271
293. Norazmi N, Abdul Rasad ZR, Mohamad M, Manap H (2017) IOP Conf Ser Mater Sci Eng 257:012031. https://doi.org/10.1088/1757-899X/257/1/012031
294. Mak KF, Lee C, Hone J, et al (2010) Phys Rev Lett 105:136805. https://doi.org/10.1103/PhysRevLett.105.136805
295. Diao KK, Xiao Z, Zhao YY (2015) Mater Chem Phys 162:571–579. https://doi.org/10.1016/j.matchemphys.2015.06.031
296. Khairy M, Mahmoud BG, Banks CE (2018) Sens Actuators B Chem 259:142–154. https://doi.org/10.1016/j.snb.2017.12.054
297. Khairy M, Khorshed AA, Rashwan FA, et al (2017) Sens Actuators B Chem 239:768–775. https://doi.org/10.1016/j.snb.2016.07.165
298. Yamaguchi KS, Sawyer DT (1985) Isr J Chem 25:164–176. https://doi.org/10.1002/ijch.198500026
299. Inagaki M, Itoi H, Kang F (2022) In: Porous Carbons. Elsevier, pp 239–540
300. Lu S, Li C, Zhao YF, et al (2016) Appl Surf Sci 384:360–367. https://doi.org/10.1016/j.apsusc.2016.05.038
301. Ma L, Zhang Q, Wu C, et al (2019) PtNi bimetallic nanoparticles loaded MoS2 nanosheets: Preparation and electrochemical sensing application for the detection of dopamine and uric acid. Anal Chim Acta 1055:17–25. https://doi.org/10.1016/j.aca.2018.12.025
302. Selvam SP, Hansa M, Yun K (2020) Sens Actuators B Chem 307:127683. https://doi.org/10.1016/j.snb.2020.127683
303. Wang X, Yao Q, Tang X, et al (2019) Anal Bioanal Chem 411:943–952. https://doi.org/10.1007/s00216-018-1524-6
304. Raju CV, Ramya R, Imran K, et al (2024) Microchem J 198:110189. https://doi.org/10.1016/j.microc.2024.110189
305. Lynch BS, Delzell ES, Bechtel DH (2002) Regulatory Toxicology and Pharmacology 36:198–210. https://doi.org/10.1006/rtph.2002.1585

306. Yeung D, Kantor S, Nacht S, Gans EH (1983) Int J Dermatol 22:321–324. https://doi.org/10.1111/j.1365-4362.1983.tb02149.x
307. Mallaret M (1995) Arch Dermatol 131:112. https://doi.org/10.1001/archderm.1995.01690130116031
308. Cunningham AA (1956) Arch Dis Child 31:173–176. https://doi.org/10.1136/adc.31.157.173
309. Pan Z, Puente-Urbina A, Bodi A, et al (2021) Chem Sci 12:3161–3169. https://doi.org/10.1039/D1SC00654A
310. Ren W, Zhang Y, Liang WY, et al (2021) Sens Actuators B Chem 330:129390. https://doi.org/10.1016/j.snb.2020.129390
311. Iftikhar T, Asif M, Aziz A, et al (2021) Trends in Environmental Analytical Chemistry 31:e00138. https://doi.org/10.1016/j.teac.2021.e00138
312. Kumar M, Kumara Swamy BE, Hu B, et al (2021) Microchem J 168:106503. https://doi.org/10.1016/j.microc.2021.106503
313. Ta'alia SAH, Rohaeti E, Putra BR, Wahyuni WT (2023) Results Chem 6:101024. https://doi.org/10.1016/j.rechem.2023.101024
314. Ramya M, Senthil Kumar P, Rangasamy G, et al (2022) Chemosphere 308:136416. https://doi.org/10.1016/j.chemosphere.2022.136416
315. Ganesha H, Veeresh S, Nagaraju YS, Devendrappa H (2023) Inorg Chem Commun 156:111228. https://doi.org/10.1016/j.inoche.2023.111228
316. Silambarasan S, Maiyalagan T (2021) Mater Lett 299:130075. https://doi.org/10.1016/j.matlet.2021.130075
317. Hu Y, Yu X, Liu Q, et al (2022) Carbon N Y 188:70–80. https://doi.org/10.1016/j.carbon.2021.11.050
318. Chen J, Walker WR, Xu L, et al (2020) ACS Nano 14:5636–5648. https://doi.org/10.1021/acsnano.9b10182
319. Aslam R, Fatima B, Hussain D, et al (2021) Int J Environ Anal Chem 101:2785–2795. https://doi.org/10.1080/03067319.2020.1711895
320. Ngamchuea K, Tharat B, Hirunsit P, Suthirakun S (2020) RSC Adv 10:28454–28463. https://doi.org/10.1039/D0RA06111E
321. Lopes da Silva AR, Jhones dos Santos A, Martínez-Huitle CA (2018) RSC Adv 8:3483–3492. https://doi.org/10.1039/C7RA12257H
322. Ameen S, Kim E-B, Akhtar MS, Shin HS (2017) Mater Lett 209:571–575. https://doi.org/10.1016/j.matlet.2017.08.100
323. Zhang H, Bo X, Guo L (2015) Sens Actuators B Chem 220:919–926. https://doi.org/10.1016/j.snb.2015.06.035
324. Yin H, Zhang Q, Zhou Y, et al (2011) Electrochim Acta 56:2748–2753. https://doi.org/10.1016/j.electacta.2010.12.060
325. Ding Y-P, Liu W-L, Wu Q-S, Wang X-G (2005) J Electroanal Chem 575:275–280. https://doi.org/10.1016/j.jelechem.2004.09.020
326. Huang K-J, Wang L, Liu Y-J, et al (2013) Electrochim Acta 107:379–387. https://doi.org/10.1016/j.electacta.2013.06.060
327. Wang Y, Li S, Yi J (2016) Sci Rep 6:24153. https://doi.org/10.1038/srep24153